Modélisation numérique et imagerie de la propagation des ondes ultrasonores à travers des interfaces tribologiques

Vipul Vijigiri

N d'ordre NNT: 2020LYSEC07 Année 2020

THÈSE DE DOCTORAT DE L'UNIVERSITÉ DE LYON

opérée au sein de
l'École Centrale de Lyon

ECOLE DOCTORALE MEGA ED162
Mécanique, Energétique, Génie Civil, Acoustique
Spécialité : Mécanique, Acoustique

Soutenue le 11/02/2020

par
Vipul VIJIGIRI

Numerical modelling and imaging of ultrasonic wave propagation through rough interfaces

---

Devant la Commission d'examen composée de :

Rob Dwyer Joyce	Professeur, Univ. Sheffield UK	Rapporteur
Maxence BIGERELLE	Professeur, Univ. Hauts-de-France	Rapporteur
Jean-Luc GENNISSON	DR CNRS, Univ. Paris Sud	Examinateur
Juliette cayer-barrioz	DR CNRS, EC Lyon	Directeur de thèse
Guillaume Kermouche	Professeur, EMSE	Directeur de thèse
Cedric Courbon	Maître de Conférences, ENISE	Directeur de thèse

Laboratoire de tribologie et dynamique des systèmes - Ecole Centrale de Lyon

36, Avenue Guy de Collongue, 69134 Écully Cedex (FRANCE)

Acknowledgements

I would like to thank my PhD supervisors, Dr. Cedric COURBON , Dr. Guillaume KERMOUCHE and Dr. Juliette KAYER BARRIOZ, for supporting me during these past three years. Cedric is one of the smartest people I know. He is an advisor who is enthusiastic, energetic and has the patience to not just supervise students but also to carefully guide them in the right way. He has been supportive and has given me the freedom to explore and as well to learn. He has also provided insightful discussions about the research and what can be adapted.

I am also very grateful to Guillaume Kermouche for his scientific advice and knowledge and many insightful discussions and suggestions. He is the primary resource for getting my research questions answered and was instrumental in helping me crank out this thesis, all in time. I would also like to thank Juliette for her thoughtful discussions and meetings that are but the reasons for me to correct myself and move in the right path. She has been helpful in providing advice many times during my PhD. I also have to thank the members of my PhD committee, Professors Denis MAZUYER, Fabrice THOUVEREZ for their helpful career advice and suggestions in general.

I am grateful to LABEX MANUTECH-SISE (ANR-10-LABX-0075) of Université de Lyon, for the financial support for my PhD within the program Investissements d'Avenir (ANR-11-IDEX-0007), operated by the French National Research Agency (ANR). Also, I am thankful to LTDS laboratory and ENISE that offered me office space to work and also with all the technical support during the PhD period.

I thank all the members of École nationale d'ingénieurs de Saint-Étienne especially Iabelle PLETTO who is extremely knowledgeable in just about everything. She is helpful, and friendly who is always there to help me in the administrative work. Ioan Alexandru IVAN who i worked with for a short time, is a nice and helpful person who has been pretty supportive. I wish to thank Han SANGIL who is a fun and friendly guy to talk with. I am also very grateful to all the academic staff who have always given me a hand to deal with the practicalities of working and being organized with in a group, that made me feel integrated.

I also would like to thank my friends and colleagues Rafal KAMINSKI, Wenxi WANG, Jian CHAO, Axel GIOVENCO, Irati MALKORRA and Synthia DIVIN for their support and friendly environment during my years as a PhD student. Rafal has always been my stress relief. I thank him for his help, guidance and friendship. Wenxi is the one who was there during my hardest of the days. His caring and supporting nature made me

forget all the problems. I will never forget all the funny yet thoughtful conversations that we had in the office.

Jian replaced Wenxi after he left and quickly bonded as a best friend. He is the one with whom I had the best coffee breaks. Irati and Synthia are 2 good friends who have always been a major source of support. All of them are a fun group with lots of enthusiasm and optimism which made it easy for me at ENISE. I would also like to thank all the other who i got to meet but haven't had a chance to really get to know them.

I especially thank my mom, dad, and brother. My hard-working parents have sacrificed their lives for my brother and myself and provided unconditional love and care. I love them so much, and I would not have made it this far without them. My brother had been my best friend all my life. I know I always have my family to count on when times are rough. I thank my beloved uncle Pavan kumar who cared and motivated me like a brother. He is the one who encouraged me to aim high and achieve them. Special thanks to the newest additions, my brother in law Chandrshekar, my wife and as well her wonderful family who all have been caring.

The best outcome from these past three and a half years is finding my best friend, soul, and wife. I married the best person and i give this credit to destiny. Renuka is the only person who can appreciate and sometimes tolerate my quirkiness and sense of humor. There are no words to convey how much I love her. Renuka has been a true and great supporter and has unconditionally loved me during my good and bad times. She has been non-judgmental and instrumental in planning our future. These past several years have not been an easy ride, both academically and personally. I truly thank Renuka for sticking by my side, even when I was irritable and depressed. I feel that what we both learned a lot about life which strengthened our commitment and determination to each other and to live life to the fullest.

I dedicate this thesis to my family, my wife, Renuka
whose unconditional love, encouragement and support made it possible.
I love you all

Abstract

When two surfaces are brought into contact and slide against each other, junctions are formed at the interface. The dynamics of formation, rupture, and evolution of these junctions governs the tribological response of the macro-contact. Getting insight into the real-time behavior of these junctions is a challenging task. Theories state that contacts and asperities are continuously altered in two bodies due to applied pressure and shear, which increases the number of active contacts. To address such conditions, a numerical model of wave propagation through the tribological interface was developed. This method was used to analyze and relate crucial parameters like stiffness, contact width, number of asperities that form a basis for an interface. The first part covers the finite element modeling and mathematical formulation of the interaction of an ultrasonic pulse wave in tribological static contacts, from mono to multi-asperities contacts. The robustness of the model was initially investigated in terms of frequency, mesh size, material properties, etc. Then simulations were carried out using 10 MHz ultrasonic pulse wave propagating along with two aluminium bodies in contact. The transmission coefficient was primarily analyzed as a function of the number and shape of asperities in contact concluding on relating it with the interface stiffness. In the last parts, based on the conclusions obtained from the stiffness analysis, the imaging method was employed considering the potential of data extracted from an ultrasonic array instead of a single transducer. Full matrix capture and total focusing methods were mainly used in extracting data to image the interface and the individual asperities. Frequencies from 10 MHz to 50 MHz were tested in this context to boost the resolution of the image.

Keywords- Wave propagation, Reflection coefficient, contact ratio, Global stiffness, Local stiffness.

Resume

Lorsque deux surfaces sont mises en contact et glissent l'une contre l'autre, des jonctions sont formées à l'interface. La dynamique de formation, de rupture et d'évolution de ces jonctions régit la réponse tribologique du macro-contact. Obtenir des informations sur le comportement en temps réel de ces jonctions est une tâche ardue. Les théories affirment que les contacts et les aspérités sont continuellement modifiés dans deux corps en raison de la pression appliquée et du cisaillement, ce qui augmente le nombre de contacts actifs. Pour faire face à ces conditions, un modèle numérique de propagation des ondes par interface tribologique a été mis au point. Cette méthode a été utilisée pour étudier et mettre en relation des paramètres cruciaux tels que la rigidité, la largeur de contact, le nombre d'aspérités constituant la base d'une interface. La première partie traite de la modélisation par éléments finis et de la formulation mathématique de l'interaction d'une onde à impulsions ultrasonores dans les contacts tribologiques, des contacts mono aux contacts à aspérités multiples. La robustesse du modèle a été initialement étudiée en termes de fréquence, de taille de maille, de propriétés des matériaux, etc. Des simulations ont ensuite été effectuées en utilisant une onde ultrasonore de 10 MHz se propageant le long de deux corps en aluminium en contact. Le coefficient de transmission a été principalement analysé en fonction du nombre et de la forme des aspérités en contact, en concluant par une relation entre celui-ci et la rigidité de l'interface. Dans les dernières parties, sur la base des conclusions tirées de l'analyse de la rigidité, une méthode d'imagerie a été utilisée en considérant le potentiel de données extraites d'un réseau à ultrasons au lieu d'un transducteur unique. Les méthodes de capture matricielle complète et de focalisation totale ont été principalement utilisées pour extraire des données afin d'imaginer l'interface et les aspérités individuelles. Des fréquences de 10 MHz à 50 MHz ont été testées dans ce contexte pour améliorer la résolution de l'image.

Mots-clés: propagation des ondes, coefficient de réflexion, rapport de contact, rigidité globale, rigidité locale.

Table of Contents

List of Figures

Nomenclature

C_{rc}	Real contact area.
C_{ac}	Apparent contact area.
C_s	Contact space.
C_w	Contact width.
N	Number of asperities.
C_r	Contact ratio.
b	Constant value.
K_{BUSH}	Stiffness equation defined in Bushan, 1992.
F	Load applied as defined in contact stiffness section.
m_o	Rms roughness.
t_{dim}	Dimensionless separation between the contacts.
E	Young's Modulus.
ρ	Material density.
μ	Poisson's ratio.
λ	Wavelength.
c	Speed of sound.
f	Frequency.
z	Acoustic impedance.
ω	Angular frequency.
I	Wave intensity.
A	Real amplitude of the propagating wave.
A_0	Attenuated amplitude of the propagating wave.
l	Length of the propagating medium.
R_c	Reflection coefficient.
T_c	Transmission coefficient.
a_i	Amplitude of the incident wave.

a_r . . . . . Amplitude of the reflecting wave.

a_t . . . . . Amplitude of the transmitting wave.

N . . . . . Near field distance.

d . . . . . Element diameter.

m . . . . . Mass per unit area.

k . . . . . Stiffness per unit area.

k^* . . . . . Stiffness of isolated contact.

a . . . . . Radius of the punch.

$R(L,T)$ . . . . . Reflection in lateral and transverse directions.

$T(L,T)$ . . . . . Transmission in lateral and transverse directions.

T_{min} . . . . . Transmission coefficient according to kralikowski.

k_t . . . . . Stiffness of lubricant layer.

B . . . . . Bulk modulus.

h . . . . . Gap thickness.

k_l . . . . . Stiffness of the lubricant film.

d . . . . . Spacing between transducers in array.

t_d . . . . . Time delay.

(x_i,z_i) . . . . . Coordinates of the excited transducer element.

(x_f,z_f) . . . . . Coordinates of the focal point.

A_r . . . . . Axial resolution.

L_r . . . . . Lateral resolution.

F_d . . . . . Focal distance.

D . . . . . Width of the ultrasonic array.

SNR . . . . . Signal to noise ratio.

H_t . . . . . Hilbert transform.

$A(t)$ . . . . . Time domain amplitude data.

$I(t)$ . . . . . Signal with real and complex data.

E_t . . . . . Envelope of the signal.

$D(x,z)$ . . . . . Delay matrix data.

x_p . . . . . Target position in axial direction.

z_p . . . . . Target position in lateral direction.

x_{tx},z_{rx}	Transmitting and receiving coordinated of the transducer array.
$A(tx,rx)$	Amplitude matrix data.
$I(x,z)$	Intensity matrix data for all transmitting and receiving combinations of array.
$I(x,z)$	Intensity matrix data for all transmitting and receiving combinations of array.
CFL	Courant- Freidrichs-Levy
NDT	Non destructive testing.
TFM	Total focusing method.
FMC	Full matrix capture.
$SAFT$	Synthetic Aperture Focusing Technique.
SNR	Signal to noise ratio.
$A-scan$	Amplitude scan.
$B-scan$	Brightness scan.
$C-scan$	Contrast scan.

Introduction

Tribology is the field of study that deals with the behaviour of two interacting bodies in relative motion and especially friction, lubrication or wear. The word tribology derives its name from the roots 'Tribos' and 'Ology'. 'Tribos' is a Greek word which means rubbing and 'ology' is the science or study involving interfacing bodies or surfaces. Tribology as a practice existed since 3500 BC but got more prominent as an engineering field since the 19th century and seen its zenith in the 20th century. Traces of the past indeed proved that human early used lubrication methods such as the Egyptian depiction circa 1338 BC (figure 1a) showing workers using a liquid to lubricate the cart movement. Nowadays, with applications and research ranging from wheel and rail contacts, gears, bearings, rolling, manufacturing processes to biomedical applications, etc, tribology has attracted multiple fields of interest.

The really first scientific approach to friction was hypothesised by Leonardo Da Vinci (1493). He formulated the governing laws of motion of a block moving over a flat surface as seen in figure 1b and especially the friction coefficient, first relation between the resulting tangential force for a given normal load, which was further reformulated by Guillaume Amontons (1699). If perfectly flat surfaces were first considered macroscopically, the investigation of contact between rough surfaces was then developed by Greenwood and Williamson (1966) leading to a new theory on elastic contacts but this time at the asperity scale.

Towards the use of ultrasound in tribology

Whether in dry or lubricated contacts, the phenomena occurring at a micro scale between the asperities of both surfaces, directly govern the real contact area and their tribological behaviour in terms of friction, wear, adhesion or even thermal contact resistance. Being able to predict the real contact area remains a challenge in tribology according to the complex nature of real surfaces. Modelling approaches can be seen as relevant alternatives

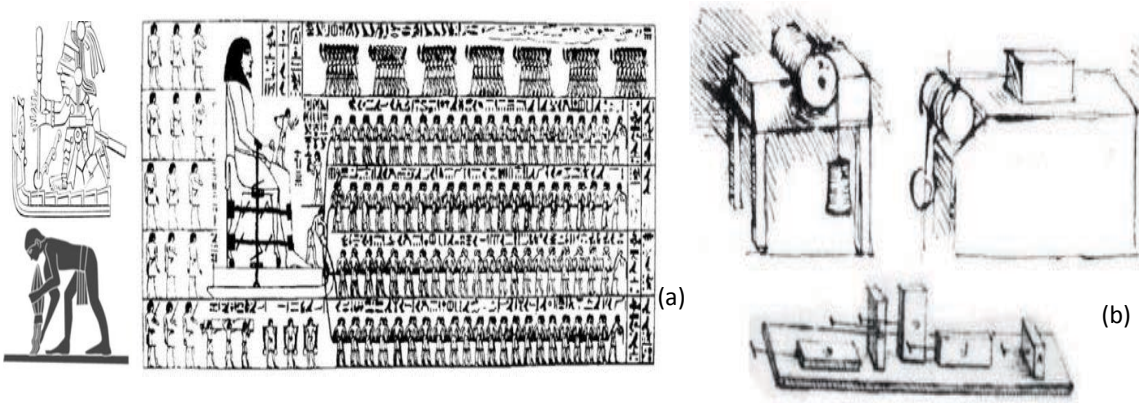

Figure 1: Tribal man rubbing stick on stone to produce friction and heat, an Egyptian cleaner using grease like substance to lubricate the tomb of one of the Pharaohs (Credit: lubewhiz), Egyptian depiction of people pulling the cart state of a Pharaoh and in the close proximity of it is a person pouring lubricant to make the ride smooth (Credits: A. G. Layard, 1983).

but raising questions about their validation and leading to the key issue: how to assess the real contact area in a tribological system?

Widely used in Non-Destructive Testing (NDT), ultrasounds are high frequency sound waves that can be propagated within almost any type of materials and that will be partially transmitted or reflected depending on the acoustic discontinuities they faced. Successfully employed in medical imaging, their main advantages are that original materials of the tribo-system can be used and that data can be collected from regions that would be impossible to access otherwise. The first use of ultrasounds in tribology dates back to [Kracter, 1958] paving the way to (Kendall and Tabor, 1971), (Tattersall, 1973) or N. F. Haines (1980) who investigated, based on reflectometry, the wave interaction with contacting surfaces or cracks revealing a great potential.

Knowledge gap and Motivations

In any static or sliding rough contacts, the number of asperities and their size are the local surface parameters that control their behaviour via the real contact area but also the interface stiffness. Extensive research has been carried out in the past focusing on how to use ultrasounds to measure these parameters (Dwyer-Joyce, 2000). Whereas a valuable relationship was established between the interface stiffness and the reflected part of the wave, its correlation with the number of asperities and size has never been

reported. Limitations regarding the employed experimental setups, the considered scale of investigation, hypotheses related to the proposed wave propagation models could be the reason why this correlation has never been fully defined.

Moreover, significant improvements were achieved in NDT over the last two decades especially with the development of techniques, not only based on a single transducer but rather on an ultrasonic array. Combining relevant excitation procedures and signal processing led to the capability of imaging the inside of a solid and identifying some defects. One can wonder if these developments could be extended to some other fields of application such as tribology, and open some perspectives in terms of instrumentation.

Objective of the work

Considering the ever-existing challenges in tribology, there is a clear need to propose alternative methodologies to probe a contact interface and get new insight. If ultrasounds are appealing, the key issue is to investigate not only the reflection of the ultrasonic wave but its whole propagation at the asperity scale between two contacting rough surfaces.

This thesis aims at assessing the capability of an ultrasound-based measuring technique and improving the understanding of the interaction between an ultrasonic wave and a rough contact interface. A numerical approach has been specifically developed. Following are the key aspects that will be covered in this work:

- To develop a numerical model representing the wave propagation through rough contacting bodies;
- To study the relationship between the contact parameters and wave propagation parameters;
- To develop a method to map or image the real contact zone using several ultrasonic transducers and signal processing methods.

Outline of the Thesis

The thesis is drafted in 6 chapters, where Chapter 1 covers a detailed literature review on fundamentals of tribology defining the interface parameters, ultrasonic wave propagation, ultrasound assessment methods, and ultrasounds applied in tribology.

In Chapter 2, a finite element based approach is developed to model the ultrasonic wave propagation and investigate systematically its interaction with a contact interface. The numerical model has detailed as well as the boundary conditions, modeling of the ultrasonic sensors, and data extraction methodology. Further, a sensitivity study of the model is carried out on a single solid body when subjected to change in the geometrical and physical properties.

Extension to the numerical modelling of a more complex contact interface is done in chapter 3. Using the flexibility of the numerical model, the change in the reflection of an ultrasonic wave concerning the contact morphology is studied in terms of size and number of contact asperities. A special focus is put on the contact stiffness and the relation with the wave transmission is discussed.

Chapter 4 introduces the use of a phased array transducer in studying a rough contact interface. It includes fundamentals, working principle, and state of the art of ultrasonic array-based inspection. A review of the existing imaging methods based on different detection and reconstruction algorithms is presented in detail.

Finally, the numerical modelling of phased array transducers and their use on a rough contact interface is performed in Chapter 5. Design and optimization of the transducer array based on the change in element width and space are presented first, followed by frequency analysis. A reconstruction algorithm is programmed and applied with a specific pulsing sequence leading to the acoustic imaging of different contact configurations. The capabilities and limitations of the techniques are emphasized. The possible implementation of delay laws is discussed to steer the beam over the whole interface and improve the resolution.

A general conclusion ends this thesis by summarizing its contribution and presenting some further perspectives.

Mon cerveau n'est qu'un récepteur. Dans l'Univers, il existe un noyau dont nous tirons connaissance, force et inspiration....

My brain is only a receiver, in the Universe there is a core from which we obtain knowledge, strength and inspiration....

Nicola Tesla

1 Literature review

Contents

1.1 Tribological interface between solids

1.1.1 What is a tribological interface?

A tribological interface is formed when two bodies are pressured on to one another resulting in a geometrically defined interaction. The contact is commonly supposed to be perfect which means that it occurs over the whole surface delimited by the contour of this interaction, leading to an apparent contact area. In reality, at a microscopic scale, the surfaces of the two solids are characterized by rough peaks (asperities) and valleys that contribute to forming the real contact area. The latter is then directly characterized by the way the contact points or asperities are distributed at the microscopic scale as seen in figure 1.1.

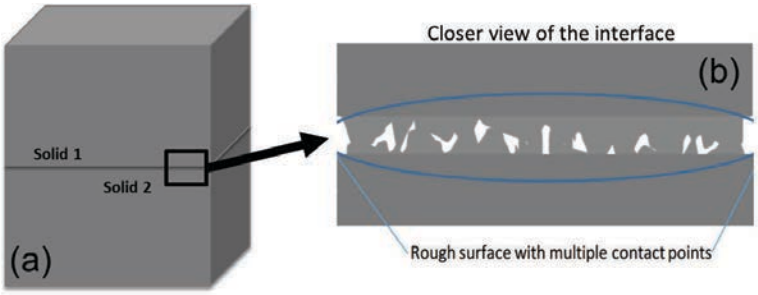

Figure 1.1: (a) General representation of a solid-solid interface with apparent contact zone (b) close or microscopic view of the real contact interface with asperities and spaces in between them.

The real contact area is pretty small in magnitude compared to the apparent one and is calculated based on the number and size of all the asperities in contact. It can vary a lot because in contacting bodies rapid changes can occur depending on the contact conditions such as an increase in the normal load, a sliding motion or the occurrence of a material transfer. Moreover, depending on the surface topography and loading conditions, the exact distribution of the real contact area may cover different interface configurations as seen in figure 1.2. These patterns represent different general cases of contacts ranging from complex pattern of cracks to array of penny-shaped cracks. These

interfaces are inconsistent based on the changes in the fractional area of contact that depends on number of asperities in contact region.

In most of the wear, film thickness or generally speaking any tribological measurements, the knowledge of the contact conditions is very important for various applications.

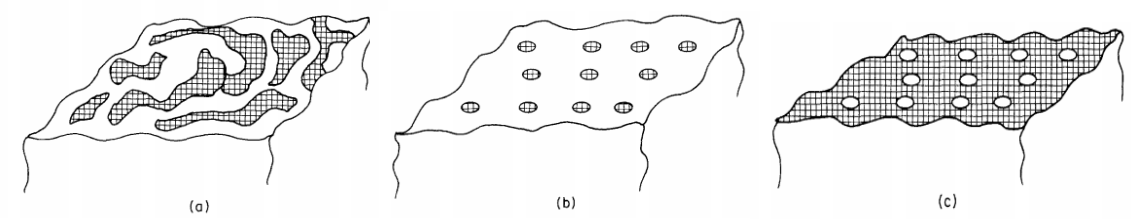

Figure 1.2: Different interpretations of contact interfaces from a general contact to penny shaped contacts (a) General complex contact (b) Non-interacting penny shaped contacts (c) Non interacting penny shaped cracks [Credits: Baik and Thompson, 1984] [1]

1.1.2 How is the interface characterized?

In tribology, a rough contact interface is defined based on asperity distribution over the contacting region. These asperities are the core of any interface and are vital in defining the crucial interface parameters. To understand interface at the asperity level, definitions of interface parameters (contact asperity, contact ratio, real and apparent contact area, stiffness) are given as follows.

1.1.2.1 Contact asperity

Asperities are very small peaks in a contact interface that are not smooth in micro-scale. Two asperities are shown in figure 1.3a when they are closely touching, many such asperities contribute to a rough surface interface.

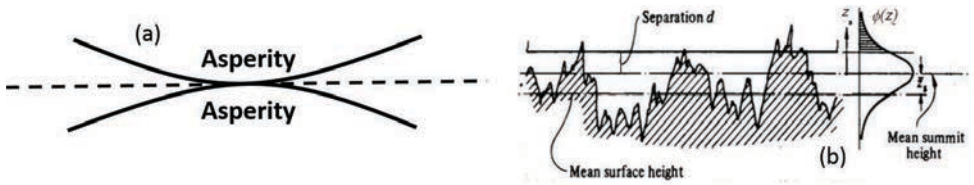

Figure 1.3: (a) Representation of two asperities in contact (b) Gaussian distribution representation of asperity distribution (Greenwood and Williamson, 1966) [2]

Based on the load applied on the interface, the asperity distribution at the surface region could be very uneven and usually defined to be a statistical distribution (like Gaussian, etc) in most of the analytical representations as seen in figure 1.3b. The number of contact points tends to increase and decrease in an interface based on the alteration in the load applied. Figure 1.4 shows a difference in the interface configuration at the asperity scale when subjected to (a) no-load (b) load.

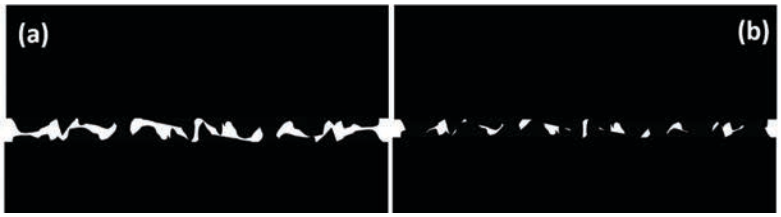

Figure 1.4: (a) Asperity in the interface under no load (b) Asperities in interface when subjected to load

When subject to a normal load, the asperity deformation is consistent in some cases where a uniform asperity distribution is assumed, but in reality, the deformation and distribution get more complicated due to friction, wear, and deformation at the asperity peaks. This was observed by Greenwood, 1966 [2] who developed the theory on micro-asperities and their effects on the real area of contact when subjected to load concluding that, asperity number depends on load alone. Also, for Gaussian distribution, the mode of separation or spacing between asperities, asperity shape are all not important which does not apply to the real rough contacts. This phenomenon was also explained by Yoshihisa Minakuchi, 1985 [3] who studied the contact pressure distribution between two elastic beams and concluded that the pressure distribution on asperities is proportional to the increased load.

1.1.2.2 Real and apparent contact area

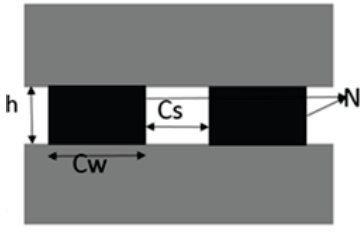

Figure 1.5: Parametric representation of a modelled interface with two asperities

The real contact area is the actual interface area that is formed when two solids are pressed together. It is an important feature that characterizes the interface. If a simple model is assumed with defined asperities distribution as seen in figure 1.5.

then the real contact area C_{rc} and apparent contact area C_{ac} are defined as,

$$C_{rc} = NC_w \tag{1.1}$$

$$C_{ac} = N(C_w + C_s) \tag{1.2}$$

Where Cw is the contact width of each asperity in contact, Cs is the contact space, N is the number of asperities in contact. The defined contact area also defines another important parameter called contact ratio.

1.1.2.3 Contact ratio

Contact ratio is defined as the ratio between the real contact area and the apparent contact area as seen in equation 1.3 and its value falls between 0 and 1. Contact ratio is considered as an important parameter defining the contact conditions at the interface.

$$C_r = \frac{real\ contact\ area}{apparent\ contact\ area} \tag{1.3}$$

In most of the referred works in this thesis, contact ratio is not addressed in great detail due to its complexity and dependency on the real changes occurring in the contact such as asperities distribution and properties. Direct analysis cannot be conducted on the contact ratio. However, if the crucial parameters (number of asperities, contact width, space) are assumed to be known, the contact ratio can be used to study the interface changes.

1.1.2.4 Contact stiffness

Contact stiffness, i.e. the stiffness of the interface between the two contacting bodies, is the interface property that will govern the relative displacement of the bodies when applying a normal load as shown in figure 1.6. If the contact is assumed to be perfect, meaning a contact ratio close to 1, the stiffness goes to infinite. This is not the case in a real rough contact where the interface will be able to withstand a certain degree of deformation.

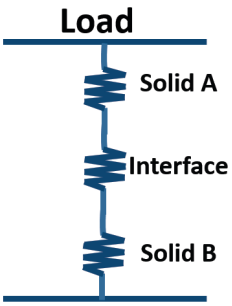

Figure 1.6: Spring indication of individual bodies with its own stiffness

This stiffness parameter is very important in contacting surfaces in various applications where the friction, contact area, and vibrational response is of vital importance. A first approach to the study on rough contacts was conducted on a contact interface between two elastic paraboloids resulting in a relationship between the nominal force and contact area defined as Hertzian solution for spherical contacts (S. Timoshenko and J.N. Goodier, 1951)[4]. It has been reported that the contact area proportionally increases with force and thus the stiffness. From the contact area analysis, several analytical approaches were developed based on two nominally contacting surfaces, one of which is the work done by A. W. Bush, 1975 [5]. They used the random process model (The random process model is based on an assumption of the surface height and its derivatives at a particular contact) developed by Longuet Higgins [6] to analyze the static contact of elastic rough surfaces. Conclusions are that there is a strict proportionality between the load and contact ratio for large asperity separation and stiffness for this case will be very small and approximately linear for large separation given as,

$$K_{Bush} = (\frac{\omega_1 z_1}{2})\frac{C_{ac}}{\sqrt{m_o}}\frac{dF}{dt_{dim}} \tag{1.4}$$

Here C_{ac} is the nominal contact area, F is the load applied, m_o RMS roughness, t_{dim} is the dimensionless separation, ω_1 is the Hertzian displacement and z_1 is the height above mean plane. Based on the above equation stiffness is proportional to load and inversely proportional to the roughness. Based on the presented analytical models, the theoretical explanation to normal and tangential stiffness per unit area is derived by Krolikowski Szczepek, 1993 [7] who worked on modelling rough contacts by assuming a statistical distribution of the surface topography. Their work is mostly concentrated

on the shape of the asperities, which gives the estimate of the real contact area and stiffness. Polycarpou, 2005 [8] worked on an experimental procedure to relate the stiffness to rough contact parameters and concluded that stiffness is low for Hertzian type of contacts when compared to plane surfaces. Also, in both the contact types, contact stiffness increase with contact load is not linear.

M.E. Kartal, 2011 [9] worked on an experimental procedure and finite element modelling (Digital image correlation method) to accurately measure the tangential stiffness between rough contacts using titanium alloy as the test sample. It is concluded that the tangential stiffness is proportional to the contact area (further discussed based on results in section 4.3). In recent years the work done by Dayi Zhang, 2017 [10] is mentioned based on a theoretical model that predicts the interfacial stiffness (calculated based on integrating the stiffness of a single elastic asperity) of fractal rough surfaces. The prediction process makes use of an inverse identification method based on a finite element model of an interface and tries to fit the experimental results. There have been many analytical and experimental approaches to study rough contacts and stiffness but very few finite element approaches were documented at the asperity scale such as those developed by Wei Wang, 2012 [11], T. A. Laurson, 2013 and L. Kogut, 2003 [12]. This motivates a detailed study on contact stiffness in the interfaces.

1.1.3 Challenges in interface characterization

In most of the wear and contact interface related measurements, the knowledge of the contact condition is crucial. Knowing the contact area in a rough contact or a sliding contact is still an up to date research issue in tribology, even when considering only the apparent one. Based on Hertz's theory, if it is considered that an interface is comprised of multiple asperities, the real contact area can be evaluated by summing the apparent area for every single asperity which is not true for rough sliding contacts where asperities are shaped differently. Challenge with such conditions is that, to date, characterizing the interface (real contact area, stiffness) is very difficult at the micro-level and even more difficult in-situ or ideally, on-line. Apart from the modelling developments, NDT methods were developed and attempted to assess in-situ such contact interfaces. A few of the methods are explained in the following sections.

1.2 Non-destructive testing assessment methods

Non-destructive testing is a compilation of methods that are used in evaluating the test subjects without altering its current status. There are numerous methods that are and can be adapted in tribological applications.

1.2.1 Optical Interferometry

Optical interferometry is a very popular method in tribology as it allows to detect apparent and real contact area [13], film thickness distribution for lubricated contacts [14], etc. This method uses light (monochromatic or white light) and the interference patterns created when the optical path is modified by the presence of a medium of a different index (gap, lubricant, etc). However, it requires one of the two bodies in contact to be transparent, limiting its development to a few tribological applications or more fundamental investigations.

1.2.2 Radiography

This technique uses radioactive X-rays or neutron sources. By using multiple receivers, a tomographic arrangement can also be realized for three-dimensional (3-D) reconstruction of the interior of the structure. The advantages are that it is sensitive and can be used to study cracks of different shapes and sizes. The limitations of using radiography are that it is not safe due to radiation devices, it is time-consuming and expensive, efficiency is dependent on the geometry and orientation of the crack. Due to the limitation in radiation scaling or penetration strength, it cannot be applied to detect very small cracks or defects. It requires testing to be done in multiple angles to attain accurate results. Some of the recent works on fretting testing using this method to study cracks are done by Buffiere, 2005, and Fouvry, 2007 [15] [16].

1.2.3 Thermal Imaging

Thermal imaging is a technique that gives the image of heat distribution over the testing subject. This method makes use of infrared cameras to capture temperature changes. It has applications in lamination and leak detection in thermal ducts, clack detection, and

condition monitoring. The defect/gap detection is possible by measuring the difference in the thermal conductivity due to the presence of a defect [17]. This method is fast and requires minimal processing to produce images, it can then be applied and adapted from very small surfaces to large air crafts. It can accurately produce the images of the testing sample. Limitations are that only the surface can be imaged, a critical temperature always has to be maintained to image the target. It has a very low penetrating power and thus cannot detect deep flaws.

1.2.4 Acoustic emission

Acoustic emission is a technique that relies on the resulting energy released during the formation and opening of cracks when heavy stresses are exerted on the testing sample. This process makes use of piezoelectric sensors mounted on top of the structure to monitor structural integrity. Acoustic emission has been widely used in studies like aircraft efficiency study, structural health monitoring, material testing, wind turbine analysis, submarine leak detection, etc, [18]. Advantages are that it is non-destructive, highly sensitive, can be used as an in-situ study method, high accuracy crack detecting, etc, although, the limitations are that it is not always accurate under conditions where it experiences a lot of noise and attenuation.

1.2.5 Electric conductivity

Electric conductivity is the basic property of the material which defines to what extent it can conduct electric current. It has been extensively studied to characterize a contact interface based on conductivity [19]. As the size and number of contacting asperities increases, the solid junctions conducting electricity become a transport tool, resulting in changes in the interface conductivity that is measured. However, the measurement method is providing an average measurement of the whole contact interface and is found to be sensitive to the formation of an oxide layer.

1.2.6 Ultrasonic techniques

The ultrasonic inspection technique is the most recent yet popular method that holds strong ground in NDT. It uses active sound to propagate along with the test subject to study the geometrical changes i.e. cracks, gaps, etc. Ultrasound is not limited to any material types and can propagate through any material. It has a wide range of applications in various fields due to its high penetrating power for deep sample testing. Ultrasonic inspection is efficient in addressing material thickness, it can accurately locate surface and subsurface cracks and defects and image them. It is cost-effective (piezo transducers available in the market but expensive for commercial ultrasound probes) and fast. Limitations are that transducers that emit ultrasound have to be perfectly coupled to have high signal information and often a high optimization is previously needed. In some cases, special signal processing techniques are needed to process the collected signals.

1.3 Conceptual background of Ultrasound

1.3.1 Wave propagation basics

An acoustic wave is characterized by the frequency at which it is operated. Those with a frequency larger than 20,000 Hz, i.e. above the limit of human hearing range, are referred to as ultrasounds. In ultrasonics, the wave propagates as a vibrating or oscillating pressure that creates a certain displacement in the medium that it is being concentrated.

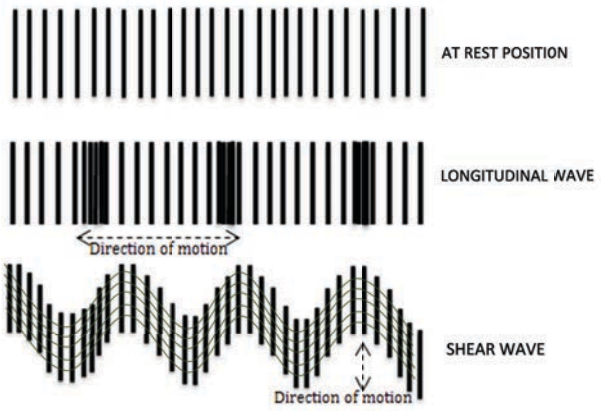

Figure 1.7: Wave propagation mode types

A common method to generate ultrasounds is via the mechanical vibrations induced by a piezoelectric crystal. The traveling wave from the transducer follows a constructive and destructive wave pattern (nodes and anti-nodes). There are two basic types of waves traveling patterns as seen in figure 1.7. The first is the longitudinal or compressional wave, in which the motion of a particle in the medium is only in the direction of propagation. Second is a shear wave, with the motion of a particle in the medium is transverse to the direction of propagation. Other waves such as Lamb or Rayleigh waves, can also be generated and will travel over the surface and thus are referred to as surface waves. Any ultrasound propagating in a medium is characterized based on the parameters that form an acoustic wave, i.e. wave intensity, velocity, and frequency.

1.3.2 Ultrasonic wave properties

1.3.2.1 Ultrasonic wave intensity

Wave intensity is the power with which the wave propagates through a medium and is defined as the power per unit area given as,

$$Intensity(I) = \frac{Power(W)}{area(m^2)} \tag{1.5}$$

Power is calculated based on square times the amplitude of the propagating wave. A wave is transmitted along the targeting body with a specific intensity, making sure that the reflections and transmissions are recorded through the interfaces. In general terms, it is given by equation 1.6.

$$dB = 10log(\frac{I}{I_o}) \tag{1.6}$$

where I_0 is the intensity of the given signal and I is the intensity of the reflected signal. In most of the wave propagating applications, the energy that manages the wave intensity level is defined by the power or voltage given as input. The wave with a defined intensity and amplitude spreads out in all the possible directions. This spreading will result in the reduction of wave intensity. The wave intensity is then related to the amplitude and inversely proportional to the distance that the wave travels, equation 1.7.

$$I \propto \sqrt{A} \propto \frac{1}{d} \tag{1.7}$$

It also varies based on the direction of the wave. For example, when a wave is traveling from the source, as it reaches twice the distance from the source, the amplitude at that point will be half of the initial intensity due to backscattering. The above-mentioned criteria have to be maintained between the distance and amplitude in order to avoid the problem of wave attenuation.

1.3.2.2 Ultrasonic wave velocity

A sound wave propagates as a varying pressure within a defined medium. Every particle of this medium exhibits a relative displacement at a given speed which directly depends on the elastic properties (Young's modulus and Poisson coefficient) and density of the medium. The velocity of the compressing wave is then given as in the equation 1.8.

$$c = \sqrt{\frac{E}{\rho} * \frac{1-\mu}{(1+\mu)(1-2\mu)}} \tag{1.8}$$

Here c is the wave velocity, E is Young's modulus, ρ is the material density and μ is the Poisson's ratio. For example, the speed of sound in air is 343 m/s whereas the speed of sound in water is around 1500 m/s. For a defined ultrasonic wave, the velocity is calculated based on the compressibility of a relative medium. A subject with high compressibility has a slow speed of sound and vice versa. For instance, liquids have slow velocity compared to solids.

1.3.2.3 Ultrasonic wave frequency

Most of the ultrasonic testing frequency range falls between 20 KHz to 100 MHz. Low ultrasound frequencies in the range of 20 KHz-2 MHz are mostly used in cleaning, processing, power ultrasound, or sonochemistry. High-frequency measurements are used in precision testing due to their focused wave propagation. The frequency is an important feature of the wave as it, combined to the wave velocity, determines the wavelength as given in Equation 1.9.

$$\lambda = \frac{c}{f} \tag{1.9}$$

Wavelength is considered important for shaping the beam profile and also to define the near field distance. Also, high-frequency waves have a shorter wavelength, meaning larger resolution but also reduced penetration. On the contrary, lower frequency waves have a longer wavelength, reduced resolution, and effective or strong penetration in a solid. As a consequence, assuming an application in tribology, ideally, at the asperity scale, high frequencies (200 KHz-50 MHz) are expected to be needed. This can already be foreseen as a challenge of applying this technique.

1.3.3 Reflection and transmission coefficients

Acoustic impedance is a physical property building the relationship between sound pressure and particle velocity. In ultrasound-based applications, impedance is the resistance that an ultrasonic wave experiences when propagated along a specific medium. The figure corresponding to the impedance of two solids is given in 1.8 In terms of velocity and density, it can be written as seen in equation 1.10,

$$z = \rho c \tag{1.10}$$

Here z the acoustic impedance, ρ and c are density and wave velocity respectively. Let us assume that two solid bodies are in contact and perfectly coupled with each other as shown in figure 1.8. An ultrasonic wave is generated from a transducer and passed through the medium A.

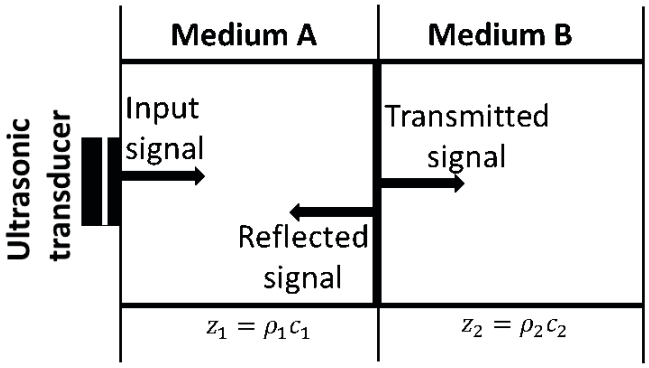

Figure 1.8: Reflection and transmission of an ultrasonic wave when propagating through two different media

If both the media have the same material type, a perfect impedance match is expected and almost all the waves will be transmitted, without any reflection. If the medium A and

medium B are made of different materials, due to the differences in acoustic impedance, the wave will be completely or partially reflected. Acoustic impedance for some of the most commonly used materials are shown in table 1.1.

Material type	Aluminium	Steel	Titanium	Copper
Acoustic impedance (kg m^2s)	17*10^6	46*10^6	28*10^6	41*10^6

Table 1.1: Reflection and transmission of an ultrasonic wave when propagating through two different media, (NDT resource 2018)

As seen in figure 1.8, if we assume the geometry and wave is incident on to the interface, the reflection coefficient is measured as the ratio of the displacement or pressure amplitude of the reflected wave on the incident wave. Accordingly, the transmission coefficient is the result of the ratio between the transmitted one on the incident one, as given in equations 1.11 and 1.12.

$$R_c = \frac{a_r}{a_i} \tag{1.11}$$

$$T_c = \frac{a_t}{a_i} \tag{1.12}$$

a_i,a_r,a_t are the amplitudes corresponding to the incident, reflecting and transmitting waves. If we relate the same expressions in terms of density and velocity, then the reflection and transmission coefficient can be computed as

$$R_c = \frac{\rho_2 c_2 - \rho_1 c_1}{\rho_2 c_2 + \rho_1 c_1} \tag{1.13}$$

which can be written as

$$R_c = \frac{z_2 - z_1}{z_2 + z_1} \tag{1.14}$$

$$T_c = \frac{2z_2}{z_2 + z_1} \tag{1.15}$$

R_c and T_c are the reflection and transmission coefficients respectively. When a wave is propagated along an interface, the wave is partially reflected or transmitted based on asperity size and distribution. The reflected/transmitted coefficients are valued between

0 and 1. These parameters R_c and T_c are the basis for studying defects and cracks in materials, E. R. Generazio, 1984 [20].

1.3.4 Energy losses during the propagation

When an acoustic wave propagates through a medium, the energy at which it travels is dissipated along its propagation path. Three main modes such as attenuation, scattering, and diffraction are responsible for this energy loss. This leads to a reduction of the intensity or amplitude and thus it attenuates the wave along the direction of the propagation.

Attenuation

Attenuation is prominent in most of the applications that use ultrasound but depends mainly on the propagating material. The equation corresponding to it is given as,

$$A = A_o.e^{-\alpha d} \tag{1.16}$$

Here A_o is the real amplitude of the propagating wave, A is the attenuated amplitude of the travelling wave, α is the attenuating coefficient and d is the distance travelled over time. The attenuation coefficient of ultrasound is designated as α in dB/cm given as,

$$\alpha = l * f^n (approximated\ to\ n = 1) \tag{1.17}$$

Here l is the length of the propagating medium and f is the wave frequency. In terms of frequency, attenuation factor increases at higher frequencies due to a decrease in the wavelength that affects the propagating speed, F. S. Foster, 1986 [21].

Attenuation could happen for example due to wave absorption when the ultrasonic energy is converted to other energy forms (temperature) during the wave propagation (NDT, 2007).

Scattering

The second mode is wave scattering which is reflection of sound in all the other directions excluding the direction of incidence. Figure 1.9 shows a simple interpretation of incident wave and scattering when the wave hits the rough interface between two bodies in contact , J. Blitz, 1995 [22], J. L. Rose, 2014 [23].

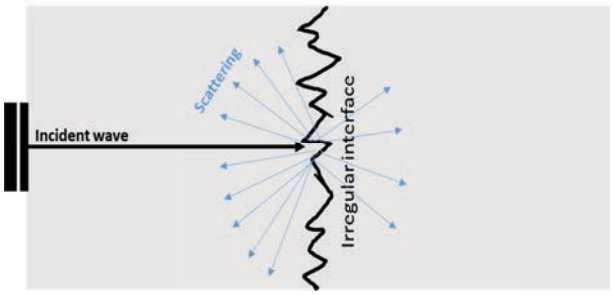

Figure 1.9: Scattering when an incident wave propagates through the interface

Generally, in rough surfaces and contact, the wave scattering energy depends on the size (width) of the asperities in the interface compared to the wavelength. If the interface is small enough compared to the wavelength, a part of the wave is reflected and a part is transmitted, a very small amount is scattered. On the contrary, if the defect or asperity size is small, the wave experience high scatters in all directions depending on the morphology of the interface. These scatters interfere with the expected reflected signal resulting in a noisy output spectrum. In general, to reduce the noise, signal processing filters are adapted to filter out the unwanted scatters and retain the original signal.

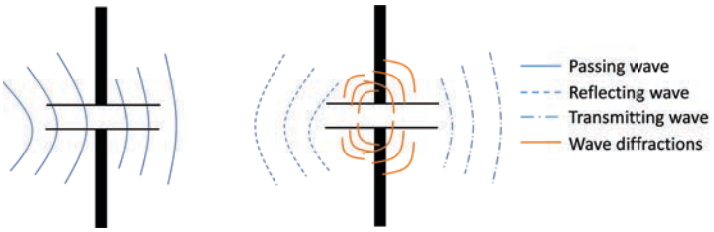

Figure 1.10: Diffraction effect representation between two asperity edges

Diffraction

Diffraction is a third attenuation mode similar to scattering where, when the wave reaches a discontinuity, at each of the discontinuity edges, the wave will spread as seen in figure 1.10. If a defect/gap/valley is considered, scattering happens around the contacting region in larger amplitudes whereas diffraction happens at the contacting edges in very low amplitudes, M.G. Silk, 1979 [24]. In a contact, these diffractions could happen at a very small scale and will have less effect compared to scattering. In most of the ultrasonic measurements, the diffractions are not particularly investigated as they are dominated by the scattering, unless if they disrupt the original signal.

Near and far field effect

When a transducer is pulsed, multiple waves are generated and interact with each other along a certain distance within the ultrasonic beam. These interactions lead to a fluctuating pressure amplitude due to the constructive and destructive combinations of the waves.

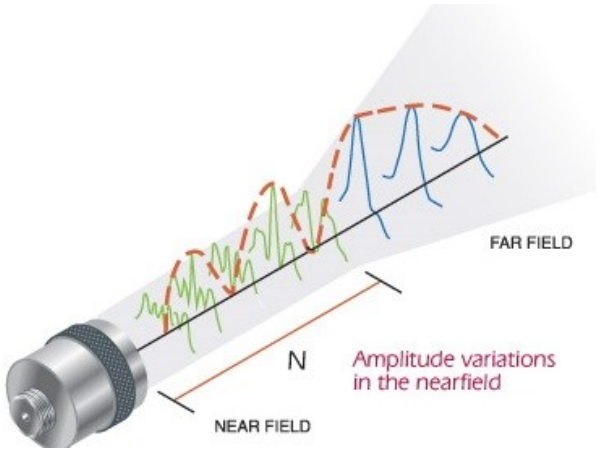

Figure 1.11: Near and far field representation of a wave with varying amplitudes (Credits: Olympus NDT 2018)

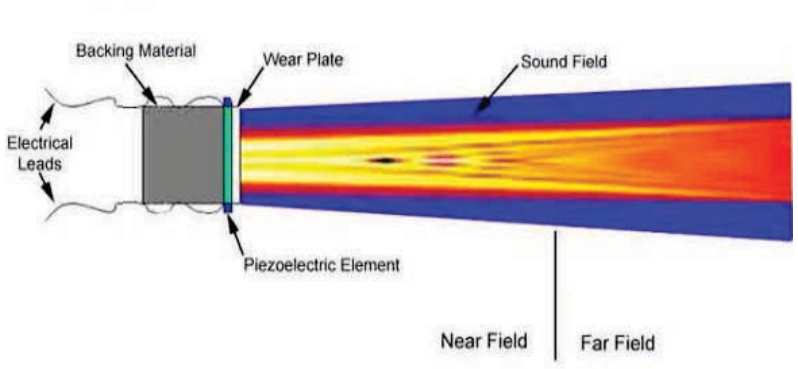

Figure 1.12: Beam profile representation of the near field and far field effects (Credits: NDT resource center 2018)

The distance after which this phenomenon stabilizes is called the near field or the Fresnel region and is illustrated in figure 1.11. In the near field, the amplitude fluctuations are so large that in flaw detection applications, these multiple amplitude levels can lead to misinterpretation of the reflected signal. Once the sound wave crosses the Fresnel region, the wave has a more stable amplitude distribution called the Fraunhofer region. In figure 1.11, N_{near} is the distance defining the end of the near field. For a given transducer

width, the near field distance is proportional to the frequency. Also, in the near field, the intensity along the projected beam is inconsistent which would look more like concentric rings within the beam profile as seen in figure 1.12.

The near field distance N_{near}, is related to the element diameter D, frequency f and speed of sound c as,

$$N_{near} = \frac{D^2}{4\lambda}(\lambda = \frac{c}{f}) \tag{1.18}$$

This concept of near field is important in ultrasonic measurement because in most of the contacting bodies the interface could happen at a particular distance that falls under the Fresnel or Fraunhofer zone. Consider a pulse receiver very close to the interface, the reflecting changes might be corrupted with the amplitude changes that are already there in the near field. To avoid this problem, the transducer has to be placed considering the width and distance of the inspecting element.

1.4 Ultrasound assessment methods

Various methods using ultrasound exist to detect subsurface heterogeneity. The pulse-echo method is the most used ultrasonic measurement method, which is based on the time of flight between the pulsed and reflected signal collected by the same transducer. Pitch catch method is another one, which measures the time taken for a pulse to be reflected from the target to a second transducer.

1.4.1 Through transmission technique

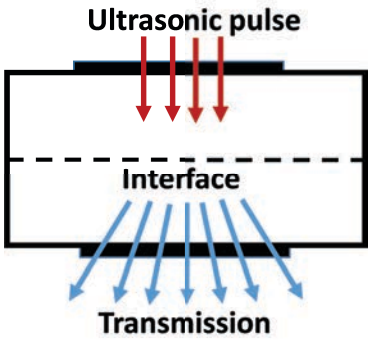

Figure 1.13: Through transmission method with Incident pulse in red and propagation in blue

Through transmission employs two transducers placed on both sides of the test sample as seen in figure 1.13. The transducer on one end of the sample is used as the transmitter and the other one as the receiver. This method is usually employed where the sample can be accessed from both sides. Through transmission has a limitation because it needs two-way access and sometimes misconfiguration (misalignment of the transducers) may lead to inaccurate results. J. L. Rose, 2014 [23] refers to the through-transmission method as being efficient in dual-probe imaging where the dual-frequency is implemented. Gregory Sharat Lin, 2002 [25] patented this dual frequency-based through-transmission method. Apart from these, it remains one of the strong methods in two-way structural analysis.

1.4.2 Pulse echo method

Pulse echo method is the most widely used ultrasonic testing technique. In this case, a single transducer is placed on one side of the test sample and acts as both transmitter and receiver as seen in figure 1.14.

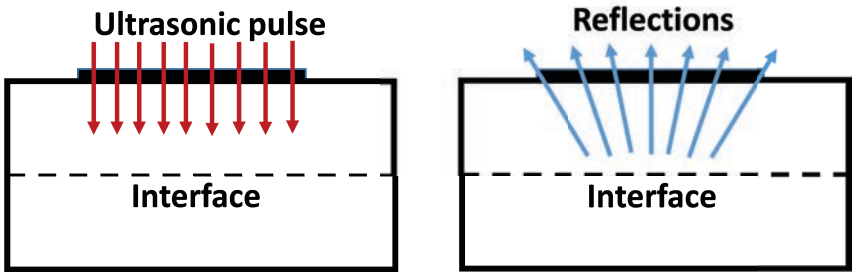

Figure 1.14: Pulse echo method (In red is the transmitted pulse and in blue are the reflections)

The concept of through transmission and pulse-echo are similar in terms of sending a wave but unlike through transmission, only the signals that are reflected are measured. In the pulse-echo method, once the reflections are recorded, the scattering, attenuation, and velocity of the waves can be determined as shown by, A. R. Selfridge, 1985 [26]. This method is simple as only one surface access is needed and it can be applied where there is no possibility of through transmission. The pulse-echo method in recent years has been researched for application in various fields.

1.4.3 Pitch catch method

Pitch catch method as seen in figure 1.15 is a hybrid of pulse-echo method and through transmission method. Two transducers are used to excite and receive, and both the transducers are placed on the facing side of the material. The wave is propagated into a test material at a specific angle to hit the target and is reflected following the angle of trajectory. Pitch catch method is limited to applications where precise information is known about the target region.

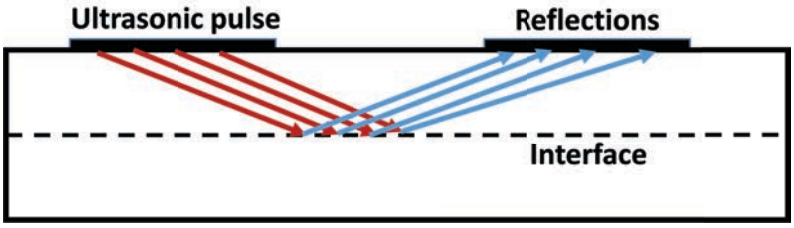

Figure 1.15: Pitch catch method (In red are the transmitting lines and in blue are the reflections)

It also experiences a calibration problem on the distance between the placement of the transducer: a prior study is needed to place the transducer accurately for all the reflections to be recorded. High attenuation and scattering due to multiple reflectors that travel from one edge to another in multiple directions in some of the regions is another problem that limits the pitch-catch method to large defects. This is not the case with the through transmission and pulse-echo, as the beam profile is expected to be more focused reducing reflections along the edges.

1.4.4 Phase transducer array

Phased transducer array is a group of very small piezoelectric elements that can be individually pulsed. This transducer array similar to the previously mentioned methods, but the major advantage is that they are adaptive and can be implemented in multiple ways [27]. An array consists of N number of elements organized in linear, annular, or 2D patterns. Each transducer can be individually excited and recorded in pairs or multiples. The ultrasonic wave can also be beamed at a specific point or angle by adapting a delay law between each element. The major advantage over traditional methods is their ability to produce acoustic images within the depth of a solid by using a proper pulsing sequence

and post-processing of the signal thus making them popular in imaging. This reduces the inspection time and complexity in measuring complex interfaces but requires some development in the processing algorithms and the hardware that can deal with a significant amount of data. [28], [29], [30], [31] are some of the researchers who initially worked on phased transducers specifically focusing on NDT.

1.4.5 Immersion based testing

Immersion testing is a non-destructive method that uses liquid as a medium of sound propagation. In this method instead of using a transducer directly mounted on the test subject, it is immersed in water. This is an advanced method that is used in a crack or flaw detection and also in characterizing an interface. Immersion testing provides uniform coupling with less attenuation and loss but specific transducers have to be used to precisely focus on to the target region, M. A. Goni Rodrigo, 2013 [32], X. Yin, 2003 [33]. However, it applies to limited sizes that fit in the immersion tanks. Phased transducer array and immersion method, in this case, are complementary as the beam can be focused at any angle, and also high resolution can be achieved with the use of high frequencies which is not possible with direct contact measurement methods, Rob Dwyer Joyce, 2008 [34].

1.5 Ultrasound application in tribology

A tribological interface, be it static or sliding, is very complex and its behaviour results from multi-scale physical phenomena. The interfacial zone between two static contacting materials is prone to changes due to pressure exerted on them and between two sliding contacts, due to the friction, deformation, etc. As already emphasized, an important factor that is still very complicated to assess, even in static configurations, is the contact area. It is indeed complicated to directly in-situ access the contact zone without disturbing it.

In the micro-scale, the asperities in a real contact area smaller than 10µm and it is complex to define the exact relation between crucial parameters such as stiffness and real area of contact. As introduced in Section 1.2, several NDT methods have been developed in this context of which ultrasound-based NDT stands strong as far as tribological issues are concerned.

1.5.1 The spring model / Reflection through the interface

The early use of ultrasounds in tribology settled the first theoretical basis relating the reflection and transmission from a tribological contact and was put forth by Tattersall, 1973 [35]. He developed the now very popular spring model, as illustrated in figure 1.16 a, where the interface is represented as a homogeneous layer between the two contacting bodies. The interface is thus assumed here as a combination of springs with a defined stiffness, k as seen in figure 1.16b.

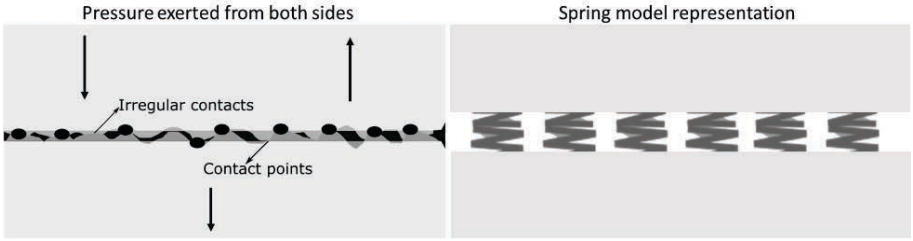

Figure 1.16: (a) Real contact interface representation (b) spring model representation

The spring model simplifies the complicated morphology of a contact interface by building the relationship between ultrasonic wave parameters and the analytical stiffness. In this model, the interface is assumed as the combination of springs that in the end contribute to the global stiffness and a uniform pressure is exerted on both sides of the solids. As the number of asperities in an interface increases, the increased density makes the wave to propagate through it completely or partially. In some cases, for perfect contact, the wave is completely propagated. If a real interface is assumed, the ultrasonic reflection relating to stiffness is given as follows,

$$R_c = \frac{z_1 - z_2 + i\omega(z_1 z_2/k)}{z_1 + z_2 + i\omega(z_1 z_2/k)} \tag{1.19}$$

Here R_c is the reflection coefficient, z_1,z_2 are the impedances of two interfacing bodies, ω the wave angular frequency and k is the stiffness. The equation can take a simpler form if the contacting solids are made of the same materials, i.e. same acoustic impedance (z_1=z_2=z), equation 1.20.

$$|R_c| = \frac{1}{\sqrt{1 + (\frac{2k}{\omega z})^2}} \tag{1.20}$$

With this approach, the author presents the first method to assess in-situ the stiffness of an interface based on ultrasonic measurements using reflected signals. Based on this spring model, various approaches were later presented on rough contact study or lubricated contacts. The relationship between reflection coefficient and stiffness forms the basis for much interesting analysis as an interface can be accessed for different loading conditions based on the amount of reflection recorded for each amount of load applied. Also, using stiffness, the lubricant film thickness at the interface can be studied.

1.5.2 From contact mechanics to ultrasounds

Greenwood, 1966 [2] worked on the dry contact of two rough bodies. Assuming either a Gaussian or an exponential distribution of asperities for both surfaces, they were able to calculate the area of contact and the local contact pressure. They showed that the real contact area and the number of micro-contacts between asperities are proportional to the applied load and depend on the average radius of curvature of the asperity.

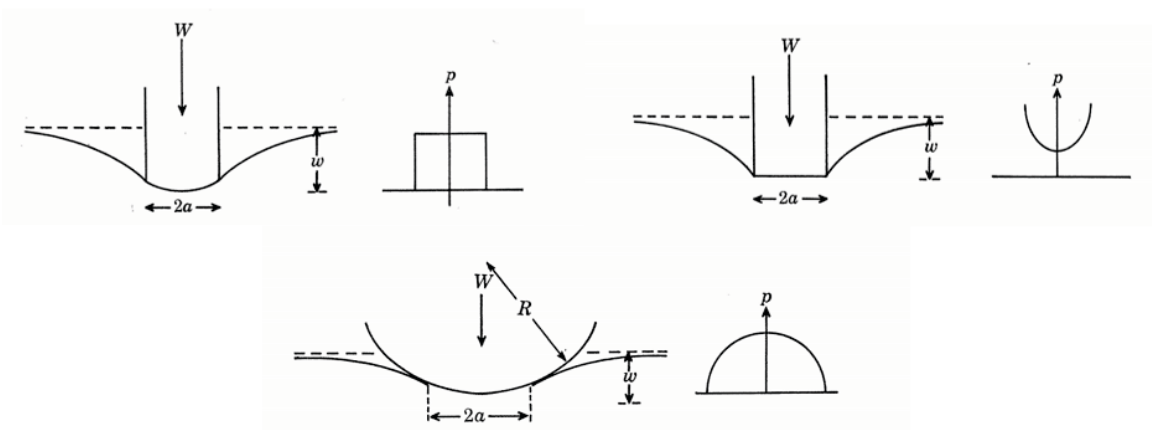

Figure 1.17: . Solid deformation with change in pressure (a) Uniform pressure distribution (b) Sharp punch with infinite pressure (c) Spherical punch aero pressure (Kendall and Tabor, 1971)

From contact mechanics to ultrasound implementation, Kendall and Tabor 1971 [36] were the first ones to attempt an application of ultrasonic techniques to true contact area measurement. They assumed a single solid punch pressed on to an elastic solid with a normal force W, with different variations of pressure, as seen in figure 1.17. In reference to the derived equations by them in the paper [36]. Stiffness equation is given as follows,

$$S = C_x.Ea \tag{1.21}$$

Here C_x is a constant, E is Young's modulus, a is the radius of the punch. As specified, the constant here C_x varies from $\pi/(2(1-v^2))$ and $2/((1-v^2))$. For instance, for rubber, this parameter lies between 1.9 and 2.4. This leads to a small dependency of the stiffness with the pressure distribution, as shown in figure 1.18 where the evolution of the stiffness can be seen as a function of the diameter of brass cylinders pressed against a soft rubber block.

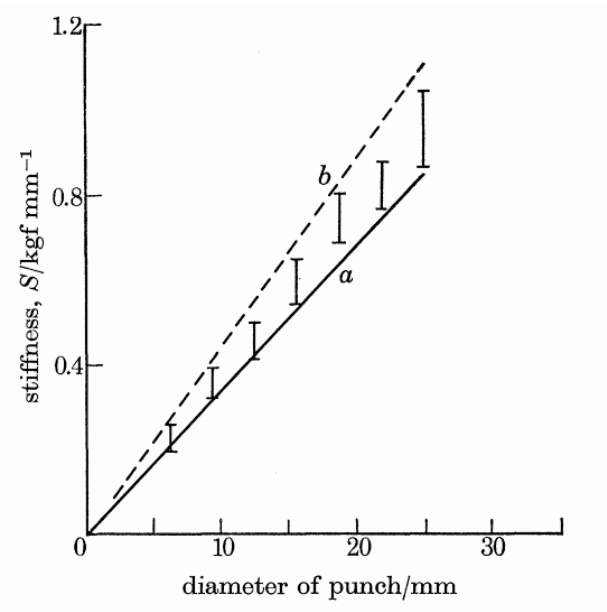

Figure 1.18: Surface stiffness as a function of diameter of punch for soft rubber (a) sharp edge punch (b) punch giving uniform contact pressure (Kendall and Tabor, 1971)

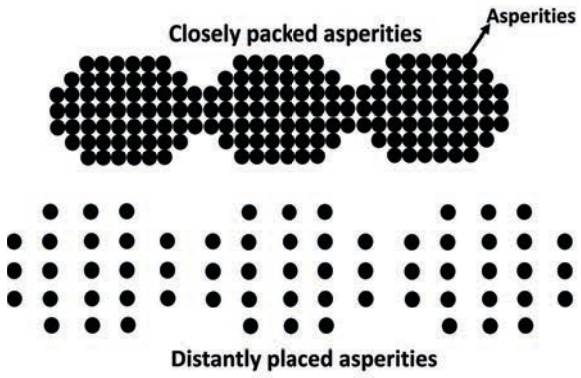

Figure 1.19: Asperity distribution types in a contact (a) asperities when they are far apart (b) Asperities when they are closely placed

An important conclusion that can be drawn from figure 1.18 is that stiffness for a single punch is proportional to its diameter (i.e. contact width), regardless of the pressure distribution. This means that stiffness linearly increases with the local contact changes irrespective of the type of pressure being exerted. This also can be related to any material type or to the interfaces with multiple contacts.

Their work was extended to multiple contacts using a series of N number of circular asperities of identical size distributed in a regular hexagonal array as seen in figure 1.19. The separation distance between the contacts was varied.

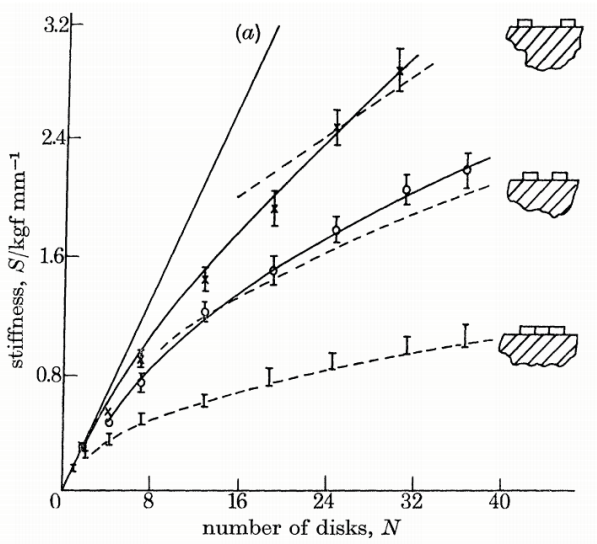

Figure 1.20: Stiffness related to number of asperities when the soft rubber blocks are pressed in between two elastic bodies (Kendall and Tabor, 1971)

The stiffness evolution is plotted in figure 1.20 as a function of the number of disks. The stiffness S, was then derived for two extreme cases when the asperity-mimicking disks are so close that they touch each other and when the asperities are placed three diameters apart. The stiffness becomes,

$$S = NS_o \ (when\ disks\ are\ placed\ far\ apart) \tag{1.22}$$

$$S = \sqrt{N}S_o \ (when\ disks\ are\ closely\ packed) \tag{1.23}$$

For the above equations 1.22 and 1.23, it can be concluded that stiffness is proportional to the number of asperities when they are far apart, and the proportionality is reduced to square root time when they are closely placed.

These experimental and analytical trends were then confirmed by the ultrasonic measurement between two solid bars separated by soft metal thin disks as shown in figure 1.21. In the observations by Kendall and Tabor, the transmission coefficient proportionally increases with the increase of the disk diameter, i.e. with the contact stiffness. This promising analysis had a few limitations: for instance, in figure 1.21a, the asperity was limited to a single soft disk on the scale of several millimeters. It is highly unlikely that it would be consistent for real rough surface contact with asperities size smaller than 20 µm and asperity number as high as thousands.

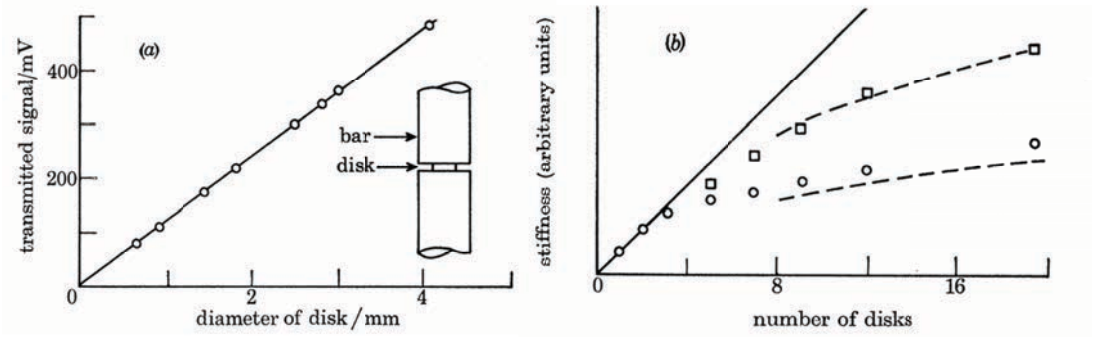

Figure 1.21: (a) Transmission coefficient in comparison to diameter change of the disk (b) Stiffness change with respect to change in number of disks, Hard line is the theoretical curve for isolated disks and dotted lines are for interacting disks and marked in circle is when disks are 1 diameter apart and square when 2 diameters apart (Kendall and Tabor, 1971)

It can be noticed in figure 1.21b stiffness is not directly proportional to the number of asperities when either they are too close or far but is linear for isolated disks, which means that active contacts cannot practically be linear to stiffness and there is dependence on other parameters.

They also concluded that a systematic study of stiffness is lacking, this provides the back up for further investigations. In their work, they also included the study on gap thickness between two solids which was conducted to assess the transmission in thin gaps at a frequency of 200 kHz. It was concluded that the technique was efficient even for air gaps of 10 nm, as seen in figure 1.22.

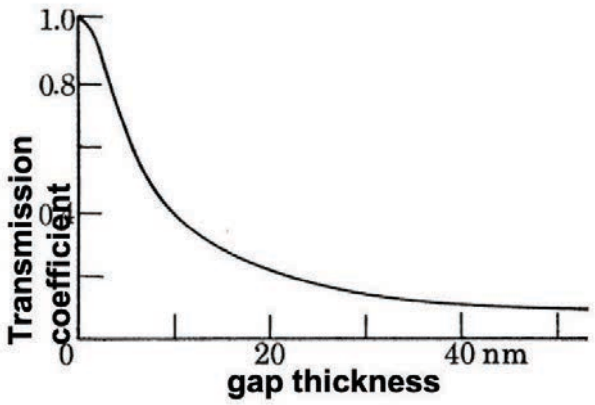

Figure 1.22: Transmission coefficient compared to air gap thickness across a parallel gap in a steel bar (Kendall and Tabor, 1971)

1.5.3 Application to dry static contacts

In dry static contacts, the interface changes can be studied using reflected or transmitted ultrasound. Kracter, 1958 [37] worked on the ultrasonic reflection variations from a loaded interface and found that the reflection coefficient decreases with an increase in the applied load. Later, N. F. Haines, 1980 [38] worked on wave transmission and reflection through contacting surfaces and also on wave scattering from the contacting surfaces and cracks. The model is a more direct representation of the spring model reflection relating to the contact pressure given as,

$$R = \frac{(\frac{z\omega}{p})}{\sqrt{[4 - (\frac{z\omega}{p})^2]}} \tag{1.24}$$

Here P is the contact pressure, ω is the angular frequency of the wave and z is the acoustic impedance. It is important to note that the asperities are assumed to have a circular shape. O. Buck, R. B. Thompson, 1984 [39] worked on experimental and theoretical analysis on the contacting asperities of partially closed fatigue cracks in closer detail and concluded that ultrasonic transmission and reflection in static contacts was a useful tool to evaluate the stress and density of the asperities.

Also, in 1986, the same authors worked on the influence of asperity contact on the reflection of the wave from fatigue cracks. A discrete contact model was developed which includes the distribution of contacts. They showed that based on the stress intensity factor (a parameter that is used in evaluating the stress state in cracks due to load changes

[40]), it was possible to determine the size and density of the contacting asperities. In the later years, O. Buck along with D. D. Palmer, 1988 [41] studied non-destructive characterization of the mechanical strength in diffusive bonds using ultrasound (10 MHz). The experimental procedure consisted of disks of copper with 25 mm in diameter and 12.5 mm inch in thickness. The reflection was measured for a given fractional contact area based on the spring model approach.

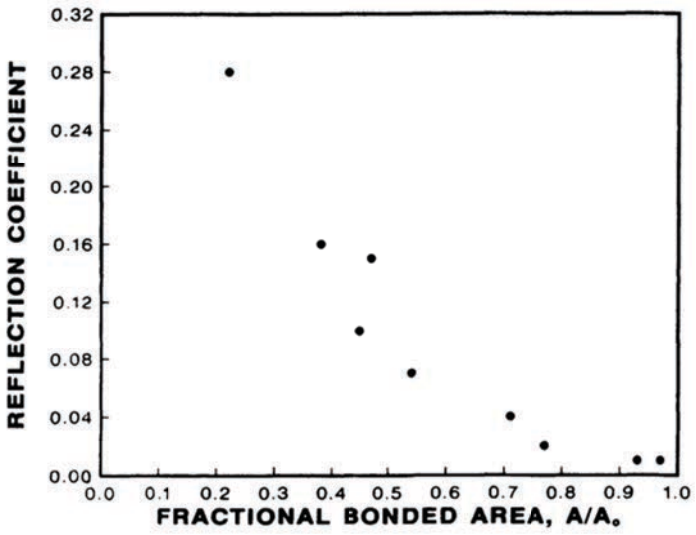

Figure 1.23: Reflection coefficient plotted with respect to fractional bonded area (D. D. Palmer, 1988)[41]

From figure 1.23 it can be noticed that the reflection coefficient reduces with increased bonding area. In addition, 1.23 two values of reflection coefficients with a difference of a factor close to 2 were measured for the same fractional bonded area, here 0.4. This was further supported by J. O. Taylor, 1997 [42].

Peter B. Nagy, 1992 [43] worked on the classification of the imperfect interface based on the ratio between the normal and transverse interfacial stiffness. Stiffness in this case was measured based on the reflection coefficient. His work includes theoretical and experimental analysis on ultrasound propagation through different interface types (kissing, partial, etc). These bonds were distinguished based on the strength of forming an interface. For a given normal interface, reflection and transmission coefficients can be drawn as the function of interface frequency (not to be confused with the wave frequency).

Interface frequency can be referred to as the number of contact regions in an interface. For instance, a near-perfect contact region with very few contact points will have low interface frequency. For very low frequency (high contact ratio), the interface appears to be near perfect and vice versa. Equations corresponding to reflection and transmission coefficients are then given as seen in equation 1.25 and 1.26.

$$R_{L,T} = -\frac{\frac{i\omega}{\Omega_{(L,T)}}}{1 + \frac{i\omega}{\Omega_{(L,T)}}} \tag{1.25}$$

$$T_{L,T} = \frac{1}{1 + \frac{i\omega}{\Omega_{(L,T)}}} \tag{1.26}$$

Ω here is the interface frequency. Notable conclusions that can be drawn from his work are that the normalized reflection coefficient is not proportional to the contact ratio as seen in figure 1.24. This also means that the transmission coefficient will also not be proportional to the aspect ratio.

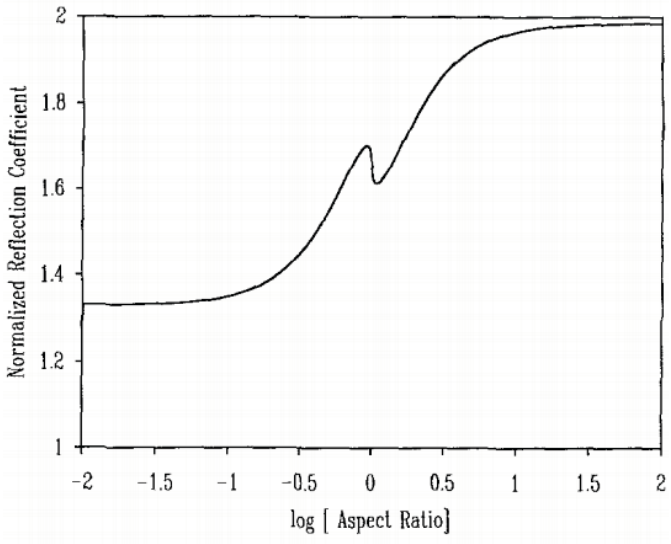

Figure 1.24: Reflection coefficient in relation to the aspect ratio (i.e.contact ratio) of a partial contacting surfaces (Nagy, 1992)

In the figure, the trend was mapped for a partial bond containing a random distribution of elliptical cracks. The trend follows a sigmoid with the aspect ratio change (axis in log scale). This means that reflection coefficient change follows a linear increment between -1 and 1 and maintains consistency at the highest and lowest values of aspect ratio.

An important point to be noticed in figure 1.24 is that the x-axis is a logarithmic representation of aspect ratio (contact ratio). In conclusion, the reflection coefficient is indeed dependent on the interface distribution. To work on this further, Krolikowski, 1991 [44] established an analytical relation between real contact area and contact stiffness using the ultrasonic transmission.

The test samples in their case were two polished flat steel surfaces. In their analysis, Krolikowski assumed that in the equation contact stiffness, k was not directly defined and was dependent on internal interfacial parameters. Krolikowski and coauthors proposed an updated version by equating the transmission coefficient to the contact ratio given as,

$$\frac{A}{A_0} = (T_{min})^2 = \frac{1}{[\frac{z}{2\eta} + 1]^2} \tag{1.27}$$

The equation 1.27 states that the contact ratio was proportional to the square time the transmission coefficient. When compared to the Kendall and Tabor hypothesis, this seems to indicate that transmission was not always proportional to the real contact area or stiffness and was dependent on how the asperities are distributed and spaced (for instance, different asperity configurations could result in same stiffness but not transmission coefficient and vice versa). Similar research was carried by J. O. Taylor, 1997 [42] on the use of ultrasonic wave propagation to study the kissing bonds configurations. In the modelling analysis, two aluminium solids were placed in contact such that the kissing bond was created. The latter was modelled with air gaps and with a solid filling such that there was a difference between the contact areas. This analysis was able to predict the reflection coefficient for two cases based on the surface separation (not too much information was provided by the author in the paper). The resulting reflection coefficient was plotted in figure 1.25. From the figure, two important points need to be highlighted. One is that the reflection coefficient follows a sigmoid trend with surface separation and the other is that, for a given separation (1nm), two different reflection coefficient values exist for air and solid filled interfaces. This means that, for the same contact ratio (there could be a difference in the number of solids or asperities filled compared to air), there could be a different reflection or transmission coefficients. This was a very interesting observation that was not addressed in this point of view.

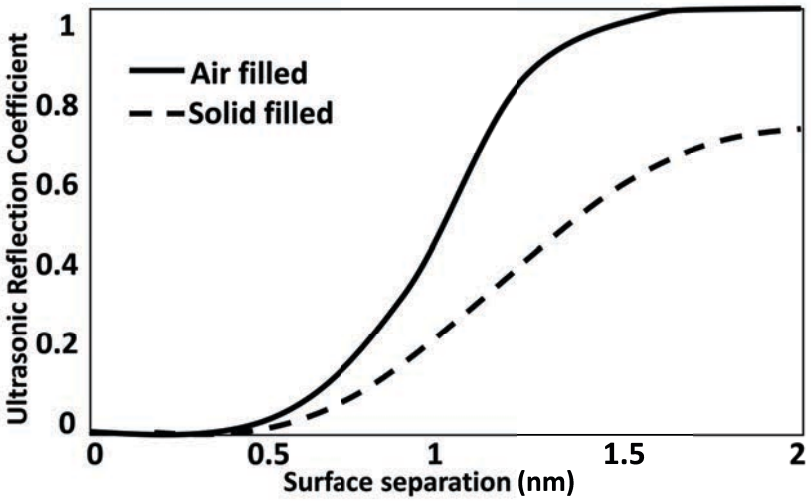

Figure 1.25: Surface separation compared to reflection coefficient (recreated from J. O. Taylor, 1997)

Another important point specified by the author referring to J. Szilard, 1964 was that the results were maybe overestimated and this phenomenon could happen in much lower scales than that specified in figure 1.25.

Polijaniuk, A. and Kaczmarek, J. (1993)[45] conducted wave propagation tests on steel bar with a defined interface and concluded that the real contact area was equal to square times the reflection coefficient in contrast to the findings from Kendall and Tabor. Massimiliano Pau, 2003 [46] worked on the evaluation of the nominal contact area and contact pressure distribution in a steel-steel interface by experimental and numerical validation. They focused on the reliability of ultrasound in accessing contact parameters, such as size, the shape of the contact area. They concluded that a relationship could exist with the load and that the quality of reflection itself was dependent on wave frequency, impedance, and roughness of the surface.

Further development to Tattersall's theory was developed by Drinkwater, 1996 [47] who specifically worked on rough surfaces. He extended the spring theory to rough contacts, considering an incomplete interface and characterized it as a spring layer. He could theoretically relate the reflection coefficient to impedances of the two bodies in contact using a quasi-static approach (Marshall, 2004 [48]).

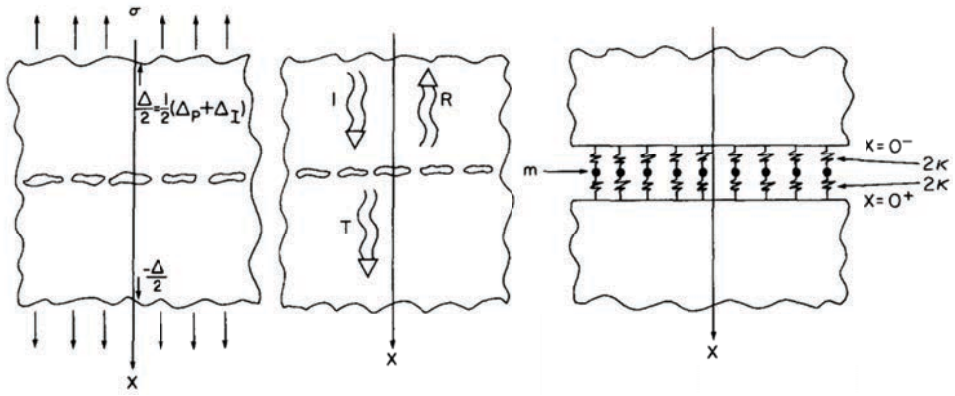

Figure 1.26: Reflection and transmission representation from the interface and Quasi- static model of the interface (Baik and Thompson, 1984)

S. Biwa, 2005 [49] dealt mainly with the wave propagation parameters and stiffness considering theoretical assumptions based on spring theory. Baik's work is important to be mentioned in this context as he mainly dealt with ultrasonic scattering from imperfect interfaces using a quasi-static model as seen in figure 1.26. His work covered interfaces consisting of strip circular, elliptical cracks, and random distribution of contacts. In this model, the interface is assumed to be a combination of springs and masses and, based on the wave that is propagated in the interface, the reflection and transmission coefficients, R, T for two similar material types were formulated as,

$$R = \frac{j\omega(\frac{z}{2k} - \frac{m}{2z})}{(1 - \frac{m\omega^2}{4k}) + j\omega(\frac{z}{2k} + \frac{m}{2z})} \tag{1.28}$$

$$T = \frac{(1 + \frac{m\omega^2}{4k})}{(1 - \frac{m\omega^2}{4k}) + j\omega(\frac{z}{2k} + \frac{m}{2z})} \tag{1.29}$$

In the above 1.28 and 1.29 equations, z is the impedance, m is the mass per unit area, k is the stiffness for unit area and ω the angular frequency. The equation was further studied based on a condition that (m ω^2)/4k should be very small and close to unity.

Based on these equations, the conclusions were that the reflection coefficient is proportional to ω and it increases monotonically, transmission decreases vice versa. Further explanation and results corresponding to the reflection coefficient can be studied at the following reference, Baik and Thompson, 1984. To calculate the spring stiffness based on the analytical quasi-static approach, two interfaces with strip cracks and penny shaped cracks were considered as seen in figure 1.27.

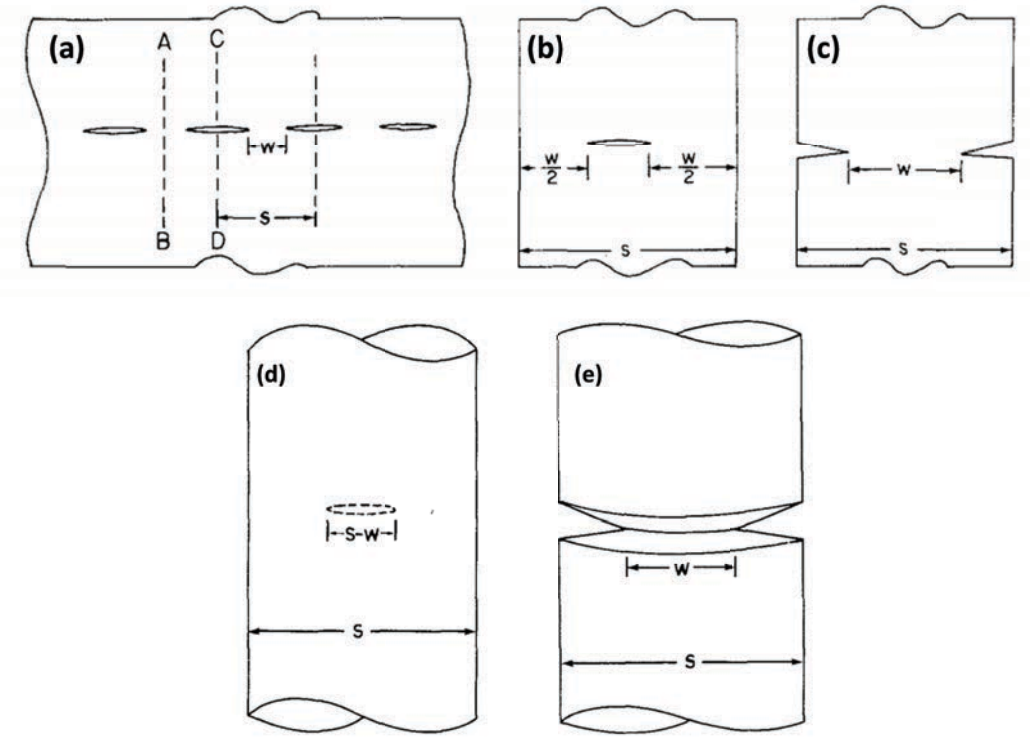

Figure 1.27: Periodic strip cracks (b) one single strip crack (c) double edge crack (d) Center penny shaped crack (e) circumferential edge crack (Baik and Thompson, 1984)

From the figure 1.27, w is the uncracked region (contact width), s is the spacing between the cracks. Based on the Paris equation principle, the stiffness of the whole is derived as,

$$k = \frac{E^{'}}{s} k^{*}(\frac{w}{s}) \tag{1.30}$$

$$k^{*}(\frac{w}{s}) = \frac{4}{\pi} ln[sec(\frac{\pi(1-\frac{w}{z})^{2}}{2})](\ for \ periodic \ strip \ cracks) \tag{1.31}$$

Here k^{*} is the stiffness for the isolated contact based on the ratio between the cracked and spacing regions, sec in the equation is Secant, $E^{'}$ is the elastic constant. The same stiffness equation for penny shaped crack after simplification would be,

$$\lim_{\frac{w}{s} \to 0} k^{*} = \frac{3\pi}{8}(1-\frac{w}{s})^{-3} \tag{1.32}$$

Based on these relationships for change in the crack width and spacing, the stiffness for these two cases was plotted as seen in figure 1.28. In both cases, stiffness monotonically increases with w/s. It was also stated that for both cases, the ratio w/s can be comparable

to contact ratio, meaning that stiffness infinitesimally increases and decreases at the highs and lows of the contact ratio and follows a sigmoid path. The contact ratio or w/s as it is known is an important parameter that characterizes the stiffness which defines the transmission or reflection of an ultrasonic wave. This ratio of w and s is dependent on the distribution. In conclusion, the stiffness of an interface is mainly dependent on the crack or contact distribution and is defined, based on the number of cracks and contacts and also on the width and spacing of and between the cracks. Baik and Thompson also worked on Kendall and Tabor hypothesis on stiffness and commented that there was a lack of observations concerning measuring real contact area based on stiffness and number of asperities as the area of contact were not only dependent on the stiffness, k, but also on the number of asperities, N.

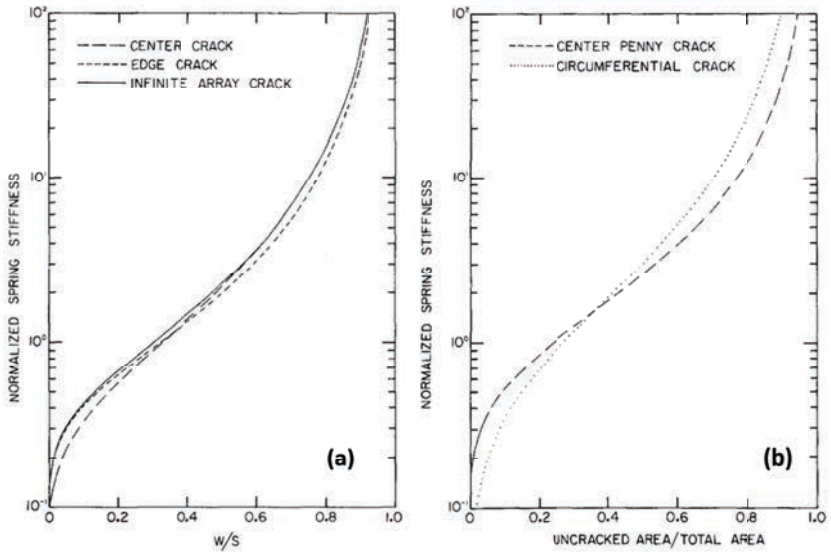

Figure 1.28: Stiffness with change in w/s plot for (a) interfaces having strip and edge cracks (b) circular or penny shaped and elliptical cracks (Baik and Thompson, 1984)

Further, Tattersall [35] work was also addressed concluding that they did not fully focus on the understanding of the interface topology. In recent years, M. E. Kartal. 2011 [9] worked on the experimental and numerical modelling of rough surfaces to study the tangential contact stiffness. They propose an experimental technique to accurately measure the tangential stiffness. In the proposed work, they developed a model in which the solid bar (the geometry of the bar was changed to produce different contact areas) was

pressed against another solid. They showed that the tangential stiffness was proportional to the contact area as seen in figure 1.29.

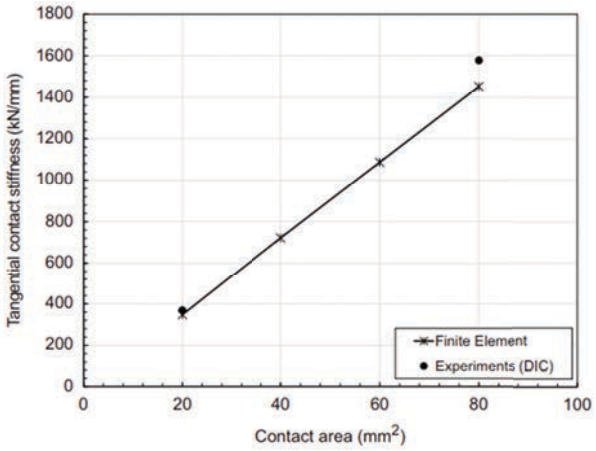

Figure 1.29: Change in tangential contact stiffness with contact area (M. E. Kartal, 2011)

1.5.4 Application to lubricated sliding contacts

In many tribological applications, lubrication is used to avoid unwanted wear. Ultrasound reflection to study the lubricated contacts was first proposed by T. E. Tallian 1964 [50].

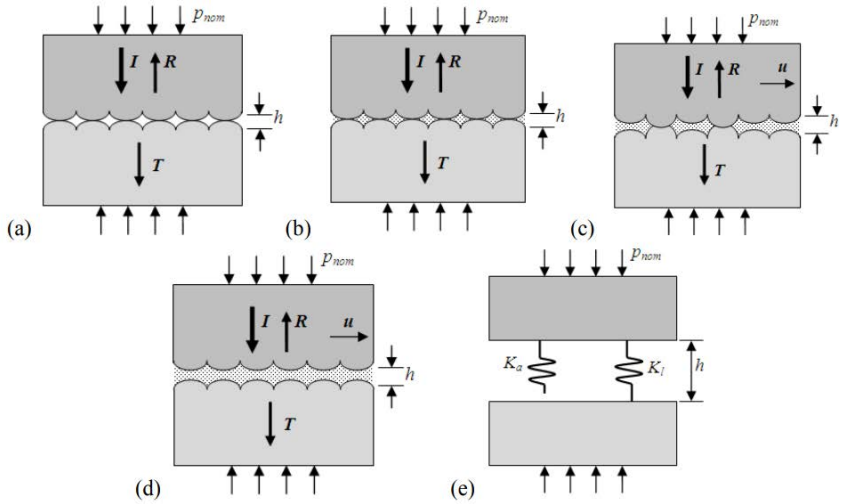

Figure 1.30: Tribological interface representation for (a) Dry contact (b) wet static contact (c) lubricated contact (d) oil film contact (e) spring model (Dwyer Joyce, 2011)

In the proposed work, experimental study and mathematical formulations were given for the stiffness analysis in lubricated contacts. R. E. Challies, 1990 [51] presented his work on using acoustic wave propagation in thin layers of adhesive polymer (50 µm) which were

placed between two glass substrates: an ultrasonic wave was propagated using transducer from one side and recorded through transmission on the other side. D. Anderson 1999 [52], 2000 [53] worked on experimental analysis on detection of lubricant film collapse in a mechanical seal using ultrasonic wave propagation and showed that ultrasound was an effective method to study the lubricants in sealed faces. Rob Dwyer-Joyce, 2011 [54] used ultrasonic wave propagation as a means to evaluate film thickness in contacts (1.30).

In their analysis, a lubricating layer between the two bodies in contact acts as a supporting layer where the ultrasonic wave is sent and resulting reflections through the contact are studied. It was stated that the lubricant layer could be described using the spring model. This implied that the thickness of the lubricant film was related to stiffness as follows:

$$k_t = \frac{B}{h} \tag{1.33}$$

Here k_t is the stiffness of the lubricant layer, B is the bulk modulus and h is the film thickness. By considering the lubricated layer as a spring contact as assumed in spring model, then the total stiffness would be the sum of the asperity stiffness, k_a and the stiffness of the lubricant film, k_l, given as,

$$k_t = k_a + k_l \tag{1.34}$$

Jie. Zang, 2005 [55] explained three approaches to evaluate the film thickness: the time of flight, the resonant layer model, and the spring layer model. Accordingly, as seen in figure 1.31 it can be noticed that the time of flight method was applicable when the film layer was very thick (above 100 µm), the reflections being separable over time.

For a thin lubricant layer, the through-thickness resonance method, Holsten 1991 [56], Pialucha. T 1994 [57] was applicable. From this method, the thickness can be calculated based on the resonance frequency which can be found using equation 1.35.

$$h = \frac{cm}{2f_m} \tag{1.35}$$

Here c is the speed of sound, h is the film thickness, m is the mode number of the resonance and f_m is the resonance frequency.

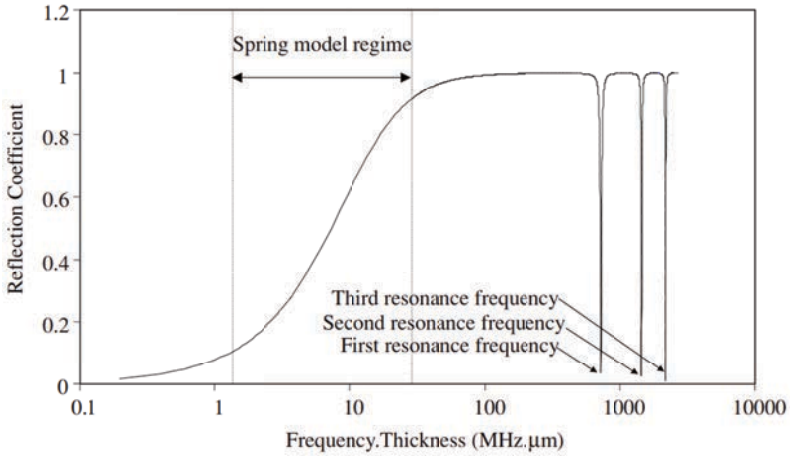

Figure 1.31: Relationship between ultrasound reflection coefficient and the product of the film thickness by frequency (Jie Zang, 2005)

Dwyer-Joyce and co-authors conducted experiments to find film thickness using high-frequency transducers (around 35 MHz to 50 MHz) based on the combination of liquid and asperity stiffness. They showed that it was possible to compute the film thickness based on the comparison of the incident and reflected signals extracted for a given frequency. Meng Li 2014 [58] proposed an improved ultrasonic measurement method for studying lubricated film thickness in cylindrical roller bearings. In this case, the thickness was measured under light radial load. The ultrasonic frequency used was 50 MHz. Tao Geng, 2015 [59] used ultrasonic wave propagation to find the lubricant film thickness in sliding bearings. They proposed a new spectral analysis method to measure thickness for thin lubricant where the time of flight was very low and resulting reflections overlapping over time.

Bernhard Praher, 2017 [60] worked on ultrasonic wave propagation in the measurement of liquid layer thickness based on a time-domain approach. This was a new algorithm developed to increase the resolution of measurement by studying the overlapping signals and compensating them with weighted functions. The application of ultrasound to rough lubricated contacts was tested for stationary conditions which are not prone to drastic changes. However, when large sliding is introduced, there may be a major disturbance in terms of fatigue, wear, and structural damage within the interface. It is then a real challenge to study sliding contacts in-situ and in real-time.

1.5.5 Application to dry sliding contacts

In 1971, Kendall and Tabor presented a short experimental insight on acoustic wave propagation through sliding contacts. An experimental apparatus was designed by loading a hemispherical rider on a horizontal flat surface. A transducer that emits ultrasound was located on top of the rider and the strip transducer that received the transmitted signal was located at the bottom as see figure 1.32. Based on the measured transmitted signal, the authors concluded that ultrasonic transmission was able to provide data allowing one to study the stiffness of the interface. A defined load was applied to a clean glass-glass contact and sliding was implemented on the lower surface. Based on the recorded transmission, the stiffness was proportional to $W^{1/3}$ with W the applied normal load.

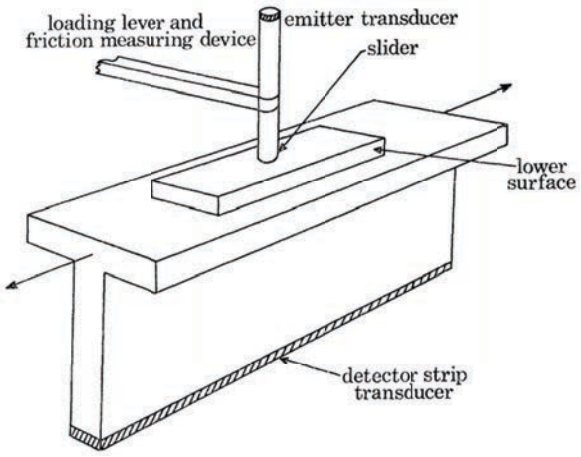

Figure 1.32: Experimental setup to study the interface conditions during sliding (Kendall and Tabor, 1971)

Further testing was also done on the sliding of metal surfaces but convenient results were not attained from the analysis, due to the sliding and loading conditions that tend to change the interface configuration. However, the authors concluded that the ultrasonic method could provide in-situ measurement for various types of materials as long as the formation of debris does not disrupt the penetration.

Brunskill et al, 2013 [61] presented a deep experimental insight on dry machine element contacts using ultrasound on various set-ups (wheel-rail contact, pin on disk, metal to metal seal contact, etc). The author addressed the issue of complexity in studying the real contact area or mapping the real contact zone due to debris formation. Hyo-Sok Ahn,

2001 [62] published work on the in-situ evaluation of wear surface using ultrasound wave propagation and the focus was to evaluate the worn surface during dry sliding conditions and explained the relationship between the reflection and surface damage.

Other researchers like Dwyer Joyce [34], Kralikowski[44], Y. C. Tasan, 2005 [63] stated that ultrasound is mostly used in in-situ monitoring of roughness or film thickness and less likely to study the real contact area. The major drawbacks were that only the global changes in the interface were measured and local changes (change in asperities, asperity width, etc) were not addressed due to rapid volumetric changes. Fei Du, 2014 [64] worked on stiffness measurement of a tribological interface using ultrasound based on the spring model, and the focus was limited to the interface stiffness variation with a load rather than with the interface topology. To address these issues, and easier, yet efficient, the method is the finite element approach. Nevertheless, very little work was documented on finite element modelling of dry contacts to study wear and friction using ultrasound.

1.6 Goals of the thesis and strategy

The need for in-situ measurement in tribology has drawn great attention for the past years. In parallel, high-intensity focused ultrasound and modelling of such systems have been developed. The analysis of ultrasonic waves generated from transducers travelling in or on to an interacting medium was focused on evaluating oil film thickness, viscosity characteristics, wear, and fatigue of the interfacing surfaces. This measurement method termed ultrasound reflectometry could also be used effectively in evaluating rough contacts, providing unique information on real contact area distribution and evolution.

The literature review presented in this thesis investigated the use of ultrasound in characterizing an interface under various conditions. Different methods were proposed that provide a relationship between the wave propagation parameters and the interface ones. Many researchers pioneered the work in tribology during the past 60 years strengthening the ultrasonic capability in the field. But there remains a lack of knowledge regarding the interaction of an ultrasonic wave with an interface at a microscopic scale and even more in real-time. One reason could be the lack of models giving access to such a scale. The following points of interest can be thus identified:

- The relation between the interface stiffness and the transmission coefficient could be discussed according to the simplifications from the analysis by Kendall and Tabor. Several studies mentioned in this review tend to show that the relationship is not so straight forward. This gives a great scope in further extending the study and focus on perfectly controlled surfaces.

- All the interface parameters were experimentally studied relating to change either in load or frequency but the direct relationship between the ultrasonic signals and the interface morphology was never studied.

In the literature review, most of the analysis related to the interfaces were either experimental or analytical. Not much was proposed using numerical approaches such as finite element modelling. In recent years, there has been an increased usage of finite element modelling to model complex interfaces but very little literature exists on modelling ultrasonic wave propagation through interfaces [65], [66], [67]. The major advantage of using FEM is the ability to model the wave propagation within a solid and through an interface but also to implement more complex surface topography and perform a mechanical simulation to compute the actual stiffness of the selected interface.

Summary:

- This chapter introduced the basic concepts of ultrasound with detailed explanation on various measurement method associated with tribology.
- Literature relating to wave propagation and interface is established with background relating to the ultrasonic applications in tribology ranging from contact mechanics to dry static and sliding contacts.
- Concept relating to stiffness and interfacial parameters is explained with a focus on how the stiffness was characterized and what is lacking.

Nous devons croire que nous sommes doués pour quelque chose et que cette chose, à n'importe quel prix, doit être atteinte....

We must believe that we are gifted for something, and that this thing, at whatever cost, must be attained....

Marie Curie

2

Finite element modelling of wave propagation

Contents

2.1 State of the art

In many scientific fields, numerical simulation has become a common analyzing tool to provide clear insights into complex systems. Especially, numerical models enable a problem to be designed in a virtual and flexible way in order to perform numerical experimentations, assess assumptions, perform sensitivity studies or analyze phenomena happening at a scale that cannot be experimentally assessed. Finite element modelling is one of the various existing numerical methods. It has been proved to be efficient when complex problems

have to be investigated, either due to their geometries, existing coupling multi-physics aspects. When it comes to tribological applications, the problem is again complex due to the multiple scales involved, ranging from the macroscopic first bodies to the local micro contact asperities, but also due to the inherent difficulties to exactly know the problem configuration, i.e. the exact contact point distribution.

Building experimentally a model contact interface is still a real challenge, leaving a great opportunity to investigate them numerically instead. However, if modelling them is not easy and requires an approximate design based on assumptions, how can one then study the interaction of an ultrasonic wave with these model contact surfaces? Combining the numerical simulation of a tribological problem and the propagation of an ultrasonic wave definitely shows great potential and has been the driving force of this thesis.

Early attempts to use FE simulation of ultrasonic wave propagation were conducted by Ludwig and Lord, 1988 [68], [69], [70], and Cawley and Alleyne, 1992 [71], [72], to characterize the propagation of Lamb waves through different defects in plates. The conclusions were that the lamb wave propagation was sensitive to the mesh size and characteristics of the defects, i.e. distribution and separation distance between them.

Karunasena, 1995 [73] conducted 2D finite element modelling with a guided lamb wave to study the reflection in the plates and concluded that FE modelling is an efficient way to estimate the deflection of the waves through the model specimen due to the complexity in designing and experimenting in real-time. G. R. Liu et al 2001 [74] worked on FE modelling of wave propagation and focus the work on the boundary conditions, especially the non-reflection ones. They presented a work corresponding to implementing various boundary elements to avoid scatters and concludes that FEM could produce satisfactory results in terms of the amount of wave energy that reaches and reflects from the interface, also in terms of reduced scattering effect that is obtained with right boundary conditions and meshing.

Bartoli et al, 2006 [75] conducted work on modelling guided wave propagation for defect detection in railroad tracks. They followed a 3D approach in which the high-frequency pulse was sent through the track to find reflection changes through the crack. They concluded that finite element modelling provides a strategic approach dealing with cracks and observing the wave propagation through them. They also commented on the 3D

modelling stating that, the computational time required for such models is very high and also complexity associated with meshing them resulting in increased computation time. In any model dealing with wave propagation, based on the frequency and type of model, it is important to output the data at a high sampling rate to capture the complete propagating wave, resulting in a severe increase of the computation and storage cost.

Z. You et al 1989 [76] work is considered prominent due to the various factors they addressed in the initial stages of finite element modelling implementation. They developed a 2D finite element code that solves the interaction of elastic waves with cracks or defects. They conclude that in any wave propagation model, it is very important to approximate time and dimension to precisely validate a displacement-based mechanical model. The explicit integration scheme made it possible to study the crack development in an aluminium block where an ultrasonic wave was propagated on to it. The result in the end provided an aspect of using an explicit scheme in modelling.

Seth S. Kessler et al, 2002 [77] worked on finite element modelling of lamb wave propagation for health monitoring of composite structures and to detect delamination using Abaqus CAE. They used the explicit scheme to model an aluminium block. Results show that the accuracy in terms of the model results in comparison to experimental is promising enough to show the credibility of adapting modelling in various other applications.

Many other researchers like J.J. Ditri et al 1992 [78], Hosten and Castaings et al 2003 [79], Putillath et al 2008 [80] worked on using finite element modelling as a tool to efficiently characterize various mechanical parameters concerning wave propagation and application and processing them later using signal processing methods. Ditri used FE model wave propagation through hollow cylinders and concluded upon the fact of modelling as practical importance to non-destructive testing. Hosten worked on lamb wave propagation through plates to identify the sensitivity of the dispersion curves and thickness mode shapes. He concludes on how modelling can enhance the structural phenomena when prone to physical changes. He emphasizes the potential of modelling in NDE. Although, there is a difference in what the application motivation was, they all prove the possibility of adapting the methods to new studies like tribology.

Advantages concerning FE modelling are that it provides wave propagation simulation and makes it easy to visualize the propagating pattern, this is dependent on the way material physical properties and boundary conditions are defined. Many physical conditions can be taken into account such as the losses due to attenuation, diffraction, wave scattering can be visualized. Sensitivity studies can be carried out to assess the most influential parameters in order to reduce them. Another main benefit of FEM is the possibility to couple the acoustic wave propagation to any other mechanical or thermal phenomena and take into account varying materials properties over space or even time (varying elastic properties along a solid induced by a temperature gradient).

Finite element modelling also comes with some disadvantages as it may require high memory and computation power to solve a large complex model. Generally, any wave propagation model can be developed in 3D or 2D based on the requirements, hypothesis, and propagation configurations. Although the 3D model appeals for its visualization capabilities, it increases the computation time and complexity. On the other hand, if a proper propagation configuration and corresponding hypothesis are selected, 2D seems to be an efficient design approach as it solves all the above-mentioned problems with maintaining the model accuracy.

2.2 Development of finite element model

2.2.1 Integration Scheme

In the present study, the commercial FE package Abaqus was employed to simulate the wave propagation phenomena. From a basic point of view, the finite element method relies on the space discretization of the problem into a series of elements, the approximation of the field values within each of these elements calculated from the shape functions and the direct computation of the nodal values by solving the equation of motion. Properly modelling the wave propagation into an elastic solid requires a transient dynamic analysis to be performed. This can be achieved by two different schemes to integrate the equation of motion: an explicit or an implicit integration procedure.

Selecting the proper integration scheme when modelling wave propagation has been nicely discussed by Lord 1989, Maio et al 2015 [81] and more extensively by M. Drozdz

2008 [82]. In an implicit integration scheme, a set of simultaneous non-linear equilibrium equations is solved at each time increment using an iterative algorithm, for example, Newton's one. It is often seen as the most robust approach to solve linear elastic problems as it is unconditionally stable, i.e. no mathematical limit on the time increment size to integrate the equation system, and usually leads to faster and more accurate results than an explicit one. This is not necessarily true for dynamic problems, shock studies, and especially for high-frequency wave propagation problems happening during an extremely short time of a few microseconds. The constraints on the spatial and time discretization that will be discussed later, are very crucial as the time step size required to capture the transient wave phenomena is much smaller than that required by the algorithm itself. As a summary, it has thus been shown that the implicit method is usually preferred to solve wave problems in the frequency domain when a solid is subjected to a continuous harmonic excitation. Indeed, in this case, the steady-state overall dynamic response of a structure is studied instead of wave propagation problems associated with really local interaction in the media. Based on these findings, an explicit dynamic analysis was used as a direct time-stepping method to solve the equation of dynamic equilibrium at each node given as,

$$[M]\ddot{u} + [C]\dot{u} + [K]u = [F_a] \tag{2.1}$$

Here $\ddot{u}$, $\ddot{u}$, u are the acceleration, velocity and displacement respectively. [M] is the lumped mass matrix whose values are determined by the density of the material used. [K] is the static stiffness matrix whose values are defined by the Young's modulus and Poisson's ratio. [C] is the viscous damping matrix which is determined by the Rayleigh damping with,

$$[C] = C_M[M] + C_k[K] \tag{2.2}$$

Here, C_M is the mass coefficient and C_k is the stiffness coefficient. In ABAQUS/Explicit, these equations are integrated using the explicit central difference integration rule, this rule will link the displacement and force as seen in equation 2.4 ,

$$\dot{u}^{(i+\frac{1}{2})} = \dot{u}^{(i-\frac{1}{2})} + \frac{\delta t^{(i+1)} + \delta t^{(i)}}{2}\ddot{u}^{(i)} \tag{2.3}$$

$$\dot{u}^{(i+1)} = \dot{u}^{(i)} + \delta t^{(i+1)} \ddot{u}^{(i+\frac{1}{2})} \tag{2.4}$$

This integration operator is explicit in the sense that the kinematic state can be predicated using known values of velocity and acceleration at both the current and previous increments. This method is especially well-suited when solving high-speed dynamic events that require many small increments to obtain a high-resolution solution. If the duration of the event is short, the solution can be obtained efficiently. Moreover, the efficiency of this procedure is directly connected to the use of a lumping technique that brings the full mass matrix to a diagonal approximation leading to an easy and fast computation of its inverse as used in equation 2.1 to compute the acceleration. However, this integration method is conditionally stable and the solver time step must be lower than the critical time step defined by the equation 2.5.

$$\delta t \leq \delta t_c r = \frac{2}{\omega_{max}} \tag{2.5}$$

Here δt is the time step, ω_{max} is the maximum frequency of the system. Approximating the equation to the critical time step results in the transit time of the wave propagating through the smallest element in the whole model. It is given as,

$$\delta t \leq \delta t_c r = \frac{\delta L}{c} \tag{2.6}$$

δL is the element with smallest size and c is the speed of the propagating wave. H. Lewy et al further prioritized the condition in equation 2.6, calling it the CFL (Courant-Freidrichs-Levy) that is implemented in the explicit for stable time step.

$$\delta t = CFL \frac{\delta L}{c_L} (CFL = \frac{\delta t}{\delta t_c}) \tag{2.7}$$

Important factors that need to be considered during defining a step time is the rate at which the pressure defined in the model changes, the complexity of non-linearity in the designed model, time period of displacement of the wave in the solid structure. Also, It has to be noted that the time increment based on the above-mentioned equations for Abaqus/Explicit is controlled by the model (the controlling parameters that are defined

in the model). The advantage of using explicit simulation is that it uses an iterative method to determine the boundaries for the defined mesh and solve it accordingly. Another advantage of using an explicit scheme is that the global mass and stiffness factors do not need to be defined or computed which will dramatically reduce the computation time.

2.2.2 Geometry and Input data

In order to settle the methodology, a simple first case study is selected modelling and ultrasonic bulk wave propagation in an elastic solid. This section provides a basic overview of the 2D model to simulate the propagating wave. The latter is simply excited at one end with a pressure pulse generating an incident wave. The resulting displacements can then be extracted on both ends of the solids and plotted with respect to time. The model is created in 2D assuming a plane wave propagation, i.e. plane strain problem with an infinite dimension of the solid in the Z out of the plane direction, as presented in figure 2.1.

Figure 2.1: 10 MHz Pulse wave used as the input

Density $\rho(kg/m^3)$	Young's modulus E(GPa)	Poisson's ratio
2700	69	0.33

Table 2.1: Properties of the material that is defined in FE model

The test material is aluminum which is considered isotropic and homogeneous within the whole solid with the elastic properties defined in table 2.1.

2.2.3 Boundary conditions and pulse modelling

In this case study, modelling the entire piezoelectric element and its implementation as the wave propagator are not followed. Many uncertainties would indeed remain, especially regarding the bonding of the element into the solid surface. Rather, the incident wave

with a specific frequency is applied as a pressure pulse for exciting the guided waves through the solid. A simple line load is defined on the edge of the structure with the exact dimensions of a transducer and a load boundary condition is applied. The load is defined as a tone burst following the equations given as,

$$X = \begin{cases} sin(2\pi ft) & 0 \leq t \leq \mathrm{T}_c \\ 0 & \mathrm{t} \geq \mathrm{T}_c \end{cases} \tag{2.8}$$

Here $x(t)$ is the carrier signal, $T_C = N_c T$ is the total time of the wave, N_C is the number of counts respectively. As the tone burst is a Hanning windowed function, the window is then defined as,

$$w(t) = \frac{1}{2}[1 - cos(\frac{1}{N_c} 2\pi ft)] \tag{2.9}$$

By convolving both the carrier and windowed functions, the result is a tone burst given as,

$$F_b(t) = x(t) * w(t) \tag{2.10}$$

In this first case study, the pulse is modelled as tone burst of center frequency 10 MHz with its corresponding time-domain presented in the figure 2.2. The size of the load line is 4 mm that mimics the transducer. The time signal is Fourier transformed within a time frame to extract the amplitude of excitation, reflected, and transmitted signals as seen in figure 2.3.

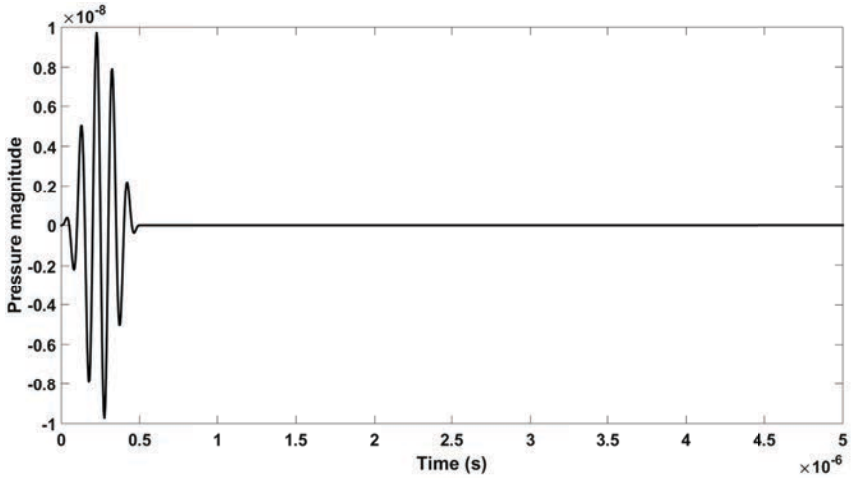

Figure 2.2: 10 MHz Pulse wave used as the input

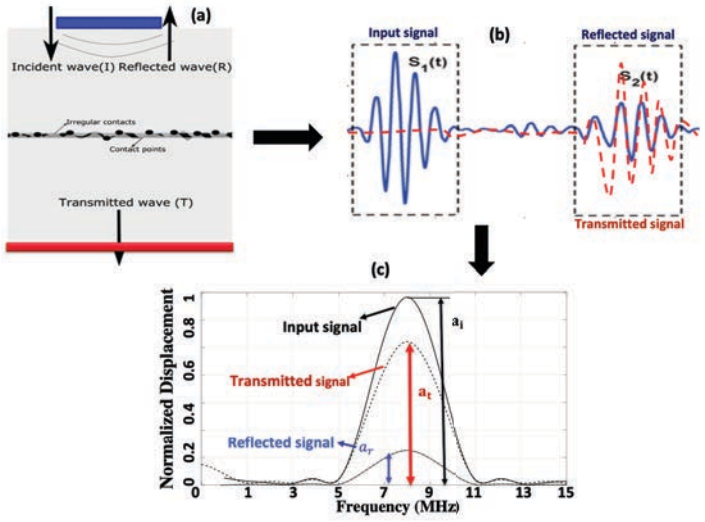

Figure 2.3: (a) Solid-solid interface (b) Time domain representation of input, reflected and transmitted waves (c) FFT or frequency domain representation of input, reflected and transmitted waves.

In the above figure $S_1(t)$ is the time signal representing input pulse and $S_2(t)$ is the time signal representation of the reflecting and transmitting parts. Also, a_i,a_t,a_r are amplitudes of the input, transmitted, reflected signals that are recoded.

2.2.4 Mesh type and step time

It is previously known that in explicit, every single iteration is based on the step time and frame rate. Normally, for high-frequency wave propagation, the step time has to be smaller and in line with the wavelength of the signal. For high time step increment, the high-frequency wave information can be lost leading to inaccuracy, on the contrary, lower time step will increase the unwanted simulation process time. So, for perfect harmony, the precise step time has to be defined based on, speed of sound and length of the solid element. Equation corresponding to stable time increment is given as,

$$\delta t = min(\frac{L^e}{c_d}) \tag{2.11}$$

Here L^e is the element length and dilatational wave speed. For a given propagating material the dilatational wave speed can be calculated using the equation 2.12,

$$c_d = \sqrt{\frac{\lambda + 2\mu}{\rho}} \tag{2.12}$$

Here, λ is the wavelength, ρ is the density and μ is the poisson's ratio. Based on this, the critical step time in an explicit scheme can then be calculated based on criteria given in equation 2.12,

$$\delta \leq \frac{L_m in}{c} \tag{2.13}$$

A mesh type can be assigned once the problem is spatially discretized. Seeding in Abaqus is the processing of defining the number of nodes that contribute to the mesh density. High seeding will have a dense mesh and low will have coarse mesh. In all the simulations, mesh size is fixed to 20 microns. It is defined so that the time increment is sufficient to capture the smallest region of interest. There are 400 frames (it refers to the output of data extracted at different time intervals) for the whole wave propagation process for each time frame that is recorded at 500 microseconds rate (this is the sampling rate). Each frame corresponds to the total time take for the wave to travel i.e. in this simulations the total time or maximum time is fixed to 100 microseconds. From the work by Karl F. Graff, 2001 [83] and J Achenbach 2012 [84] the mesh size has to be defined in such a way that there should be at least 10 elements per wavelength in the model. In this case, the model has 50 elements per wavelength leading to a total of 67685 nodes distributed uniformly.

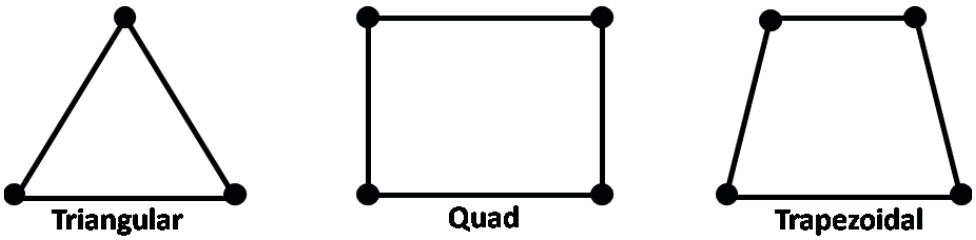

Figure 2.4: Different types of mesh controls that are mostly used in 2D analysis

Based on the wavelength λ (500 microns calculated using c/f), it can be said that for a 15 mm solid, it would take 3 microseconds for the wave to reach the other end. It is also given in Abaqus manual, 2018 that the mesh size has to be more than 10 times the wavelength to capture wave propagation. In that case, this simulation shows that it is 25 times the wavelength. The distance between each node will be 20 microns and different mesh types can be then assigned. In the types of mesh shown in figure 2.4, although all the models look similar to 4 nodes, a quadrilateral is much efficient in comparison to

the remaining two as they are accurate in presenting displacement changes to a higher degree which cannot be the case with the deformed mesh types.

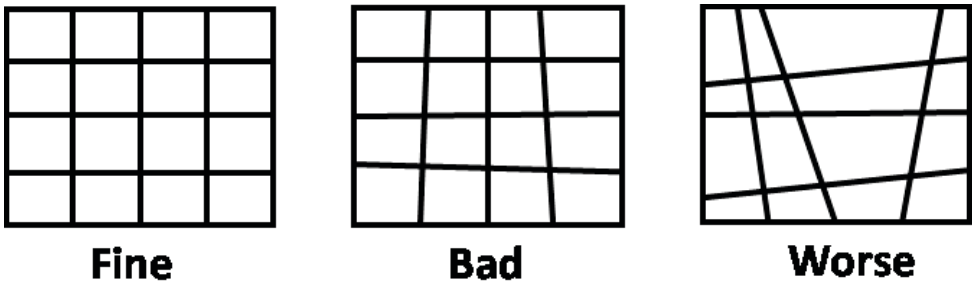

Figure 2.5: Different quality mesh types for quad type mesh distribution

For second-order models, if the quad shape is considered to be efficient enough, further quad assignment has to be in good agreement with the nodes and number of elements. Most of the developed finite element models have complex conditions that make them difficult to validate using experiments. Also, even with the FE, it has to be sure that the model behaves naturally and does not include adverse effects. To do that a fine or optimal mesh has to be assigned. As seen in figure 2.5, for wave propagation analysis, the mesh with fine distribution tends to have displacement spread over the model but if the mesh is deformed, the displacement will have a rather distorted path. The characteristic element type used in this simulation is 4-node uniform strain quadrilateral (CPE4R). It is in good agreement with some of the previously proposed works like M. Drodtz 2006 [82].

2.3 Mesh sensitivity analysis

The level of accuracy of a wave propagation model is greatly influenced by the mesh density and time step. This section will project upon the influence of 2 mesh distributions to quantitatively define a suitable mesh distribution that will be further used in later simulations. The mesh distribution is scaled from a coarse 200 to a fine 20 microns mesh in this sensitivity analysis. For the complex micro-scale structures the mesh density has to be very high as in time-domain wave propagation, for each node, displacements are calculated and averaged. Although time consumed to process is very high, wave propagation within the solid is depicted in precise detail. The quadratic element mesh distribution was used

considering its advantage of meshing small scale structures (Abaqus manual, 2014). The effect of the mesh distribution/quality was first investigated by applying a tone burst on one side of the solid, whereas displacement amplitudes were extracted on both sides.

From the results shown in figure 2.6, it can be seen that the propagated wave is seriously affected by the mesh distribution as it reaches the right end of the solid, whereas the scale for the 2 simulations is similar. There are two obvious observations, one is that the wave itself, as it starts propagating, has different displacement patterns. On the other hand, as it propagates through, the wave energy when using the coarse mesh is completely lost with almost zero transmission along the field.

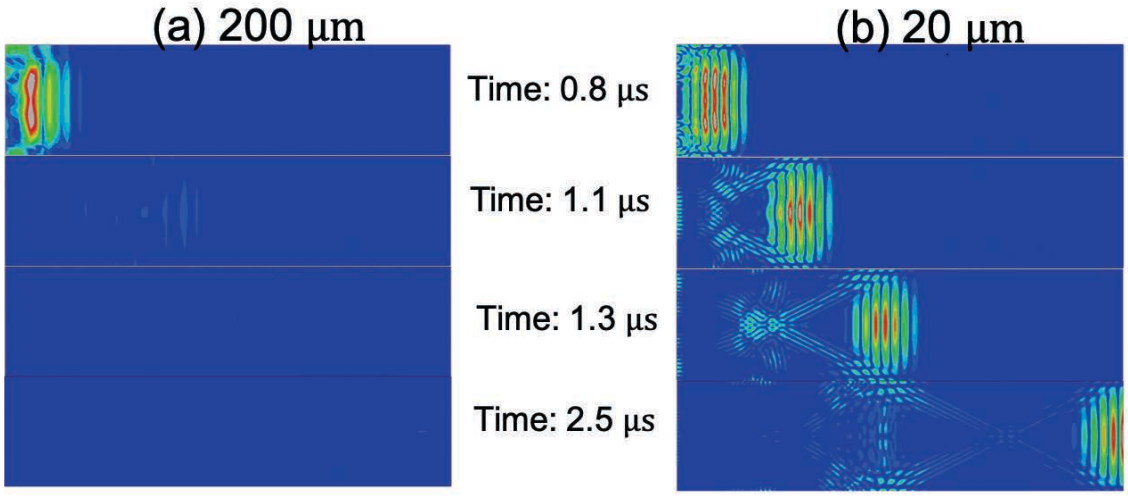

Figure 2.6: Time lapse of travelling as it reaches the right end of the solid for (a) coarse mesh distribution (b) Fine mesh distribution

When using the fine 20-micron mesh, in figure 2.6(2d), the peak amplitude is almost maintained until the end of the solid despite the slight beam spreading and scattering on the side walls. On the contrary, figure 2.6(1c) proves that the wave pattern is rapidly lost leading to a strong decrease in the wave amplitude. In practice, this will not be the case as based on the length of the solid, there could be a clear wave traveling along and reflecting unless altered due to attenuation or scattering.

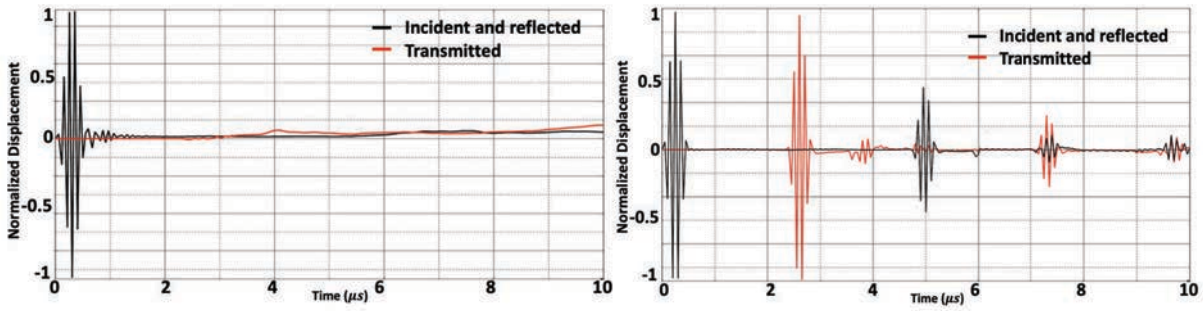

Figure 2.7: (a) Displacement magnitude plotted for the coarse mesh distribution along with the amplitude reflections shown over time (b) Displacement magnitude plotted for the fine mesh distribution along with the amplitude reflections shown over time

Figure 2.7 presents the total displacement recorded in the propagation direction on both sides of the solid. In figure 2.7b, it can be noticed that the wave is almost fully transmitted to the right end of the solid whereas the first echo recorded on the left at 5 µs is weaker in amplitude. When using a coarse mesh distribution, the whole signal intensity is lost over the few propagation steps which are noticeable in 2.7a. Based on the meshing rule, these simulations prove that the smallest mesh size is necessary to reach an accurate performance of the model and vice versa. This concludes that change in mesh density does affect the wave propagation efficiency and also introduce numerical inaccuracies.

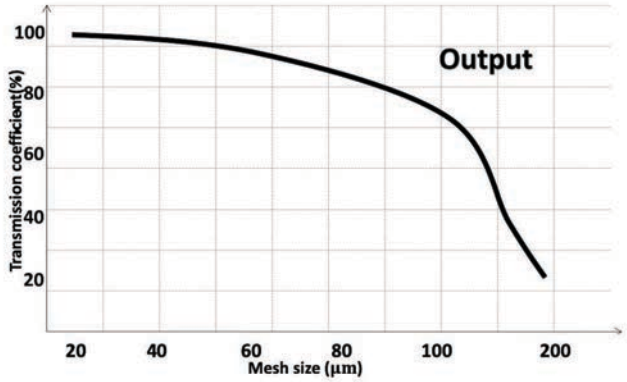

Figure 2.8: Mesh distribution size and its efficiency curve

From multiple analyses on different mesh distributions, an efficiency curve versus mesh size was drawn as seen in figure 2.8. Efficiency here is defined as the ratio of the incident amplitude to received amplitude given as seen in the equation,

$$\eta = \frac{Output\ amplitude}{Input\ amplitude} * 100 \tag{2.14}$$

Based on the resulting curve, it clearly shows that when increasing the mesh size, the efficiency of the output reduces to nearly 10 percent. This concludes that 20 microns are a very good mesh size than can be adapted to the present model. Usually, the mesh size has to be 1/10 elements per wavelength to simulate the wave propagation and in this case, the mesh size is 1/25 elements per wavelength.

2.4 Influence of geometry

Geometrical modulation analysis is the first step process to assess how the dimensions of the propagating solid may affect the collected signals. From a tribological point of view, this step is important to define the size of the first body on which an ultrasonic sensor will be bounded such that the wave that is propagated through, experiences less attenuation due to scattering and back propagation. The same mechanical properties for aluminium were used as well as the same 10 MHz tone burst input wave.

2.4.1 Length of the solid

Wave propagation corresponding to change in the length of the solid is shown in figure 2.9. Wave propagation corresponding to 3 different time intervals (wave as it emerges from the transducer, wave as it reaches to the right end of the solid and the wave as it reaches back to the left end to the transducer) is shown.

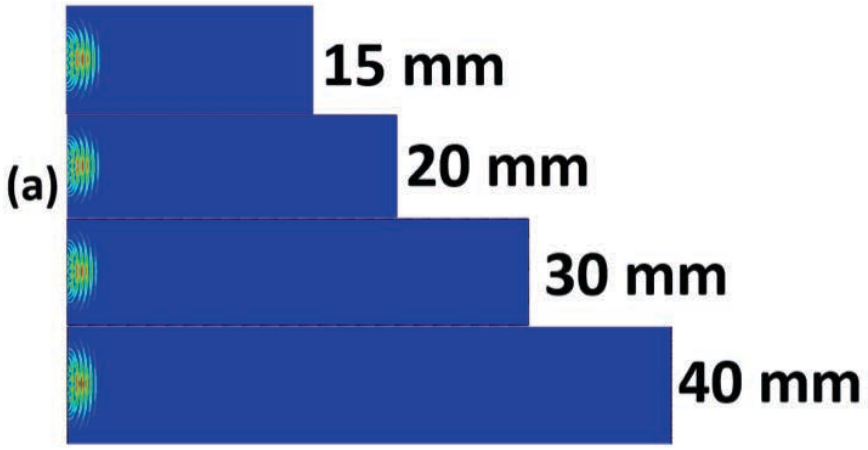

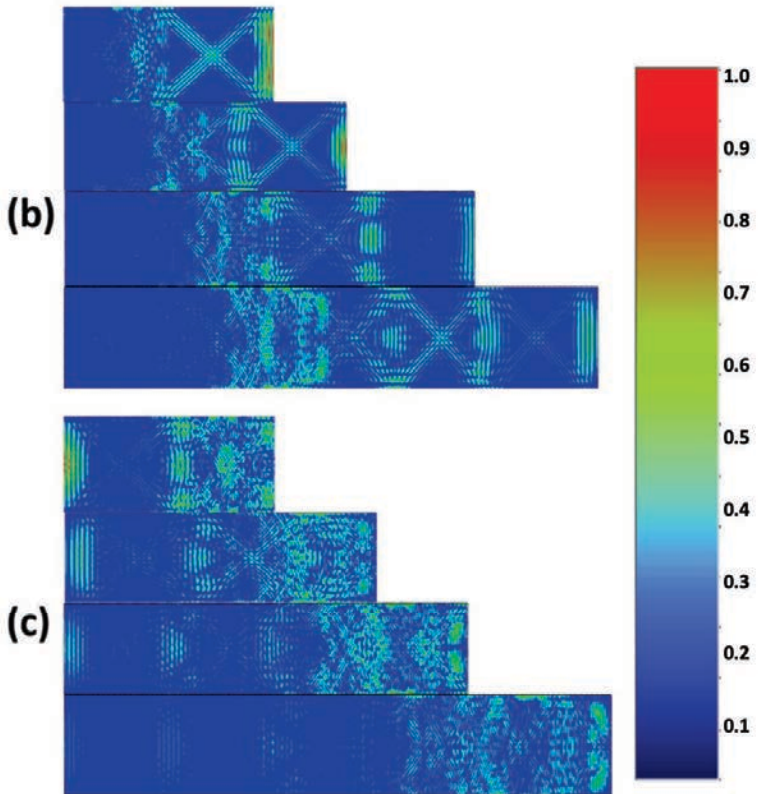

Figure 2.9: Displacement change imaged (a) when the wave is just propagated from the left boundary (b) when the wave reached the right boundary (c) when the wave reaches back to the left boundary

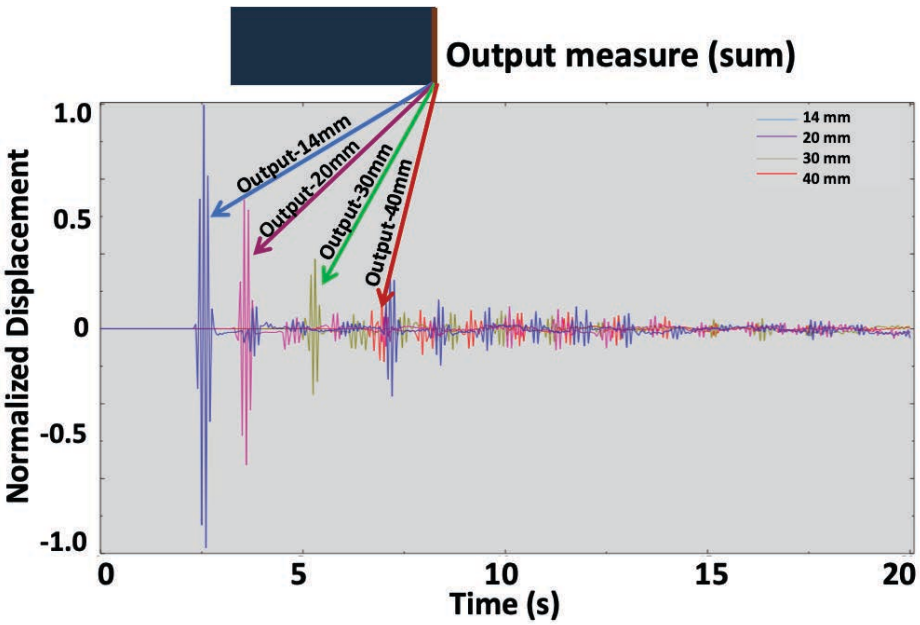

Figure 2.10: Sum of the displacements extracted at the transmitting side of the solid and plotted over time for 4 combinations of lengths

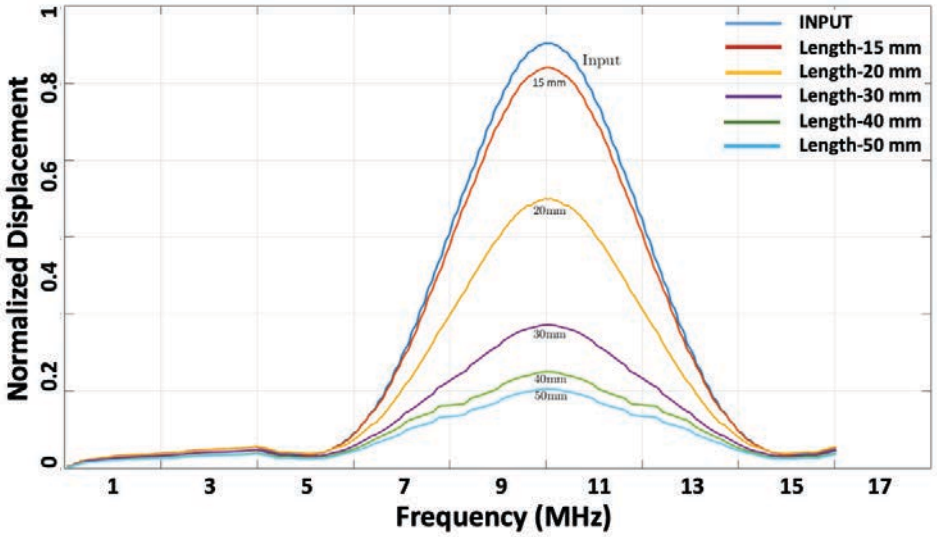

Figure 2.11: FFT plot corresponding to change in the length of the solid (15 mm-50 mm)

From figure 2.11, it is obvious that the time taken for the wave to travel in the shortest solid is shorter than in the longer one. However, one can notice from the figure 2.10 that the wave undergoes multiple scattering and reflections on the walls of the solid which are unwanted to have a high signal to noise ratio. This is even amplified as the length of the solid, i.e. the propagation path, increases. For a 50 mm long solid for instance, the amplitude of the wave is reduced to a third of the one recorded at 15 mm (Figures 2.11 and 2.9 c) showing that a 10 MHz frequency wave tend to severely attenuate. Considering this, the shortest 15 mm long solid is chosen for further simulations.

2.4.2 Effect of the material type

Material type	Young's modulus (GPa)	Poisson's ratio	Density (g/cm^3)	Impedance
Aluminum	68	0.33	2.70	17
Steel	210	0.3	7.5	45.7
Glass	70	0.22	2.5	13
Titanium	120	0.32	4.5	27.3

Table 2.2: mechanical properties of most commonly used material types

Assessing the effect of the material type is important as the latter directly controls the wavelength of the pulse, the speed of sound, and the acoustic impedance of the propagating

media. These will obviously affect wave propagation. As seen in table 2.2, Aluminum, Glass, Titanium, and Steel covers a large range of acoustic impedance.

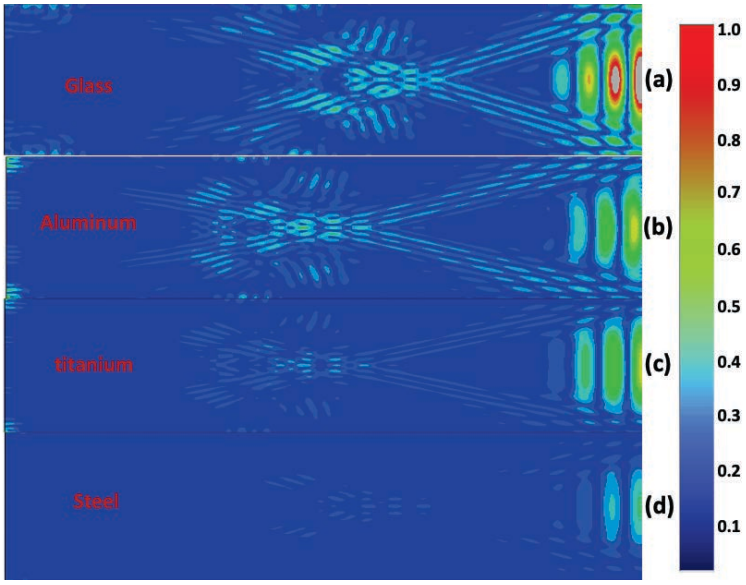

Figure 2.12: Wave propagation in different material types as it reaches the right boundary of the solid

Figure 2.12 shows the wave as it reached the right boundary. It must be noted that, for a given pressure pulse, the input amplitude does change with the type of material and so does the transmitted signal. Increasing the input power could compensate for the amplitude reduction in the less propagating materials. To explain, steel has the least transmitting wave energy due to the fact that its high impedance which will eventually reduce the bulk transmission. According to the study by A. Ishimaru et al 1999 [85], the wave propagation through dense material can be compensated by choosing the right resonance frequency which is similar to the natural frequency of the solid. For instance, 10 MHz frequency performance is high in glass and aluminium due to the fact that the impedance is very low making it possible for the wave to propagate along with fewer losses. This proves that wave interacts differently with material type and such properties play a major role in efficient wave propagation.

2.4.3 Effect of boundary conditions

When modelling a complex wave propagation configuration, the question of the boundary conditions has to be carefully addressed. Indeed, if the excitation pulse is considered to be

small in terms of size against the propagating solid, then one could assume the latter to be an infinite or semi-infinite one. In these cases, the borders of the solid are so far from the excitation source that the wave will be fully attenuated when reaching them and will not be reflected back. Such assumptions thus require the modelling of a large propagating solid which may lead to an artificial increase in the computation time and data storage. One solution is thus to reduce the simulated area and apply some specific boundary conditions to avoid reflections on these walls. There are various approaches in designing a boundary layer and Michael Drozdz, 2008 in his thesis listed the four main methods: infinite elements, absorbing layers, non-reflecting boundary condition, and perfectly matched layer.

Absorbing elements is a method where the edges of the medium are defined to be absorbing the reflections. Researchers like U. Basu, et al 2003 [86], F. Collino et al 1998 Collino2001application, D. Givoli et al 1991 [87], A. Sommerfeld. 1949, J. Lysemer, 1969, CH. Liu, 1999 [88] worked exclusively on defining different boundary conditions. Most works suggest the use of absorbing layers as an efficient and easy way to be defined and implemented in a model such that it can reduce unwanted reflections over the boundary layers. Drozdz, 2004 in his work proposed that to be efficient, the absorbing layer has to be three times the length of the largest wavelength in the model. Using infinite elements is a boundary condition applied on an element with the same mechanical properties implemented as an infinite space.

Figure 2.13: Sketch corresponding to solid with infinite elements applied to the boundaries

A pictographic representation of the finite element development of continuous space can be seen in figure 2.13. The corners of the elements are overlapped with the extra surface with infinite elements. The absorbing layer is defined in this model as a damping layer (material

type) which is coupled around the surface such that it absorbs the waves that travel along the edges. This is not a built-in option in Abaqus and is defined as a material type that can later be assigned to the geometry. The absorbing layer is similar to the concept of infinite layers but in this case, a thick layer is attached to the corners of the solid element.

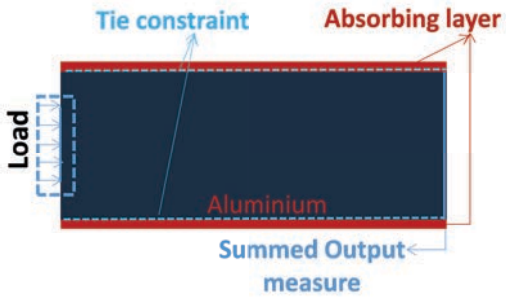

Figure 2.14: Sketch corresponding to the absorbing layer applied on the solid element

The previous case study performed on the 15 mm long and 5 mm wide at an ultrasound frequency of 10 MHz has been simulated using these two boundary layers to investigate the effect of the wave propagation pattern.

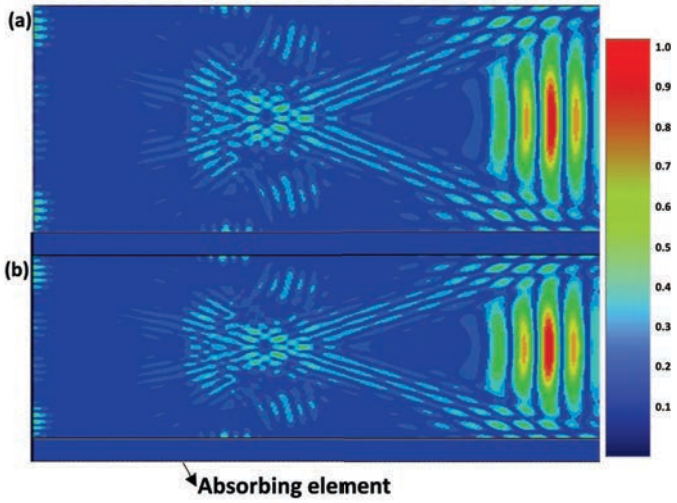

Figure 2.15: Result of wave reaching the right end of the solid a) without and b) with an absorbing layer

Figure 2.15 shows the wave travelling through the solid when using and not using absorbing layers whereas figure 2.16 shows it when the infinite element boundary condition is implemented or not. There is no change in both cases proving that the material type doesn't damp the back scatters and refraction.

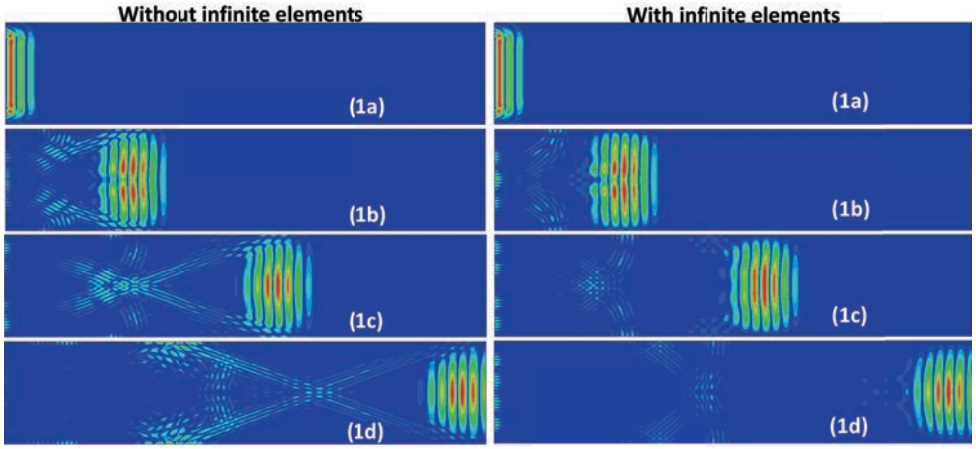

Figure 2.16: Time lapse of wave propagating through solid without (left) and with (right) infinite elements

It can be noticed that the back scatters are reduced to a considerable amount and the waves that travel on the wall are completely avoided. This shows the effectiveness of using infinite elements. Both approaches present the advantages in studies that involve wave propagation because they suppress the low unwanted harmonic interference.

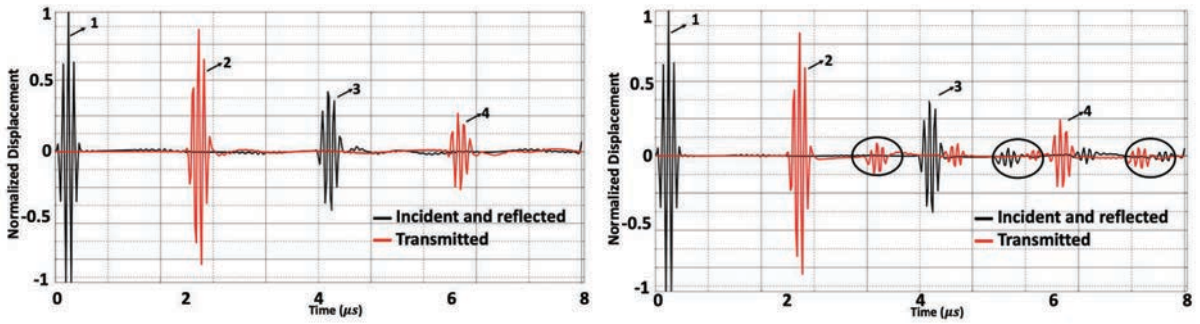

Figure 2.17: Time domain plot of input, reflections and transmission through solid with infinite elements

Figure 2.17 shows the time domain plot corresponding to the simulations and it clearly shows the reductions of small amplitudes (circled in black) whereas the main echoes and reflections exhibit a slightly higher amplitude. As the aim of this thesis is to work on the interface definitions, the following element types are no further discussed and kept in as a future perspective.

2.5 Summary and conclusions

In this chapter, a basic overview of finite element modelling was presented which started with a brief state of the art on the previous work followed by the advantages of using FE modelling. Further, this chapter described the development of the proposed numerical approach to simulate wave propagation. Modelling using Abaqus/Explicit was explained covering the background of the method along with the various key steps in the process. Basic knowledge of the effect of the mesh type and distribution was covered as well as the effect of the solid dimensions on the propagation pattern. Later wave propagation through different material types was presented and, in the end, the application of two absorbing boundary conditions was discussed.

In this chapter, it is thus shown that in the modelling process, right model definitions are important to accurately define the working conditions. In conclusion, mesh density is the crucial factor to have accurate results for any model. The implementation of using absorbing layers and infinite elements has also been briefly highlighted. It was shown that infinite elements are superior to the absorbing layers and can strongly reduce the very small harmonic interference. As the aim is to define a modelling strategy, the dimensional analysis of the solid is important to have the right balance for the wave to propagate and reflect back with minimum loss. The conclusions drawn from this chapter are applied in the next one, but infinite elements are not considered due to the fact that, in a real configuration, the harmonics are persistent and it is important to include them in a model to assess how they interfere with the main reflections and subsequent signal processing.

Summary:

- This chapter introduced the basic modelling concepts with an initial overview of the Abaqus/Explicit scheme.
- Basic modelling study of wave propagation through a single solid is proposed focusing on working on mesh sensitivity and the effect of various boundary conditions.
- Influence of geometry in terms of change in reflection and transmission coefficients is shown later concluding up of the defined geometry, mesh size.

Toutes les pensées intelligentes ont déjà été pensées,
il suffit d'essayer de les repenser....

All intelligent thoughts have already been thought,
what is necessary is only to try to think them again.....

Johann Wolfgang von Goethe

3

Numerical analysis of the wave propagation through a contact interface

Contents

In Chapter 2, the wave propagation analysis on a single solid was presented along with the investigation of the effect of meshing, geometry, and boundary condition. The challenge in the later phase would be to model a contact interface and study it in terms of varying interface conditions. It is very important to develop this study on the basis that the wave propagation through a tribological interface was less studied with a numerical approach. So it is necessary to develop an easy yet efficient model that can be used to extract important information which is usually complex to address otherwise.

For the study, a 2D finite element model is developed to simulate the interface when two solids are in close contact and an ultrasonic wave propagated through it. The focus will be to evaluate reflection and transmission and relate them to the crucial parameters that define the interface morphology. As the first step, a simple model is designed with one single asperity which was altered in terms of width and thickness. Later, a model is presented to study the wave propagation with different contact configurations and relate them to the interface parameters.

3.1 Height of the asperity

To demonstrate the working conditions of the finite element model, initially, a simple geometry is tested with a single asperity placed exactly in the center of the interface as seen in figure 3.1.

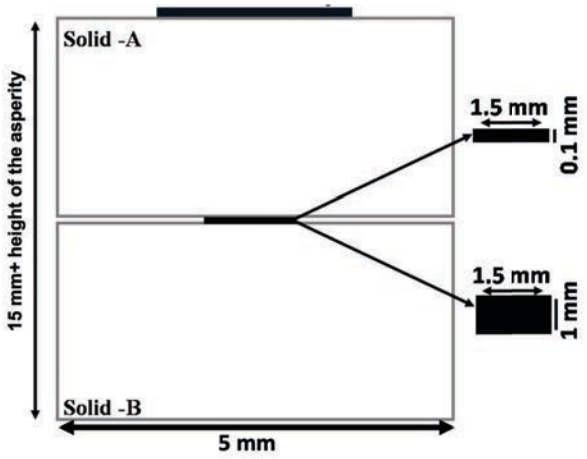

Figure 3.1: Schematic of the proposed geometry with one single asperity with 2 different height configurations (1 mm, 0.1 mm)

Two height configurations are tested in this context. Plane-wave propagates in the same way for both cases as seen in figure 3.2. It can be observed that the wave in the case where the asperity is high, the wave propagates slower than with a thin one, figure 3.2b. The difference is that the higher asperity due to its high thickness acts as buffer sandwiched in between the two solids, which results in the delay of the wave reaching the right boundary. This will affect the amount of energy reflected and transmitted which can be observed in figure 3.3.

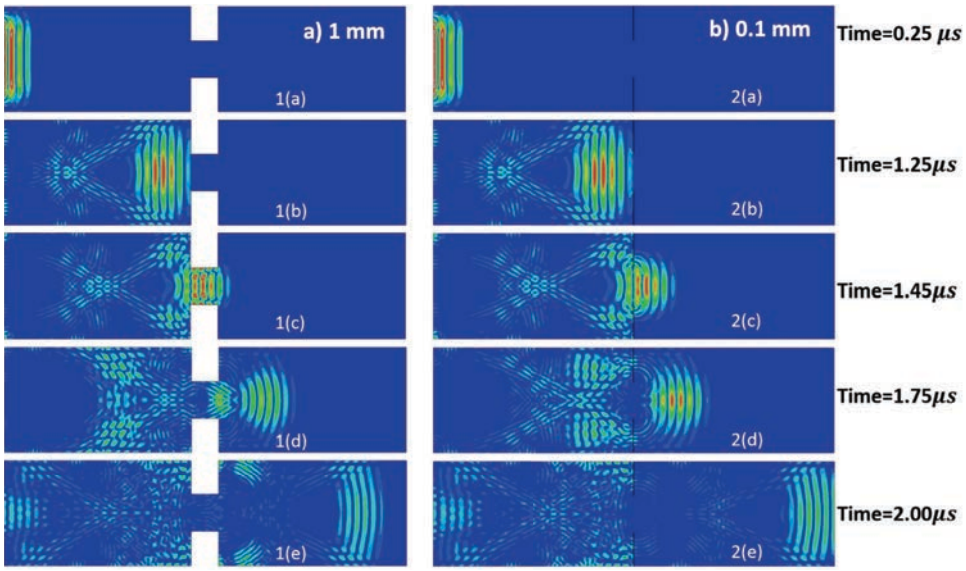

Figure 3.2: Time lapse of wave propagation through a single asperity with 2 different height configurations (a) 1 mm (b)0.1 mm

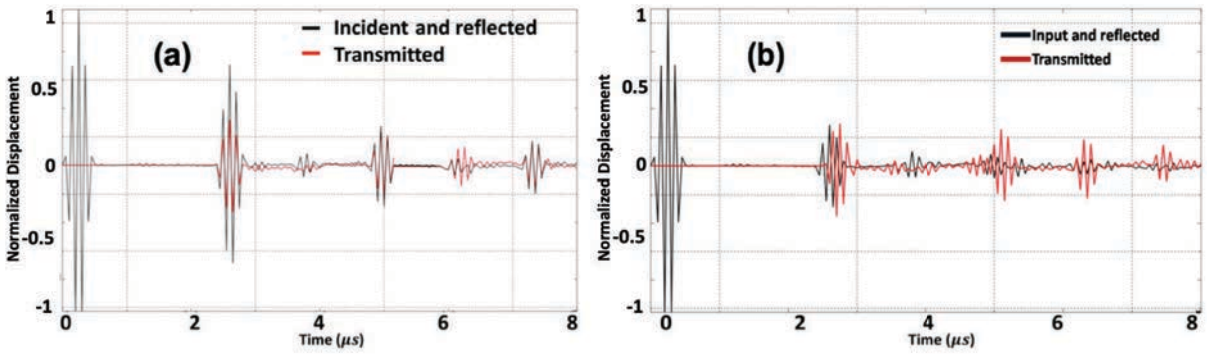

Figure 3.3: Time domain plot showing input, reflected and transmitted parts for (a) 0.1 mm and (b) 1 mm

Once the input is pulsed, the reflection and transmission at the left and right boundaries are recorded between 2 to 3 microseconds. It can be noticed that in the case where the asperity is 100 microns, it presents better reflection and transmissions compared to the large one.

Furthermore, as the height of the asperity goes down, to as small as 10 microns, the behavior is quite similar to 100 microns. Also with the large asperity height, lateral reflections are corrupted by small reflections at 4 and 6 microns which could make it more difficult to process. However, this tends to show that there is a certain sensitivity of the reflected signal to the asperity height.

3.2 Width of the asperity

3.2.1 Effect on the the wave transmission

Considering a configuration with a 10-micron thick asperity, the study is focused on assessing the evolution of the reflection coefficient to the change in the width of a single asperity. Geometry in this case is similar to the previously defined model as seen in 3.1, except that the width is changed from 0.1 to 5 mm. Figure 3.4 shows the corresponding images of the wave as it partially reflects and transmits at the asperity.

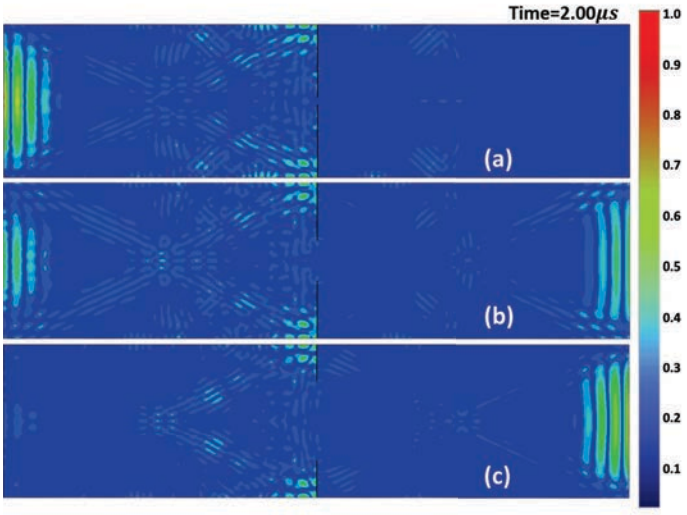

Figure 3.4: Comparison of the wave propagating through different asperity width (a) 0.1 mm where all the wave is reflected back (b) 2 mm where part of the wave is transmitted and part reflected (c) 5 mm where most of the wave is transmitted (results are extracted at same time frame)

It can be noticed that as the width of the asperity increases, the amount of wave that is reflected reduces to near zero (once the asperity reaches 5 mm, this is the whole width of the solid), and transmission increases gradually and reaches highest transmission level. In such cases with increased width, the fronts cannot interact with free spaces between the two contacting bodies which result in an increased propagating wave. Also, asperity size above 5 mm will have similar kind of transmission effects that which changes with the width of the solid. For instance, if the width of the solid is 10, the values of transmission might differ but the relationship will still be linearly proportional. Figure 3.5 shows the relationship between the width of the asperity and the transmission coefficient

as defined in section 1.5.2. It can be concluded that the transmission coefficient is directly proportional to the width of the asperity.

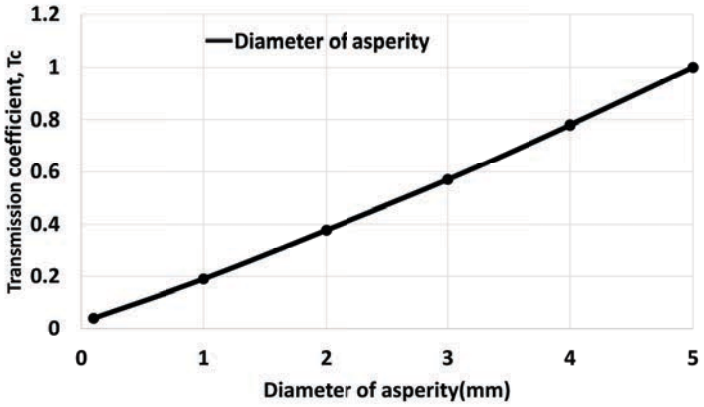

Figure 3.5: Relationship between width of the asperity to transmission coefficient

This appears to be in good agreement with the work presented by Kendall and Tabor [36] (Chapter 1, section 1.5.2, figure 1.21), confirming the consistency of the modelling approach and the potential use for further analyses. The wave is completely transmitted at asperity half the size of solid is because it depends on the wave front and asperity placement where the wave transmission is much lower than expected in the centre.

3.2.2 Relationship with the stiffness of the interface

Kendall and Tabor, 1971 [36] stated that transmission is proportional to the stiffness of the interface resulting from the increase of the asperity width.

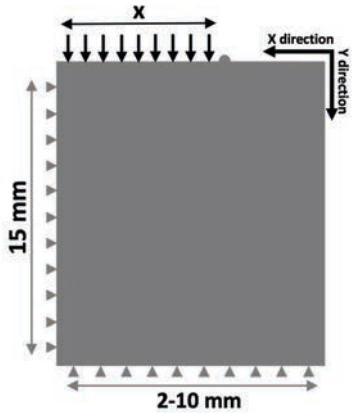

Figure 3.6: Schematic representation of the model assumed with load and the boundary conditions defined

To verify this relationship, numerical simulations were carried out to assess the stiffness of each asperity size configurations. A simple 2D axi-symmetric single asperity punch model is developed and studied in terms of changing contact width. The model is simulated in static, general and the element type is a 4-node bilinear plane stress. The asperity or punch or contact width here is defined as x and changes from 0.01 mm to 10 mm. A short displacement of -0.1 is applied on the top boundary x and a symmetry boundary condition is applied in both X and Y directions. Reaction Force is measured as output over time. A sketch of the geometry is shown in figure 3.6 with the corresponding input data in Table 3.7.

Part definitions	**Part type**	**2D deformable**
	Material	**Aluminum**
	Step	**Static general**
Load	**Displacement, Y**	**-0.1**
	Output	**Force**
	Symmetry	**X direction**
	Symmetry	**Y direction**
Boundary conditions	**Signal window**	**Hanning**
	Element size (mm)	**0.25**
	Element type	**Explicit/Plane stress**
Meshing dimensions	**Mesh control**	**Quad dominated/Free**

Figure 3.7: Table corresponding to the load, boundary conditions, mashing rules implemented in this section

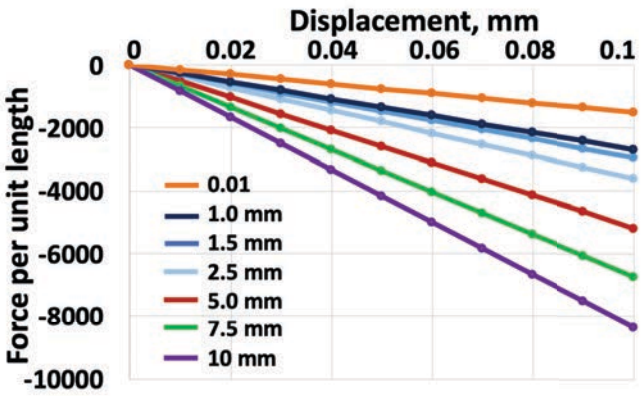

Figure 3.8: Reaction force over displacement for different asperity width configurations

Figure 3.8 shows the reaction force plotted versus the punch displacement.The stiffness, slope of this force-displacement curve, can then be easily extracted, whereas one can also observed the increase of the stiffness with the increase of the asperity width. Stiffness is later plotted along the asperity or contact width (figure 3.9) and proportionality is confirmed above a critical value 0f 2 mm contact width but there is deviation below that level. The stiffness approaches close to zero with reduced contact width i.e. lowest 0.01 where the nonlinearity is observed.

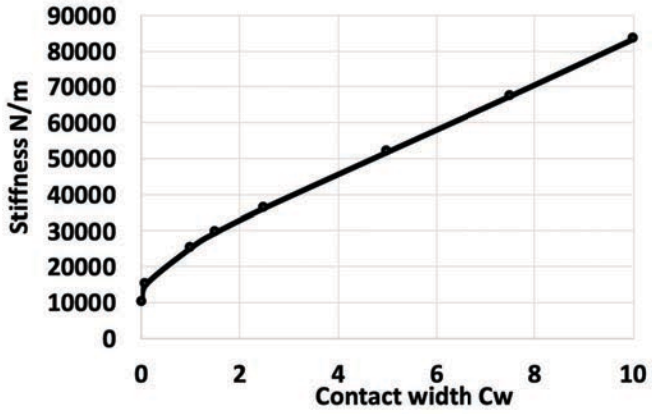

Figure 3.9: Resulting contact stiffness versus the asperity/contact width

This is in perfect agreement with the literature from Kendall and Tabor 1971 [36] for value above 2 mm (or close to above 1.5 mm) and gives a valid reason for the assumption that stiffness is proportional to the contact changes. Indeed, it can be concluded that the transmission coefficient is proportional to the contact stiffness in the case of this single asperity where the condition is valid for values above 2 mm (or close to above 1.5 mm) and differs below. This could be due to the fact that although the transmission coefficient is linear to the diameter of the asperity, it cannot be true with stiffness in the lower asperity width regime. To assess the real contact area based on the stiffness, one should know the contact regions and the number of asperities in contact which in reality is difficult. The conclusion from Kendall and Tabor [36] that transmission only depends on the contact stiffness cannot be supported only by a single asperity configuration due to the fact that in the lower stiffness region and lower contact widths, there is a problem of linearity that

need to be further studied. Thus, the present work proposes to address this by simulating the wave propagation with multi-asperity contact configurations.

3.3 Number of asperities and contact spot distribution

3.3.1 Change in the number of asperities

The numerical model is then extended to investigate the effect of a change in the number of asperities or contact spots in an interface. The dimensions of two solids in contacts are set to 7.5 mm each in length and 5 mm in width. As the width of the solid is fixed and height being 10 microns, changing the number of asperities cannot be performed without changing and combining different contact space and contact width values. This preliminary investigation is the first step to assess if it is sensitive or not to any change in the contact interface morphology. The number of asperities for the four selected configurations is N=3, 5, 11, 25 respectively. The contact width and space are thus defined between 20 microns to 100 microns such that the lowest to the highest case could be covered. Geometrical representation concerning the tested configurations are shown in figure 3.10. Here, C_w and C_s are definitions for contact width and contact space. figure 3.11 shows the wave propagation capture obtained at the time interval when the wave reaches the left and right boundaries.

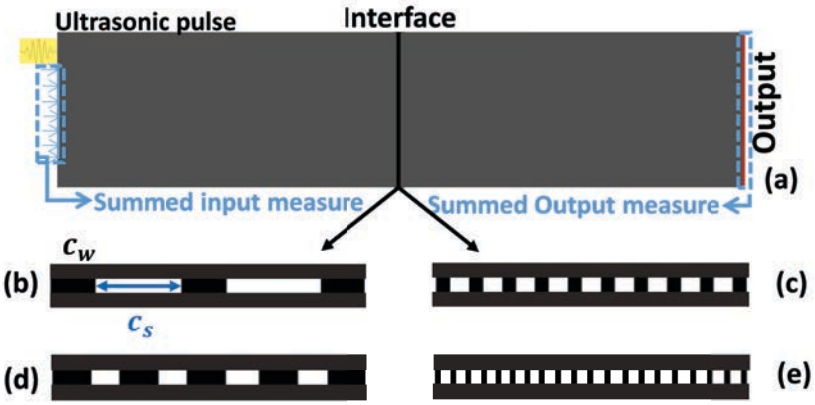

Figure 3.10: (a) Solid-solid contact interface with the interface shown in black strip (b) Simple configuration of a 3-asperity interface (c) (d) (e) Interface showing increased number of asperities and reduced width and space

The signal on the left and right represent the reflected and transmitted part. With an increased number of asperities, the spacing between each asperity reduces and so is the amount of energy reflected. The reduction of the wave corresponds to increases contact area that which will result in an increased stiffness in the interface. This shows that reflection and transmission coefficients are both affected by a varying number of asperities with respect to the reduced contact space.

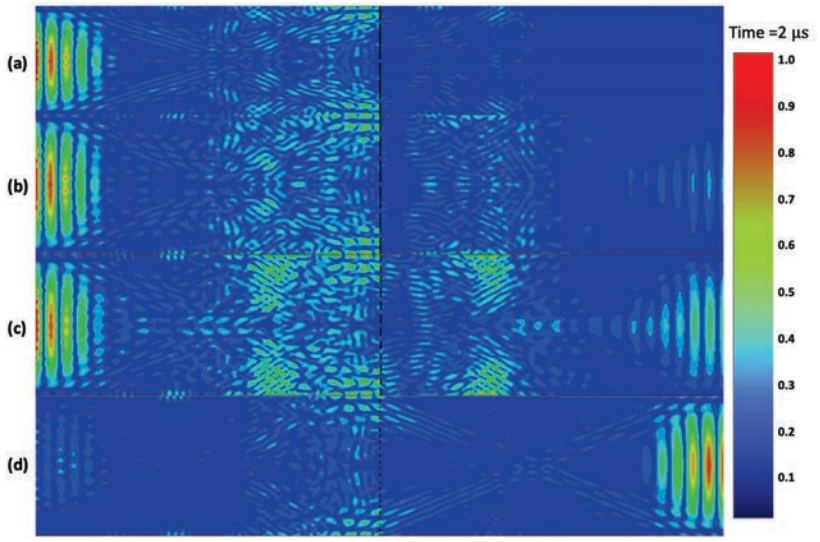

Figure 3.11: Wave propagation modes as the wave reaches the right end after crossing the interface for four asperity combinations (a) For N=3 (b) N=5 (c) For N=11 (d) N=25

Although what actually missed in this analysis is the systematic parametric relationship. In this section, all the parameters (contact width, contact space, and the number of asperities) are simultaneously changed to give the initial perspective. This example also shows the ability of the proposed model to address interface distributions efficiently and investigate a model contact interface that would be almost impossible to manufacture experimentally.

3.3.2 Random contact distribution

In the previous section, a rectangular-shaped asperity with a varying size was uniformly distributed to assess the effect of a change in the number of contact spots only. The question now could be, how does the wave behave for a given number of contact asperity but with a variable spatial distribution? In this modelling part, the size of solids remain same as specified in the previous section, but the interface configuration is designed with

a constant N=50 number of asperities with spacings of 60 microns and 20 microns in combination as seen in figure 3.12, the height of all the asperities is fixed to 10 microns. All the cases result in the same contact ratio, C_r of 0.5.

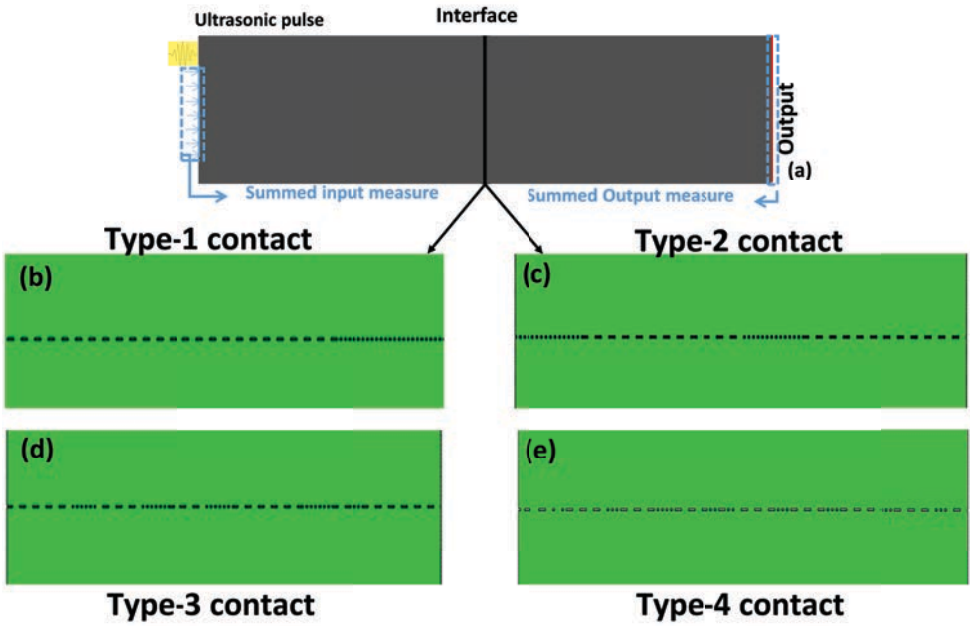

Figure 3.12: (a) Solid-solid contact interface with the interface shown in black strip (b) (c) (d) (e) four different contact distribution types

Referring back to Chapter 1 about contact ratio and stiffness, it is stated that contact ratio is proportional to stiffness which relates here that in all the cases the stiffness is the same. Figure 3.13 shows the displacement fields at different time interval. It can be observed that in all the cases, the wave propagation and distribution remain almost unaltered at both the extreme end boundaries of the test sample. But at the interface, as seen in 1d, 2d, 3d, 4d, based on how the interface is shaped, the wave experiences unique traveling patterns (multiple transmissions). This happens as the wave is transmitting through the asperities depending on their positioning and as it travels further, the wave is convolved to have a similar wavefront. This tends to show that the interface at such a scale will not have a drastic effect on what is measured at the transmission end. This concludes that a change in interface configuration for a given contact ratio will have minimal impact on the simulation capacity. Figure 3.14 shows the FFT plots for four type of irregular interface distributions types. As mentioned earlier, they do not experience a major change

except that short unwanted pulses are experienced in type 2 and 3 interfaces, it can be explained as the distortions that happen when the residual waves are recorded.

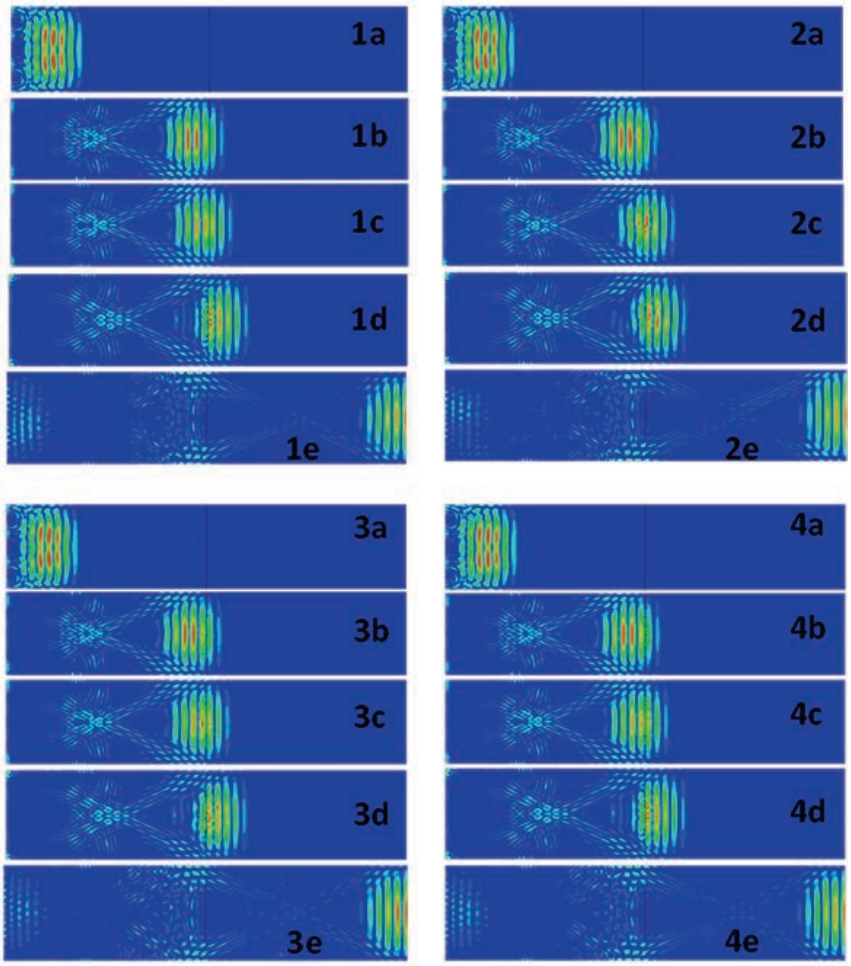

Figure 3.13: Time lapse of wave propagation through different interface combinations with (1) (2) (3) (4) Irregular or asymmetrical asperity distribution corresponding to (a) (b) (c) (d) type interfaces

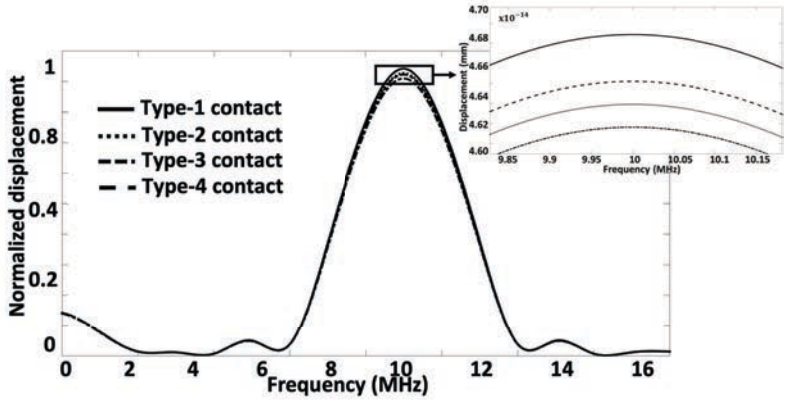

Figure 3.14: FFT plot (Transmission) of the four time domain plots corresponding to irregular interfaces

3.4 Relationship between the wave propagation and interface parameters

3.4.1 Relation between the interface morphology and transmission coefficient

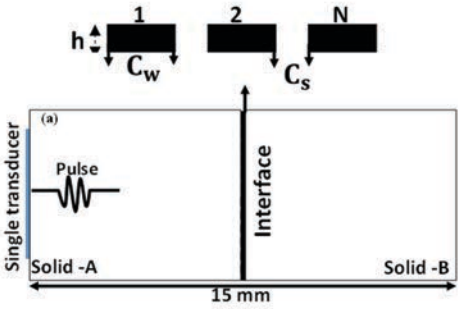

Contact Space (Cs) (microns) \ Contact width (Cw) (microns)	20	40	60	80	100
20	Cr=0.5 N=100	Cr=0.67 N=66	Cr=0.75 N=50	Cr=0.8 N=40	Cr=0.83 N=33
40	Cr=0.33 N=66	Cr=0.5 N=50	Cr=0.66 N=40	Cr=0.67 N=33	Cr=0.7 N=28
60	Cr=0.25 N=50	Cr=0.4 N=40	Cr=0.5 N=33	Cr=0.6 N=28	Cr=0.63 N=25
80	Cr=0.2 N=40	Cr=0.33 N=33	Cr=0.42 N=28	Cr=0.5 N=25	Cr=0.55 N=22
100	Cr=0.18 N=33	Cr=0.28 N=28	Cr=0.38 N=25	Cr=0.45 N=22	Cr=0.5 N=20

Figure 3.15: Sketch of the geometry and summary of the studied contact configurations with N being the number of asperities and Cr the contact ratio

As emphasized in the previous sections, the relation between the transmission coefficient and the interface parameters is not that straight forward. Therefore, a systematic analysis was needed to clearly extract the relation with the interface morphology. The model used in this section is similar to the model presented in 3.10. Figure 3.15 summarises the 16 selected contact configurations, combining various contact widths and contact spaces resulting in different contact ratios and a number of asperities. Contact width and space

are changed between 20 to 100 microns and the number of asperities from 20 to 100 in different cases. The height of all the asperities is fixed to 10 microns. The interest of this work is that it covers a large range of contact ratios, from 0.18 to 0.83. It should also be noted that diagonally from left to right the different combinations result in the same contact ratio and from right to left, resulting in the same number of asperities. Transmission coefficients will be considered because existing literature is mainly dealing with the reflection coefficient. The following figures 3.16 3.17 3.18 3.19 3.20 and 3.21 show the wave propagation images with the corresponding frequency domain plots for a fixed contact width (20 microns) and changed contact space with varying number of asperities.

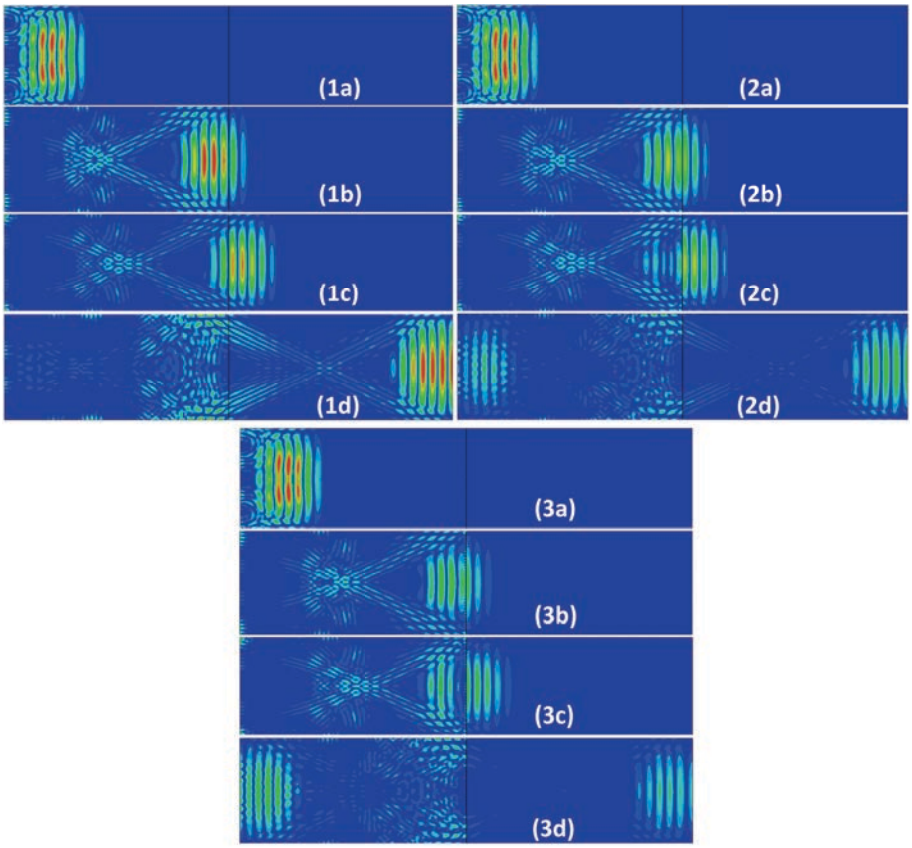

Figure 3.16: Wave propagation time lapse for 3 configurations (a) Cw 20 and Cs 20 microns, N=100 (b) Cw 60 and Cs 20 microns, N=50 (c) Cw 100 and Cs 20 microns, N=33

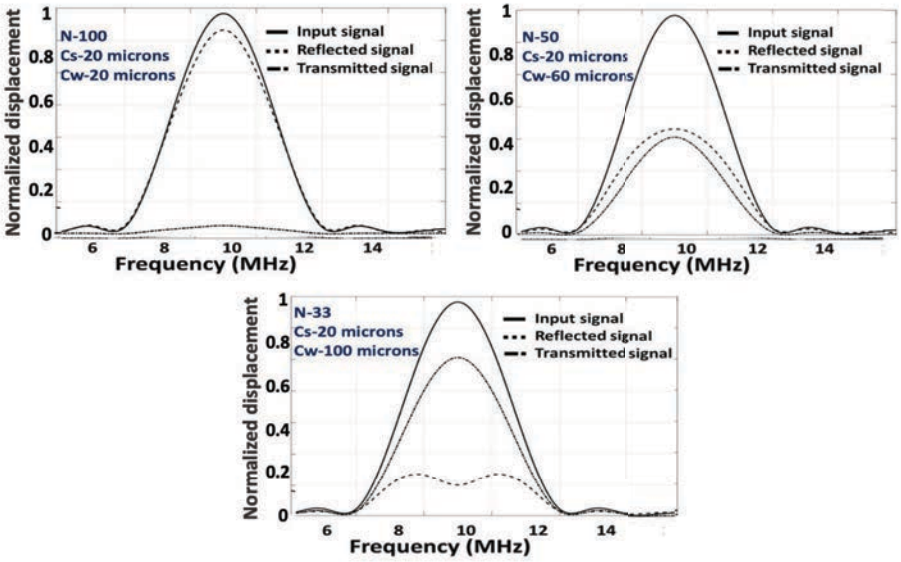

Figure 3.17: FFT plot for 3 configurations with (a) Cw 20 and Cs 20 microns, N=100 (b) Cw 60 and Cs 20 microns, N=50 (c) Cw 100 and Cs 20 microns, N=33

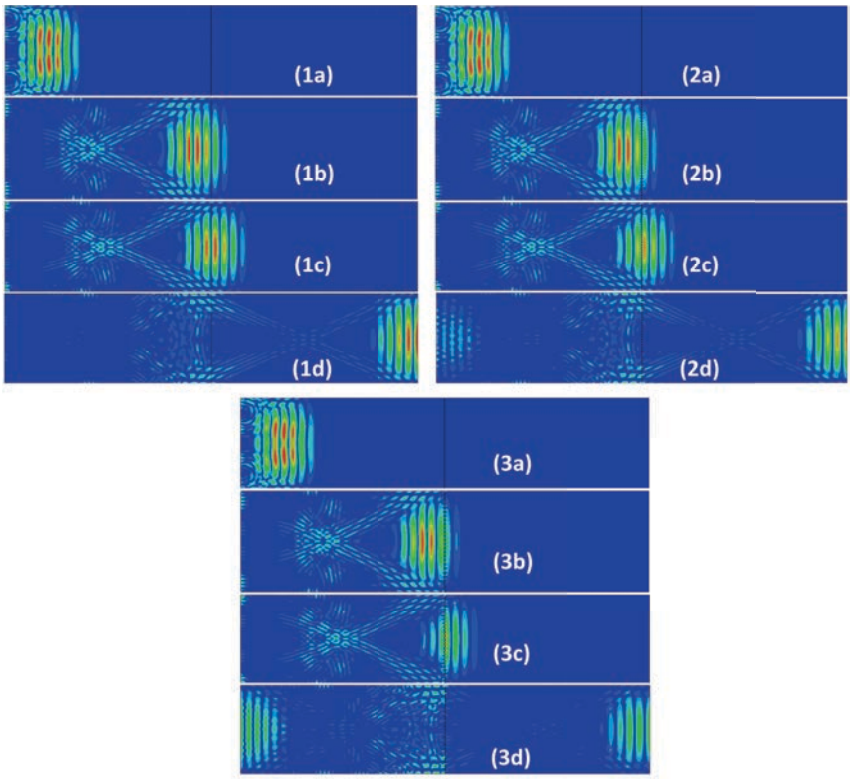

Figure 3.18: Wave propagation time lapse for 3 configurations (a) Cw 20 and Cs 60 microns, N=50 (b) Cw 60 and Cs 60 microns, N=33 (c) Cw 100 and Cs 60 microns, N=25

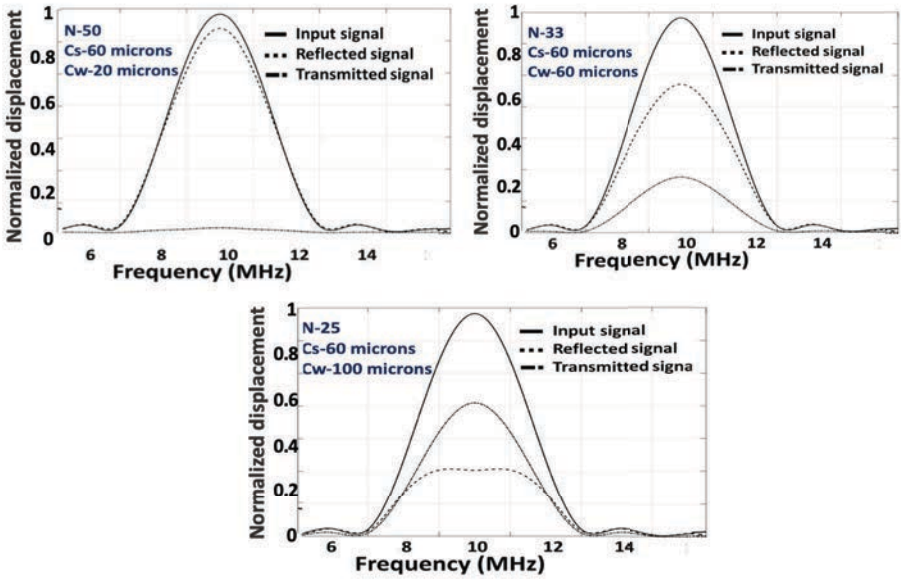

Figure 3.19: FFT plot for 3 configurations with (a) Cw 20 and Cs 60 microns, N=50 (b) Cw 60 and Cs 60 microns, N=33 (c) Cw 100 and Cs 60 microns, N=25

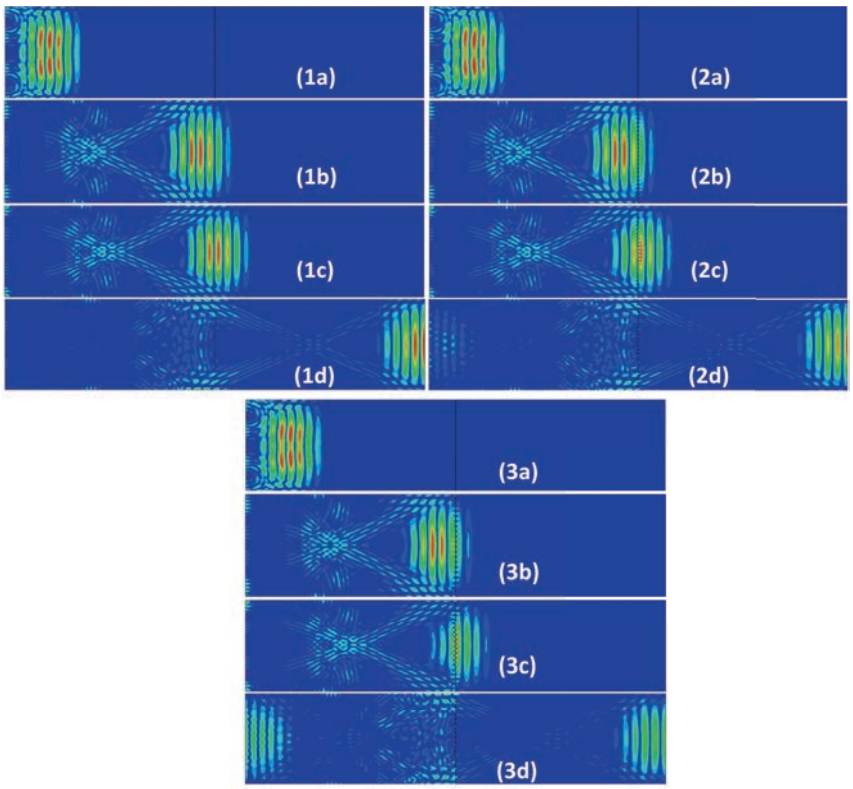

Figure 3.20: Wave propagation time lapse for 3 configurations (a) Cw 20 and Cs 100 microns, N=33 (b) Cw 60 and Cs 100 microns, N=25 (c) Cw 20 and Cs 100 microns, N=20

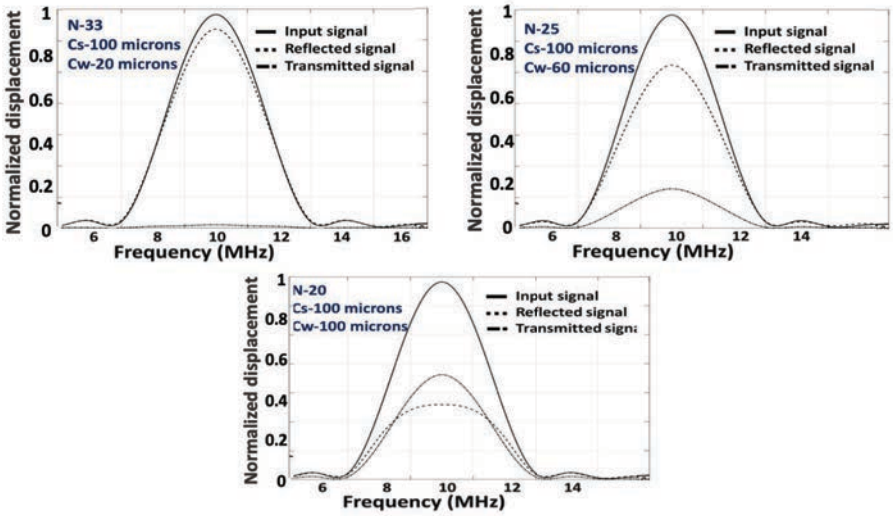

Figure 3.21: FFT plot for 3 configurations with (a) Cw 20 and Cs 100 microns, N=33 (b) Cw 60 and Cs 100 microns , N=25 (c) Cw 20 and Cs 100 microns, N=20

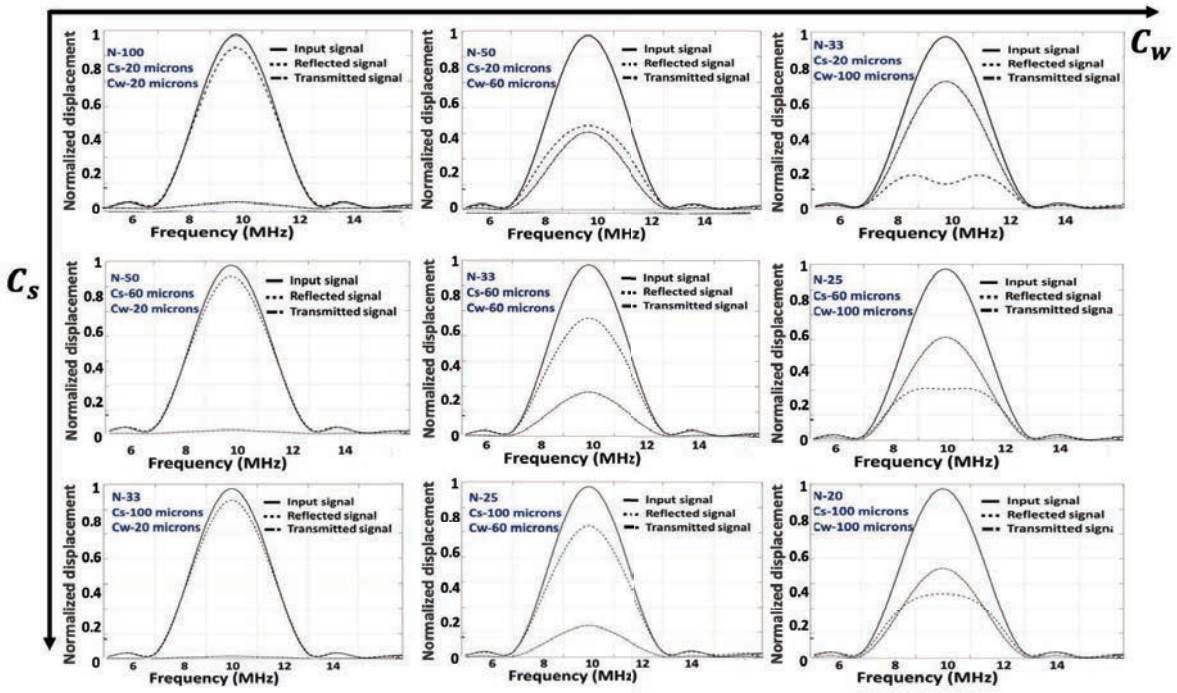

Figure 3.22: Compilation of frequency domain plots showing difference in the transmission and reflection coefficients with their respective configuration changes.

As seen in figure 3.22 from left to right, when the width of the asperity is increased, the resulting number of asperities is reduced too, causing the wave to propagate through

asperities of the interface. As observed from top to bottom, reflection and transmission more or less remain consistent for contact width of 20 microns but as the width is increased to 60 microns, reflection increases but with an overall reduced magnitude compared to when contact width is 20 microns. It further reduces to have high transmission in the end. This shows the double dependency on the number of asperities and contact width in an interface.

To evaluate this dependency, the transmission coefficient is calculated for different interface geometries and a first comparison plot is drawn comparing the change in number of asperities for all the contact width and contact space configurations figure 3.23. The transmission coefficient is seen monotonically increasing as a function of the number of asperities. Important conclusions that can be drawn from the figures 3.21, 3.22 and 3.23 are that for a given contact width, transmission coefficient increases with an increased number of asperities.

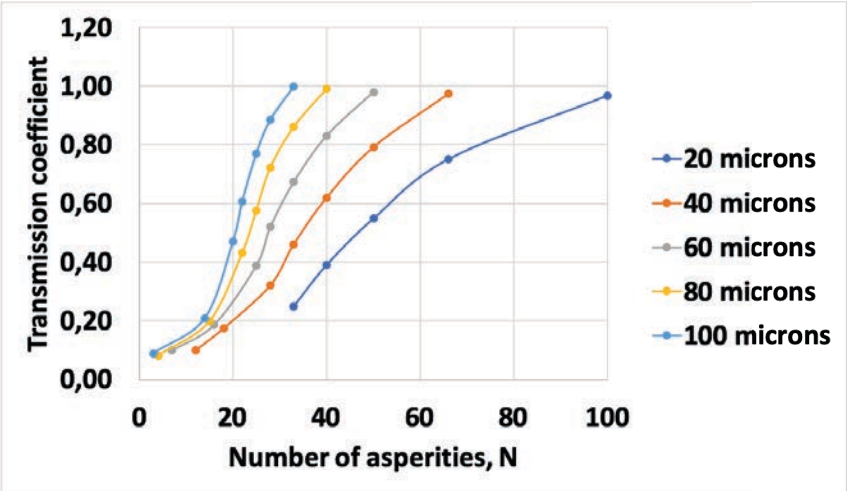

Figure 3.23: Transmission coefficient plotted in comparison to change in number of asperities for different contact width configurations, Tc $\propto N$

Further, the transmission coefficient change with respect to the contact width can be seen in figure 3.24. For a given number of asperities, it is shown to linearly depend on the contact width, which can be connected to the single asperity case previously shown in figure 1.29. Based on the two figures 3.23 and 3.24, referring to the equation of contact ratio from the Chapter 1, transmission as a function of Cr is drawn as seen in figure 3.25.

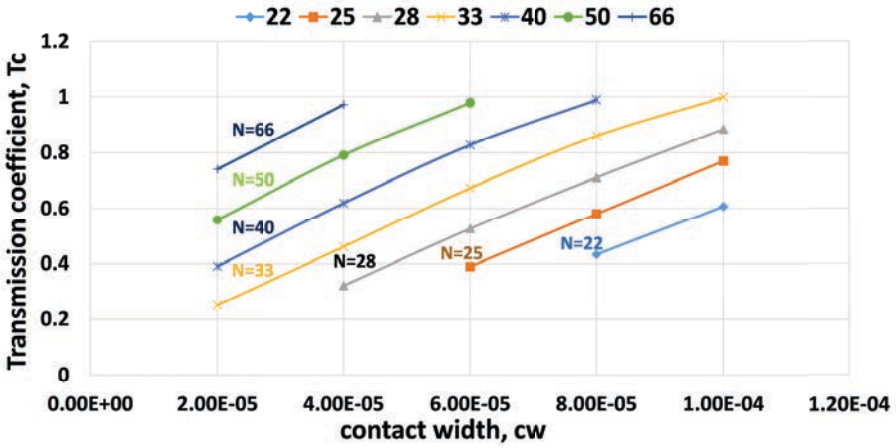

Figure 3.24: Transmission coefficient plotted in comparison to change in contact width for different number of asperity configurations, Tc $\propto Cw$

The transmission coefficient increases as a function of the contact ratio but a unique relationship cannot be identified. Indeed, various transmission coefficients can be extracted for a single contact ratio depending on the contact morphology. As an example, when a fixed contact ratio of 0.5 is considered, the wave transmission increases from around 0.45 to 0.95 with the growing number of asperities and reduced contact width.

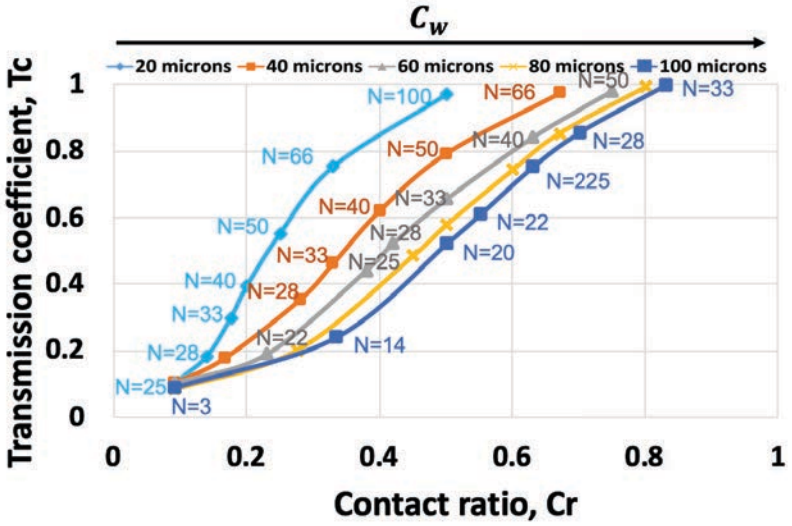

Figure 3.25: Transmission coefficient plotted in comparison to contact ratio for different contact width configurations and number of asperities, Tc $\propto Cr$

Also, the transmission coefficient linearly increases for N=33 covering all the combinations of contact width and space. This concludes that the wave transmission or

reflection does not just depend on the number of asperities or contact width but depends on the combined parameters of the interface.

If the interface parameters cannot be individually and independently considered, one should recall the main finding from Kendall and Tabor [36] or Tattersall [35] tending to show that the key parameter governing transmission is the interface stiffness.

3.4.2 Relation between contact stiffness and transmission coefficient

Now that the relationship between the transmission coefficient and other contact parameters is established, it is important to relate the transmission coefficient to the interface stiffness. To do so, a simple stiffness analysis has been performed for each contact configuration previously described in figure 3.15. Moreover, complementary contact configurations using the same contact widths but fewer asperities were added in order to extend the range of contact ratios, especially towards the lower values. The contact space has been increased up to 2mm for some configuration.

The selected model is similar in terms of mesh density, material type, and interface distribution. However, the study is carried out in static analysis and no wave propagation is implemented. Instead, a small displacement is applied at a reference point and the values of the interface stiffness in each case are extracted based on the reactive force. Various new boundaries and constraints are involved which are shown in figure 3.26.

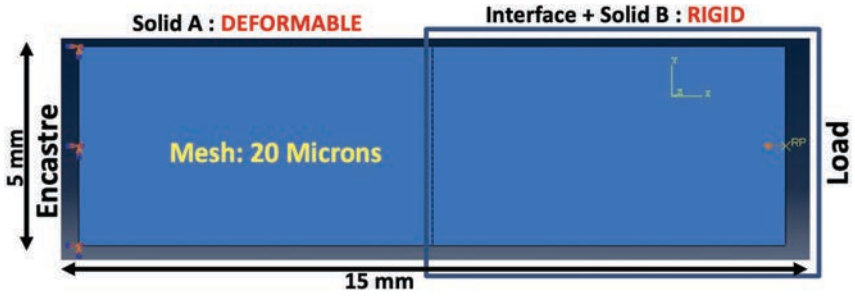

Figure 3.26: Geometry corresponding to the model used in determining the interface stiffness

In the above figure, RP to the right is the reference point at which a 1E-11 amplitude displacement is applied in the negative x-direction. A rigid body constraint is applied

to both the interface and the solid B making it combined solid indenting the solid A defined as deformable. Solid A is encastre on the left side ensuring zero displacement. The whole simulation is carried out in ABAQUS/static general case. The simulated reactive force versus displacement curve is extracted and the stiffness value calculated based on the equation:

$$Stiffness,k = (Reactive force)/Input\ displacement\ amplitude \tag{3.1}$$

The figure 3.27 summarises the evolution of the interface stiffness with the number of asperities for the different contact configurations. It is important to remind that the absolute value of the stiffness has to be carefully considered as it is extracted based on a 2D plane strain model. The figure 3.27 shows the evolution of the computed interface stiffness with the number of asperities.

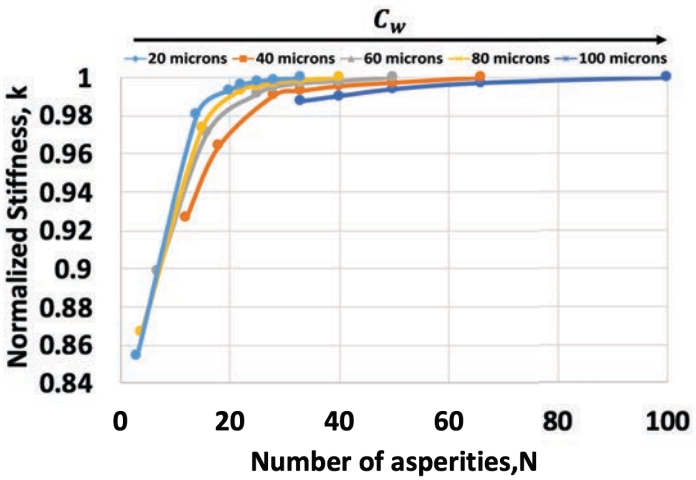

Figure 3.27: Relationship between the interface stiffness and the number of asperities

The observed trends appear to be in good agreement with the contact mechanics exposed by Kendall and Tabor [36]: for a given contact width, the stiffness linearly increases with the number of asperities up to a certain point beyond which asperities start to interact with each other, leading to a slow increase of the stiffness when further increasing N. When focusing on the stiffness computed beyond N = 20, one can still see that a small variation of stiffness from 2 to 4% can occur when increasing the number of asperities or the same order of magnitude when increasing the contact width for a

given number of asperities. To conclude, a further relationship is built between stiffness and contact ratio as seen in figure 3.28,

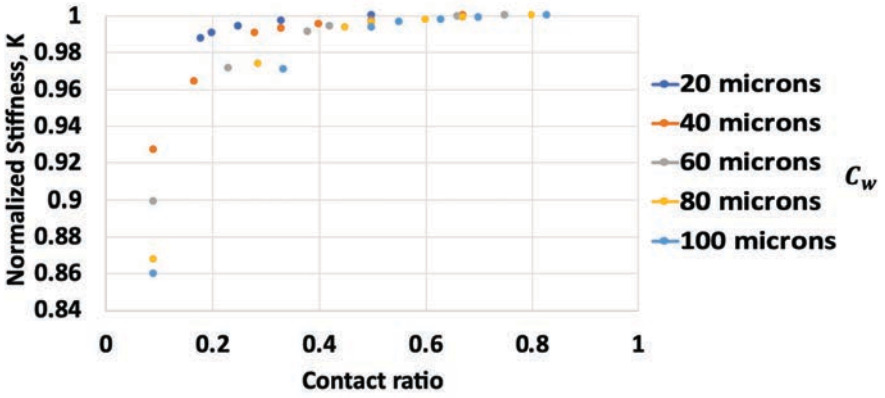

Figure 3.28: Relationship between stiffness to contact ratio Included contact ratios in the range of 0.09-0.33

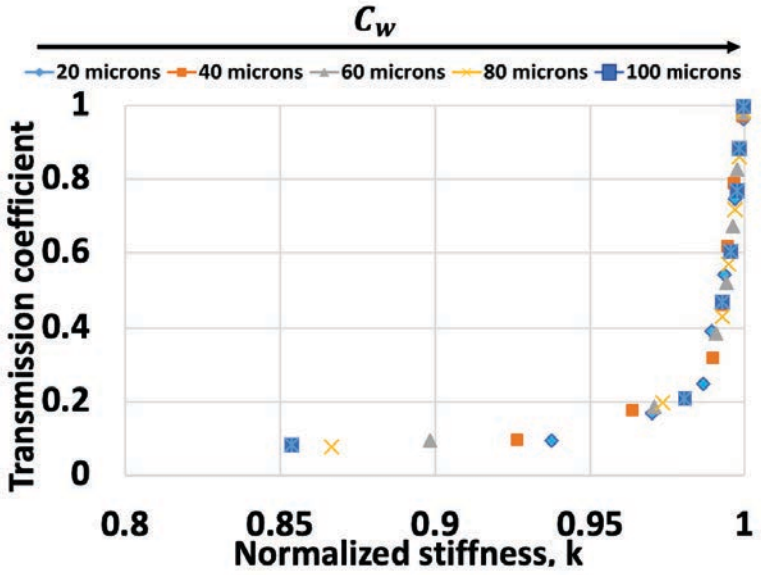

Figure 3.29: Transmission coefficient versus the interface stiffness for different contact widths

When combining this analysis to the wave propagation one, the transmission coefficient can now be plotted versus the interface stiffness (figure 3.29). It can be noticed that it follows a relatively unique bi-linear evolution with a slope change around the stiffness value of 3.79E+10 N/m. Over the lower stiffness value range, i.e. for contact ratios from

0.09 to 0.33, the transmission coefficient is not highly sensitive to a change in stiffness. However, beyond this point, a slight change in stiffness induces a larger variation in terms of the transmission coefficient. This could be due to the fact that at that point, the space between asperities decreases twice to 10 times the value of the previously defined configurations which results in the sudden growth of the transmission curve.

It should be important to state that interface stiffness is internally dependent on local interfacial parameters (size, shape, and asperity distribution). But also stiffness could be the same for different Interface configurations. In an interface, the asperities initially are far apart, they tend to be very close once new contact points are created, around the existing contacts due to an increase in load. This will affect wave propagation and also the influence of local contact parameters.

Also, it was previously noted that the transmission coefficient is proportional to the diameter of asperity which was limited to a single asperity. In that analysis, for a single asperity, it was noticed that above 0.5 mm change in diameter is independent it is contact ratio that has to be assessed. But, as the interface deals with multiple asperities, diameter and number are intrinsically dependent, it can in terms of contact ratio be said that above 0.5 different contact ratio combinations will lead to the same stiffness which means the same transmission value.

It can be concluded from the above analysis that stiffness is partially proportional to the transmission coefficient and contact ratio and deviates above a critical value due to change in internal geometrical parameters that are complex to study in reality. Based on the above-mentioned results, the following conclusions are drawn.

3.5 Conclusions and discussions

In this chapter, a novel numerical approach based on a 2D finite element model was developed to study the relationship between the interface parameters, stiffness, and ultrasonic wave propagation. The transmission coefficient was measured for different model contact configurations and related to the corresponding contact stiffness. The relationship between the interface parameters such as contact width (Cw) and the number of asperities (N), was also obtained.

However, the approach is dedicated to 2D proving that ultrasound wave propagation in 2D can be used to study interface parameters and only gets more complex when a 3D model is considered likewise the research proposed by Kendall and Tabor (1971) for multiple asperities and contact width. Derived stiffness is not proportional to the transmission coefficient but linear to the number of asperities in multiple asperity cases as for the same stiffness, there can be different contact configurations and resulting transmission coefficients. On the other way, there could be the same transmission coefficients for different stiffness values.

Summary:

- This chapter covered an in-depth analysis on the wave propagation through the interfaces when either a single asperity or multiple asperities are involved.
- A modelling part relating the transmission coefficient to interface parameters was established and analyzed based on the literature review. It was concluded that transmission coefficient cannot be uniquely connected to one of the parameters defining the contact morphology.
- The study is further extended to stiffness analysis and showed that the transmission coefficient depends on the interface stiffness through a bilinear relation with a varying sensitivity for contact ratios larger than 40%.
- It can be concluded from the figures 3.27, 3.26 that transmission coefficient and interface changes indeed characterize the stiffness of an interface. Although the relating curves are drawn, they do not explicitly conclude on how stiffness affects the interface. So, curves can be considered as the basis that can be used for further study.
- Modelling in 2d did have a high advantage in showing the wave interaction with the interface. The results obtained and conclusions are drawn are not extended further considering the complexity and the modelling part form the basis for adapting imaging methods that are proposed in the following chapters.

Personne n'entreprend des recherches en physique dans l'intention de gagner un prix, c'est la joie de découvrir quelque chose que personne ne savait auparavant.....

No one undertakes research in physics with the intention of winning a prize. It is the joy of discovering something no one knew before.....

Stephen Hawking

4

Ultrasonic mapping of the interface using detection based algorithms

Contents

Previously in Chapter 3, the analysis of the ultrasonic reflection using a finite element model has been presented for different contact interface configurations changed at the asperity scale. Although the primary objective of studying the real contact area could not be well reached, it has been shown that it is still complicated to directly identify the exact morphology of a rough interface. In all the simulations, a single element transducer was used

to generate an ultrasonic wave which appeared to be a limiting factor of the methodology. Now the question still remains if it is possible to develop an ultrasonic based method able to provide exact information regarding the interface at the asperity scale. To address this point, a new approach using ultrasonic arrays is developed and discussed. Using an array is an alternative to conventional single element transducer, which shows a promising potential to study the smallest regions in a tribological contact interface. A detailed explanation about ultrasonic array and its implementation is discussed in this Chapter.

4.1 Phased array transducer network

An ultrasonic array is a group of transducer elements placed together to form a network. This transducer array network generates ultrasound waves as a beam profile or as a pulse profile that travels through the solid. The concept of phased array was first studied by Karl Ferdinand Braun, 1905. He developed the method to direct a wave in the proposed direction by carefully arranging antennas. He was awarded Nobel Prize in physics for his pioneering work in wave transmission using arrays. During the time of World War 2, the phased array was mainly used for radar and sonar-based applications but got a major uplift only later. Phased array applications were initially confined to medicine but later widened to various other fields due to its performance and imaging capabilities, Jan C Somer, 1968, J. D. Achenbach 1979 [89], [84], Thunderstone, Olaf Von Ramm 1976 [90]. Developments especially grew in NDT, where the objective is to exploit the signal data in order to find areas of reflectivity. In other words, this technique gives the possibility to test materials for crack and defects and image them. M. G. Silk, B. H. Lidington 1975 [91] were the first ones who worked extensively on using an ultrasonic approach to characterize defects based on time-delay approach, they proved that it is possible to efficiently map the defects using the phased array approach.

Conventional transducer arrays consist of several individually connected elements with an optimized spacing and pitch width. Each element in the array is individually excited to generate a high frequency (1-100 MHz) pressure pulse which is later reflected and recorded. These reflections are processed using signal processing algorithms to produce a final acoustic image.

4.1.1 Design and working principle

The working principle of transducer array is similar to a single element excitation and functions as a two-way transmitter and receiver. Every single element in the array is excited and the reflections are collected as raw data which is further processed by the algorithm.

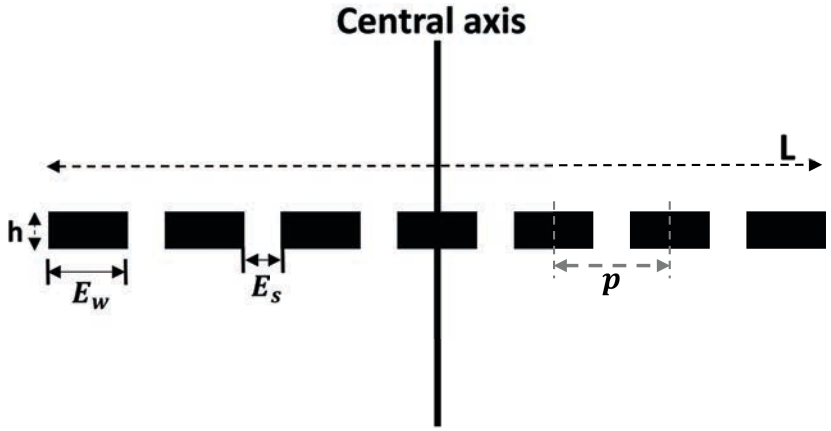

Figure 4.1: 1-D linear array representation

This array can be implemented in many ways based on the type of application and targeting region. Here a simple integration of a linear array is shown in figure 4.1 where E_w is each element width, E_s is the element space or gap between transducers, p is the element pitch or central axial distance between adjoining transducers and L, h are the length and height of the array. In any phased transducer array the important parameters that change the beam profile are:

- Frequency that ranges between 2 MHz-10 MHZ for increased depth penetration and 10 MHz-100 MHz for high resolution and image sharpness.
- Number of elements, the depth and thickness of the testing material. Although high number of transducers results in increased resolution in both axial and lateral directions.
- Element dimensions, width and spacing important for beam steering capability.

If it can be basically used as a pulsing and receiving device, a more advanced level will consist of the implementation of 'delay laws'. Separate variable time delays forming a

delay law are incorporated at each signal path to control the phases of the signals before combining all the signals together at the output.

There exist many transducer arrays types classified based on the type of application and scanning as shown in figure 4.2.

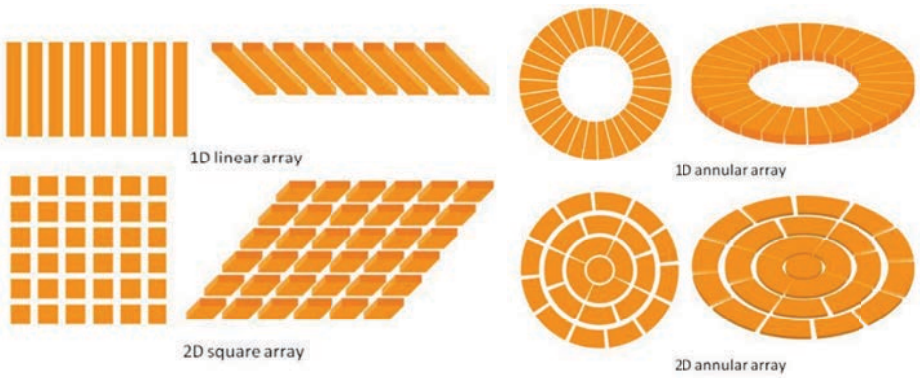

Figure 4.2: Transducer array types (Olympus, 2011)

A 2D square array is a parallel combination of many 1D linear arrays that can focus and steer the beam in 3 dimensions which enhances the spatial resolution, but the use of more elements increases the complexity in designing and computing. The processing time of phased arrays is generally expected to be fast such that they can be adapted to online monitoring. This becomes obviously more difficult with 2D, 1.5D, and 3D arrays due to a large amount of generated data.

4.1.2 Data Visualisation

Be it a single element measurement or an array implementation, the signals that are collected from the transducer are displayed in different formats. The most used types are, A-scans, B- Scans, and C- Scans formats.

A-scans

A-Scans, i.e. Amplitude Scans, display the amplitude of 1D echoes of a single pulse, after as a function of the travelling distance/time.

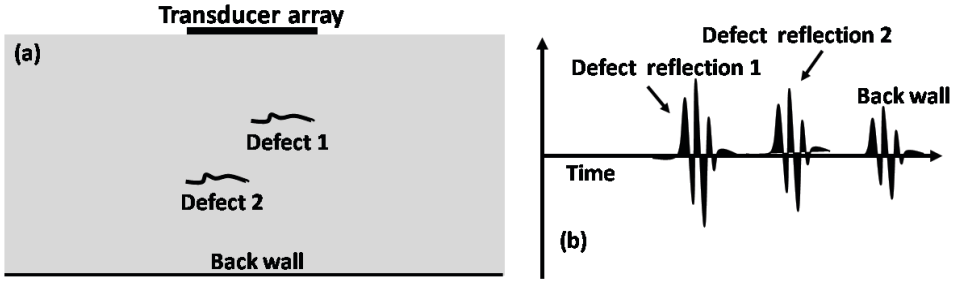

Figure 4.3: (a) Schematic of transducer array implemented on single defect (b) A-scans with amplitudes corresponding to the defect and back wall

For instance, in a solid characterized by two discontinuities (figure 4.3 a), two different reflection peaks will be observed at two different time intervals as plotted in figure 4.3 b. It should be important to specify that the recording of A-scans is affected by the number, placement, and distribution of the discontinuities.

The A-scans are very crucial in ultrasonic measurements as they carry information of amplitudes and time of flight corresponding to the reflection and form the basis for recently developed signal processing methods.

B and C scans

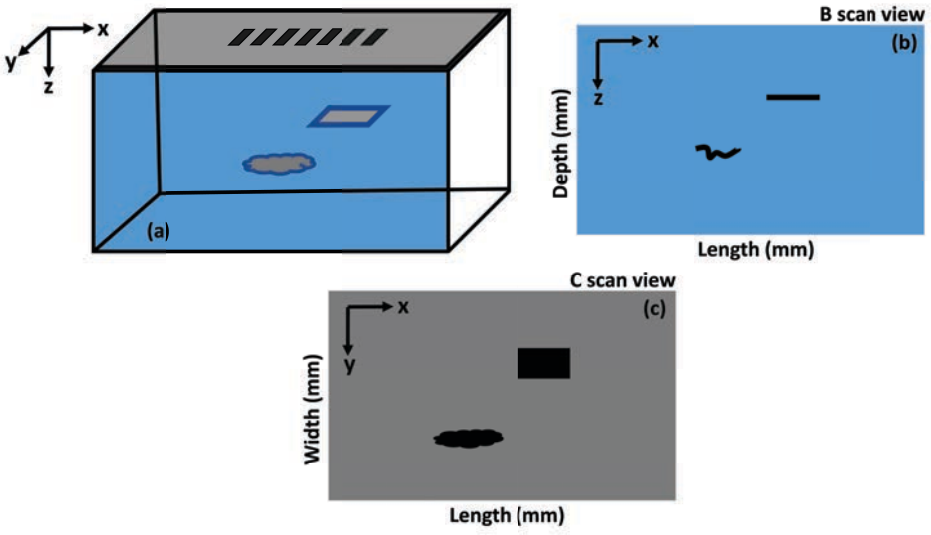

Figure 4.4: Implementation of transducer array on 2 different defect types (b) B scan (c) C scans

Brightness scan or B-scan is a 2D image representation of several A-scans. The image consists of all the summed reflected signals. Figure 4.4a) shows a 3D view with two

different defect types and the corresponding B-scan in figure 4.4b). This can be simply viewed as a cross-sectional view of the test subject.

C-scan is also a 2D image representation of the test subject but the reflection from the defects is displayed from a top or surface view perspective. In any testing case, the images are mapped based on the extracted data from the x, y, and z positions (axis, angular, and depth). This requires moving mechanically or electronically the transducer along one or two of the x and y-axis for these two types of visualization.

4.2 Focusing methods

Pulsing methods have improved from the past 50 years and range from simple sequential pulsing to most complicated delay-based beam steering methods. In ultrasound applications, focusing methods gives the possibility of steering and focusing the beam to a specific target point without altering either the position or angle of the transducer array itself.

4.2.1 Sequential pulsing

The simplest way to use an array is to pulse it element by element, sequentially until the last one in the array is covered. This is a straight forward data acquisition strategy that produces a number of A-scans recorded by each element in the array, depending on the transmission and receiving strategy. Recording and storing the A-scans corresponding to each element combination is a method called the Full Matrix Capture and will be detailed in section 4.3.2. This method has advantages in terms of easy data acquisition, processing, and imaging, although this procedure is limited to applications where steering and focusing are not required. The aperture of the array attained in this method is directly connected to the array position and to target a different position, the array has to be manually moved to the corresponding region. This process is tedious to be able to collect the data from the array and process (slow data acquisition time). Also, the consistency is questionable due to the continuous moving and clamping of the array.

4.2.2 Beamforming steering and focusing

When a single element transducer is used, only its frequency and shape can be modified to control the propagating pattern, but the direction of the ultrasonic beam will remain in the axis of the transducer. Steering the beam or changing its shape can be achieved by using a phased array. Beamforming is an electrical steering phased array procedure where an ultrasonic wave is propagated through the combination of several independent element excitations that merge into a single beam. Based on the selected delays, the beam can be steered and focused on a region of interest [92]. The beamforming is achieved by strategically exciting carefully selected elements in the array and will lead to different beam profiles when it is steered or focused as shown in figure 4.5.

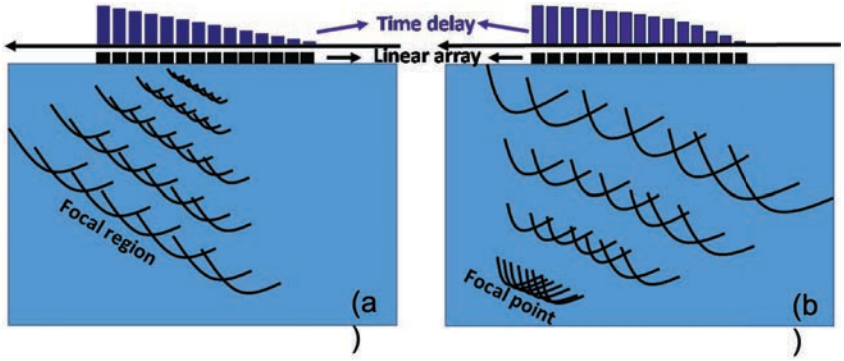

Figure 4.5: Schematic beam profile using a phased array (a) steering without focusing (plane wave) (b) focused beam (Inspired from Peter J. Shull, 2002)

The major advantage of implementing beam steering and focusing is that they can cover an inspection area larger than the simple total aperture of the array without disturbing the array position. Properly combining the excitation of each element can lead to different scanning strategies such as linear, sectorial, or depth based on the target as seen in figure 4.6. In sectorial scanning, the wave is propagated along with each transducer with multiple delay laws to scan over different angles for a given depth.

Depth scans can focus at multiple depths for a given beam direction using a delay law for each selected depth. Depth focusing has the advantage of increased depth field with steady sensitivity over its counterparts, Cochran, 2006 [93], NDT Olympus 2007, [94], [95] . With electrical scanning, the pulse repetition can attain the maximum rate with

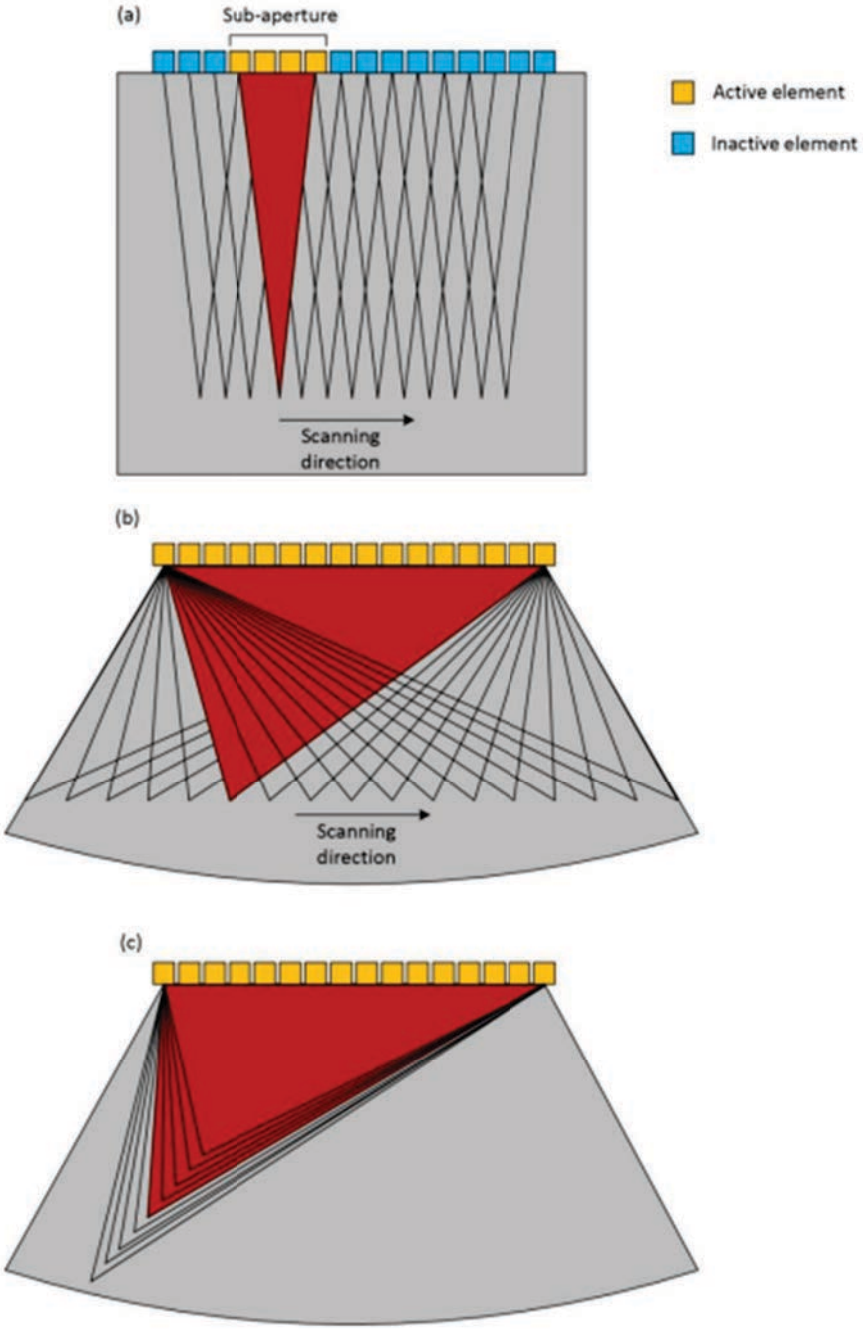

Figure 4.6: Transducer array scanning modes (a) Linear scanning (b) Sectorial scanning (c) Depth scanning (Miles Weston, 2011))

delay law adaptation. This possibility makes electrical scanning faster than mechanical and single element scanning.

In all these scanning strategies, the delay law is derived based on the target and transducer coordinates. The delay is the time difference between each transducer excitation

and is defined in such a way that the constructed beam is focused on a specific target point. The equation regarding the delay can be expressed as,

$$t_d = (\frac{1}{c}\sqrt{(x_i - x_f)^2 + (z_i - z_f)^2}) \tag{4.1}$$

Here c is the speed of sound and (x_i,z_i) are the coordinates of the firing element and (x_f,z_f) are the focal point, Jensen 1999,[96]. In the reception process, the A-scans corresponding to the reflected signal from the focal point are then collected and summed as seen in figure 4.7. However, the signals after the reception are adjusted using a counter delay. This counter delay corresponds to the delay law selected in transmission and is applied to compensate the time shift between each A-scans and properly sum the amplitude of the reflections.

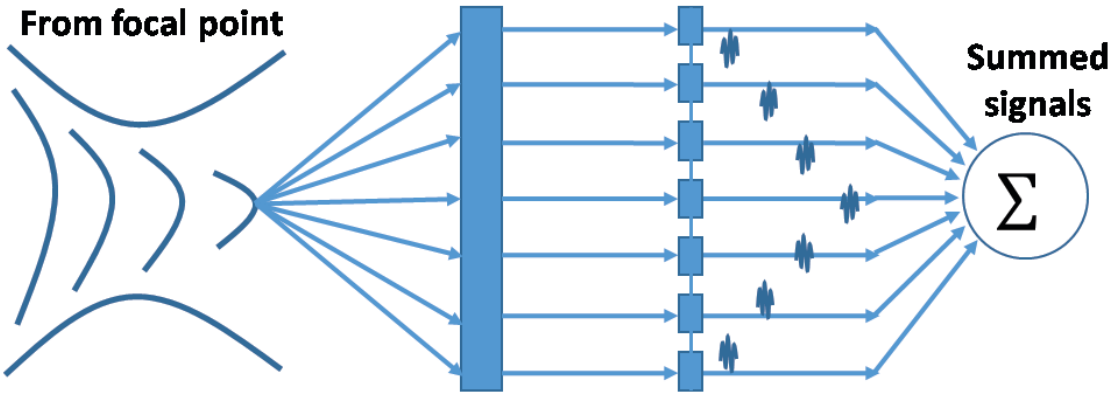

Figure 4.7: Summation of all the reflections received from the focal point

4.2.3 Grating lobes

Grating lobes are the unwanted reflections that are usually experienced in any phased transducer array due to the constructive interferences of the waves outside the focusing region. This grating lobes or side lobes could happen either due to un-optimized usage of the phased array such as an unsuitable element size and spacing or in some cases due to the conditions of testing (complex geometry). Shi Chang Wooh et al 1998 [97], [98] conducted an interesting study on the effect of array parameters on its performance especially to increase the main lobe amplitude. By changing the inner element spacing, they showed that attenuation on the side tends to appear for larger spacing values. They concluded that if the inner element spacing in the array is larger than half of the wavelength, the

grating lobes will tend to appear. One important observation is that to achieve high efficiency, the inter-element spacing has to be lower than half the wavelength for steering over 180 degrees. Following is an example of a 7-element linear array for which the spacing between each element is changed to illustrate this effect. It can be noted in the figure 4.8, that when the spacing between the elements is half the wavelength (figure 4.8 a), the beam is more focused and generated with a larger beamwidth right in the axis of the array. If the spacing is increased to one wavelength, the beam profile is more disturbed with grating lobes on the sides and the main lobe with a narrow beamwidth [99].

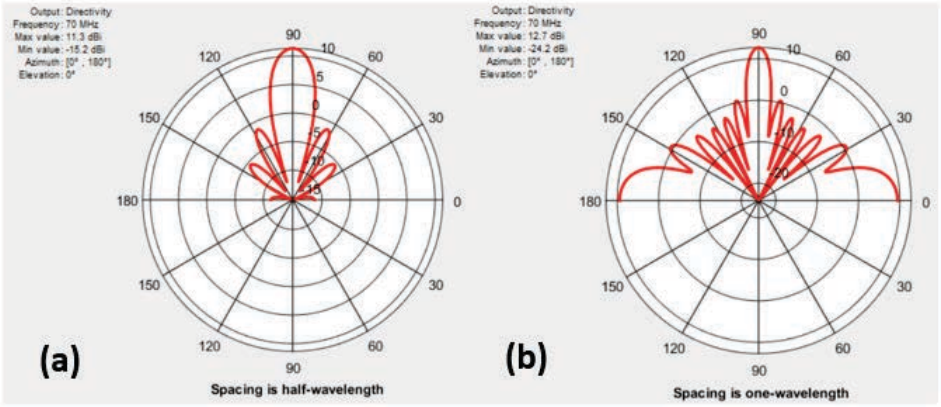

Figure 4.8: Effect of the element spacing on the directivity pattern for (a) half wavelength spacing and (b)one wavelength spacing (MATLAB, 2016)

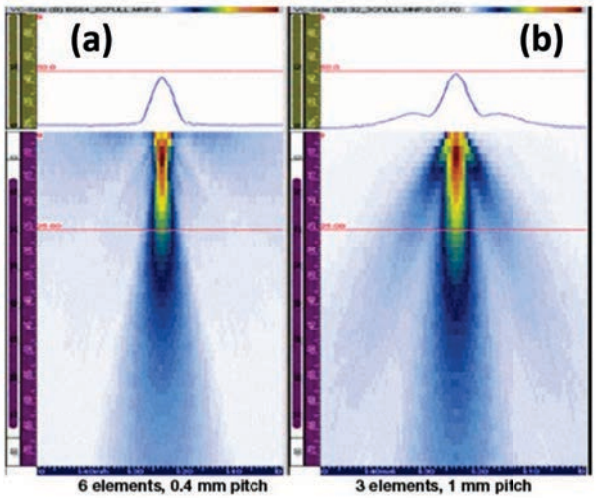

Figure 4.9: Comparison of beam profile for (a) 6 elements (b) 3 elements (Olympus, 2018)

Figure 4.9 represents two examples of an array composed of 6 elements, 0.4 mm each (figure 4.9 a) and 3 elements, 1 mm each, 4.9 b. It is shown that the array with

6 elements will have a focused beam with no or negligible grating lobes whereas the array with 3 elements exhibits larger ones. The spacing here is the distance between each transducer element and wavelength here refers to the length of one full wave that corresponds to the specific frequency.

In conclusion, the grating lobes can be avoided by using the right element size, number, and spacing considering the wavelength in the propagating material. This will also define the spatial resolution achievable for a given array definition.

4.2.4 Image resolution

In any ultrasonic imaging applications, the quality of the image is evaluated based on the achieved spatial resolution. The latter is defined in both the axial and lateral directions as seen in figure 4.10.

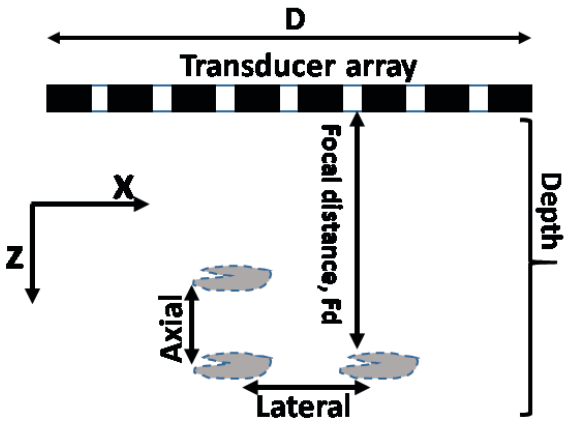

Figure 4.10: Representation of the axial and lateral resolutions

The axial or longitudinal resolution is the smallest distance that can be observed between two discontinuities along the propagation direction. It depends on the wavelength and frequency of the ultrasonic wave. The axial resolution, A_r defined by Foster, 2000, can be given as,

$$A_r = (\frac{c}{f}\frac{number\ of\ pulse\ cycles}{2}) \tag{4.2}$$

Here c is the speed of sound in the propagating material and f is frequency. For frequencies in the range of 10-20 MHz lower than 0.5 mm axial resolution can be achieved

in materials like aluminium and steel. When the pulse length is small, whether by reducing the pulse cycle or increasing the signal frequency, high axial resolution can be achieved, Ng. Alexander 2011, [100]. However, as discussed in Chapter 1 about attenuation, increasing the frequency will limit the propagation depth of the wave due to a more intense attenuation. A compromise thus has to be found between resolution and penetration depth when large structures have to be investigated.

Lateral resolution is the array ability to differentiate two discontinuities that are in the perpendicular direction compared to the propagation of the ultrasonic beam. Lateral resolution is high when the focal length of the ultrasonic beam is short which is given by the equation 4.3,

$$L_r = (\lambda \frac{F_d}{D}) \tag{4.3}$$

Here L_r is the lateral resolution, λ the wavelength, F_d is the focal distance and D is the width of the ultrasonic array. With the phased array, it is possible to increase the lateral resolution by steering and focusing at each focal point based on changes to frequency, focal length.

4.3 Detection and reconstruction algorithms

In the previous sections, different methods of manipulating the ultrasonic beam were presented. However, building an acoustic image from the collected signals requires processing using a reconstruction algorithm. This section will review three methods developed to generate images.

4.3.1 Synthetic aperture focusing technique (SAFT)

Synthetic aperture focusing technique (SAFT) is a data acquisition and processing method based on exciting a single element and receiving from the same in trans-receiver combination as seen in figure 4.11. It was first proposed by Passmann et al 1996, [101]. The major advantage of SAFT is its ability to achieve focusing for both transmission and reception without repeating the wave propagation process with all elements in the

array for an individual focal zone, this reduces computational time requirements for the delay- sum beamforming.

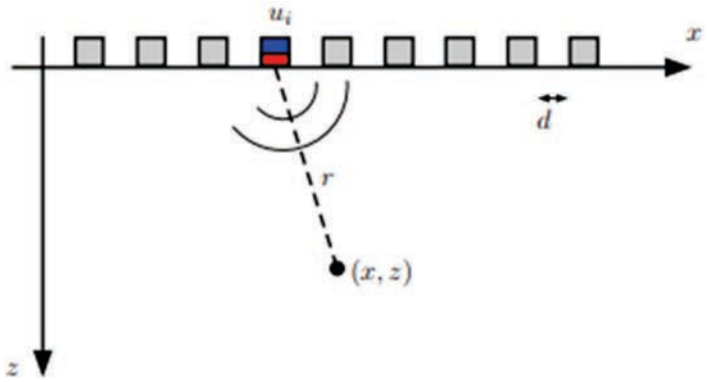

Figure 4.11: SAFT implementation, in red and blue is the transmitting and receiving element (Ewen Carcreff et al, 2015)

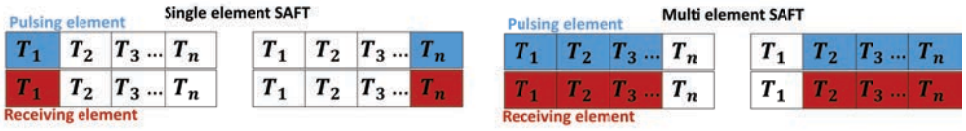

Figure 4.12: Pulsing and receiving element in SAFT (data acquisition process)

First proposed by Passmann et al 1996 [101], SAFT is developed as a delay sum imaging method within the mind to improve the lateral resolution. In this method, a signal is transmitted from a transducer perpendicular to the target position and the lateral reflections are recorded by the same transducer, [102]. In the next iteration, the transducer is moved by a slight distance in the direction of the array and is excited propagating waves on to a new target. It is the same for an array where the moving array is pulsed in a sequence and reflections are recorded as seen in figure 4.12. In the single element case, one element is fired and one element is recorded and the process is repeated with all the transducers and in multi-case, one element is fired and all transducers record data. Once the data processing is finished, based on the target point, a mesh is built to which time of flight is calculated for each of the points until the whole mesh matrix is covered. Correlation is then derived for each of the signal lines by windowing to position the amplitudes concerning its time coordinates. Later resulting matrix is plotted as an image. Although SAFT has its advantages in terms of resolution, the process could not cover the whole array aperture and signal to noise ratio is very low.

4.3.2 Full matrix capture (FMC)

Drinkwater and C. Holmes et al, 2005 [103], 2008 [104], 2014 [105] S, Robert, 2014 worked extensively on the use of phased arrays. If their initial work was a full review of already existing transducer array methods, they later developed a specific pulsing technique in combination with the reconstruction algorithm. The Full Matrix Capture is an array-based pulsing strategy that consists in capturing a matrix of raw time data acquired from every trans-receiver transducer combination. Figure 4.13 illustrates the FMC method where one element is pulsed at once while all the elements in the array are recording the signals from a reflector. This process is carried out with each element in the array until all the data is collected. In the figure, T is the firing element that ranges from 1 to n (4 in the example case). A combination of all the A-scans results in an N×N matrix as seen in figure 4.14, T_n, and R_n being the transmitting and receiving transducers in an array.

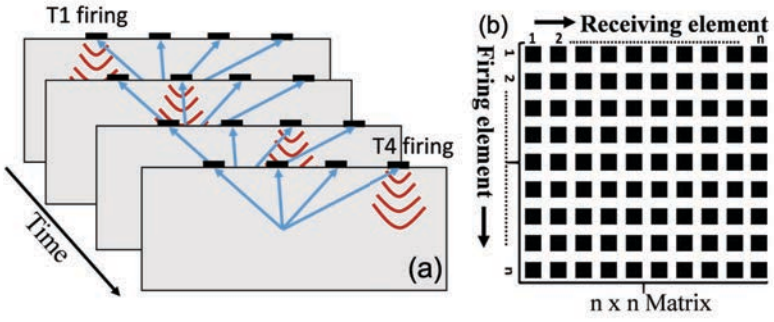

Figure 4.13: (a) Full matrix representation with each single element being fired (b) Matrix representation of the full matrix data(Inspired by Jan Carl Grager, 2018)

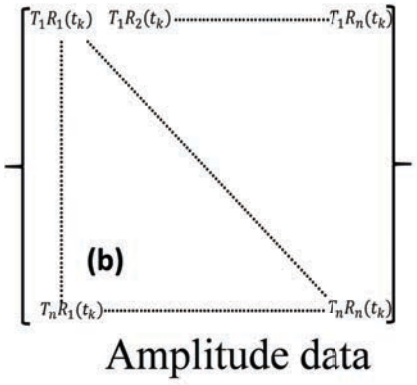

Figure 4.14: Amplitude matrix representation for trans-receiver combinations fired

4.3.3 Total focusing method (TFM)

To generate an acoustic image, the matrix that is obtained through FMC has to be post-treated using a reconstruction algorithm. One of them referred to as the Total Focusing Method (TFM) has been specially developed by Drinkwater et al 2004 [103], Lines et al 2011 [106]. It is an ultrasonic array post-processing technique which is used to synthetically focus at every image point in a target region. The main principle is to sum, for every point within the target region, the time domain signals collected via the FMC, i.e. from every transmitter-receiver combination, and corresponding to the same time of flight. This method results in a final B-scan image without moving the transducer as in with the SAFT algorithm.

Recently, DJ Huggett et al 2017, [107] or CW Tseng 2017 [108] conducted a comparative study of TFM and other focusing methods and reconstruction algorithms when tested specifically on concrete. They concluded that using a phased array is very efficient to detect a small target at a particular depth, but that FMC coupled to TFM works well to target a larger testing space while still detecting the smaller targets. It was shown that the TFM has better resolution and better SNR compared to conventional methods [93]. A. Velichko 2010 [109] presented a detailed comparison of ultrasonic array imaging algorithms, accordingly, it was shown that TFM has high flexibility and higher resolution can be achieved.

4.4 Applications of phased array and imaging algorithms

4.4.1 NDT applications

The work done by S. Mahaut et al 2008 [110], S. Chatillon et al 2000 [111] or Lakovleva et al 2014 [112] show the most conventional use of the previously described algorithm and ultrasonic features. To detect defects within a structure, the sectorial scan is used to steer the beam over a certain angle. The defects were holes with 1 mm in diameter and depth of the solid was 20 mm with frequency 5 MHz. This method makes sure that all the defects that are placed at different depths or tilts are successfully detected as seen in figure 4.15. However, the exact sizing of the holes was still an important issue and only an

approximate location was possible due to the problem of inaccurate steering angle and wrong projection of holes without angle correction in post-processing.

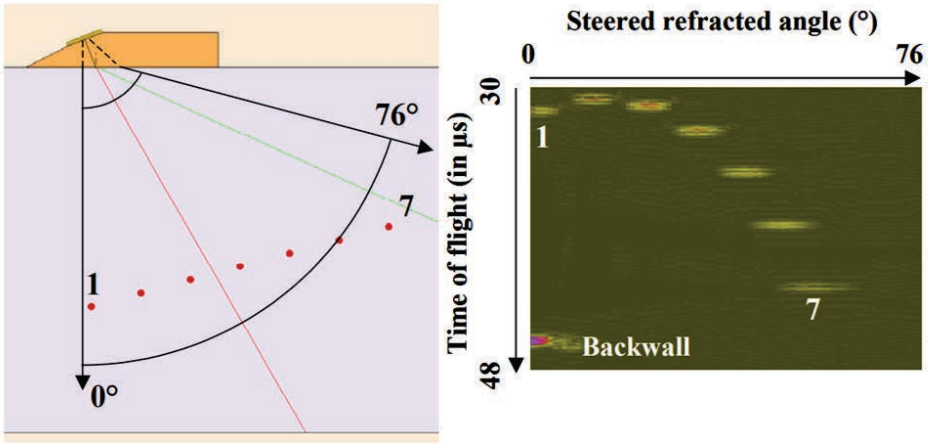

Figure 4.15: The sample and image corresponding to sectorial scanning method (S. Mahaut, S. Chatillon, 2008)

To evaluate the performance of different imaging techniques, Drinkwater et al 2005, 2006 [103], [113], conducted an experimental analysis on a simple geometry where a single point reflector (1 mm) is located along the central line of an array at a depth of 25.2 mm. An ultrasonic array with 16 elements pulsed at a frequency of 5 MHz was then used with different focusing methods such as B-scan or focused B-scan as seen in figure 4.16. It was concluded that the use of TFM enhanced the detection capability of the technique in comparison to various conventional scanning methods but most importantly, the ability to define the shape and size of the defect.

Davies et al 2006 [114] and L. Qiu et al 2013 [115] worked on TFM application in plates and also compared its performance to other imaging algorithms like Synthetic Aperture Focusing Technique (SAFT), conventional phased array and Common Source Method (CSM). Their works concluded that SAFT attains reasonable resolution but with reduced image quality and contrast whereas TFM on the contrary results in both. The same conclusions were drawn from the work performed by the Phased Array Company, 2014 comparing SAFT, TFM, and Conventional phased array methods as presented in figure 4.17 on a block with side-drilled holes of 1 mm in size. The array used in this case studies has 64 elements and operated at 5 MHz. From the processed images, 4.17b,

4.17c, 4.17 d it can be noticed that TFM is more efficient than other algorithms, which confirms the previously cited studies.

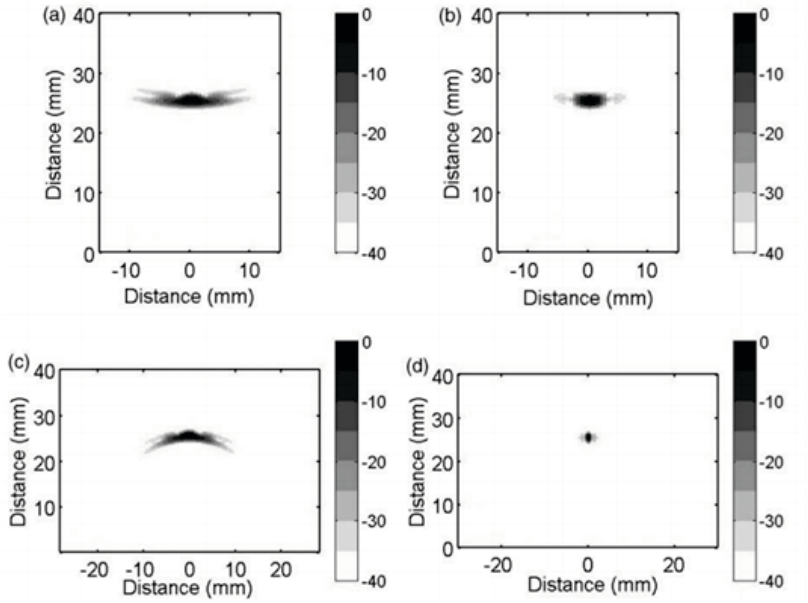

Figure 4.16: Reconstructed images for (a) plane B-scan (b) focused B-scan (c) Sector B-scan (d) TFM scan (Drinkwater, 2004)

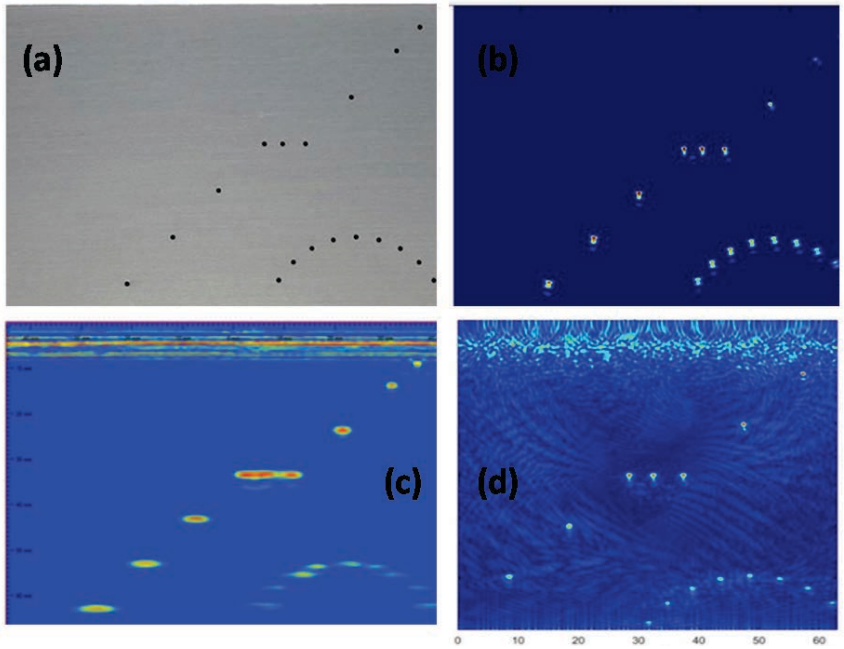

Figure 4.17: (a) Geometry of the testing sample (b) TFM implementation (c) Conventional phased array (d) SAFT (The phased array company, 2014)

Minghui Li et al 2011 [116], [117] developed an imaging technique using transducer

arrays and adaptive excitation. The adaptive process works by taking the weights of the data and appropriately delaying the time of excitation for each transducer. This is a data acquisition process that does not depend on full matrix capture but a delay law. An example corresponding to the adaptive implementation with point reflectors located at different depths can be seen in figure 4.18. The homogeneous material is aluminium, and 64 element transducer arrays with 5 MHz central frequency and inner spacing of 0.63 mm is used in testing.

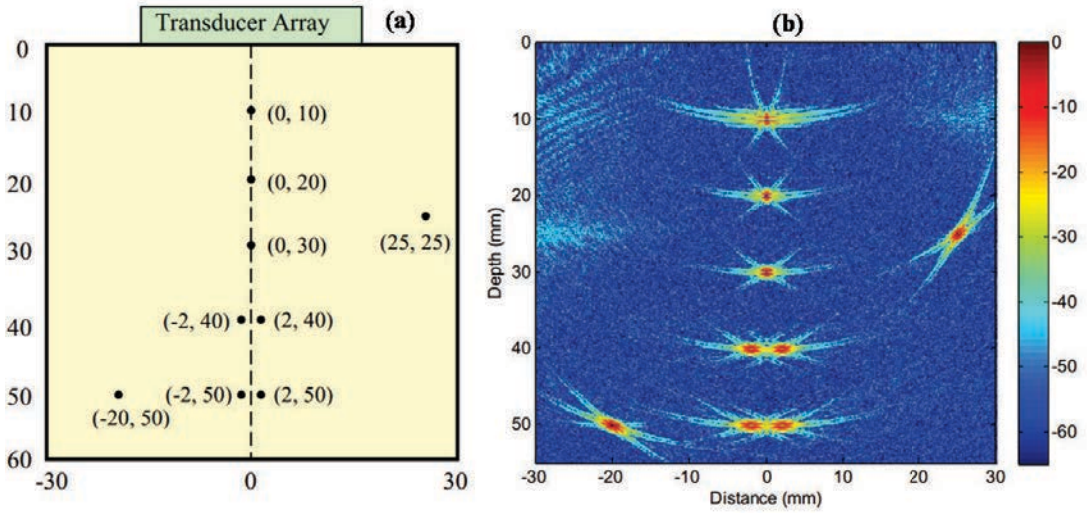

Figure 4.18: (a) Testing geometry with defects (b) TFM image (Minghui, 2011)

The plotted TFM image is in good agreement with proposed geometry. Although falls short as the hole shape is not identifiable as the depth increases, which could lead to wrong misinterpretation of the actual size. This happens when the reflectors from the holes interfere with small diffracts that will result in an over-sized amplitude spot. The author concluded that although the method is not as robust as TFM, adding a right filtering could make it become a strong direct image technique. Indeed, this method holds advantages in terms of computation time and could find possible application in in-situ methods.

Trying to further improve the performance of these techniques, K. Nakahata, 2016 [118] worked on developing a specific flexible ultrasonic array in combination with TFM to image flaws in aluminium solid. Two test conditions are selected, a cylindrical specimen with 2 defects and a rectangular specimen with 5 holes (size is 2 mm) is tested with a 32-element

flexible array and 3.4 MHz frequency. Data acquisition and processing is achieved by FMC and TFM. Results corresponding to the proposed work are shown in figure 4.19.

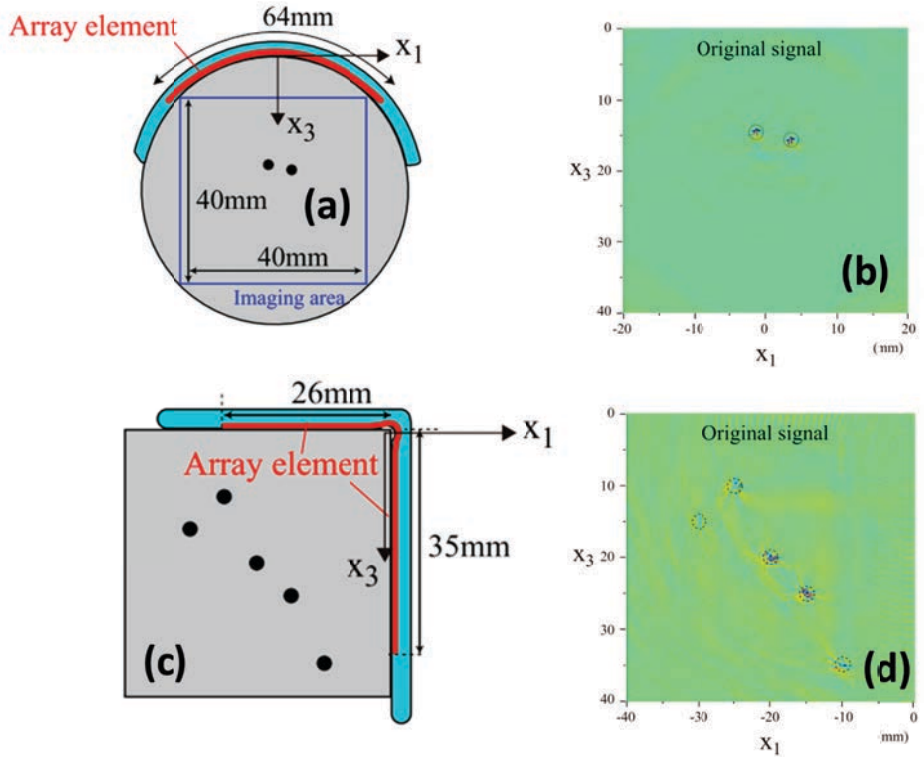

Figure 4.19: Implementation of flexible ultrasonic arrays on (a) circular geometry with 2 holes (b) corresponding TFM image and (c) a rectangular geometry with 5 holes (d) corresponding TFM image (K. Nakamura, 2016)

They concluded that a flexible array in combination with FMC results in precise location of holes. Although, what can be observed is that with 2 holes, FMC and TFM result in true representation but as the number of holes increased, concerning the depth and position, holes located further are not precisely resolved compared to those placed exactly close and in center. It has to be noted that frequency used was 3.4 MHz. In this context, frequency is a strong parameter that relates both depth and spatial resolution. Change in frequency will effect the wavelength and precious focusing can be achieved on to smaller targets. This will then increase the quality of differentiating two different defects and their actual size.

Finally, to compare the data acquisition performance for each of the data extraction methods (FMC and phased array) a simple simulation is presented by, TWI global, 2018. A 32-element array was used to test a six side drilled holes with a 2 mm diameter

as seen in figure 4.20. FMC and a sectorial scanned phased array were implemented in combination with TFM.

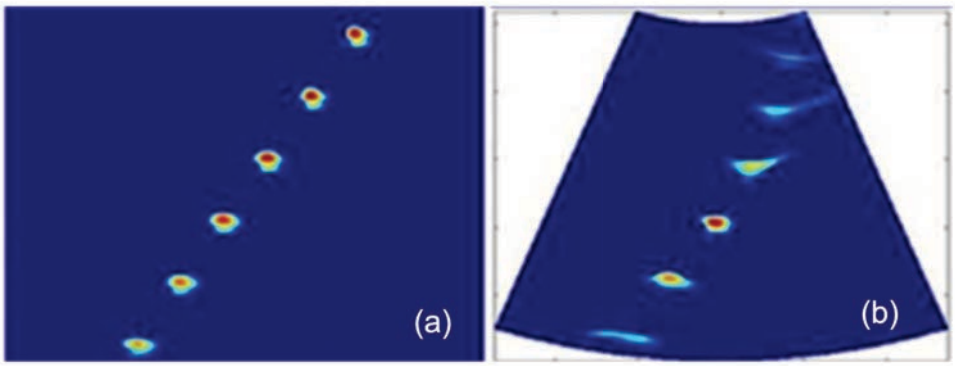

Figure 4.20: TFM image of six holes (a) Plotted with FMC data (b) plotted with phased array data (TWI, 2018)

In figure 4.20a, all the holes are plotted clearly with equally distributed amplitudes which shows that FMC works well although problems associated with steering could be due to amplitude being stretched over the steering angle (a usual problem with steering). They conclude that FMC can be applied in most of the application unless a steering and focusing is required or with a complex geometry where literally, signal from FMC does not result in a quality image.

Regarding the use of high frequency ultrasound, in the recent years, the works done by M. C. Jonathan, et al 2006 [119] and R. Manwar, et al 2018 [120] are promising showing imaging with 10, 20 MHz transducer array with 128 elements. In this, TFM is applied on an aluminium specimen (figure 4.21) with each defect size being 1 mm. Their focus was to highlight the effect of the array frequency on imaging for a given depth.

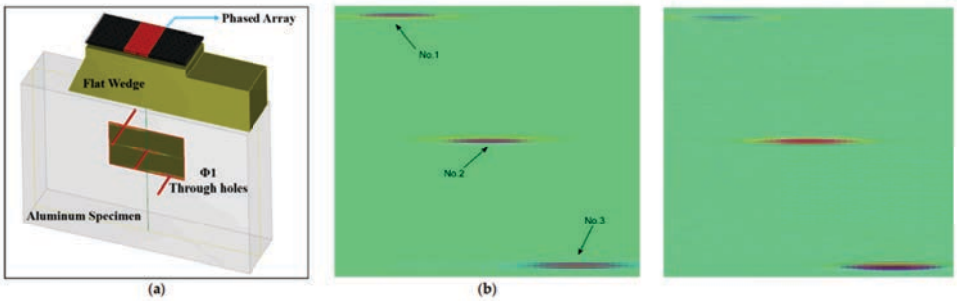

Figure 4.21: (a) Tested geometry with 3 holes (b) TFM image for 10 MHz (c) TFM image for 20 MHz (R. Manwar, 2016)

There is not too much of a difference between what 10 MHz and 20 MHz frequency results in terms of plotting hole coordinates in the image as seen in figure 4.21. Although, there is a difference in the amplitude distribution for the top hole and also the holes in the center and bottom are a bit amplified. The reason for this phenomenon was not explained clearly, but it can be assumed that the array itself is not optimized correctly for 20 MHz which otherwise would result in a sharper resolution image.

In the past 5 years, innovative use of signal processing methods to develop imaging algorithms grew in parallel with the development of phased arrays and led to not only research works but also new commercial solutions. D. L. Hopkins et al, 2011 [121] (founder of Bercli Phased array solutions) presented extensive work and developed various measurement devices of which few are focused on using high-frequency array and trying to map defects as large as 1 mm. The emphasis is on exploring the commercial aspect of phased arrays.

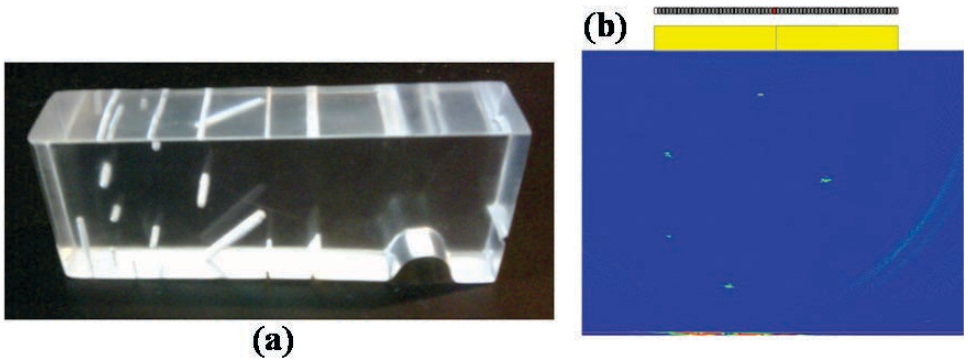

Figure 4.22: (a) Sample used in testing CIVA (b) Image reconstructed using TFM

At Bercli, the work combines both modelling and imaging of wave propagation through an array. EXTENDE, a nondestructive testing company developed CIVA software to detect flaws based on the TFM algorithm. Figure 4.22 shows an implementation of CIVA on a test sample with its TFM reconstructed image. In this case, a 64-element linear array with a frequency of 5 MHz was used in scanning a rigid translucent plastic piece with side drilled holes of 1mm. Once the data processing with the CIVA software is completed the TFM image is plotted as seen in figure 4.22 b. The holes were identified and plotted relatively precisely although showing the exact size is still questionable due to the use of

low frequencies. Another popular company, M2M, develops and manufactures phased array software and hardware for NDT. Gekko is a portable scanner that processes and maps using TFM. Their products range from small ultrasonic gauge to array devices that are mostly applied in crack detection. Figure 4.23 a shows a portable ultrasonic device that commonly uses 5 MHz to 10 MHz frequencies to extract TFM images as shown in figure 4.23 b. In the commercially developed devices, the array can be made of 128 or even 256 elements.

Figure 4.23: (a) Gekko measurement system (b) User interface of Gekko to image using TFM (Credits: M2M)

In conclusion, the full matrix holds a strong advantage compared to other data acquisition methods for imaging larger defects (1 mm). In tribology, the use of ultrasonic arrays is definitely new whereas studying the interfaces from the inside is still needed. Making a parallel with NDT, a contact interface can be seen as a series of defects (valleys) separated by several solid junctions (asperities). Using TFM to image such interface configuration would have considerable advantages as compared to a single transducer. With TFM, high resolution of the interface could be achieved, and also higher frequencies could be adapted to increase the measurement size and precision. The main disadvantage of using TFM would be that the processing time is high. Also, it would need many delay laws to steer the beam on to each targeting region thereby increasing the computation complexity.

4.4.2 Potential tribological applications

In the previous chapters, ultrasonic wave propagation with a single element transducer was simulated on to a tribological interface and studied in terms of changing the crucial parameters that define the real contact area. It was shown that extracting the exact interface morphology, i.e. number and size of the asperities in contact seems impossible

with the use of a single transducer. On the other hand, high frequency phased array and associated image reconstruction algorithms have strong roots in various medical and non-destructive testing applications. In all the previously referred works, their applications showed the possibilities of mapping discontinuities within the depth of a solid. This appears as a promising alternative to be able to map in-situ a contact interface.

However, different imaging algorithms and focusing techniques were discussed but in each of the cited works, the scale of measurement was relatively large, never smaller than 1 mm, and frequencies mostly between 1 and 5 MHz. Moreover, the expected results from the mapping remain in the location of a defect and not in its exact sizing. The solutions to study smaller defects at the micro-scale have never been considered and appear as a real challenge. Also, the use of frequencies higher than 10 MHz has never been addressed. Based on these conclusions, the question still remains on "How to access the real contact or even the apparent contact area in a tribological interface". The solution is to put forth an analysis of fusing phased transducer array implementation and the study of the tribological interface. H, Brunskill, 2013 [122] in his thesis presents the use of 10 MHz phased array in studying stiffness in a pressured seal. Although no imaging method is proposed, this proved the use of phased arrays in studying the interfaces from a purely mechanical perspective. J. N. Kim et al, 2018 [123], worked on using high frequency phased array for non-destructive evaluation of piping materials. They developed the finite element model in characterizing surface and subsurface defects and microstructural changes although not in a tribological perspective. They emphasized the application to high-frequency ultrasound to study microstructures.

B. Dupont, 2014 [64] contributed to the characterization of small defects (crack width 0.025 mm) using the total focusing method by modelling the test samples and propose to replace the complex experimental analysis. Although this study is focused on NDT, the size at which the crack is tested is of interest in tribology. He concludes that finite element modelling and imaging is the new approach to address complex geometries that are of primary importance in tribology. M. V. Felice, 2014 [124] studied on accurate depth measurement of small surface cracks (crack width 0.025 mm) using post-processing methods using half skip TFM method. Different crack models were tested in this context

and concluded that for the cracks that are close to the surface, half skip TFM outperforms the other methods. These studies are more than relevant due to defect size at which they are tested and could be the basis for testing the tribological interface.

4.5 Conclusions and discussions

In this chapter, a literature review has been conducted on the use of phased transducer arrays, imaging algorithms, and their applications in various fields. Classic techniques of ultrasonic data processing were presented before making a non-exhaustive state of the art of the advanced imaging methods developed in NDT. Basic theory and focusing methods were explained as well as reconstruction algorithms like FMC/TFM compared with other methods based on the findings in the literature. The analysis of reconstructed images in several case studies showed the advantage of imaging TFM in terms of resolution but also its ability to conclude on the nature of the defect.

A short discussion was presented on how the phased array can successfully be applied to the tribological interface. In conclusion, the use of phased array and TFM imaging appears promising to provide an acoustic mapping of a tribological interface. This could potentially be an innovative way to access crucial parameters from the contact itself in an in-situ monitoring technique. However, for a transition from the existing studies to a new application in tribology, it is important to develop a systematic methodology on the array optimization to be able to reconstruct a relevant indication of a contact interface. Therefore, the development of a prediction tool for the relevant modes and its application on various interface definitions will be discussed in the next chapter.

Summary:

- This chapter covered a literature review on phased array imaging methods and their applications and capabilities before concluding on what can be done further in tribology.
- Advanced methods combining the full matrix capture acquisition and the total focusing method were found to be relevant and open new possibilities to be applied in studying interfaces.

La recherche consiste à voir ce que tout le monde a vu et à penser à ce que personne n'a pensé....

Research is to see what everybody else has seen, and to think what nobody else has thought....

— Albert Szent-Gyorgyi

5

Numerical modelling of an ultrasonic array and acoustic imaging of a tribological problem

Contents

As discussed before in Chapter 4, imaging methods using ultrasonic arrays have been initially developed in non-destructive testing. Applying them to various tribological problems is innovative and appears as a promising technique to perform in-situ measurements.

Dwyer Joyce et al, 2008 [34] were the first ones to use ultrasonic arrays in experimenting on a tribological interface. They studied the use of array transducer implementation on a wheel-rail specimen when subjected to normal and lateral loads. The linear array was made of 64 elements with 0.63 mm spacing with a frequency of 5 MHz. No delay law was implemented in the data acquisition, however, only diagonal elements were fired and recorded in a direct pulse-echo method to reduce the time. The aim was to map or image the changes at the interface concerning the change in load. They concluded that the mapping obtained with arrays is relatively similar to the results obtained for static contacts when studied using a single element. Also, spatial resolution was low which lead to inaccurate results. On the contrary, useful data was acquired proving the ability of the array for additional research and implementation in the future. This reference is explicitly mentioned here because further work in this chapter is motivated based on what was done in tribology. Applying the described imaging methods in tribology instinctively leads to two main questions,

- Which array configuration would make possible the imaging at a micro scale?
- Most of all, how to manufacture calibration samples, i.e. perfectly defined contact interfaces with various configurations, to validate the generated images just like in the various NDT studies presented in the Chapter 4?

As manufacturing a perfectly controlled contact interface is a challenge itself, modelling can again be a relevant approach to assess the feasibility of these imaging methods in tribology. Computational methods like finite element modelling have attained a huge reputation in modelling complex geometries and multi-physic problems that are not possible otherwise. In this context, a numerical model indeed appears as an alternative to address different interface scenarios. This chapter thus covers the FE Modelling of a phased array and the application of the imaging algorithms to various modelled contact configurations. The particular interests of this study are i) the numerical investigation of the wave propagation from an ultrasonic array towards a contact interface that has not really been studied in the literature but also ii) the focus on imaging very small defects that actually represents a valley in a real rough contact interface. The difference here between the NDT

defect and a tribological problem is the scale at which the analysis has to be performed, rather within the millimeter range in NDT versus nanometer range in tribology. Considering this, a systematic study is conducted starting with larger valleys and getting through to smaller ones distributed in an interface to assess the capability of the proposed method.

5.1 Implementation and sensitivity of an ultrasonic array

5.1.1 Numerical implementation

The first important aspect is to model the array and be able to deal with the pulsing of each element and ensure the wave generation. To this end, instead of simulating the actual piezoelectric elements, the wave input is implemented as a pressure pulse onto the top surface of the solid. This procedure is followed to reduce the computational complexity and to avoid the modelling of the piezo itself and its bounding. Each element is modelled by dividing the top surface of the solid into elementary surfaces, spaced according to the array configuration, and onto which a pressure pulse is applied independently to model the individual element excitation as represented in figure 5.1. This pulse is a 6 cycle Hanning-windowed tone burst at the selected central frequency, for example, 10 MHz. The color code for each line indicates the independent pulsing capability of the model.

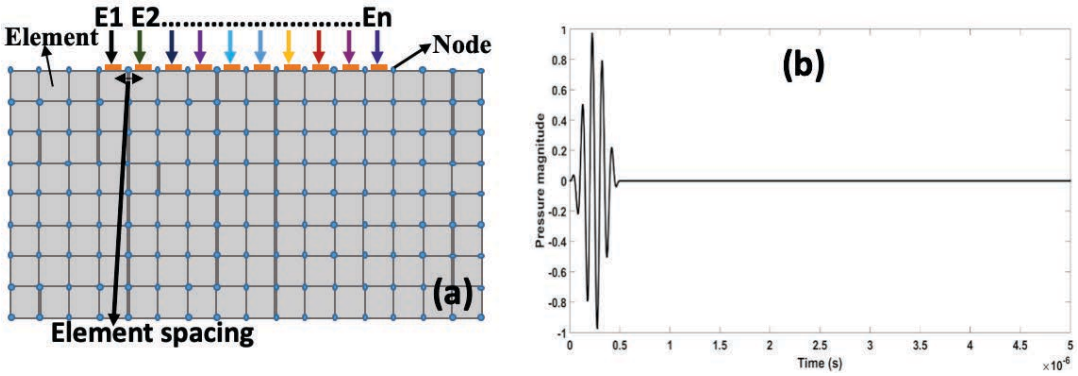

Figure 5.1: (a) Individual pressure pulse applied onto elementary surfaces to model the array excitation (b) time plot of the pulse use in excitation

The A-scans can be consequently recorded independently on each element and later used for the image processing. It should be noted that each element is individually excited and does not include any delay between them.

5.1.2 Comparison of the wave propagation from a single and a multi-element transducer

A second aspect is to assess the influence of the specificities of the array itself on the collected signals. A given interface configuration already covered in Chapter 3 was selected and three cases were simulated according to the schematic representation shown in figure 5.2: a single element, a 2-element, and 4-element transducer with a central frequency of 10 MHz. The test sample itself is partitioned into two solids with the interface. The length of the combined solid is 15 mm and the width is 5 mm. In the interface, each valley width is 20 microns and the spacing between each of them is 60 microns with a thickness of 10 microns. The wave propagation and reflection still follow the pulse-echo method where the same transducer acts as pulser and receiver. It must be remembered that the transducers here are virtual and any mismatches that exist with the real transducer coupling are ignored.

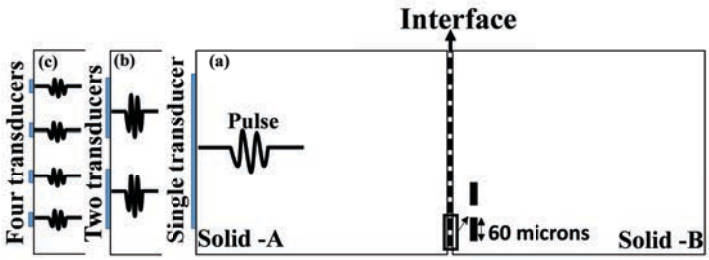

Figure 5.2: Schematic representation of the model with interface tested with (a) Single large transducer (b) Two transducers (c) Four transducers

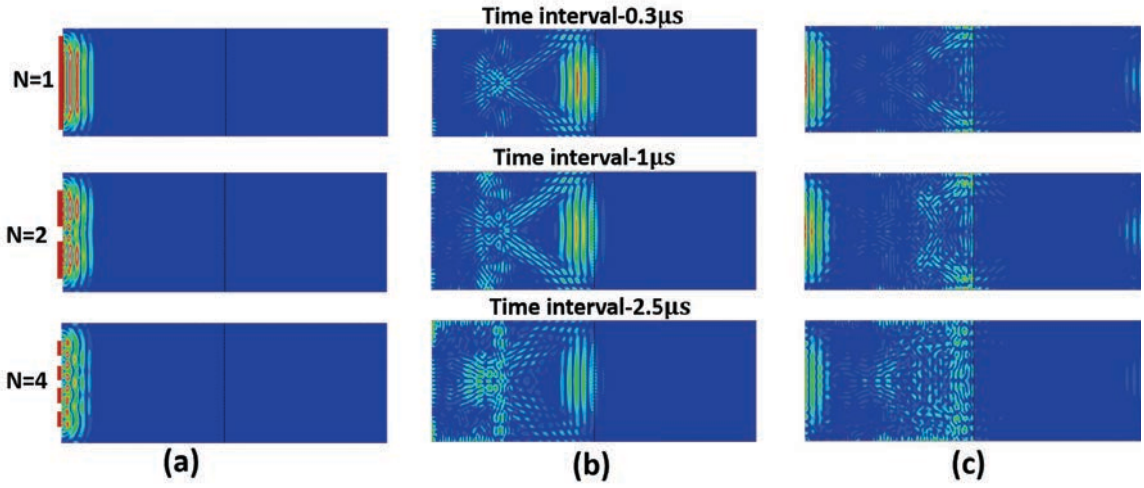

Figure 5.3: Wave propagation (a) At the time of initial pulse release (b) When the wave interacts with the interface (c) When the wave is completely reflected

The wave propagating modes at three intervals of time are extracted as seen in figure 5.3. In the first case where a wave propagation through a single transducer is simulated, the wave travels along with the solid with a wavefront and is reflected from the interface. With the 2-element array, although the wave propagates from two boundaries, they convolve to form a single wavefront which is reflected in a similar way as the first case but with a slightly lower amplitude. The same can be observed in the case of 4 transducers with a stronger attenuation.

This analysis of the number of transducers is important considering that an array is a group of N transducers that without the delay or specific data acquisition method would only be inefficient. From figure 5.4, it is evident also that the input amplitude is lower when increasing the number of transducers as the input power decreases when using smaller elements. In this case, the electrical power, i.e. the amplitude of the pressure pulse, should be increased to compensate for this power loss. If the result is interpreted in terms of reflection coefficient (summed average of all elements) as seen in figure 5.4, the amount of reflection that is recorded by the transducers is lowered by almost a factor 5 when comparing the single to the 4 element array configurations.

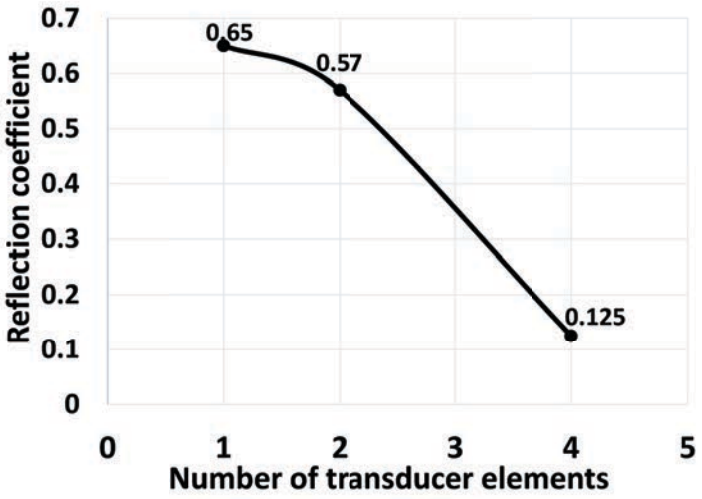

Figure 5.4: Reflection coefficient for change in number of transducer elements

In conclusion, if the elements of the array are pulsed simultaneously, the transducer array exhibits similar behavior to a single transducer. This is thus limiting the possibilities showing that an individual pulsing of the elements or delay line has to be adapted to

be able to extract local data. Indeed, increasing the number of transducers without implementing a delay will only increase adverse effects such as reduced amplitude at the wavefront and increased backscattering.

5.1.3 Study on the transducer element spacing and pitch

Even before implementing a delay law, the width and inner element spacing play a major role in the efficiency of the array. To demonstrate this, the numerical simulation is performed with the same interface geometry as in 5.2 and with 4 elements in the ultrasonic array. The schematic of the geometry can be seen in figure 5.5.

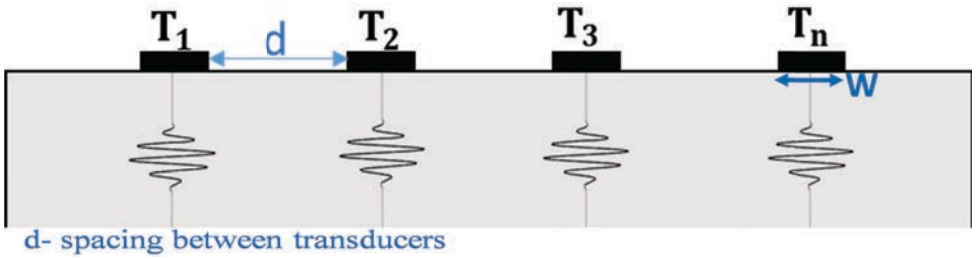

Figure 5.5: Schematic representation of the transducer design and spacing d and element width w

The wave propagating patterns corresponding to four different element spacing values can be seen in figure 5.6.

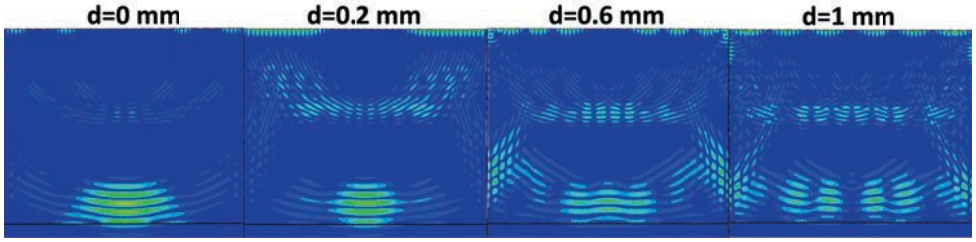

Figure 5.6: Wave propagation through the interface for 4 spacing's between transducer element combinations

The change in the distance from 0 mm (corresponding to a single transducer) to 1 mm shows an interesting wave pattern as it propagates through the solid. When the element separation is large, scattering and wall reflections are high and the wavefront experiences attenuation. The image reconstruction depends on the nature of the interaction between waves and reflectors. In the case of plane defects, the attenuation and diffraction of the

wave at the edges of defect and specular reflection along the defect face are the two main interactions that reduce the reflections. Attenuation arises due to the Omni-directional distribution of the ultrasonic wave that occurs during the wave interaction with the defects. Sometimes, depending on the size of the defect and wave magnitude, the defect behaves like an assembly of point reflectors. The reflection coefficient response is then calculated for each transducer for a given element spacing as seen in figure 5.7.

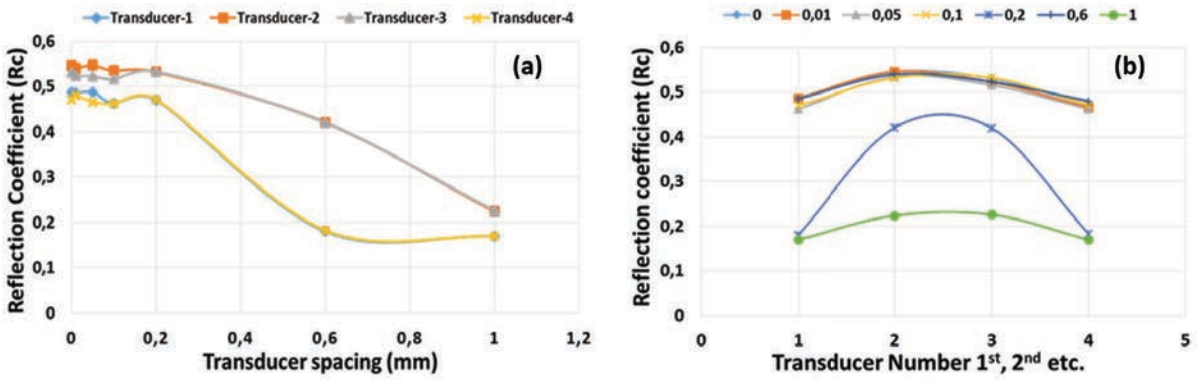

Figure 5.7: Reflection coefficient recorded by each transducer element when (a) Changing the element spacing (b) Reflection coefficient that is obtained for each transducer

It can be noticed that low reflection coefficients are recorded when increasing the spacing beyond 0.2 mm and high reflection level is maintained below 0.2 mm. This is due to the presence of the side lobes and backscatters. This condition confirms that element spacing must be below the size of wavelength itself irrespective of the number of elements in the array. Moreover, slightly lower reflections are experienced for the boundary elements of the array. For the specific spacing of 0.6 mm, the reflection coefficient for the inner elements experiences high amplitude compared to the boundary transducers showing a reflection level more than two times lower. In this case, amplified side scatters that interact with the reflection travelling towards the array has been observed. The same concept is explained by Shi-Chang Wooh 1998 [98], [125], which states that to reduce the main lobe sharpness factor, the inner element spacing must be small for a given wavelength, which is less than or equal to half the wavelength.

From the above study, it can be concluded that the wave generated from an array if executed without any delay will result in a single wavefront likewise a single large element. To fully benefit from the array, a delay law has to be implemented or the array

has to be used as a full matrix approach. The spacing has to be smaller than 2 times the actual width of the element and the wavelength.

5.2 Implementation of FMC and TFM

5.2.1 Full Matrix Capture (FMC)

As described in Chapter 4, the FMC is the acquisition strategy which consists of capturing time-domain data acquired from every transmitter-receiver combination: one element is pulsed at once while all the elements in the array are recording the signals from a reflector.

Figure 5.8 a is showing an example where a 15-element array is used in front of a large crack. Figure 5.8 b presents the signals recorded by all the 15 elements when only the first element is excited.

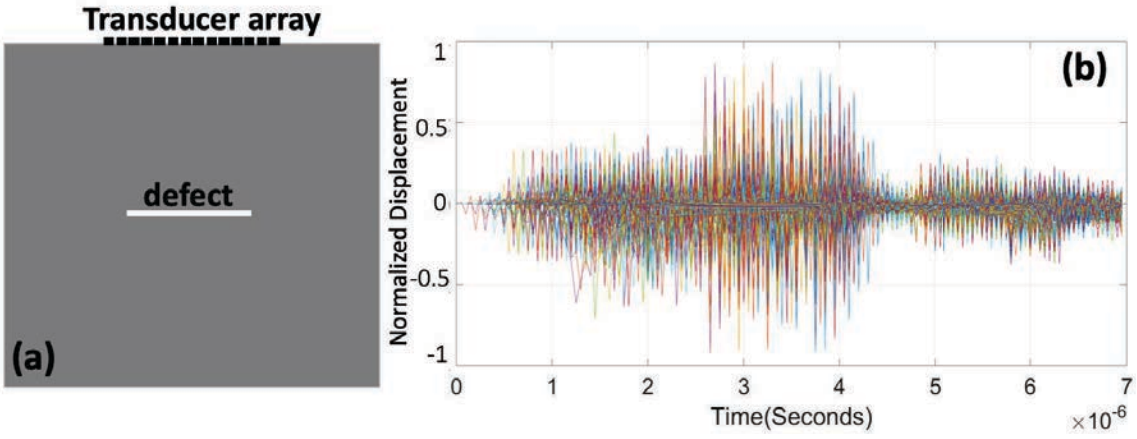

Figure 5.8: (a) Full matrix time domain data acquired with a 15-transducer array (data is recorded for 7 micro seconds and measured over displacement) (b) A-scans

In the A-scans presented in figure 5.8b, the input pulse from all the transducers is removed to show the specific reflections from the defect which can be hardly interpreted. Figure 5.9 shows an example of the A-scan recorded by T1 when only T1 is excited. The initial pulse peak is the input signal from the transducer that is sent, and later amplitude changes are its first and second reflections from the simulated defect. The figure 5.10 shows 15 A-scans recorded following the excitation of T1. The process is then repeated for each element in the array until all the transducers are covered.

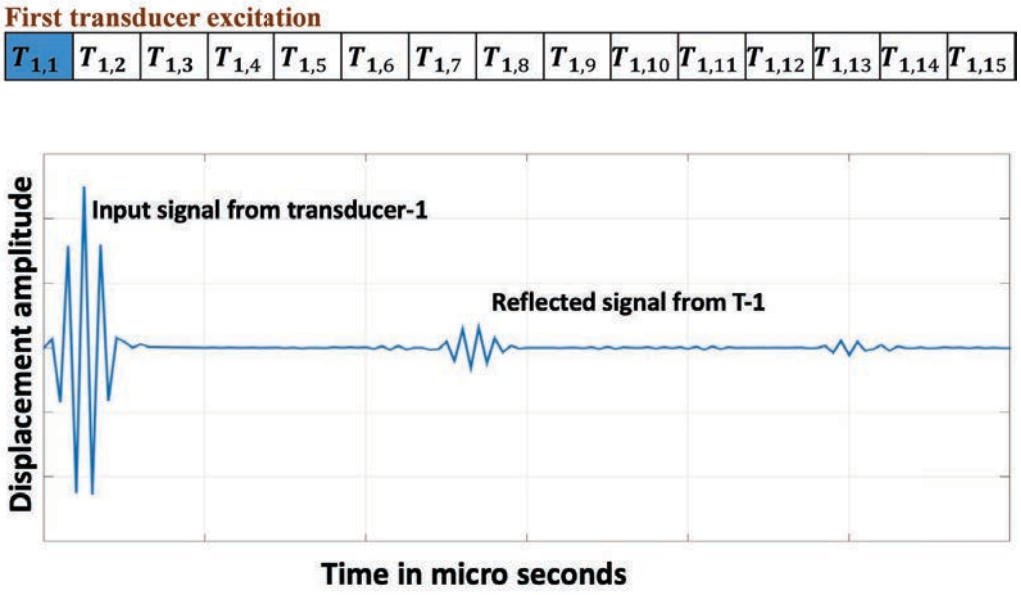

Figure 5.9: Example of an A-scan representation from Transducer-1 (T_1,1)

It can be observed from the figure 5.10 that the reflections are very low in amplitude due to the fact that a wave once pulsed experiences attenuation over time due to use of a high frequency.

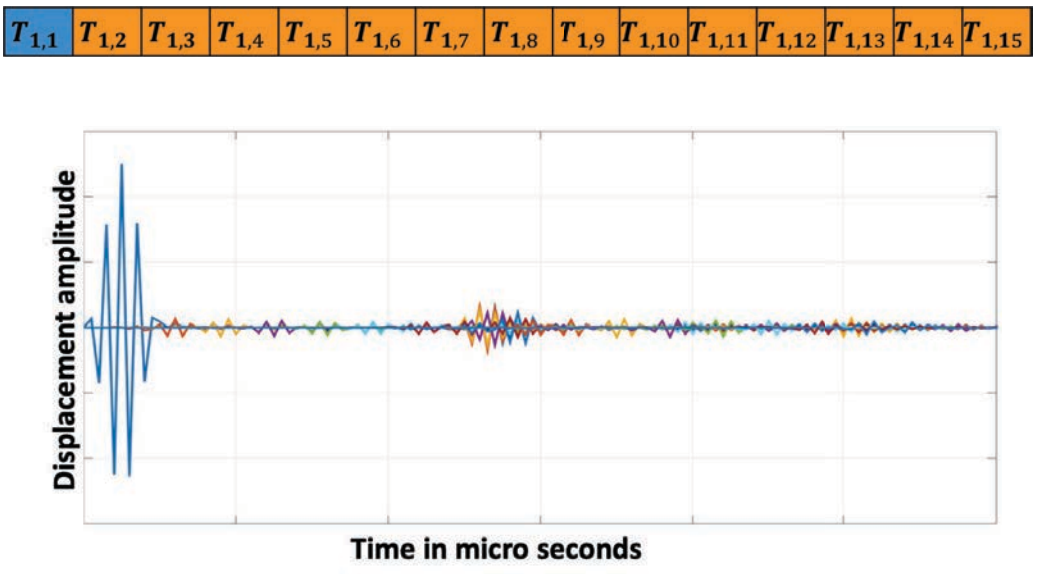

Figure 5.10: Multiple reflections recorded for a single transducer input

Also, it can be noted that the amplitudes of scatters in the signals cannot be completely neglected compared to the amplitude of the reflected signal itself. This will impose unwanted reflections in the final image.

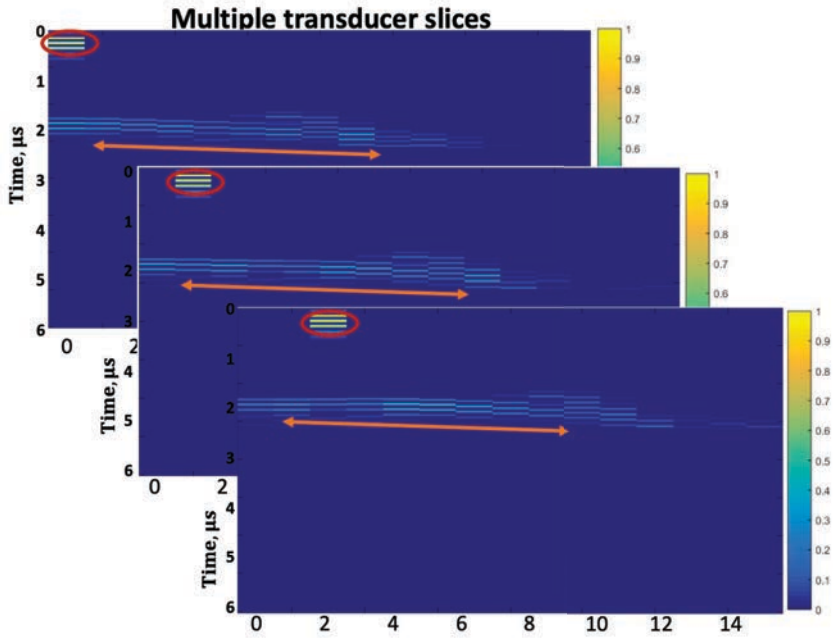

Figure 5.11: Contour plot presentation for the $T(1,N)$ combination: in red the input pulse sent from the first element, whereas the orange line indicates the reflected amplitude recorded over the 15 transducers

A-scans can also be represented as contour plots for each excitation and reception pair as shown in figure 5.11 for the $T(1,N)$ combination. The recorded amplitude changes can be clearly seen depending on the selected element showing that the 15th element will not record any reflection when the first one only is pulsed.

5.2.2 Total Focusing Method (TFM)

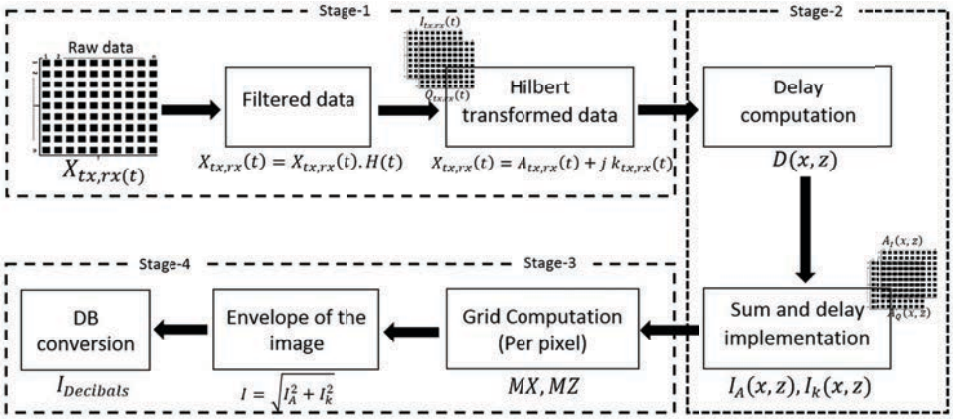

Figure 5.12: Block diagram representation of total focusing method (TFM)

The TFM is an image reconstruction algorithm that will post-process the data collected with the FMC to synthetically focus at every image point in a target region. This algorithm has been coded here based on the work done and developed by Holmes et al 2005 [103]. The block diagram shown in figure 5.12 summarises the working procedure of the TFM method.

In the TFM, relating to the region of interest or target region, all the collected data in the FMC matrix is distinguished into separate data points in which each data point is designated with a mesh grid. In this grid, TFM extracts crucial amplitude data by focusing on transmission and resulting reflection combinations at every point. The mesh grid is computed for each amplitude indices distributed over time based on the grid size (usually length and width of the test sample or the desired resolution values in x, z directions) and the number of grid points. Every point is then focused on by extracting the data of a reflected signal at a certain time instance providing the matrix with the post-treated focused data. Then the amplitude corresponding to each grid point is extracted using time of flight. Then the time delay indices are calculated by Euclidean distance between the transducer position and each grip point in the matrix. In the later part, the final TFM built image is then reconstructed by summing the delay and amplitude matrices.

It has to be noted that, in the pre-processing stage of TFM, the acquired signals from the transducer array are usually filtered. There are special filtering algorithms like spatial-temporal filtering, A. N. Evans 1996 [126], K.S. Kim 2006 [123] , G Gavriloaia et al 2011 [127], Provost et al 2015 [128] that are applied to address various issues (overlapped signals, artefacts etc) associated with ultrasonic signals. A discussion about the filtering is proposed further in this Chapter.

Further, the Hilbert transform is performed on the time domain data to extract the instantaneous amplitude of the original signal. This transform converts the time domain to a complex form and returns the amplitude of the data. Later, the envelope is detected of the corresponding amplitudes. Following equations show the transform functions.

$$H_t = \frac{1}{\pi t} \int_{-\infty}^{\infty} \frac{A(t)}{t - \tau} d\tau \tag{5.1}$$

$$I_t = (A(t) + jH(t)) \tag{5.2}$$

$$E_t = \sqrt{H(t)^2 + A(t)^2} \tag{5.3}$$

Here $A(t)$ is the time domain amplitude data, $H(t)$ is the Hilbert transform, $I(t)$ is the representation of the signal with real and complex parts. $E(t)$ is the envelope of $I(t)$. In complex ultrasonic signals, it can be difficult to get the exact time of flight corresponding to the peak reflections. The Hilbert transform makes it easier and also to compute the magnitude of the reflected signal via the positive envelope as shown in figure 5.13.

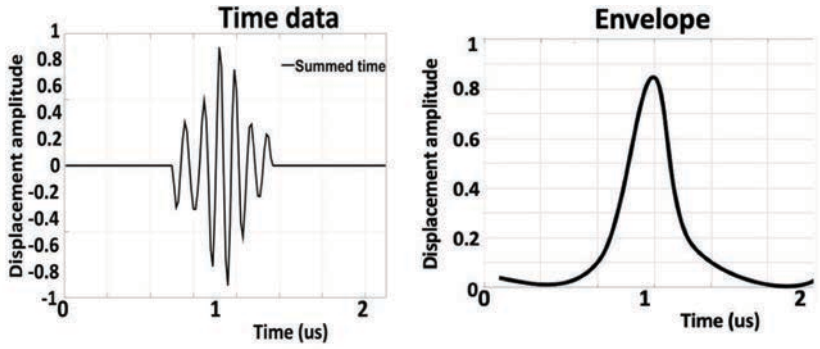

Figure 5.13: Time data and its corresponding envelope indicating the reflection time

Once the signals are transformed, the delay matrix is computed based on the following equation,

$$D(x,z) = \frac{\sqrt{(x_p - x_{tx})^2 + (z_p)^2} + \sqrt{(x_p - x_{rx})^2 + (z_p)^2}}{c} \tag{5.4}$$

Here x_p,z_p are the target position coordinates, x_{tx},x_{rx} are the transmitting and receiving coordinates respectively. The amplitude data matrix and delay matrix are then summed and concatenated representing the total amplitude of all the target points defined in the mesh grid over time given as,

$$I_{A(x,z)} = \Sigma_{i=1}^{N} A(tx,rx)(D(x,z)) \tag{5.5}$$

If the process is repeated for the complex part, i resulting equation will be as seen in equation 5.6.

$$I_{k(x,z)} = \Sigma_{i=1}^{N} k(tx,rx)(D(x,z)) \tag{5.6}$$

Here $A(tx,rx)$ is the amplitude matrix, $k(tx,rx)$ is the complex amplitude data and $D(x,z)$ is the delay matrix index and $I_A(x,z)$, $I_k(x,z)$ are the final intensity matrix computed for all the transmitting and receiving combinations.

Coming back to the use of the Hilbert transform, it is not essential to acquire the direct image, however, it is essential in some cases where the number of transducer elements are more, or high scattering is involve to accurately compute the instantaneous magnitude. This amplitude is further used to find the envelope of the reflections. In applications like imaging, data classification, and feature extraction it is recommended to use this transform. To demonstrate the effect of applying or not the Hilbert transform, a simple geometry is proposed as seen in figure 5.8a.

The 2-D model is a solid aluminum material that has a defect exactly in the center both in lateral and transverse directions. An array with 15 elements is then operated on top of aluminum solid with 10 MHz frequency. The solid is 15 L x 10 H mm in length and depth with the defect placed in the center being exactly the size of array i.e. 8mm. Once the data is acquired with FMC, the TFM implemented image is obtained with and without implementing Hilbert transform as shown in figure 5.14.

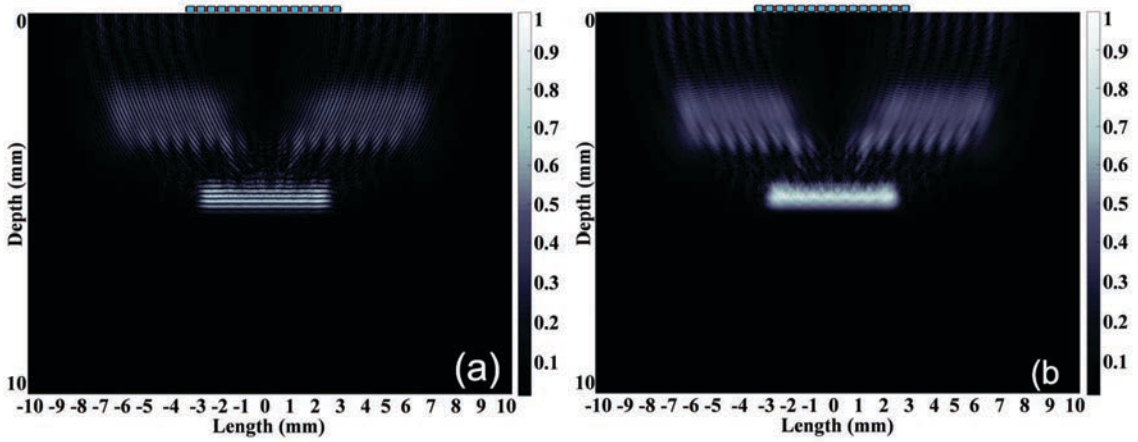

Figure 5.14: TFM image (a) without using Hilbert transform (b) using Hilbert transform

Following is an example of a resulting TFM image when applying or not the Hilbert transform. In figure 5.14, both the images carry clear details of the defect coordinates, however, the difference should be noted that in (a) pulse cycles can be clearly seen which will correspond to each peak in the A-scan matrix. Once the Hilbert is applied as seen

in figure 5.14b, the envelope is only selected which will smoothen the A-scan matrix resulting in a more smooth TFM image.

5.3 Application of FMC and TFM

In the following sections, different subsurface defects, contact interfaces and micro valleys will be investigated based on the concepts of FMC and TFM presented in the previous sections. To highlight the sensitivity of the wave propagation simulation and reconstruction modes according to the geometry of the part and the orientation of the defect, various acquisitions were made using FMC. Selected configurations (figure 5.15), representing cases of tribological interfaces or simply defects located within a solid were investigated, making it possible to highlight and apprehend the benefits and challenges of TFM imaging applications in tribology.

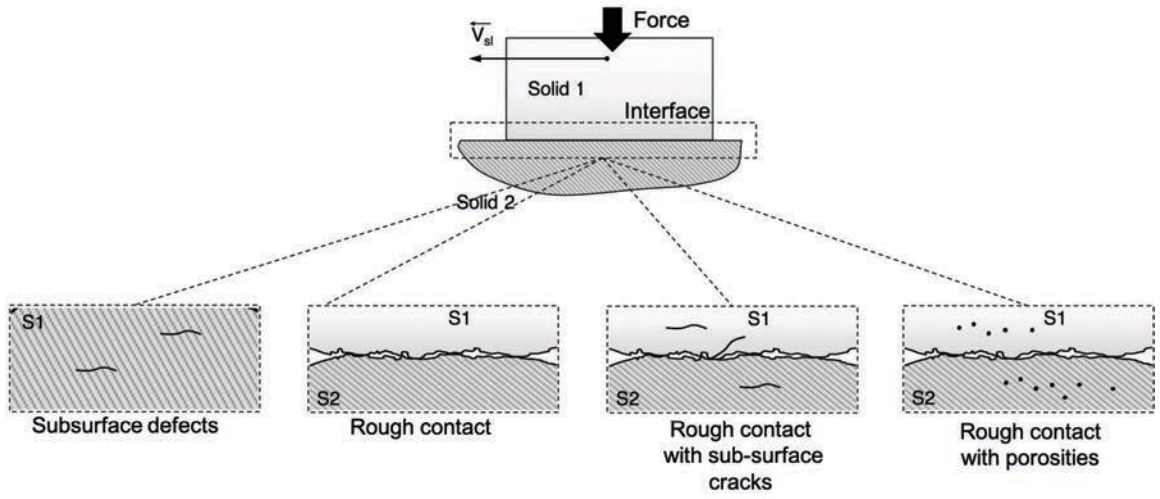

Figure 5.15: Different configuration of 4 different case studies for asperity distribution identification

5.3.1 Design of the numerical model

The basis of this chapter is to develop a FE based model to simulate the wave propagation and interaction with several types of tribological interfaces and image them using the developed processing algorithms. The finite element modelling of the phased array and the interface follow the procedure described in Chapters 2 and 3. In the following FE model, a 10 by 20 mm 2D solid is considered and is meshed as discussed in Chapter 2.

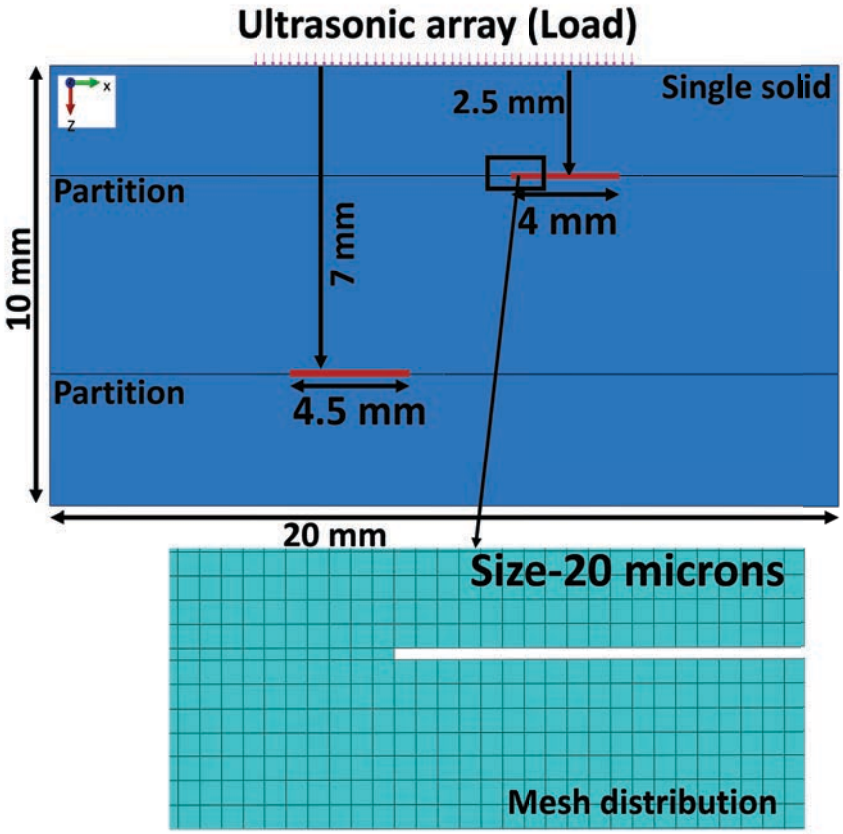

Figure 5.16: Example geometry of the model used in the TFM implementation and its corresponding mesh distribution

Partitions are then defined at different depths to exactly locate the modelled asperities and valleys, to precisely define their geometry and to ensure a homogeneous mesh distribution. An example of the corresponding geometry and mesh distribution is shown in figure 5.16 with two large defects located at two different depths below the surface. The partition is only related to the meshing procedure and does not have any impact on the wave propagation simulation. For all the following simulations, the height of the defects/valleys has been arbitrarily fixed to 10 µm and kept constant. The element type chosen in all the simulations is 4-node first-order plane strain elements with reduced integration and the problem is solved using an explicit integration scheme. Regarding the ultrasonic array, an 8 mm long 1D linear array composed of 15 evenly spaced elements is placed in the center of the solid top boundary. The width of each element in the array is fixed to 0.45 mm and spacing between them is 0.2 mm with the central frequency at 10 MHz. The array is modelled as discussed in Section 5.1 and 5.2 using 15 elementary surfaces and individual pulses.

If considering 3D wave propagation would be more relevant, modelling it as a 2D plane problem is adapted to reduce the computation time and still be able to prove the feasibility of the methodology. An example of simulated wave propagation in the selected example at different intervals of time can be seen in figure 5.17. In this simulation, a single element of the array is excited and generates a wave that travels within the solid and is then reflected. It can be noticed that when the wave interacts with the interface, some part is reflected, and some are scattered to the boundary of the solid. According to the calculations, the time taken for the wave to travel and reflect back at the back wall is 4 µs for a 10 mm solid. Time taken for the first reflection to happen will be between 2-3 µs. The reflected part is recorded by all the 15 active elements to produce a group of A-scans, so a maximum time of 6 µs is needed to observe the remaining reflections. The displacement amplitudes are recorded over time to generate the acoustic signals.

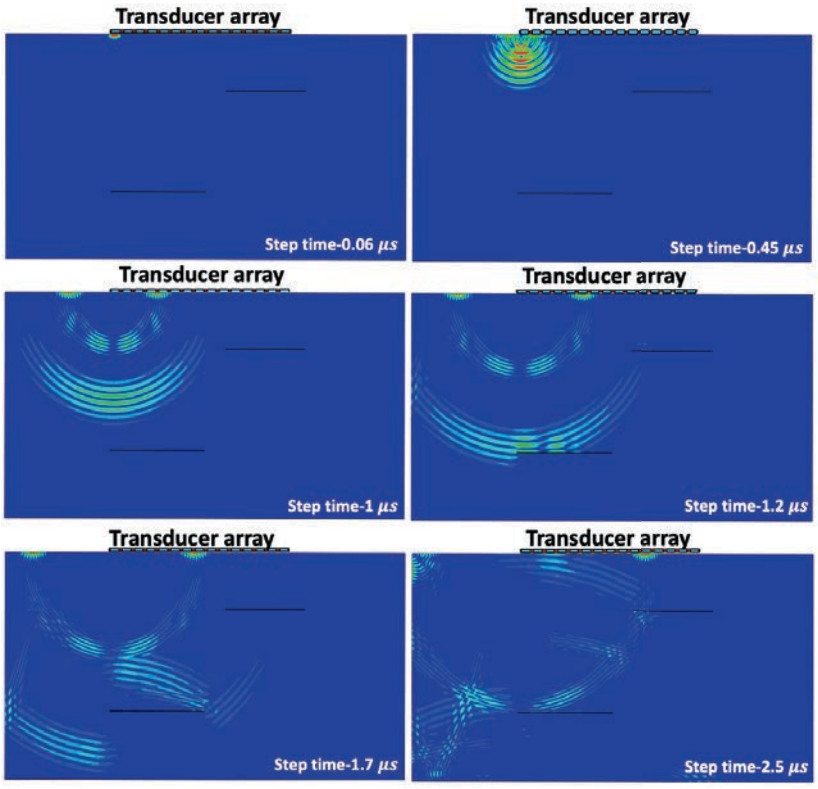

Figure 5.17: Time lapse of the wave propagation simulated through one element in the array

Such simulations provide an interesting insight into the wave propagation and interaction with a defect/valley, enhancing the analysis capability in comparison to the experimental campaign.

5.3.2 Detection of subsurface defects

As a first case study, two different defects with a width of 4 mm and 4.5 mm are placed at 2.5 mm and 7.5 mm, respectively from the top surface where the array is bonded. Figure 5.18 presents a schematic of the simulated configuration. All the properties including the solid material and the array frequency remain unaltered.

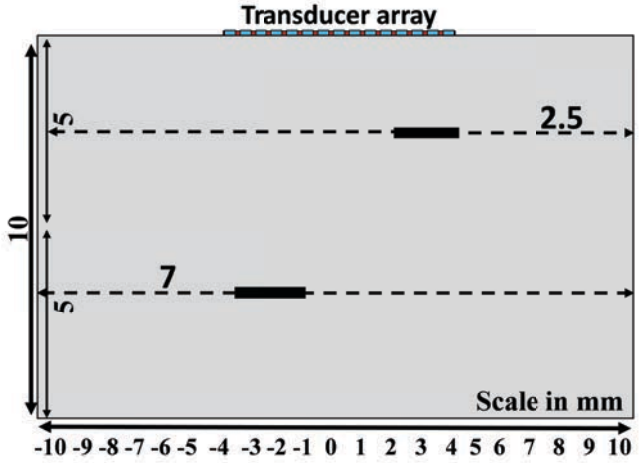

Figure 5.18: Geometry of the solid model with two subsurface defects

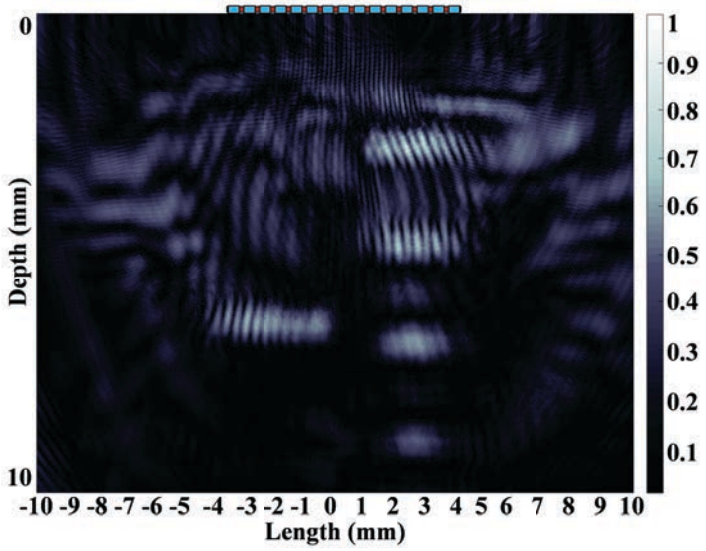

Figure 5.19: TFM image corresponding to the two subsurface defects case study

This specific configuration has been carefully selected to give a clear understanding of how signals can be misinterpreted leading to incorrect identification of the defects. The array is pulsed using a 15-element transducer combination and excitation following the FMC

method, i.e. no delay line implementation from one element to the other. Generated A-scans are later TFM processed to reconstruct the acoustic image presented in figure 5.19. It can be noticed that many reflectivity regions have been detected whereas only two groups indicate the actual simulated defects. All the remaining does not carry any physical meaning.

However, one can observe that the reflectivity regions at x=3 mm appear periodically at depths that are a multiple of the actual one. These misinterpretations are indeed artefacts that arise with multiple echoes convolving with the original information in the signal especially when the defect is close to the array. The reflector/defect located at a depth of 7 mm does not show any replications whereas the one very close to the top surface (2.5 mm) experiences multiple reflections. In TFM imaging, when the chosen target region is adaptive, the reflection is specular on the profile of the defect. If, on the other hand, the target region is not adaptive, it is possible that indications are reconstructed at positions where there is no reflector, termed reconstruction artefacts. In figure 5.20, the time domain signals recorded on two elements are presented. In all the array measurements, these two transducers are selected considering that one is close to the center of the array and one is in the extreme corner boundary.

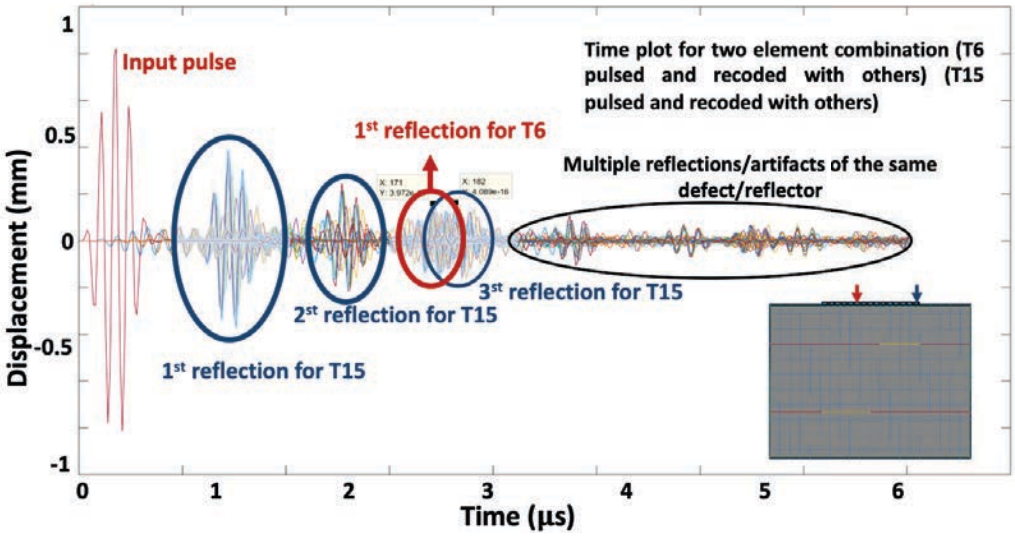

Figure 5.20: A-scans corresponding to the TFM image with an emphasis on the reflections recorded by elements T6 and T15

In this model, the minimum time for the first reflection to appear is 1.5 µs and the maximum time for the wave to reach and reflect at the back wall is 4 µs. All the

interactions happening after that add to the artefacts. Also, one important observation is that, even by limiting the time frame, there is a problem of signals overlap. As the reflector on the left is located 5 mm further than the one on the right, the closely placed one will generate multiple reflections by the time the first reflection from the distantly placed reflector is recorded. A step by step explanation about the phenomenon and manual filtering process is shown in figure 5.21.

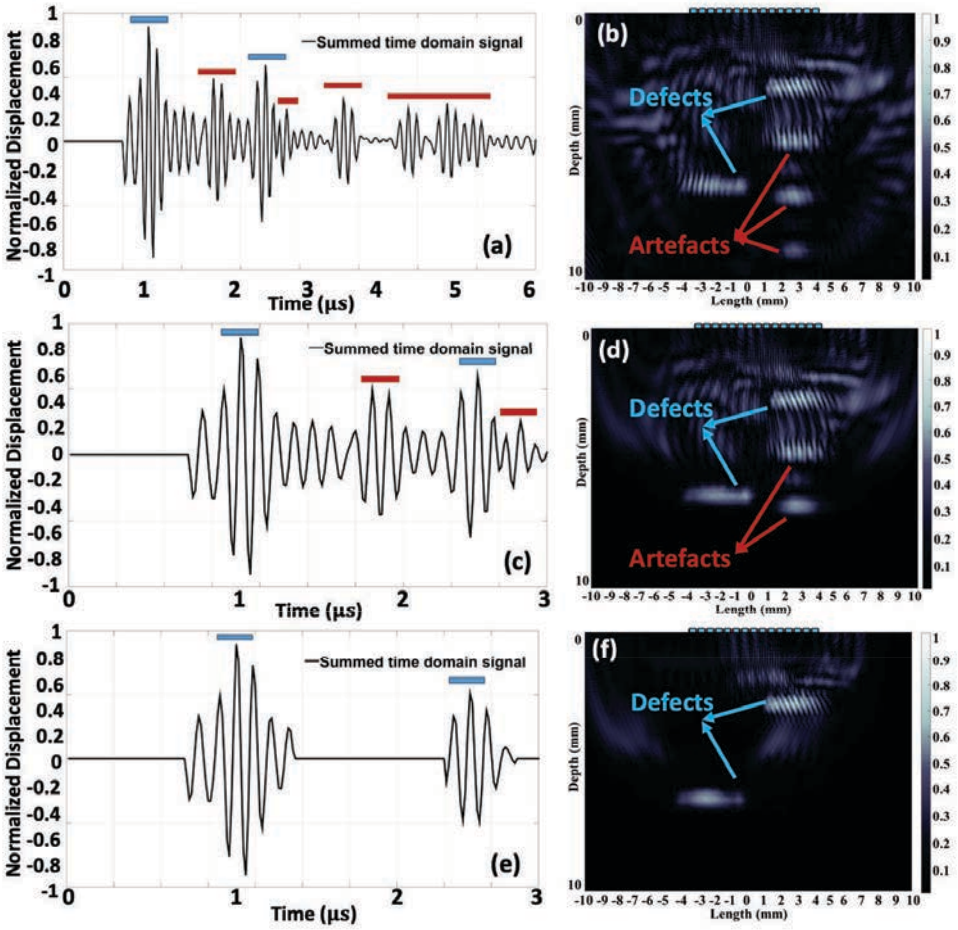

Figure 5.21: (a) Time signal corresponding to 15*15 array measurement (time length 6 µs) (b) Complete TFM image (c) Truncated signal (time length 3 µs) (d) TFM image corresponding to the truncated signal (e) final filtered signal (f) TFM image for the final filtered image

For convenience and a clear view, a summed version of the time domain signals is shown with respect to the TFM images. The figure displays all the possible reflections along with the intended defects. The formation of these artefacts is intrinsically linked to the TFM imaging algorithm as a consequence of the non-uniqueness of flight times. This

type of artefacts is called inter mode artefacts, Kombosse, 2018 [129] and they occur in two ways: one is due to a coincidence of time of flight for a given set of defects and the other is due to the prolonged time frame for a single defect. Multiple reflections result in artefacts which can create an intensity point in the image where there is neither reflector nor defect. The prolonged time frame is the lack of limiting the maximum time required for the wave to reach the defect and reflect back. Once the time is truncated to 3 µs, the reduced signals result in the corresponding TFM images shown in figures 5.21c, 5.21d. However, there are still a few artefacts due to time coincidence of the wave travelling back and forth several times from the closed defect which was clearly presented in figure 5.21. Once the filtering is applied, the final signals result in the TFM image displayed in figures 5.21e, 5.21f.

The existence of repetitive artefacts is a major concern in the imaging process as it could completely alter the perspective of the signal and characterization of the defects. To remove them, some interesting filtering methods exist in the literature and are used in the commercially available applications. N. Portzgen, 2008 [130], [131] developed a method called spatial-temporal filtering of the time of flight corresponding to the echoes in the signal. In this filtering method, spatial is the phase relationship between the transmitted waves at different reflection points in space and time. Temporal is the correlation between the transmitted wave and its lateral reflections at multiple intervals of time. As the reflections are time-dependent, the spatial-temporal filter differentiates the true defect reflections with the echoes. E. Iakovleva, 2014 [132] worked on multi-mode imaging using TFM and focused exclusively on filtering different artefacts. In the filtering method, a threshold is defined by weighting the TFM algorithm by a factor depending on the angle formed by the local directions to transmission and reception to the point of calculation considered.

In recent years, Kombosse's work [129] is promising which has detailed and presented a filtering method that makes use of both signal and image processing methods. He noticed that when using plane-wave imaging, artefacts are recorded of a single defect which strictly depends on the geometry, orientation, and characteristics of the sensor itself. A prediction tool has been developed to image the defects and filter them using the spatial-temporal filter without prior knowledge of the orientation and placement of the defect. According

to his study, there are specific filters that could be able to remove the artefacts but an important question that relates to the above analysis is that, in a tribological problem or any solids with very small defects, does the size of the defect play any role in reducing the artefacts? Indeed, the defects in the previous model are around 4 mm wide, which is about half the size of the array itself and are placed at different depths. Reflections are thus strong enough to create multiple echoes and artefacts. When two bodies are in contact, the interface is located at a single particular depth, which means that, even if the contact spots can be small, the time of flight at which the interface is expected to be found can be precisely calculated. It is thus possible to avoid the use of a filtering technique.

5.3.3 Imaging of a tribological interface

When transposing the previous analysis to a tribological problem, the previous defects can be seen as spacing or valleys separated by the contact points or asperities. Above 90% of the NDT existing publications deal with the defects that are at the millimeter scale whereas asperities in contact can range from 1 to maximum 500 µm. Thus, in this section and the following, the defects are studied in terms of critical size to be detectable. The critical size is defined based on the interface definitions described in Chapter 3. In this model, the array parameters remain unchanged, but the interface is defined as shown in figure 5.22. From the figure, the interface has 6 valleys with a given depth of 10 µm but varying width. The largest, in this case, is 2 mm and the smallest is 0.1 mm. The array configuration is the same with 15 elements with a 0.45 mm width and 0.2 mm spacing. For the given configuration, figure 5.23 shows the time-lapse of the wave travelling towards the interface and the related reflections when only the central element of the array is excited. Once the wave starts travelling in the direction of the depth, its wavefront expands in the lateral direction and experiences attenuation over time as seen in figure 5.23d. As the wave reaches the interface, part of the wave is reflected, and some part is transmitted as seen in figure 5.23e. Here, collecting the transmitted part is not considered as the process is executed in a pulse-echo process, and reflection can only be recorded.

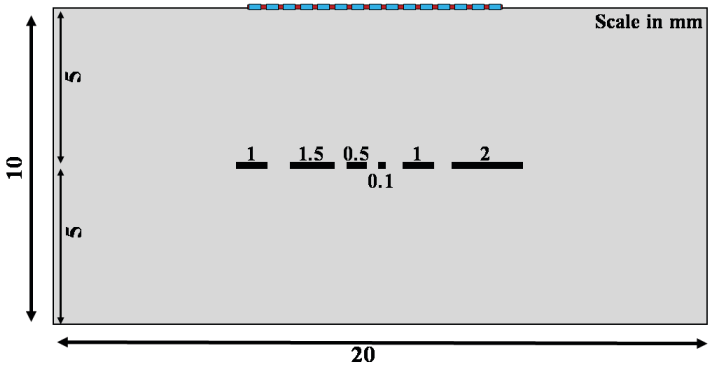

Figure 5.22: 2D sketch of the modelled interface with six valleys

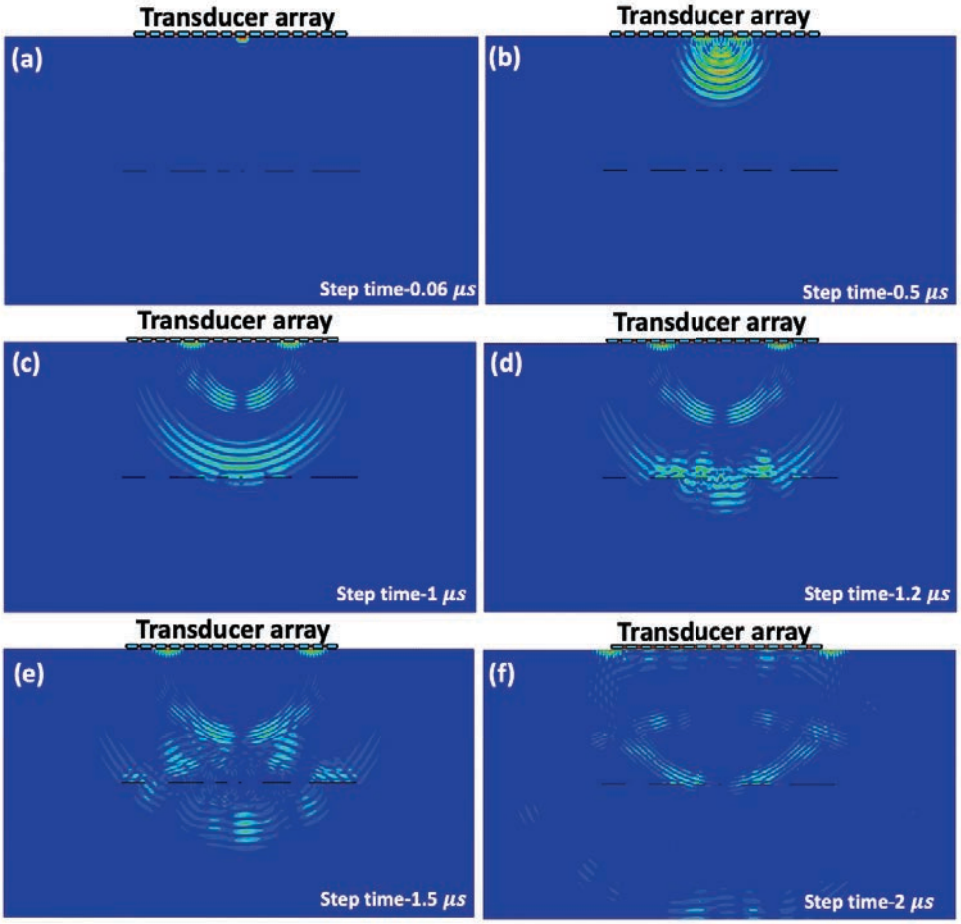

Figure 5.23: Simulated FE wave propagation through the defined geometry over different time intervals

In the last time step, figure 5.23f, the array experiences multiple reflections on each of the elements. It has to be noted that the reflection amplitude of the wave travelling back from the smallest region is relatively small which could be the reason for the very

low detection capability of the smallest defect when TFM is applied.

Two frequencies were used in this case, 10 MHz and 20 MHz respectively. Figure 5.24 shows the TFM method applied to the proposed contact interface using these two frequencies. It is evident that the valleys (spaces) and contacts are detected with both the frequency combinations. By closely focusing on the TFM images of the target region, there is a major difference in the quality of detection.

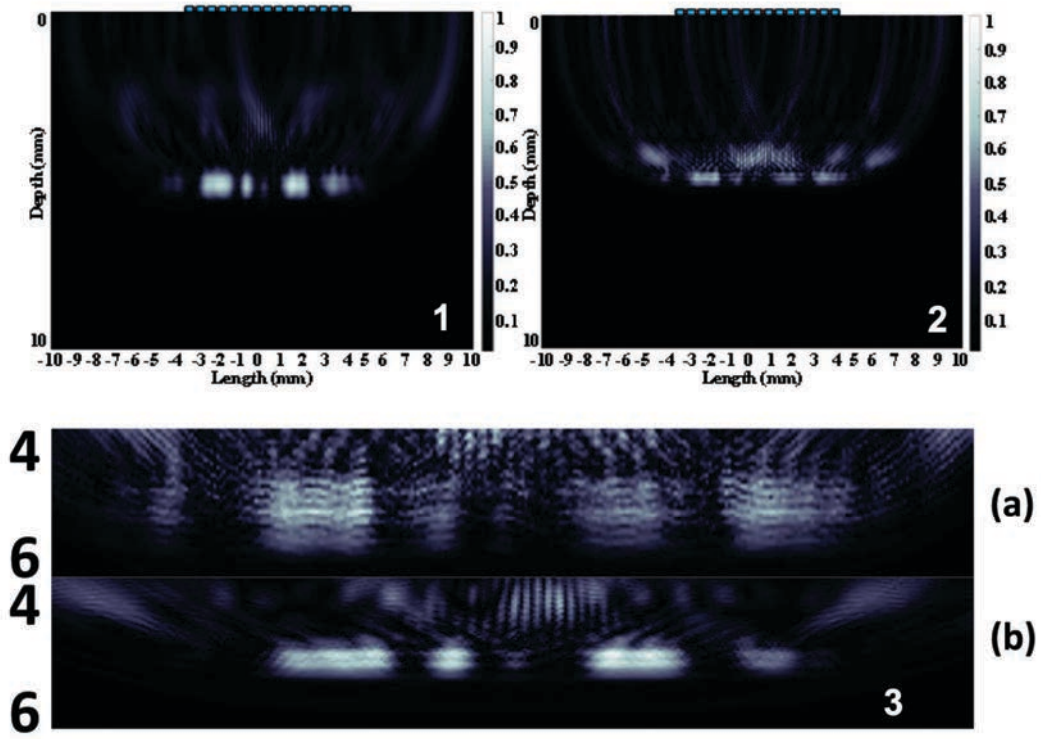

Figure 5.24: TFM image of the target interface (1) with 10MHz frequency (2) with 20 MHz frequency (3) Magnified image for (a) 10 MHz frequency (b) 20 MHz frequency

In the case of the 10 MHz frequency (figure 5.24(1)), both the large and small valleys are clearly identified, although the intensity is relatively low for the smallest one is 0.1 mm wide. On the other hand, the 20 MHz TFM image (figure 5.24(2)) does experience increased refraction at the proximity of the interface and the achieved resolution is poor which is quite noticeable in figure 5.24(3). This is because the beam is attenuated as it reaches the interface and the reflected one has a poor signal to noise ratio. On the contrary, higher frequencies experience high attenuation and could possibly affect the imaging. This will be further discussed in the following section.

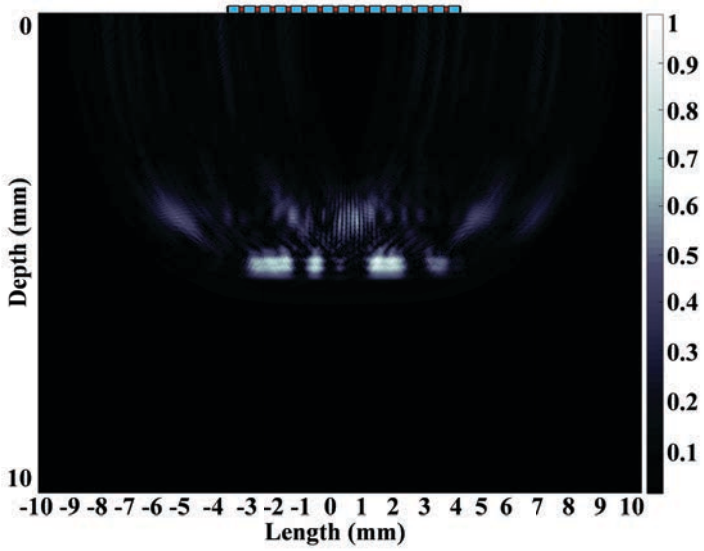

Figure 5.25: TFM image of the target interface with 20 MHz frequency and with element spacing 0.1 mm

As most of the commercially available ultrasonic arrays are usually limited to 10 MHz, further simulations are conducted using 10 MHz frequency. A second case study mimicking a tribological interface has been then developed considering this time valleys with a width down to 50 µm. The configuration and corresponding TFM image are presented in figure 5.26 and figure 5.28.

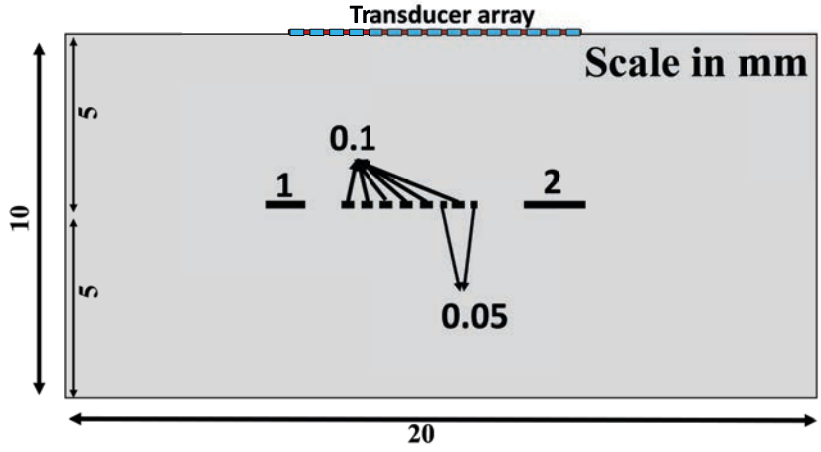

Figure 5.26: 2D sketch of the modelled interface with smaller scale valleys

The modelled configuration here includes 10 valleys placed at 5 mm in depth from the top surface of the first solid, 2 mm, and 1 mm large and 9 smaller valleys with widths 100 µm and 50 µm. The 2 large defects are placed in the end as references

as they can be easily detectable. Figure 5.27 shows the time-lapse of the wave that travels in the direction of the interface.

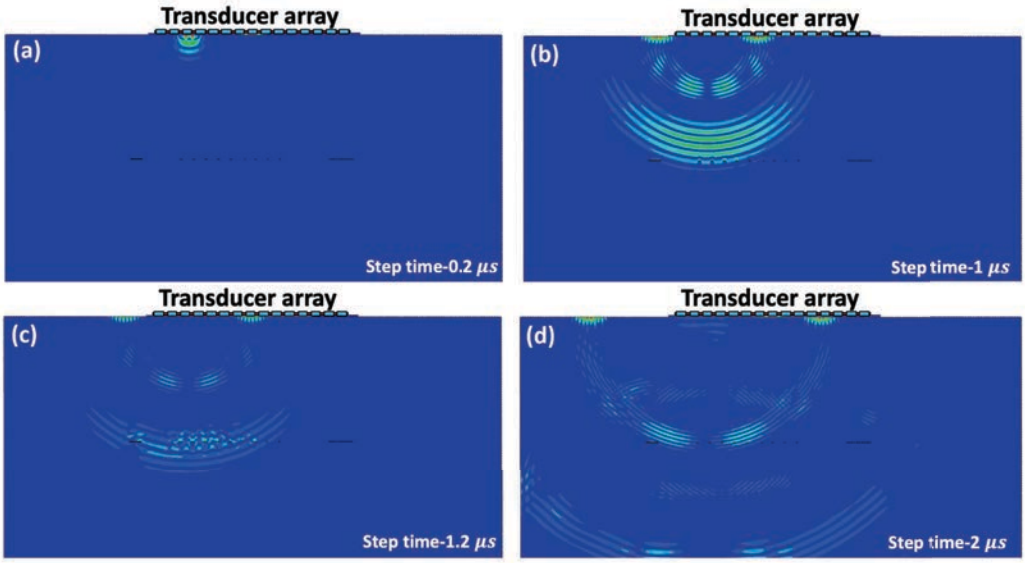

Figure 5.27: Simulated FE wave propagation when firing the third element in the array over different time intervals for the contact interface configuration with multiple micro-valleys

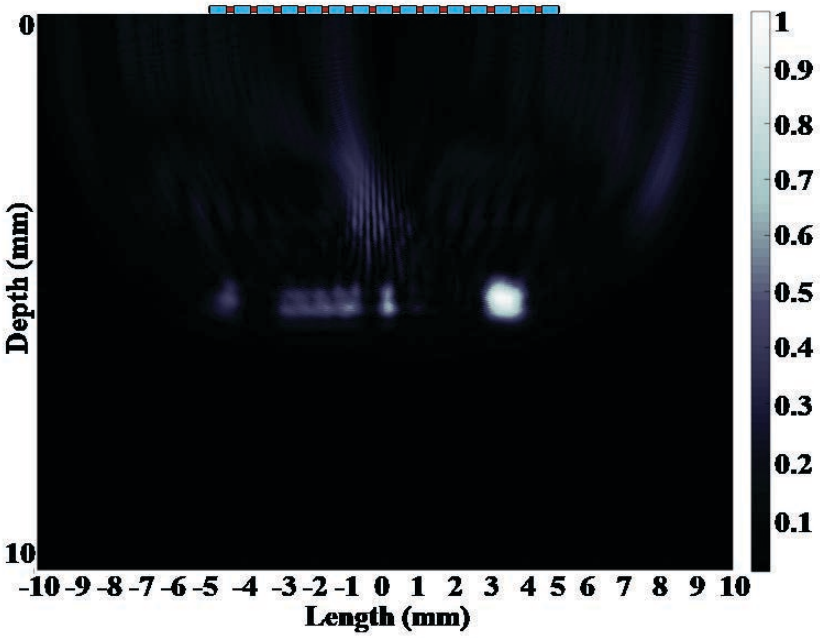

Figure 5.28: TFM image corresponding to the smaller scale valleys configuration with a 10 MHz array

It can be noticed that the amount of reflection that can be achieved through such small spaces between asperities is very small. Figure 5.28 shows the TFM plot of the

proposed geometry. The phased array with 10 MHz frequency has the strength to reflect through the smallest of the valleys and image them. Although, it can be noted that the largest defect in the interface has the highest intensity, and remaining small defects have very low amplitude resulting in an artificially reduced resolution.

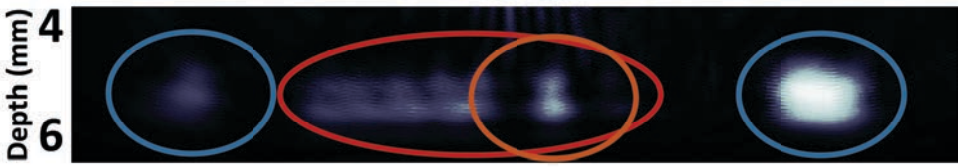

Figure 5.29: Magnification of the mentioned geometry with specific focus on the interface with a 10 MHz array

By closely looking in figure 5.29, at the smallest region of the interface (circled in red), it can be noted that 100 microns defects are clearly resolved but are not individually identifiable. In the axial direction, the resolution seems to be enough to image the exact interface configuration but not the exact height of the valleys. Also, when focusing on the orange circle, it is shown that the smallest valleys (50 µm) are completely invisible. In such cases, the transducer array must be redesigned to attain high resolution in axial and lateral directions. Increasing frequency, increasing the number of elements in the array are the factors that will improve the performance of the array.

This analysis results in the conclusion that with the present array configuration (10 MHz, 15 elements, 8 mm length), it can image valleys as small as 100 microns and will not detect the gaps smaller than 50 microns. Simply increasing the array frequency to 20 MHz makes it unsuccessful in clearly mapping the smallest gaps, which can be improved further by reducing the inner element spacing. The separation between the valleys also plays a major role in the detection due to the condition that defects side by side cannot be differentiated if the separation is larger than the lateral resolution achievable. To evaluate the width of valleys between asperities, another tribological configuration is proposed as seen in figure 5.30.

5.3.4 Detection capability of the interface

The previous results raise two main questions:

- what is the most narrow valley that could be captured when using a 10 MHz array?
- why increasing the frequency of the array does not improve the detection capability?

Critical detectable size

Firstly, a simplified configuration is defined with the width of the valley incrementally increasing until being detected by the TFM imaging method. Figure 5.30 shows the geometry of the interface with similar asperity size distribution.

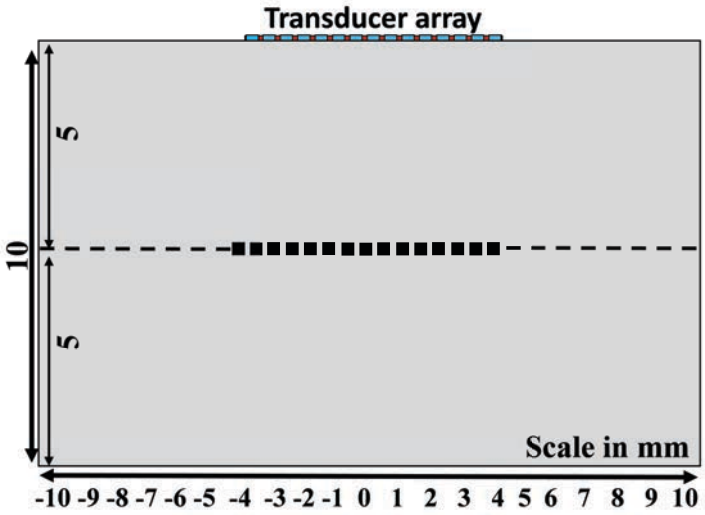

Figure 5.30: Geometry corresponding to the proposed FE model with valleys positioned in the central axis and with varying valley (in black) i.e. gap between the solid contact spots

In this case, the width of the valley is varied from 20, 50, and 100 µm, and the spacing was fixed to 50 microns. The array definitions are fixed as in the previous simulations with a frequency fixed to 10 MHz. The latter is of high interest as it corresponds to the highest frequency that can be easily supplied in terms of built-in transducer or even piezoelectric patches. Figure 5.31 shows the TFM images corresponding to each configuration of interest. It can be noticed in figure 5.31a that no valley could be identified. When increasing the size of the valleys to 50 microns, the interface starts to be observed but the quality of

the detection is still questionable. As the size is increased to 100 microns, the interface is plotted, and individual valleys start to be detectable.

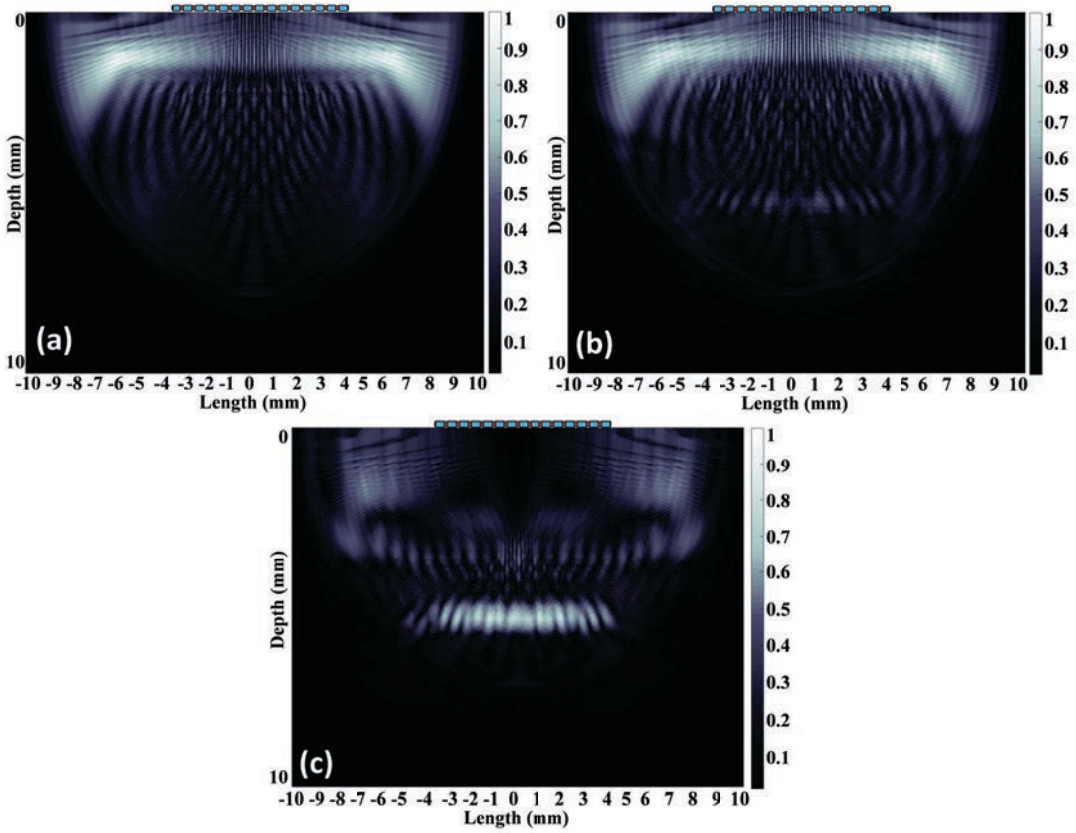

Figure 5.31: TFM image corresponding to (a) valley of 20 µm and asperity 50 µm (b) 50 µm and asperity 50 µm and (c) 100 µm and asperity 50 µm

Their exact size is however not perfectly defined showing that an improvement in the lateral resolution has to be operated. This means that although the defects are large to be detectable, it falls short in terms of resolution, which makes the image to have distorted effects as seen in figure 5.31c.

The proposed analysis is not conducted further because it was previously know that above 50 microns or close to 100 microns is easily detectable. In conclusion probability of detection is very high for the asperities whose width and valley falls above 50 μm.

Proper design of the array

Increasing the frequency of the array is the first option that can be used to increase the resolution of the technique and thus manage to detect smaller valleys. However, only

increasing the frequency without adapting the set-up can only lead to worse results as shown before. Indeed, the criteria would be that the target region has to be as close as possible to reduce attenuation and have a better resolution but also the size and spacing of the elements in the array have to be properly adjusted.

Referring to Chapter 4, the inner element spacing has to be reduced in agreement with the selected frequency and wavelength of the generated wave. The array configuration selected in section 5.3.3 has then be updated by reducing the element spacing to 0.1 when using a 20 MHz frequency and the resulting TFM image is presented in figure 5.25.

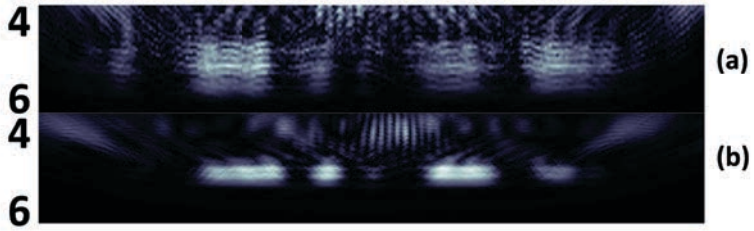

Figure 5.32: Scale magnification of the TFM image for (a) 20 MHz frequency with an element spacing of 0.2 mm and (b) 20 MHz frequency with a spacing of 0.1 mm

Figure 5.32 shows that the quality of the acoustic image and amplitude are slightly different along the interface.

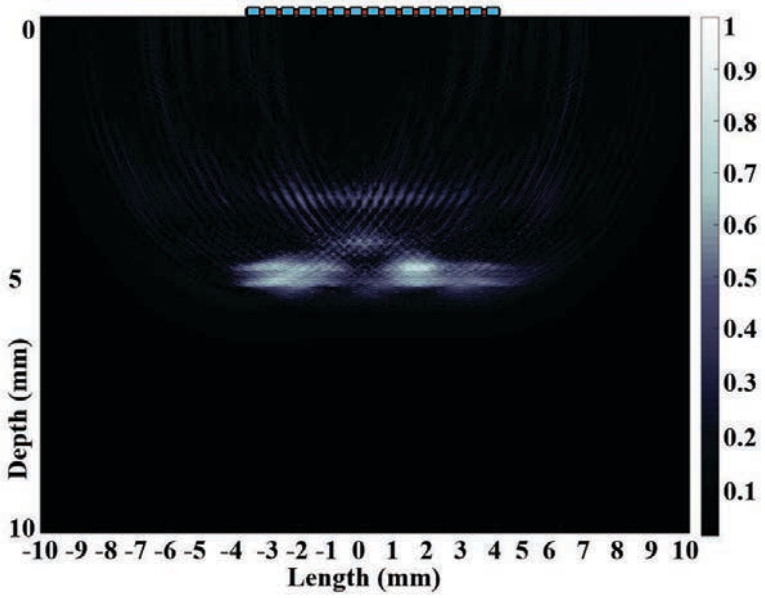

Figure 5.33: TFM image for 50 MHz frequency with array element spacing of 0.05 mm with pulse amplitude of 1E+7

Although the detection range is reduced as the corner to the left valley is not visible (due to the reduced size of the array), it can be confirmed with this analysis that 20 MHz is strong in resolving the closely placed defects. The same configuration is tested using 50 MHz frequency which results in the TFM as seen in figure 5.33.

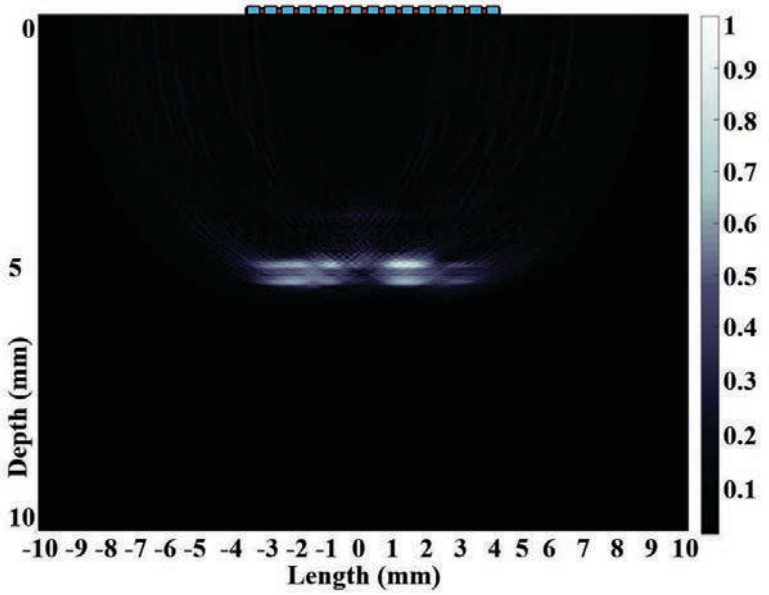

Figure 5.34: TFM image for 50 MHz frequency with array element spacing of 0.05 mm with pulse amplitude of 1E+10

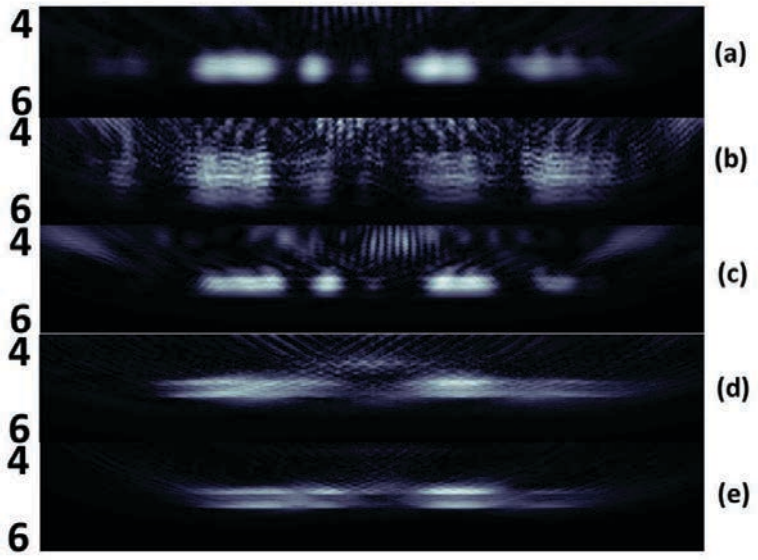

Figure 5.35: TFM image for all the frequency combinations (a) 10 MHz element spacing 0.2 mm (b) 20 MHz spacing 0.2 mm (c) 20MHz element spacing 0.1 mm (d) 50 MHz element spacing 0.05 mm amplitude 1E+7 (e) 50 MHz element spacing 0.05 mm amplitude 1E+10

It can be noticed that 50 MHz does image the interface region but with an inaccurate representation of the asperities. Also, 50 MHz has very low penetration power and the problem in such cases would be that a very small amount of energy is reflected to the array which is evident in figure 5.33. One solution could be to increase the power of the pulse (i.e. increase the amplitude of input). The amplitude of 1E+7 has thus been increased by a factor 1000 compared to the previous array configurations to confirm the possibility of imaging the whole interface at 50 MHz. Figure 5.34 shows the TFM image corresponding to 50 MHz frequency implementation with increased pulse amplitude. There is a noticeable difference in the imaging observed for 50 MHz frequency with an increase in amplitude, but it is still not clear in terms of what can be extracted or interpreted. A detailed comparison of all the possible combinations for different frequencies is shown in figure 5.35. The quality or resolution of the image is high in the case of figure 5.35a and 5.35c which corresponds to 10 and 20 MHz and low in the remaining all combinations.

This is because the high-quality imaging is acquired using an optimized array and in all the above cases, configuration 20 MHz with 0.1 mm element spacing yields results that are superior to other configurations. This can be illustrated by the results of wave propagation comparing the 10 MHz, 20 MHz, and 50 MHz configurations for a given time instance as shown in figure 5.36. It should be noted that the color scale is similar for the five subfigures whereas Amax, defined in the caption of the figure 5.36, is the amplitude of the incident pulse. The amplitudes corresponding to 20 MHz and 50 MHz are low compared to 10 MHz which can be seen in figure 5.36b and 5.36c. However, an interesting aspect is that irrespective of moderately or extremely low reflected signals for 20 and 50 MHz, the TFM can image the interface region. This could be an advantage in measurements where it is highly unlikely that high reflections can occur.

Another conclusion is that as the frequency increases the wavefront becomes shorter and more focused with reduced penetrating power which is quite obvious according to ultrasonic theory. This means that, at higher frequencies, the target region will be focused and much smaller in the x-direction. This indeed will not cover the whole targeting interface. This will indeed result in amplitude data that corresponds to only a few target

points. In such cases, array performance can be improved by steering and focusing the beam on to the targeted region which can be achieved by adopting a delay strategy.

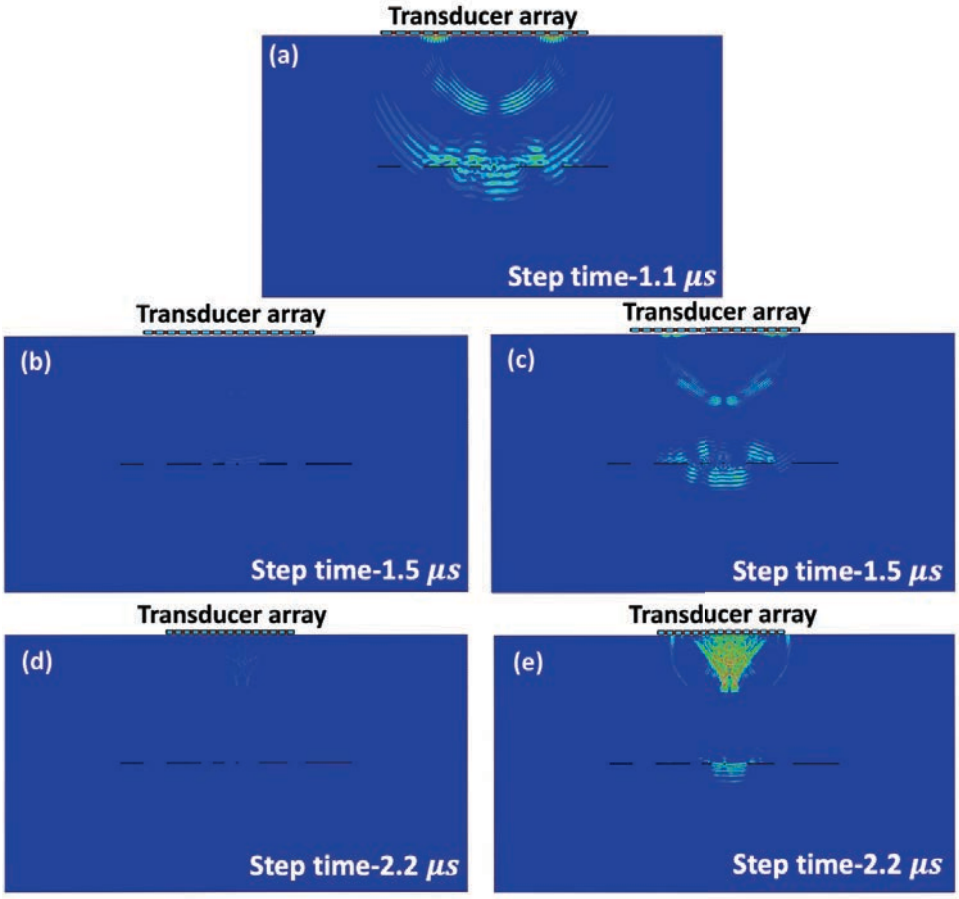

Figure 5.36: Wave propagation instance for when the wave hits the interface for (a) 10 MHz with Amax=1E+7 (b) 20 MHz with Amax=1E+7 (c) 20MHz with adjusted amplitude limit to Amax=1E+17 (b) 50 MHz with Amax=1E+7 (e) 50MHz with adjusted amplitude limit to Amax= 1E+19 , (Amax here is the amplitude of pulse and color scale of all the figures is same)

Although, the detection range is reduced as the corner to the left valley is not visible (reduced spacing reduces focusing range). It can be confirmed with the analysis that 20 MHz is strong in resolving the closely placed defects.

5.3.5 Imaging of a tribological interface with subsurface defects

In the previous sections, the whole methodology has been applied to a single contact interface assuming that the first bodies were free of internal defects. In some tribological applications, subsurface defects can be found whether due to the manufacturing process of

the employed material (casting, forging) or due to the tribological interaction itself (fatigue cracks or delamination).

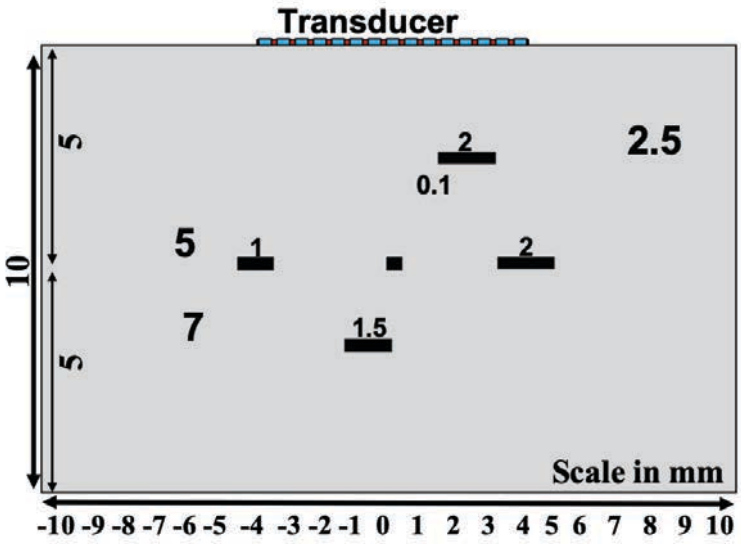

Figure 5.37: 2D sketch of the modelled interface with subsurface defects within the two first bodies

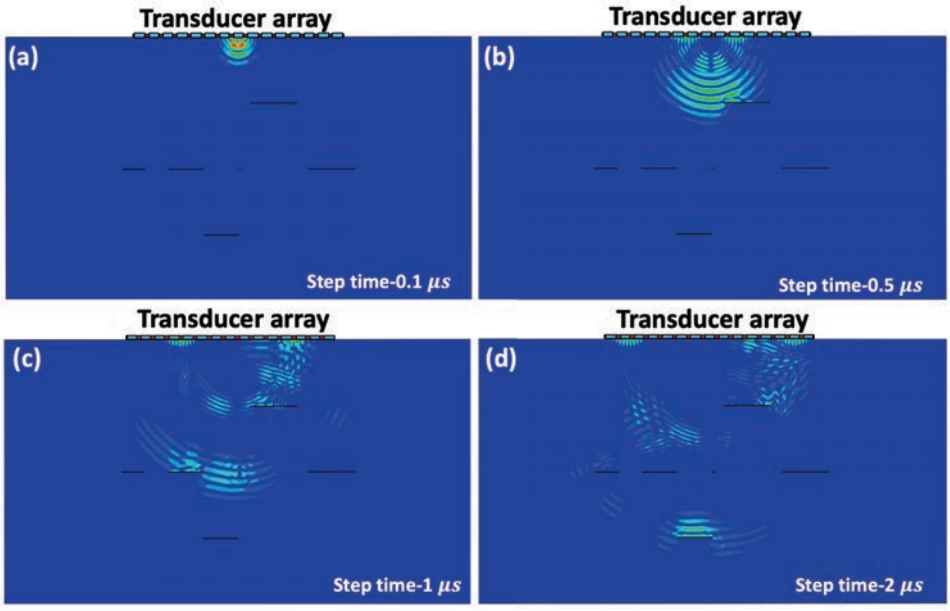

Figure 5.38: Simulated FE wave propagation when firing the eighth element in the array over different time intervals for the contact interface configuration with micro-valleys and subsurface defects

Thus, a configuration corresponding to such a situation is investigated in this section. A schematic representation of the defects and valleys distributed over different depths

in the sample is seen in figure 5.37. The modelled contact interface is exactly placed at a depth of 5 mm with two defects located at 2.5 mm and 7 mm from the top surface respectively. The size of the valleys in the contact ranges from 0.1 mm (smallest) to 2 mm (largest) with a constant height of 10 µm whereas the subsurface defects are 2 and 1.5 mm large. As in the previous simulations, the ultrasonic array has 15 elements and is operated at 10 MHz center frequency. The FMC acquisition method is followed to capture the A-scans from the FE model and later processed using the Total Focusing Method. The wave propagation pattern and its corresponding A-scan can thus be acquired for each element excitation. In figure 5.38, the 8th element is pulsed and the consequent reflections and scattering through the defects are recorded.

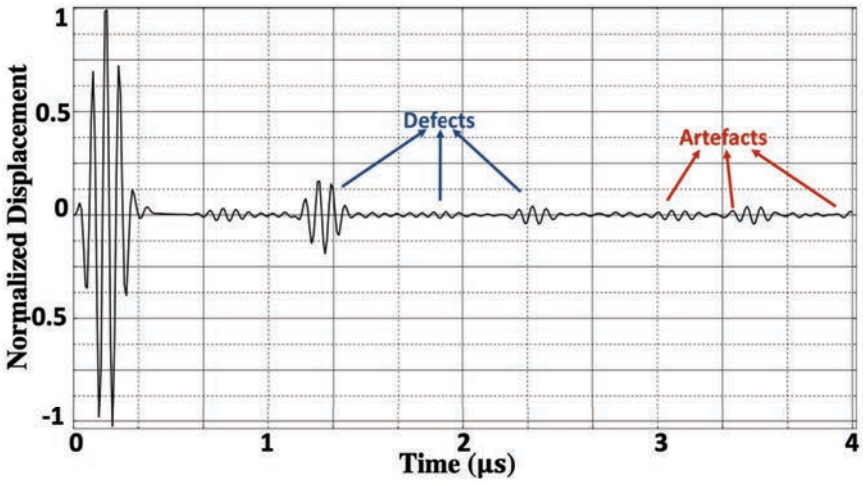

Figure 5.39: A-scan for one transmission and reception combination with in blue the signal corresponding to the actual defects and in red the artefacts

Figure 5.39 shows the time domain plot corresponding to one excitation of the 8th element and resulting reflections reconstructed over the entire measurement time. If the first large pulse is indeed the element excitation input signal, the following first three reflections not exceeding the time of 3 µs are the true defects and interface reflections. Later are the multiple echoes recorded due to the wave travelling and reflecting from the back wall or any other discontinuities that exist.

The TFM plot corresponding to all the A-scan combinations is presented in figure 5.40. The contact interface reconstructed with TFM has a low resolution and amplitude

distribution because of the additional subsurface defect added close to the top surface. For this type of configuration, however, the wave propagation is relatively smooth (considering the size of the defects), with fewer artefacts and scatters around the targeting region. Note also that in this example it is possible to observe the impact of the presence of the artefacts visible that correspond to the closest defect.

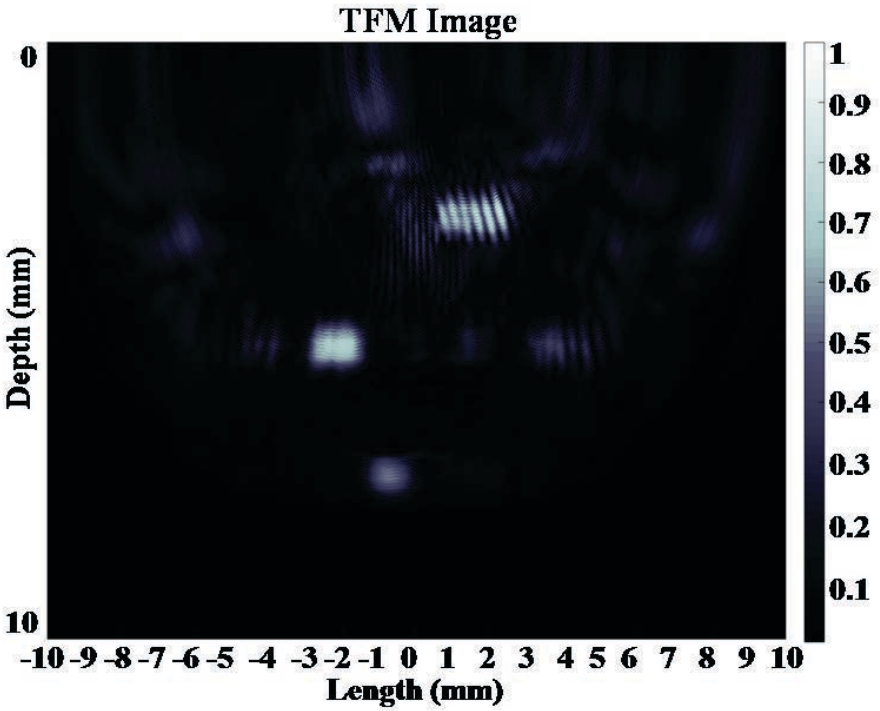

Figure 5.40: TFM image of the modelled interface with subsurface defects within the two first bodies

It can be noticed from the TFM image that even at different depths, the defects and valleys can be relatively well detected but still hardly measured to define their exact size. There are a few interesting conclusions that can be drawn from the above result. First is that due to the wave interference with the defect at a depth of 2.5 mm, closer defect to the array, the wave loses more energy as it reaches the 0.1 mm wide valley which is located beyond, in the central axis of the array. This first subsurface defect in the upper solid acts as a kind of acoustic barrier and hides the possible discontinuities located further towards the interface. Secondly, two reflections are recorded for the first subsurface defect which is marked in red in figure 5.41.

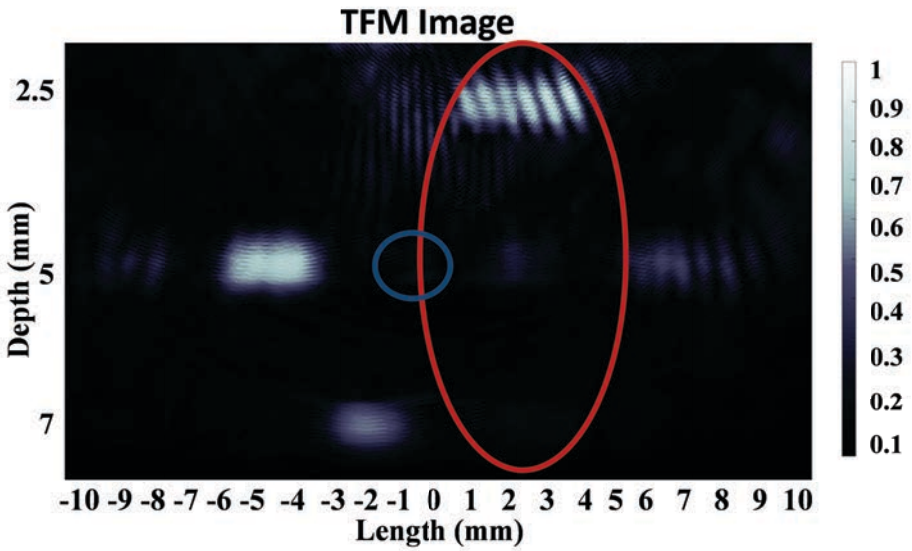

Figure 5.41: Magnified interface with smallest defect marked in blue and the first defect with its lateral reflection marked in red.

This corresponds to the acoustic artefact generated by the multiple reflections as explained in Section 5.2. It is interesting to note two reflections for the single defect at different depths. These effects can be manually filtered out or using a pre-defined filter (spatial-temporal filter for instance) that removes the reflection below a threshold.

Focusing on the detection of the second subsurface defect located at a depth of 7 mm, the figure 5.38 gives a clear image of the time-lapse where the wave is seen excited and partially reflected. On and beyond the contact interface located at a depth of 5 mm, a drop-in amplitude can be observed in the region where the wave disruption occurs. This can be observed at the depth 7 mm where the defect is shown indifferent to its original size. This makes it clear that wave propagation of imaging a contact interface without subsurface defects is different from the present configuration where both subsurface defects can affect the detection capability. This is a more complicated case where an in-depth analysis of imaging with filtering is needed. Also, in such cases, other focusing methods such as sectoral scanning or focused scanning of interest.

The previous results tend to show that the size of the subsurface defects is affecting the interface imaging capability as it will directly govern the amplitude of the propagating wave once crossing those defects.

5.3.6 Imaging of a tribological interface with porosities

A more complex configuration with smaller subsurface defects as well as contact valleys is then modelled to assess this last scenario and cover a larger range of possibilities. The schematic of this configuration is shown in figure 5.42.

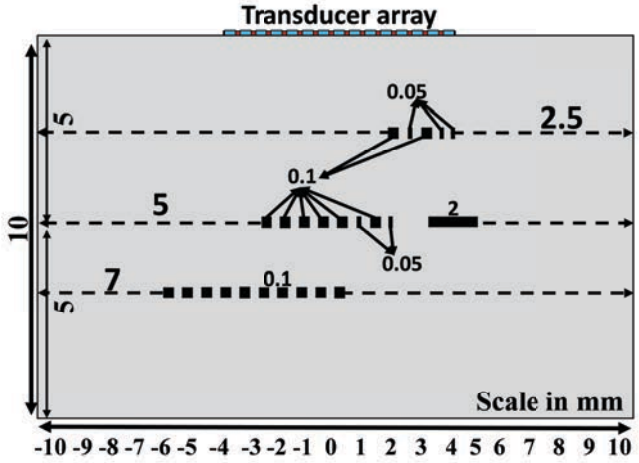

Figure 5.42: 2D sketch of the modelled interface with small subsurface defects distributed at 3 depths

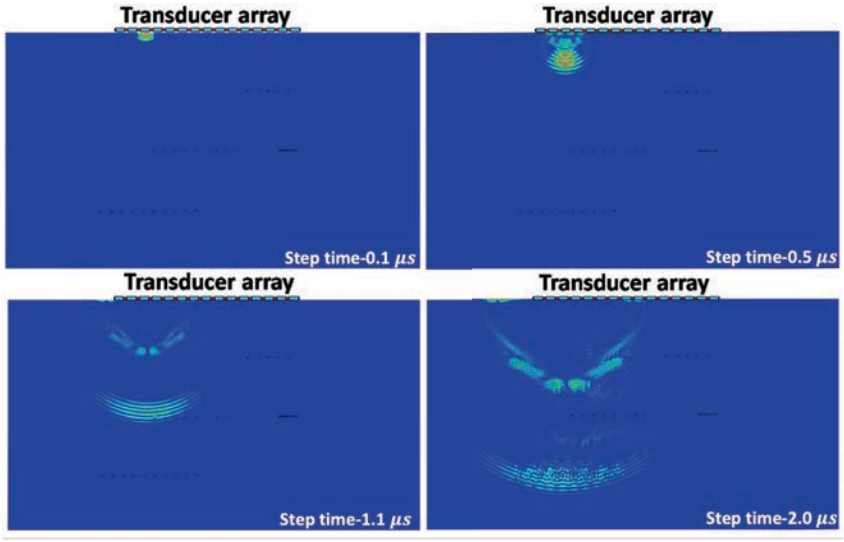

Figure 5.43: Simulated FE wave propagation when firing the third element in the array over different time intervals for the contact interface configuration with micro-valleys and micro subsurface defects

The contact interface is modelled with 0.05 mm, 0.1 mm, and 2 mm wide valleys whereas the subsurface defects range from 0.05 to 0.1 mm. The larger 2 mm wide valley is

used in this case as a reference to compare the wave intensity distribution at the interface. Firstly, a wave travelling time-lapse is shown for the excitation of three elements within the array as it is important to show the wave interference covering all the subsurface levels. Figure 5.43 shows the time-lapse of the wave travelling from the 3rd element when it reaches the contact interface and the subsurface defects.

In the figure 5.43, the images clearly show the wave interaction with the contact interface and subsurface defects, although the wave due to the positioning of the 3rd element, does not intervene directly with the micro-defects placed at 2.5 mm from the top surface. As in the previous case study, a very minimal part of the wave is reflected from the contact interface at 5 mm and the subsurface defect at 7 mm, as the amount of the reflection directly depends on the size of the gaps it interacts with.

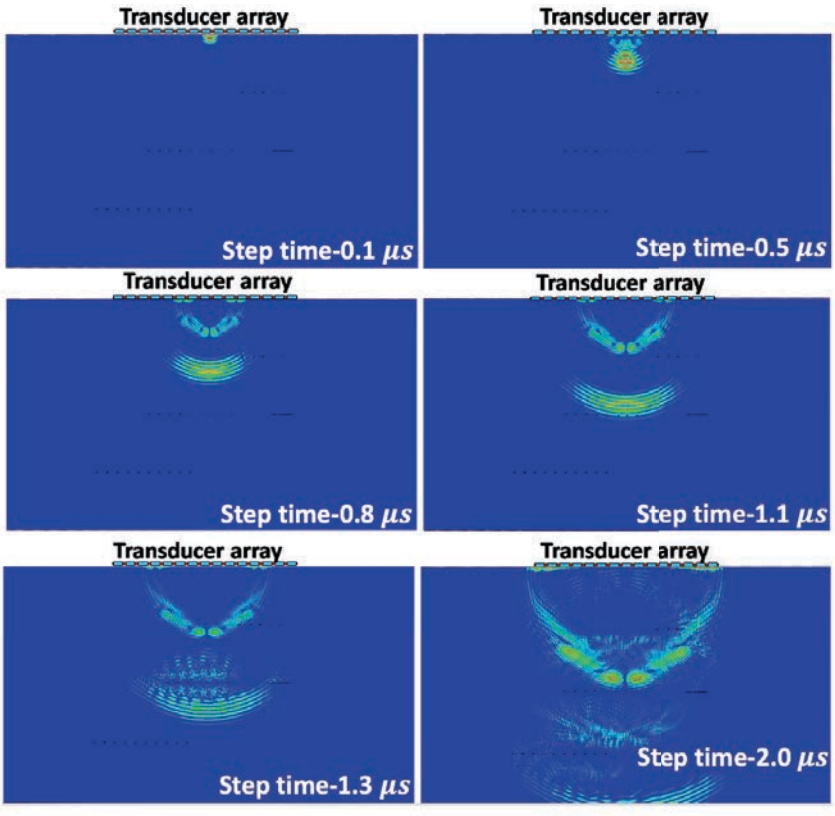

Figure 5.44: Simulated FE wave propagation when firing the 8th element in the array over different time intervals for the contact interface configuration with micro-valleys and micro subsurface defects

Further, the time-lapse of the wave propagating through the 8th element is shown in figure 5.44. The strongest amplitude at 2 µs will correspond to the interface and the

small amplitudes will carry information about subsurface defects. There is supposed to be a back-wall signal at 4 µs but as the wave experienced multi-level interference the back wall amplitude, in this case, is close to zero. The wave interacting with the three discontinuity layers can also be observed with a stronger interaction exhibited with the contact interface itself and a limited one with the two subsurface defect layers. Finally, the time-lapse when the 3rd element is pulsed as seen in figure 5.45 shows excitation of the 19th element with a major part of the wave interacts with the first subsurface defect before being propagated towards the contact interface.

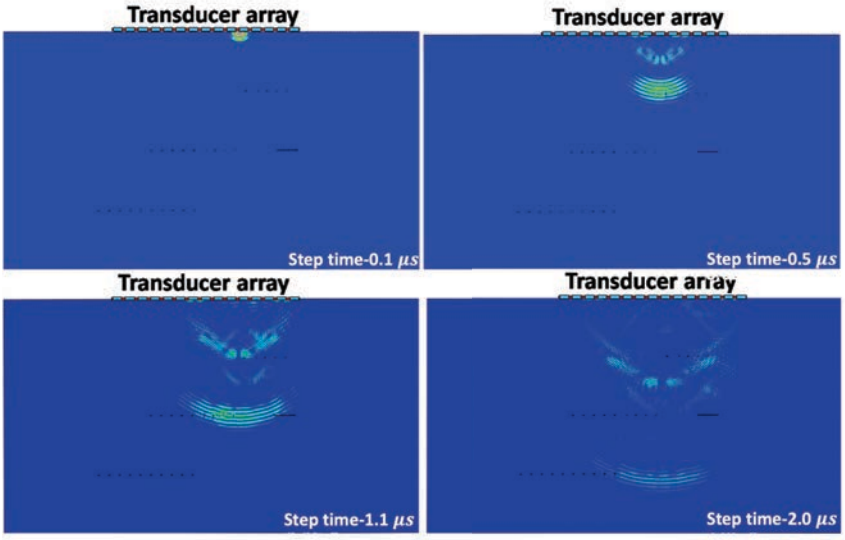

Figure 5.45: Simulated FE wave propagation when firing the 10th element in the array over different time intervals for the contact interface configuration with micro-valleys and micro subsurface defects

The objective of these images is not just to show the simulated wave propagation pattern but also to show the crucial differences that can be observed depending on the firing element. Firstly, the propagating pattern in figure 5.44 is compelling as it is transmitted through the modeled contact interface in the axis of the array and further reflected. As this element is located right in front of the contact interface, very small or negligible interaction is experienced by the element with the two subsurface defects. Secondly, for such small contact morphology, i.e. 100 and 50 µm wide valleys, the reflections present a low amplitude and most of the energy is still transmitted further in the solid, which means that the probability of detecting such small gaps will be relatively low.

When the 3rd or the 8th elements are excited, the wave directly experiences interaction with the subsurface micro-defects. This means that stronger reflections can be expected with the limited transmission. Regarding the transmissions, they are not measured in the developed methodology based on the pulse-echo mode, but they impose a strong challenge in developing the methods to treat them and used them in the TFM. The TFM plots corresponding to the above-mentioned configuration is shown in figure 5.46. The first thing to be noted from figure 5.46 is that there is a dramatic increase in the noise levels in the region close to the transducer array. A valid explanation could be that the propagated wave experiences multiple reflections from the valleys and subsurface defects before all the energy is dissipated.

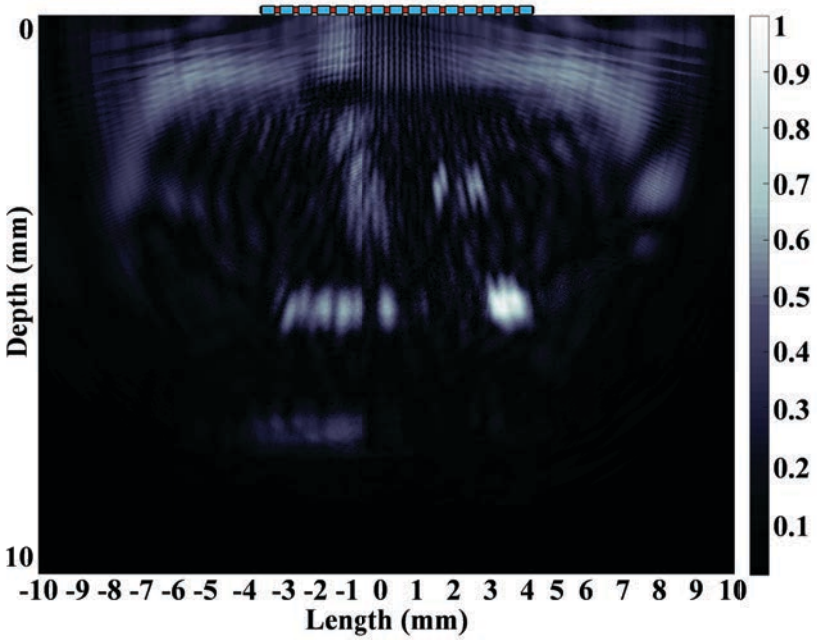

Figure 5.46: TFM image corresponding to the contact interface with multiple subsurface micro-defects with 10 MHz array frequency

Once the reflections from the interface are recorded, the part that is transmitted seems to create scatters that travel in the upward direction. This upward transmitted part worsens the signal to coherent noise ratio which can be seen as a thick cloud at the face of the transducer array. All the unwanted scatters in the model interact with the interface reflections creating a destructive environment. A solution could be to increase number of elements in the array which directly relates to reducing the space between the elements in the array.

5.4 Conclusions and discussions

This final chapter aimed to develop methods for characterizing contact interfaces based on finite element modelling and TFM imaging.

To achieve this goal, at first, it laid the foundations of the TFM imaging method by applying it on a model with 2 defects and recalling the principle of the formation of TFM images. In addition to understanding the algorithm, this initial study showed the existence of redundancy in the reflective regions. It was shown that defects very close to the array will have the possibility to exhibit multiple reflections resulting in artefacts in the TFM image. Their formation depends on the geometry of the part, the characteristics of the sensor, the defect characteristics (height, depth, orientation), and the relative position between the sensor and the defect. To remove these artefacts, a filtering process should be specifically developed which appears as an interesting perspective of this work. To facilitate the analysis of applying TFM on tribological problems, further models with various rough contact configurations and subsurface defects were modelled in FEM and imaged. Resulting images were perfectly plotted in terms of location but determining the exact dimension may differ based on how far the defects are placed compared to the ultrasonic array. Regarding the different investigated configurations, i.e. contact interfaces with or without subsurface defects, the following conclusions were drawn:

- In applications where complex geometrical interfaces occur, finite element modelling in combination with the data acquisition and imaging methods showed a great potential.
- TFM and FMC can be used in tribological applications to locate a contact interface and provide an in-situ acoustic image of the contact distribution;
- With the proper array definitions (frequency, number of elements, spacing etc), it is possible to image defects or valleys in an interface as small as 50 µm.

There are certain limitations and shortcomings in this chapter that can be addressed as a future perspective. The main focus was put on fusing finite element modelling and imaging but a detailed study relating to the array configuration itself has not been deeply

developed. A preliminary idea on applying high frequencies (>20 MHz) has however been addressed. Pulse echo method is majorly adapted assuming one-way access to the interface, but for samples where a 2-way measurement access could be possible, a dual transducer array implementation could be adapted which would give the possibility to record also the transmitted signals. On the contrary, many tribological systems only enable one-way access which will limit the above-mentioned method. In such cases, an interesting possibility would be to use a focused beam profile rather than working with FMC, especially within the mind of reducing the processing time and thus increasing the sampling rate. K. Snook, 2006 [133] explains an efficient way of developing arrays with very few transducer elements. A separate optimization based on a suitable element width and consistent spacing is needed for such limited transducers. In recent years, using dual-frequency ultrasound implementation in a single array seems to emerge as a method to increase image quality and reduce the residual noise. This method has not been discussed in this chapter and appears as a future relevant perspective combined with the beamforming capability of an array.

Summary:

- This chapter covered a detailed modelling aspects of tribological interfaces using wave propagating through phased arrays.
- Initial explanation and results related to array performance based on change in element spacing and number are shown.
- Main results corresponding to wave propagating and imaging of different interface conditions are shown.
- Imaging using high frequencies is studied and shown that although high frequencies offer better resolution, they are not always efficient in imaging.
- Study is extended to imaging subsurface defects and various rough contact interfaces.
- This chapter concludes up on the effective potential of imaging method in tribology but lacks the aspect of steering or focusing the beam on to a target region which can be seen as a future perspective.

Conclusions and Outlook

Overview of the thesis

Knowing the clear need for alternative instrumentations in tribology, this thesis aimed at assessing the capability of an ultrasound-based measuring technique to probe a rough contact interface. Considering the benefits of such an in-situ innovative method, a better understanding of the interaction between the ultrasonic wave and this interface was essential to confirm its potential. To this end, a numerical approach has been developed to model the wave propagation through rough contacting bodies and identify the relationship between the contact parameters and the recorded signals. This numerical model not only provided an insight into how does the wave propagate within the first bodies and interact with the interface but also gave the possibility to model perfectly defined and controlled surfaces. The particular interest was to dissociate the effect of each contact parameter such as the number or size of the asperities or valleys.

In a second stage, the research methodology was extended to the use of phased array transducers, which were proved to be an alternative to using a single element transducer. The flexibility of the numerical model was used to investigate the effect of various array design parameters and pulsing sequences. To fully take advantage of using an ultrasonic array, a specific pulsing technique called Full Matrix Capture (FMC) combined to an image reconstruction algorithm Total Focusing Method (TFM) was implemented to map the real contact zone. Various scenarios were investigated to assess the feasibility and sensitivity of the measuring technique and emphasize the drawbacks. This part of the work appears as a strong point considering the way it can motivate future studies focusing on tribological interfaces especially when rough contacts, wear, and damage detection is of high interest.

Main conclusions

In Chapter 3, a novel numerical approach based on a 2D finite element model was developed to study the interaction between the interface parameters and ultrasonic wave propagation. The transmission coefficient was measured for different model contact configurations and related to the corresponding contact stiffness. This study showed that, when investigating rough contact using a single element transducer, no unique relationship between the interface parameters such as contact width (Cw) or the number of asperities (N) and the transmission coefficient could be extracted. Within the mind to assess the real contact area in such contacts, it was shown that the contact ratio is also not a unique interface parameter that could be measured using this ultrasonic technique. However, a relationship has been identified when comparing the transmission coefficient to the contact stiffness. If this appears to be in agreement with the literature suggesting a proportionality, it was shown that this seems to depend on the nature of the contact interface, i.e. to depend on the contact ratio. Although being able to measure in-situ the contact stiffness of a given contact is definitely of interest, it was shown that characterizing precisely its morphology, i.e. number of contact spot and their size, required another approach rather imagine a mapping strategy.

Chapter 5 first explored the use of the ultrasonic array itself by especially optimizing the width and spacing of the individual elements in the array. It focused then on the development and implementation of an imaging method in tribology via the selected signal acquisition method and reconstruction algorithm which were further applied in imaging various contact interface configurations. It was found that while FMC could acquire the relevant signals, TFM imaging was able to map the contact interface and detect the number of contact spots and valleys down to 50 microns. Also, this thesis is successful in distinguishing the number and location of the junctions. It also provides insight on potential interaction with sub-surface cracks and porosities that form during loading or sliding conditions. This thesis found out that based on the size of the subsurface defects, they could potentially interact with the interface itself resulting in an inaccurate interface image. however, as it goes down to the porosities scale, they have very low to negligible interaction. Also, it can be concluded from the image 5.47 that increasing

frequency is correlated with the design of an array, and changing alone the frequency will not improve the image resolution.

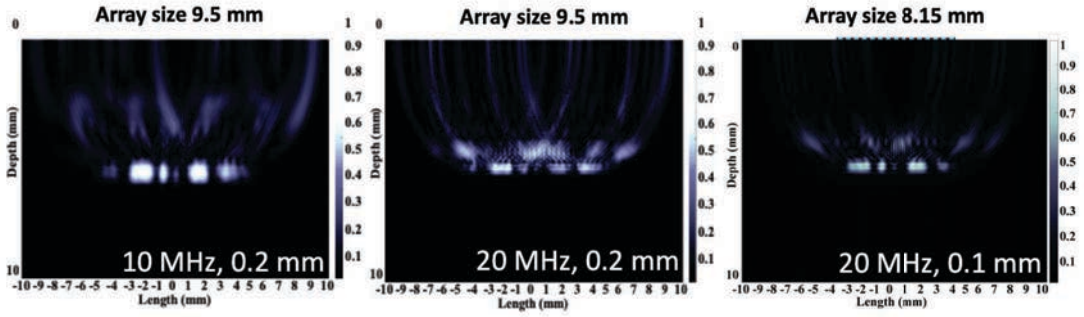

Figure 5.47: TFM image plotted for a given interface configuration with varying array parameters and frequency

However, depending on the surface and subsurface configurations, TFM could lead to the formation of artefacts or acoustic shadows at different depths depending on the asperity and valley size as well as the occurrence or not of subsurface defects. This could be connected to the characteristics of the sensor (opening, hoof slope), defect characteristics (height, depth, orientation), and the relative position between the sensor and the target. A detailed high-frequency study in the range of 10 to 50 MHz was simultaneously conducted concluding that it is indeed possible to image the interface with different quality levels owing to the correct array design, i.e. frequency, element size, number, and spacing. Nevertheless, considering the investigated ultrasonic configurations, it is highly unlikely that the exact size and shape of the valleys can be known, due to the fact that the resolution on both axial and lateral would still need to be improved by investigating deeper the array configuration.

Future perspectives

This thesis can be considered as the initial approach towards an in-situ probing of rough tribological interfaces based on ultrasounds. Therefore, certain gaps were identified and could definitely lead to further studies in the future. Several points of interest are thus listed in the following lines:

- When a model is designed in 3D, the computational complexity and time taken to process is increased. However, it would be important to perform a future study

using a 3D model which will give a deeper insight into the 3D wave propagation and confirm the consistency of a 2D assumption in the case of a 1D linear array.

- In Chapter 3, the transmission coefficient recorded when using a single element transducer could be related to the contact stiffness. However, a sudden change was observed when reaching the largest contact ratio range, i.e. beyond 0.33, where transmission experienced a strong increase. As this phenomenon has not been explained, it would be relevant to develop further analyses to clearly point out the governing mechanisms.

- In this Chapter but also in the whole thesis, the interface was assumed to be a mix of perfect square asperities distributed in different configurations. If the next first step could be to numerically assess the sensitivity to the asperity shape, a further perspective could be to import 2D or even 3D real surface topographies.

- In Chapter 5 dealing with the imaging part, a detailed study would be needed on enhancing the resolution of images to better target the ultrasonic array capabilities. One interesting option could be to adopt a multiple frequency excitation by designing an array made of elements with different properties.

- In addition, the filtering aspect was not addressed in great detail, and problems related to the quality of the image and the formation of artefacts were reported. It is evident from them that, at such a small scale, there could be a possibility of artefacts formation of one defect and that was partially linked to the multiple inner wall reflections that form a duplicate image. This can be addressed using spatial-temporal filters which could be relevant perspectives for future work.

- Finally, one possible solution to increase the performance of this ultrasonic technique could be to know the resonance frequency of the inspecting solids. This technique could allow for smaller valleys to be detected without suffering from a very deep region of focus. The concept behind resonance is that matching the frequency of the array with the eigenfrequency of solid will enhance wave propagation power resulting in amplified array performance.

- Based on the same idea, instead of only recording a reflection/transmission coefficient, another method could be to analyze the frequency changes of a tribological contact when prone to changes in the interface configuration. It can naturally be expected that the resonance frequency will change depending on the type of solids being pressed on to each other, on the number of asperities in contact and their size as well as on the level at which the interface is being pressurized.

Appendices

A
Appendix A

A.1 2D and 3D model comparison

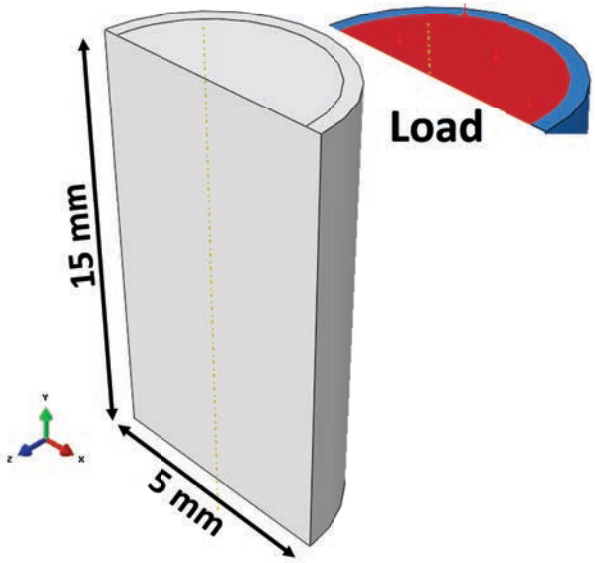

Figure A.1: 3D model of the solid with load indicated

Most of the work presented in this thesis will concern only 2D modelling but an important question remains on why 3D is not adapted. To address this, a 3D model confined to this section is presented. Model dimensions are similar to the 2D model presented in figure A.1 (Although, The model shown is circular in 2D it is assumed to be rectangular from

the top view). Sketch geometry relating to the model is shown in figure 10. Parameters such as load and material properties and mesh are shown in figure A.2.

Load	Transducer element number	1
	Transducer width (mm)	4
Excitation signal	Frequency	10 MHz
	Number of cycles	5
	Signal window	Hanning
Meshing dimensions	Element size (microns)	20
	Element type	Temp displacement
	Mesh control	Wedge (Sweep)

Figure A.2: Parameters of the 3D FE model

Figure A.1 shows wave propagation in the model which replicates similar behavior as seen in 2D. The main problem associated with this approach is related to the computation cost. Such a fine and complex meshing induced an increase in the computation time consumed 5 to 10 minutes in 2D to 4 to 6 hours in 3D.

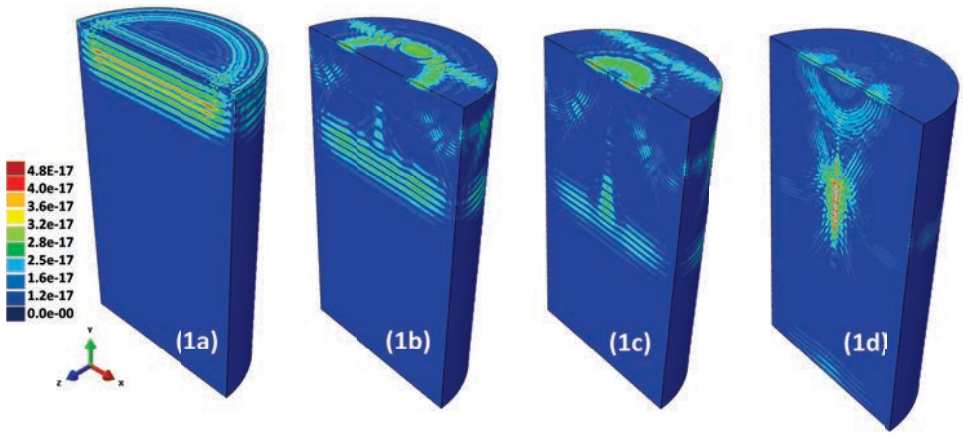

Figure A.3: Time lapse of wave travelling through solid

From the figure, A.4it can be noticed that, although wave propagation pattern is quite similar in both the cases, a difference in the amplitude of the transmitted signal can still be noticed in comparison with 2D which is agreeable due to the fact that loss factors are more dominant in a 3D model. Indeed the surrounding reflecting boundaries tend to decrease the wave amplitude while travelling as it generates larger scattering than in the 2D plane

wave assumption. In conclusion, considering the computation and complexity involved in modelling and processing a 3D problem, and as the main objective is further to investigate two contacting surfaces, 2D seems to be highly recommended. Propagation configuration will have to be carefully selected to ensure the plane wave propagation assumptions.

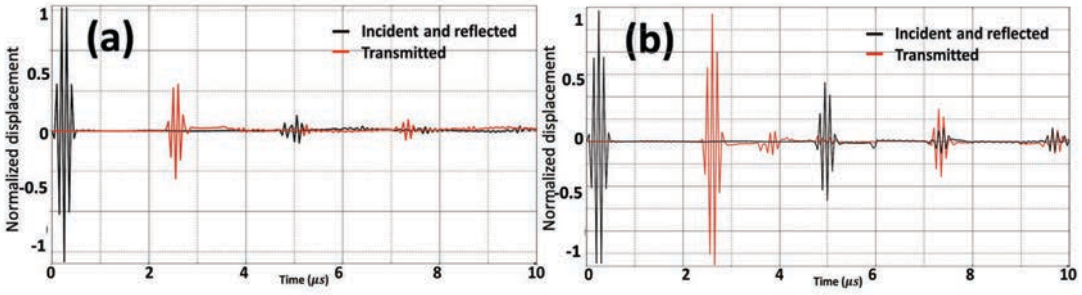

Figure A.4: Comparison of the time plot for (a) 3D model (b) 2D model

From the figure, A.4it can be noticed that, although wave propagation pattern is quite similar in both the cases, a difference in the amplitude of the transmitted signal can still be noticed in comparison with 2D which is agreeable due to the fact that loss factors are more dominant in a 3D model. Indeed the surrounding reflecting boundaries tend to decrease the wave amplitude while travelling as it generates larger scattering than in the 2D plane wave assumption. In conclusion, considering the computation and complexity involved in modelling and processing a 3D problem, and as the main objective is further to investigate two contacting surfaces, 2D seems to be highly recommended. Propagation configuration will have to be carefully selected to ensure the plane wave propagation assumptions.

A.2 Reflection coefficient difference for 10 and 20 microns mesh distribution

This analysis corresponds to the mesh sensitivity study that was carried out in chapter 3. The aim here is to see the difference of reflections coefficient for two mesh distributions i.e. 20 microns and 10 microns. The difference is that the later (10 microns) will have two times more nodes in comparison resulting in a more accurate wave propagation depiction. The model and geometry that is used in this simulation are similar to the one shown in figure 3.15. This simulation is tested on one contact width i.e. 20 microns and the contact

space is changed i.e. 20, 40, 60, 80, 100 microns. A sketch representing the simulation and results corresponding to the mesh sensitivity comparison are shown in figure A.5 and A.6.

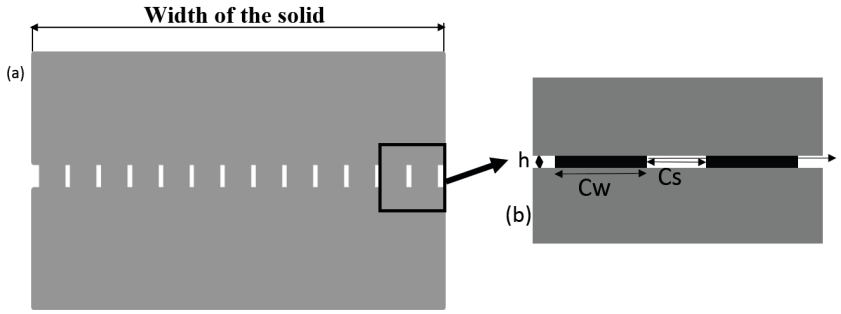

Figure A.5: Sketch corresponding to the simulation carried out with (a) complete solid-solid contact (b) close look at two interfaces

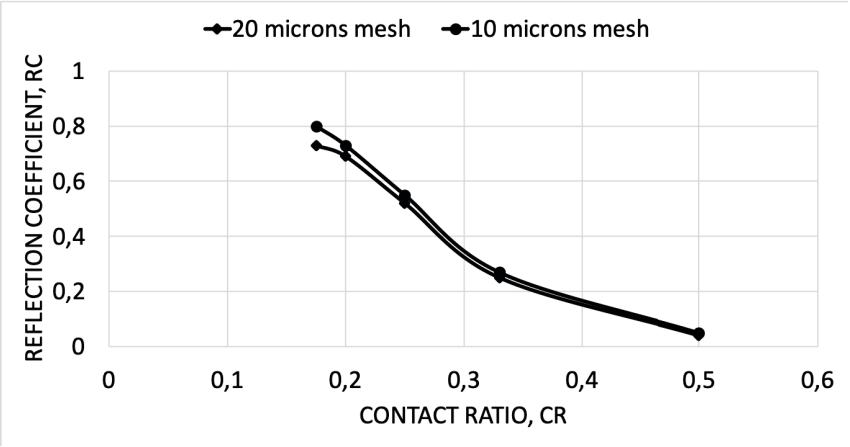

Figure A.6: reflection coefficient plotted for two different mesh distributions

From the above figure, it can be noticed that both the mesh sizes result in a similar reflection coefficient trend which concludes that changes to the mesh distribution alone do not affect the results. However, a small deviation can be observed in higher reflection points.

B
Appendix B

B.1 Application to mapping the contact curvature of a sphere/plane contact

The curved solid analysis is an additional study carried out on a curved geometry like a pin such that to give light on wave propagation imaging on a pin on disk tribological applications. The schematic of the proposed geometry of the tested FE model is shown in the figure along with the mesh distribution. The transducer array is 6 mm in length with 10 elements and each element width and spacing being 0.45 mm and 0.2 mm. The center frequency is 10 MHz.

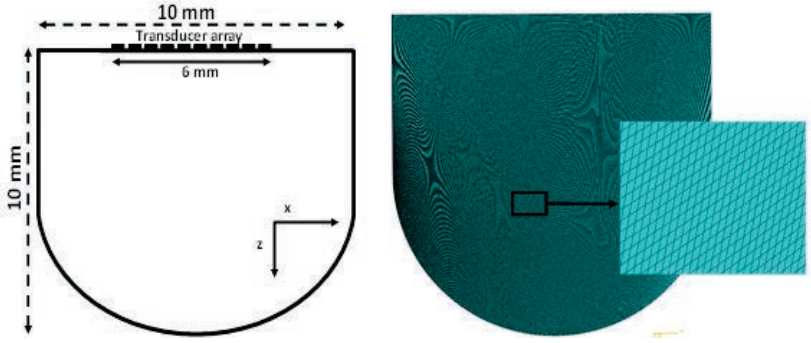

Figure B.1: Schematic representation of the sphere model and its mesh distribution (size 20 microns)

The data acquisition and processing in this model is done using full matrix capture (FMC) with total focusing method (TFM) and later with a focusing law imaged using TFM.

In the focusing process to reduce the complexity of having many delay laws, the beam is swept between negative and positive 45 degrees, where the beam profile is made suer to cover larger space thereby reducing the number of simulations to 3. The delay law follows the sectorial scanning method in this context is computed using the equation give as,

Here d_j is the euclidean distance between a given element $E(x,z)$ to the focal point $p(x,z)$ and d_o is the euclidean distance between the centre axis $E_c(x,z)$ to focal point $p(x,z)$. Initially, time-lapse corresponding to the steered beam in one particular direction only is shown in figure B.2. In this case, the transducer excitation is followed from left to right and resulting beam steering in the rightward direction. Figure B.2a shows the steered beam as it originates from the array, it can also be noticed that some part of the wave is released opposite to the beam direction which eventually travels along the walls of the sphere as seen in figure B.2c. The beam experiences the first impact from the target region and follows the curvature path (curvature of the structure) which will travel along and finally being reverted as seen in figure B.2e. Only some part of the focused beam travels back to the array as most of the energy coincides with the wave that is previously travelling in the opposite direction, this will have adverse effects on the amount of energy reflected.

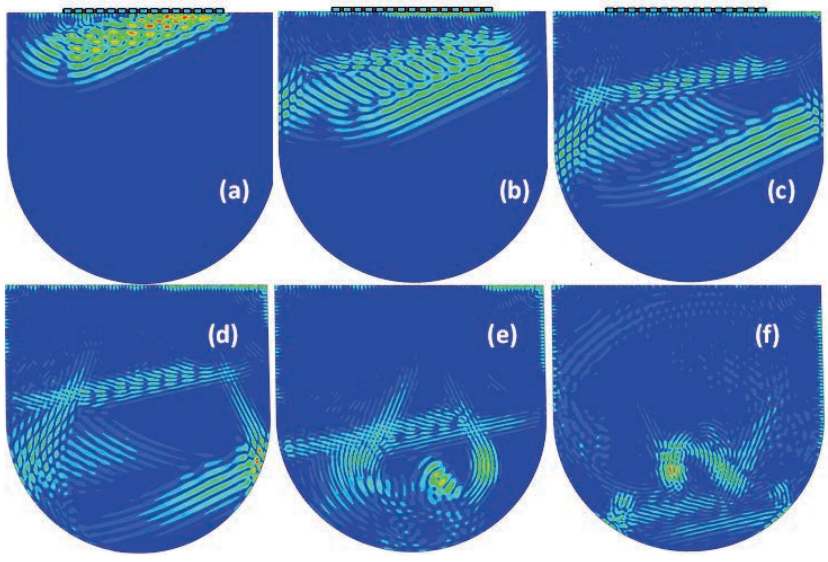

Figure B.2: Time lapse of the beam as it travels through the sphere and reflected to the array

Also in figure B.2f, once the first reflection reaches the array, the wave is drifted along the whole surface creating a cloud of scatters all along. These scatters are removed in the processing part to show a clear image.

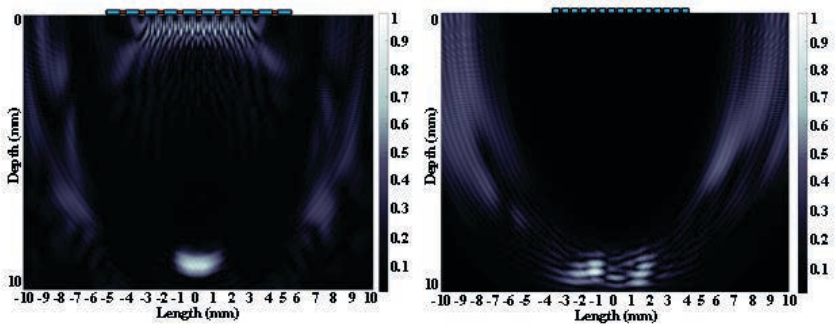

Figure B.3: Time lapse of the beam as it travels through the sphere and reflected to the array

In order to compare the imaging capability of both the methods (FMC, steered beam), the resulting TFM images are shown in figure B.3 . It can be seen that the B scan image corresponding to figure B.3b agrees well with the proposed geometry in comparison to figure B.3a, although, problem with FMC method is that on the edges (close to depth 10mm) the curvature is invisible which are shown as two gaps. These gaps are however resolved with the steering method.

But in both the cases, TFM images differ from the intended geometry. This implies the problem with either the waves that travel along the curvature interfering with the reflections or the array itself (size of the array). From the figure B.3 it can be concluded that it is indeed possible to image the curvature of the contact or in applications where pin on disk pressured contact is involved. Possible a focused or steered strategy can be adapted in comparison to the traditional FMC methods. This study can further be extended to applications where change in temperature gradient when extreme pressure is exerted on curved contacts (pin on disk) need to be imaged. Also, this can be used in applications where deformation between two solids are pressed on to one another with incremental conditions of pressure.

C
Appendix C

C.1 Stiffness validation with comparison for a different model

This section details about the additional stiffness models that is compared to the stiffness model that is used in figure 3.15. The selected model is similar in terms of mesh density, material type and interface distribution. However, the study is carried out in static analysis and no wave propagation is implemented. Instead a small displacement is applied at a reference point and the values of the interface stiffness in each case is extracted based on the reactive force. Various new boundaries and constraints are involved which are shown in the figure 3.26. The difference between the previous models and this model is that in this case, Solid A and b including the interface is deformable and the right boundary is defined as rigid. Figure C.1 describes the model configuration.

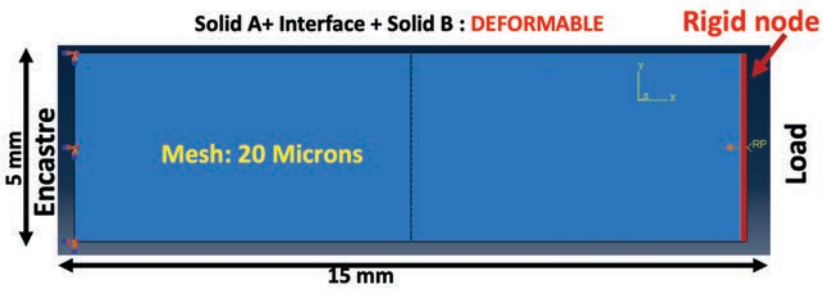

Figure C.1: Geometry corresponding to the model used in determining the interface stiffness

In the above figure, RP to the right is the reference point at which a 1E-11 amplitude displacement is applied in the negative x direction. The stiffness is extracted based on the resulting reactive force and is plotted vs transmission coefficient values.

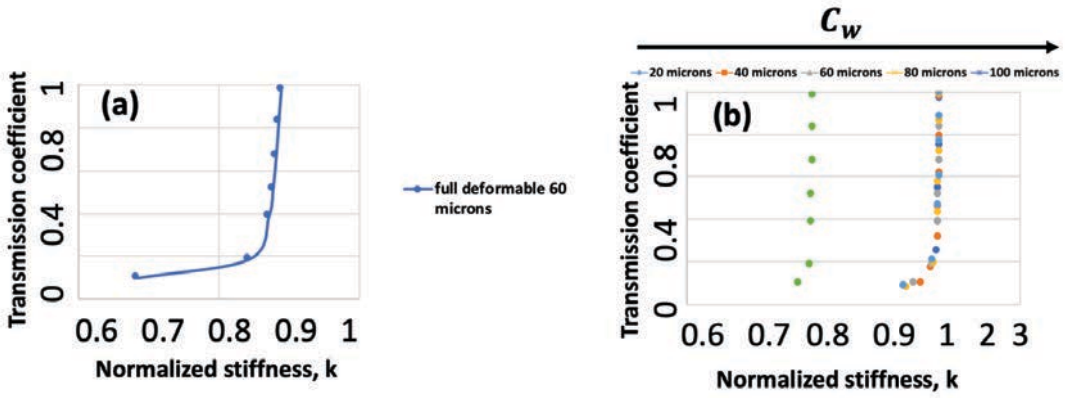

Figure C.2: (a) Transmission coefficient versus the interface stiffness for a single configuration (b) the single configuration is in comparision to the stiffness of other configuration of the previous model

From the figure it can be concluded that stiffness trend is quite the same in comparision to the previous model that was shown in 3.26. Although, it can be noticed that the stiffness value at which the transmission coefficient is recorded is much lower. This proves that the stiffness does not change concerning change in the model definitions and validates the way the stiffness is evaluated.

References

[1] Jai-Man Baik et R. Bruce Thompson. “Ultrasonic scattering from imperfect interfaces: A quasi-static model”. In : *Journal of Nondestructive Evaluation* 4.3 (déc. 1984), p. 177-196.

[2] L. A. Greenwood. “Contact of nominally flat surfaces”. In : *Proceedings of the Royal Society of London A: Mathematical, Physical and Engineering Sciences* 295.1442 (1966), p. 300-319.

[3] Yoshihisa MINAKUCHI. “Contact Pressure Measurement by Means of Ultrasonic Waves : On a Bolted Joint with a Solid-metal Flat Gasket”. In : *JSME International Journal Series C Mechanical Systems, Machine Elements and Manufacturing* 28.239 (1985), p. 792-798.

[4] S. Timoshenko et J.N. Goodier. *Theory of Elasticity, by S. Timoshenko and J.N. Goodier, ... 2nd Edition*. McGraw-Hill Book Company, 1951.

[5] A.W. Bush, R.D. Gibson et T.R. Thomas. “The elastic contact of a rough surface”. In : *Wear* 35.1 (1975), p. 87-111.

[6] Michael Selwyn Longuet-Higgins et George Edward Raven Deacon. “The statistical analysis of a random, moving surface”. In : *Philosophical Transactions of the Royal Society of London. Series A, Mathematical and Physical Sciences* 249.966 (1957), p. 321-387.

[7] J. Krolikowski et J. Szczepek. “Assessment of tangential and normal stiffness of contact between rough surfaces using ultrasonic method”. In : *Wear* 160 (fév. 1993), p. 253-258.

[8] Xi Shi et Andreas A. Polycarpou. “Measurement and Modeling of Normal Contact Stiffness and Contact Damping at the Meso Scale”. In : *Journal of Vibration and Acoustics* 127.1 (mar. 2005), p. 52-60.

[9] M.E. Kartal et al. “Measurements of pressure and area dependent tangential contact stiffness between rough surfaces using digital image correlation”. In : *Tribology International* 44.10 (2011), p. 1188-1198.

[10] Dayi Zhang et al. “Interfacial contact stiffness of fractal rough surfaces”. In : *Scientific Reports* 7.1 (oct. 2017), p. 12874.

[11] W. Wang et al. “Finite Element Analysis of Normal Contact Stiffness between Real Rough Surfaces Based on ANSYS”. In : *2012 Fourth International Conference on Computational and Information Sciences*. Août 2012, p. 127-130.

[12] Lior Kogut et Izhak Etsion. “A static friction model for elastic-plastic contacting rough surfaces”. In : *Journal of Tribology* 126.1 (2004), p. 34-40.

[13] R. Sahli et al. “Evolution of real contact area under shear and the value of static friction of soft materials”. In : *PNAS* 115.3 (2018), p. 471-476.

[14] L. Mourier et al. “Transient increase of film thickness in micro textured EHL contacts”. In : *Tribology International* 39 (2006), p. 1745-1756.

[15] A de Pannemaecker et al. “In situ fretting fatigue crack propagation analysis using synchrotron X-ray radiography”. In : *International Journal of Fatigue* 97 (2017), p. 56-69.

[16] J-Y Buffiere et al. “In situ X-ray tomography studies of microstructural evolution combined with 3D modeling”. In : *MRS bulletin* 33.6 (2008), p. 611-619.

[17] Kyle G. Rowe et al. “In situ thermal measurements of sliding contacts”. In : *Tribology International* 62 (2013), p. 208-214.

[18] Chuck Hellier. *Handbook of Nondestructive Evaluation, Second Edition*. McGraw-Hill Professional, 2012.

[19] Brice Jonckheere et al. “Assessment of the real contact area of a multi-contact interface from electrical measurements”. In : *23ème Congrès Français de Mécanique, France* (2017).

[20] Edward R. Generazio et Lewis Research Center. *The role of the reflection coefficient in precision measurement of ultrasonic attenuation [microform] / Edward R. Generazio ; prepared for the 1984 Annual Review of Progress in Quantitative Nondestructive Evaluation sponsored by the Defense Advanced Research Projects Agency (DARPA), LaJolla, California, July 8-13, 1984*. English. Lewis Research Center Cleveland, Ohio, 1984, 1 v. :

[21] F. Förster. “Sensitive eddy-current testing of tubes for defects on the inner and outer surfaces”. In : *Non-Destructive Testing* 7.1 (1974), p. 28-36.

[22] J. Blitz et G. Simpson. *Ultrasonic Methods of Non-destructive Testing*. Non-Destructive Evaluation Series. Springer Netherlands, 1995.

[23] Joseph L. Rose. *Ultrasonic Guided Waves in Solid Media*. Cambridge University Press, 2014.

[24] M.G. Silk. “The transfer of ultrasonic energy in the diffraction technique for crack sizing”. In : *Ultrasonics* 17.3 (1979), p. 113-121.

[25] Gregory Sharat Lin. *Dual-frequency ultrasonic array transducer and method of harmonic imaging*. US Patent 6,540,683. Déc. 2003.

[26] A. R. Selfridge. “Approximate Material Properties in Isotropic Materials”. In : *IEEE Transactions on Sonics and Ultrasonics* 32.3 (mai 1985), p. 381-394.

[27] Jérôme Poguet et al. “Phased array technology: Concepts, probes and applications”. In : *Journal of Nondestructive Testing & Ultrasonics(Germany)* 7.5 (2002), p. 1-6.

[28] A. McNab et M.J. Campbell. “Ultrasonic phased arrays for nondestructive testing”. In : *NDT International* 20.6 (1987), p. 333-337.

[29] Keiki Yamaguchi et al. *Linear array ultrasonic transducer*. US Patent 4,385,255. Déc. 1983.

[30] John N Antonevich. *Ultrasonic transducers*. US Patent 3,370,186. Fév. 1968.

[31] Jean-Pierre Ardouin et AN Venetsanopoulos. “Modelling and restoration of ultrasonic phased-array B-scan images”. In : *Ultrasonic imaging* 7.4 (1985), p. 321-344.

[32] Miguel Goñi et Carl-Ernst Rousseau. “On the Use of Ultrasonic Pulse-Echo Immersion Technique for Measuring Real Attenuation”. In : *Experimental Mechanics of Composite, Hybrid, and Multifunctional Materials, Volume 6*. Sous la dir. de G P Tandon et al. Cham : Springer International Publishing, 2014, p. 255-257.

[33] Xiangtao Yin. “The Study of Ultrasonic Pulse-echo Subwavelength Defect Detection Mechanism”. Thèse de doct. University of Illinois at Urbana-Champaign, 2003.

[34] S Kasolang et R S Dwyer-Joyce. “Viscosity measurement in thin lubricant films using shear ultrasonic reflection”. In : *Proceedings of the Institution of Mechanical Engineers, Part J: Journal of Engineering Tribology* 222.3 (2008), p. 423-429.

[35] H G Tattersall. “The ultrasonic pulse-echo technique as applied to adhesion testing”. In : *Journal of Physics D: Applied Physics* 6.7 (1973), p. 819.

[36] Kendall et Tabor. “An utrasonic study of the area of contact between stationary and sliding surfaces”. In : *Proceedings of the Royal Society of London A: Mathematical, Physical and Engineering Sciences* 323.1554 (1971), p. 321-340.

[37] Kracter L. “A novel method for measuring ultrasound pressure”. In : *Composite Structures* 5 (1958), p. 246-248.

[38] N. F. Haines et D. B. Langston. “The reflection of ultrasonic pulses from surfaces”. In : *The Journal of the Acoustical Society of America* 67.5 (1980), p. 1443-1454.

[39] R. B. Thompson et C. J. Fiedler. *The effects of crack closure on ultrasonic scattering measurements*. United States : Plenum Press, 1984.

[40] Ted L Anderson. *Fracture mechanics: fundamentals and applications*. CRC press, 2017.

[41] D. D. Palmer et al. “Nondestructive characterization of the mechanical strength of diffusion bonds. I. Experimental results”. In : *Journal of Nondestructive Evaluation* 7.3 (déc. 1988), p. 153-166.

[42] J. O. Taylor. “Kissing Bonds in Diffusion Bonded Parts”. In : *Review of Progress in Quantitative Nondestructive Evaluation: Volume 16A*. Sous la dir. de Donald O. Thompson et Dale E. Chimenti. Boston, MA : Springer US, 1997, p. 1215-1222.

[43] Peter B. Nagy. “Ultrasonic classification of imperfect interfaces”. In : *Journal of Nondestructive Evaluation* 11.3 (déc. 1992), p. 127-139.

[44] J. Królikowski et J. Szczepek. “Prediction of contact parameters using ultrasonic method”. In : *Wear* 148.1 (1991), p. 181-195.

[45] A. Polijaniuk et J. Kaczmarek. “Novel Stage for Ultrasonic Measurement of Real Contact Area Between Rough and Flat Parts Under Quasi-Static Load”. In : (1993).

[46] Massimiliano Pau. “Estimation of real contact area in a wheel-rail system by means of ultrasonic waves”. In : *Tribology International* 36.9 (2003), p. 687-690.

[47] Drinkwater. “A study of the interaction between ultrasound and a partially contacting solid—solid interface”. In : *Proceedings of the Royal Society of London A: Mathematical, Physical and Engineering Sciences* 452.1955 (1996), p. 2613-2628.

[48] M.B. Marhsall et al. “Measuring wheel/rail contact stresses using ultrasound”. Nov. 2004.

[49] S. Biwa, S. Nakajima et N. Ohno. “On the Acoustic Nonlinearity of Solid-Solid Contact With Pressure-Dependent Interface Stiffness”. In : *Journal of Applied Mechanics* 71.4 (sept. 2004), p. 508-515.

[50] T. E. Tallian et al. “Lubricant Films in Rolling Contact of Rough Surfaces”. In : *A S L E Transactions* 7.2 (1964), p. 109-126.

[51] RE Challis et al. “Near-plane-wave acoustic propagation measurements in thin layers of adhesive polymer”. In : *Measurement Science and Technology* 2.1 (1991), p. 59.

[52] William Anderson, Richard F Salant et Jacek Jarzynski. “Ultrasonic detection of lubricating film collapse in mechanical seals”. In : *Tribology transactions* 42.4 (1999), p. 801-806.

[53] D Anderson, J Jarzynski et R. F. Salant. “Condition monitoring of mechanical seals: Detection of film collapse using reflected ultrasonic waves”. In : *Proceedings of the Institution of Mechanical Engineers, Part C: Journal of Mechanical Engineering Science* 214.9 (2000), p. 1187-1194.

[54] R. S. Dwyer-Joyce, T. Reddyhoff et J. Zhu. “Ultrasonic Measurement for Film Thickness and Solid Contact in Elastohydrodynamic Lubrication”. In : *Journal of Tribology* 133.3 (juin 2011), p. 031501-031501-11.

[55] Jie Zhang, Bruce W Drinkwater et Rob S Dwyer-Joyce. “Calibration of the ultrasonic lubricant-film thickness measurement technique”. In : *Measurement Science and Technology* 16.9 (juil. 2005), p. 1784-1791.

[56] B Hosten. “Bulk heterogeneous plane waves propagation through viscoelastic plates and stratified media with large values of frequency domain”. In : *Ultrasonics* 29.6 (1991), p. 445-450.

[57] Tom Pialucha et Peter Cawley. “The detection of thin embedded layers using normal incidence ultrasound”. In : *Ultrasonics* 32.6 (1994), p. 431-440.

[58] Meng Li et al. “Ultrasonic Measurement of Cylindrical Roller–Bearing Lubricant Film Distribution with Two Juxtaposed Transducers”. In : *Tribology Transactions* 60.1 (2017), p. 79-86.

[59] Tao Geng et al. “Ultrasonic measurement of lubricant film thickness in sliding bearings with thin liners”. In : *Measurement Science and Technology* 26.2 (2015), p. 025002.

[60] B. Praher et G. Steinbichler. “Ultrasound-based measurement of liquid-layer thickness: A novel time-domain approach”. In : *Mechanical Systems and Signal Processing* 82 (jan. 2017), p. 166-177.

[61] D. M. Mulvihill et al. “A comparison of contact stiffness measurements obtained by the digital image correlation and ultrasound techniques”. English. In : *Experimental Mechanics* 53.7 (sept. 2013), p. 1245-1263.

[62] Hyo-Sok Ahn et Doo-In Kim. “In situ evaluation of wear surface by ultrasound”. In : 251 (oct. 2001), p. 1193-1201.

[63] Y.C. Tasan. “Measurement of deformation in rolling and sliding contacts”. Undefined. Thèse de doct. University of Twente, juil. 2005.

[64] Fei Du, Jun Hong et Ying Xu. “An acoustic model for stiffness measurement of tribological interface using ultrasound”. English. In : *Tribology International* 73.Complete (2014), p. 70-77.

[65] Ashish Kumar Singh et al. “Finite element modeling of nonlinear acoustics/ultrasonics for the detection of closed delaminations in composites”. In : *Ultrasonics* 74 (2017), p. 89-98.

[66] Yosuke Ishii, Shiro Biwa et Akira Kuraishi. “Influence of porosity on ultrasonic wave velocity, attenuation and interlaminar interface echoes in composite laminates: Finite element simulations and measurements”. In : *Composite Structures* 152 (2016), p. 645-653.

[67] John C Aldrin et Jeremy S Knopp. “Modeling and simulation for nondestructive testing with applications to aerospace structures”. In : *Materials Evaluation* 66.1 (2008), p. 53.

[68] W Lord, R Ludwig et Z You. “Developments in ultrasonic modeling with finite element analysis”. In : *Journal of nondestructive evaluation* 9.2-3 (1990), p. 129-143.

[69] Mike JS Lowe, David N Alleyne et Peter Cawley. “Defect detection in pipes using guided waves”. In : *Ultrasonics* 36.1-5 (1998), p. 147-154.

[70] Reinhold Ludwig et William Lord. “A finite-element formulation for the study of ultrasonic NDT systems”. In : *IEEE transactions on ultrasonics, ferroelectrics, and frequency control* 35.6 (1988), p. 809-820.

[71] David N Alleyne et Peter Cawley. “The interaction of Lamb waves with defects”. In : *IEEE transactions on ultrasonics, ferroelectrics, and frequency control* 39.3 (1992), p. 381-397.

[72] DN Alleyne, MJS Lowe et P Cawley. “The reflection of guided waves from circumferential notches in pipes”. In : *Journal of Applied mechanics* 65.3 (1998), p. 635-641.

[73] W.M. Karunasena, K.M. Liew et S. Kitipornchai. “Hybrid analysis of Lamb wave reflection by a crack at the fixed edge of a composite plate”. In : *Computer Methods in Applied Mechanics and Engineering* 125.1 (1995), p. 221-233.

[74] YT Gu et GR Liu. “A boundary point interpolation method for stress analysis of solids”. In : *Computational Mechanics* 28.1 (2002), p. 47-54.

[75] Ivan Bartoli et al. “Modeling wave propagation in damped waveguides of arbitrary cross-section”. In : *Journal of Sound and Vibration* 295.3-5 (2006), p. 685-707.

[76] Z You et W Lord. “Finite element study of elastic wave interaction with cracks”. In : *Review of Progress in Quantitative Nondestructive Evaluation*. Springer, 1989, p. 109-116.

[77] Seth S Kessler et al. “Damage detection in composite materials using frequency response methods”. In : *Composites Part B: Engineering* 33.1 (2002), p. 87-95.

[78] John J Ditri et Joseph L Rose. “Excitation of guided elastic wave modes in hollow cylinders by applied surface tractions”. In : *Journal of applied physics* 72.7 (1992), p. 2589-2597.

[79] Michel Castaings et Bernard Hosten. “Guided waves propagating in sandwich structures made of anisotropic, viscoelastic, composite materials”. In : *The Journal of the Acoustical Society of America* 113.5 (2003), p. 2622-2634.

[80] Padma Kumar Puthillath et al. “Ultrasonic guided waves for the inspection of adhesively bonded joints”. In : *AIP Conference Proceedings*. T. 975. 1. AIP. 2008, p. 200-206.

[81] L Maio et al. “Ultrasonic wave propagation in composite laminates by numerical simulation”. In : *Composite Structures* 121 (2015), p. 64-74.

[82] Mickael Brice Drozdz. “Efficient finite element modelling of ultrasound waves in elastic media”. Thèse de doct. Imperial College London, 2008.

[83] Karl F Graff. *Wave motion in elastic solids*. Courier Corporation, 2012.

[84] Jan Achenbach. *Wave propagation in elastic solids*. T. 16. Elsevier, 2012.

[85] Arnold D Kim et Akira Ishimaru. “A Chebyshev spectral method for radiative transfer equations applied to electromagnetic wave propagation and scattering in a discrete random medium”. In : *Journal of Computational Physics* 152.1 (1999), p. 264-280.

[86] Ushnish Basu et Anil K. Chopra. “Perfectly matched layers for time-harmonic elastodynamics of unbounded domains: theory and finite-element implementation”. In : *Computer Methods in Applied Mechanics and Engineering* 192.11 (2003), p. 1337-1375.

[87] Dan Givoli. “High-order local non-reflecting boundary conditions: a review”. In : *Wave motion* 39.4 (2004), p. 319-326.

[88] Qing-Huo Liu. “Perfectly matched layers for elastic waves in cylindrical and spherical coordinates”. In : *The Journal of the Acoustical Society of America* 105.4 (1999), p. 2075-2084.

[89] Jan Drewes Achenbach. “Quantitative nondestructive evaluation”. In : *International Journal of Solids and Structures* 37.1-2 (2000), p. 13-27.

[90] S.W. Smith, G.E. Trahey et O.T. von Ramm. “Phased array ultrasound imaging through planar tissue layers”. In : *Ultrasound in Medicine Biology* 12.3 (1986), p. 229-243.

[91] M.G. Silk et B.H. Lidington. “The potential of scattered or diffracted ultrasound in the determination of crack depth”. In : *Non-Destructive Testing* 8.3 (1975), p. 146-151.

[92] Olympus NDT. *Beam Characteristics propagation from an ultrasonic array*. 2011.

[93] Sandy Cochran. “Ultrasonics Part 12. Fundamentals of ultrasonic phased arrays”. In : *Insight-Non-Destructive Testing and Condition Monitoring* 48.4 (2006), p. 212-217.

[94] Waltham. *Introduction to Phased Array Ultrasonic Technology Applications*. 2007.

[95] Waltham. *Phased Array Testing: Basic Theory for Industrial Applications*. 2010.

[96] Jørgen Arendt Jensen et al. “Experimental ultrasound system for real-time synthetic imaging”. In : *1999 IEEE Ultrasonics Symposium. Proceedings. International Symposium (Cat. No. 99CH37027)*. T. 2. IEEE. 1999, p. 1595-1599.

[97] Shi-Chang Wooh et Yijun Shi. “Influence of phased array element size on beam steering behavior”. In : *Ultrasonics* 36.6 (1998), p. 737-749.

[98] Shi-Chang Wooh et Yijun Shi. “Optimization of Ultrasonic Phased Arrays”. In : *Review of Progress in Quantitative Nondestructive Evaluation: Volume 17A*. Sous la dir. de Donald O. Thompson et Dale E. Chimenti. Boston, MA : Springer US, 1998, p. 883-890.

[99] Warren L Stutzman et Gary A Thiele. *Antenna theory and design*. John Wiley & Sons, 2012.

[100] Alexander Ng et Justiaan Swanevelder. “Resolution in ultrasound imaging”. In : *Continuing Education in Anaesthesia Critical Care & Pain* 11.5 (2011), p. 186-192.

[101] C. Passmann et H. Ermert. “A 100-MHz ultrasound imaging system for dermatologic and ophthalmologic diagnostics”. In : *IEEE Transactions on Ultrasonics, Ferroelectrics, and Frequency Control* 43.4 (juil. 1996), p. 545-552.

[102] S.R. Doctor, T.E. Hall et L.D. Reid. “SAFT — the evolution of a signal processing technology for ultrasonic testing”. In : *NDT International* 19.3 (1986), p. 163-167.

[103] Caroline Holmes, Bruce W Drinkwater et Paul D Wilcox. “Post-processing of the full matrix of ultrasonic transmit–receive array data for non-destructive evaluation”. In : *NDT & e International* 38.8 (2005), p. 701-711.

[104] Alan J Hunter, Bruce W Drinkwater et Paul D Wilcox. “The wavenumber algorithm for full-matrix imaging using an ultrasonic array”. In : *IEEE transactions on ultrasonics, ferroelectrics, and frequency control* 55.11 (2008), p. 2450-2462.

[105] Chengguang Fan et al. “Multi-frequency time-reversal-based imaging for ultrasonic nondestructive evaluation using full matrix capture”. In : *IEEE transactions on ultrasonics, ferroelectrics, and frequency control* 61.12 (2014), p. 2067-2074.

[106] David Lines et al. “Real-Time Ultrasonic Array Imaging using Full Matrix Capture and the Total Focusing Method”. In : avr. 2011.

[107] D. J. Huggett et al. “Phased Array Ultrasonic Testing for Post-Weld and OnLine Detection of Friction Stir Welding Defects”. In : *Research in Nondestructive Evaluation* 28.4 (2017), p. 187-210.

[108] Cheng-Wei Tseng, Young-Fo Chang et Chung-Yue Wang. “Total Focusing Method or Phased Array Technique: Which Detection Technique Is Better for the Ultrasonic Nondestructive Testing of Concrete?” In : *Journal of Materials in Civil Engineering* 30.1 (2017), p. 04017256.

[109] Alexander Velichko et Paul D Wilcox. “An analytical comparison of ultrasonic array imaging algorithms”. In : *The Journal of the Acoustical Society of America* 127.4 (2010), p. 2377-2384.

[110] S Mahaut et al. “Recent advances and current trends of ultrasonic modelling in CIVA”. In : *Insight-Non-Destructive Testing and Condition Monitoring* 51.2 (2009), p. 78-81.

[111] Olivier Roy et MS Chatillon. “Ultrasonic inspection of complex geometry component specimen with a smart flexible contact phased array transducer: Modeling and application”. In : *2000 IEEE Ultrasonics Symposium. Proceedings. An International Symposium (Cat. No. 00CH37121)*. T. 1. IEEE. 2000, p. 763-766.

[112] Ekaterina Iakovleva et al. “Multi-mode TFM imaging with artifacts filtering using CIVA UT forwards models”. In : *AIP Conference Proceedings*. T. 1581. 1. AIP. 2014, p. 72-79.

[113] Bruce W Drinkwater et Paul D Wilcox. “Ultrasonic arrays for non-destructive evaluation: A review”. In : *NDT & e International* 39.7 (2006), p. 525-541.

[114] Jacob Davies et al. “Review of synthetically focused guided wave imaging techniques with application to defect sizing”. In : *AIP Conference Proceedings*. T. 820. 1. AIP. 2006, p. 142-149.

[115] Weibao Qiu et al. “A flexible annular-array imaging platform for micro-ultrasound”. In : *IEEE transactions on ultrasonics, ferroelectrics, and frequency control* 60.1 (2013), p. 178-186.

[116] Minghui Li et Gordon Hayward. “Ultrasound nondestructive evaluation (NDE) imaging with transducer arrays and adaptive processing”. In : *Sensors* 12.1 (2012), p. 42-54.

[117] Minghui Li, Gordon Hayward et Bo He. “Adaptive array processing for ultrasonic non-destructive evaluation”. In : *2011 IEEE International Ultrasonics Symposium*. IEEE. 2011, p. 2029-2032.

[118] K Nakahata et al. “Ultrasonic imaging using signal post-processing for a flexible array transducer”. In : *Ndt & E International* 82 (2016), p. 13-25.

[119] Jonathan Mamou, Jeffrey A. Ketterling et Ronald H. Silverman. “High-frequency pulse-compression ultrasound imaging using an 18-MHz annular array”. In : *The Journal of the Acoustical Society of America* 120.5 (2006), p. 3194-3194.

[120] R Manwar et al. “Fabrication and characterization of a high frequency and high coupling coefficient CMUT array”. In : *Microsystem Technologies* 23.10 (2017), p. 4965-4977.

[121] DL Hopkins et al. “Surface-adaptive ultrasound (SAUL) for phased-array inspection of composite specimens with curved edges and complex geometry”. In : *AIP Conference Proceedings*. T. 1511. 1. AIP. 2013, p. 809-816.

[122] Henry Peter Brunskill. “The real-time characterisation of dry machine element contacts using ultrasonic reflectometry”. Thèse de doct. University of Sheffield, 2013.

[123] Kang-Sik Kim, Jie Liu et Michael F. Insana. “Efficient array beam forming by spatial filtering for ultrasound B-mode imaging”. In : *The Journal of the Acoustical Society of America* 120.2 (2006), p. 852-861.

[124] Maria V Felice, Alexander Velichko et Paul D Wilcox. “Accurate depth measurement of small surface-breaking cracks using an ultrasonic array post-processing technique”. In : *NDT & E International* 68 (2014), p. 105-112.

[125] Shi-Chang Wooh et Yijun Shi. “A simulation study of the beam steering characteristics for linear phased arrays”. In : *Journal of nondestructive evaluation* 18.2 (1999), p. 39-57.

[126] A. N. Evans et M. S. Nixon. “Biased motion-adaptive temporal filtering for speckle reduction in echocardiography”. In : *IEEE Transactions on Medical Imaging* 15.1 (fév. 1996), p. 39-50.

[127] Gheorghe Gavriloaia, M Gherghe et M Gavriloaia. “Anisotropic Diffusion and Wavelet Filtering of Ultrasound Images”. In : *Ultrasound in Medicine and Biology - ULTRASOUND MED BIOL* 37 (août 2011).

[128] Jean Provost et al. “3-D Ultrafast Doppler Imaging Applied to the Noninvasive Mapping of Blood Vessels In Vivo”. In : *Ultrasonics, Ferroelectrics, and Frequency Control, IEEE Transactions on* 62 (août 2015), p. 1467-1472.

[129] Kombossé Sy. “Étude et développement de méthodes de caractérisation de défauts basées sur les reconstructions ultrasonores TFM”. Thèse de doct. Fév. 2018.

[130] N. Portzgen, D. Gisolf et G. Blacquiere. “Inverse wave field extrapolation: a different NDI approach to imaging defects”. In : *IEEE Transactions on Ultrasonics, Ferroelectrics, and Frequency Control* 54.1 (jan. 2007), p. 118-127.

[131] N. Portzgen, D. Gisolf et D. J. Verschuur. “Wave equation-based imaging of mode converted waves in ultrasonic NDI, with suppressed leakage from nonmode converted waves”. In : *IEEE Transactions on Ultrasonics, Ferroelectrics, and Frequency Control* 55.8 (août 2008), p. 1768-1780.

[132] Ekaterina Iakovleva et al. “Multi-mode TFM imaging with artifacts filtering using CIVA UT forwards models”. In : *AIP Conference Proceedings* 1581.1 (2014), p. 72-79.

[133] Kevin A Snook et al. “High-frequency ultrasound annular-array imaging. Part I: Array design and fabrication”. In : *IEEE transactions on ultrasonics, ferroelectrics, and frequency control* 53.2 (2006), p. 300-308.

ÉCOLE CENTRALE LYON

Ecully, le 5 février 2020

Direction des Etudes
Scolarité 3° Cycle

Monsieur VIJIGIRI Vipul
Laboratoire de Tribologie et Dynamique des Systèmes
ECOLE CENTRALE DE LYON

Monsieur,

J'ai l'honneur de vous confirmer les dispositions concernant votre soutenance de thèse de Docteur qui aura lieu

mardi le 11 février 2020

10h00 - Salle de Conférences - ENISE - 74 rue des Aciéries - Saint-Etienne

devant le Jury ci-dessous :

R. DWYER-JOYCE	Professeur	Department of Mechanical Engineering - Sheffield University - RC02f Mappin Mining Block - Mapping street - Sheffield - S1 3JD - Royaume-Uni
M. BIGERELLE	Professeur	LAMIH - CNRS UMR8201 - UVHC - Le Mont Houy - 59313 Valenciennes cedex 9
J-L. GENNISSON	Directeur de Recherche CNRS	Imagerie par Résonance Magnétique Médicale et Multi-Modalités - CNRS UMR 8081 - Université Paris Sud - CEA Service Hospitalier Frédéric Joliot - 4 place Général Leclerc - 91401 Orsay cedex
C. COURBON	Maître de Conférences	Ecole Nationale d'Ingénieurs de Saint-Etienne - LTDS CNRS UMR5513 - 58 rue Jean Parot - 42100 Saint-Etienne
G. KERMOUCHE	Professeur	Ecole des Mines de Saint-Etienne - LGF CNRS UMR5307 - 158 cours Fauriel - 42023 Saint-Etienne
J. CAYER-BARRIOZ	Directrice de Recherche CNRS	Laboratoire de Tribologie et Dynamique des Systèmes - Ecole centrale de Lyon

sous le n° d'ordre NNT : **2020LYSEC07**
Conservez bien ce numéro, vous devrez l'indiquer sur la page de garde de votre thèse

Vous trouverez en annexe :

- l'autorisation de soutenance signée par le Directeur de l'E.C.L. à joindre au manuscrit final (dernière page),
- les directives concernant l'enregistrement électronique de la thèse
- copie des rapports sur le mémoire

Je vous prie de croire, Monsieur, à l'expression de mes sentiments les meilleurs.

Le directeur des Etudes

Grégory VIAL

36, avenue Guy-de-Collongue - 69134 Écully Cedex - France
T +33 (0) 4 72 18 60 00
www.ec-lyon.fr
SIRET : 196 901 870 000 10 - APE 8542Z

Membre de UNIVERSITÉ DE LYON

dernière page de la thèse

AUTORISATION DE SOUTENANCE

Vu les dispositions de l'arrêté du 25 mai 2016,

Vu la demande du directeur de thèse

Madame J. CAYER-BARRIOZ et Monsieur G. KERMOUCHE

et les rapports de

M. R. DWYER-JOYCE
Professeur - Department of Mechanical Engineering - Sheffield University
RC02f Mappin Mining Block - Mapping street - Sheffield - S1 3JD - Royaume-Uni

et de

M. M. BIGERELLE
Professeur - LAMIH - CNRS UMR8201 - UVHC - Le Mont Houy - 59313 Valenciennes cedex 9

Monsieur VIJIGIRI Vipul

est autorisé à soutenir une thèse pour l'obtention du grade de **DOCTEUR**

Ecole doctorale MECANIQUE, ENERGETIQUE, GENIE CIVIL ET ACOUSTIQUE

Fait à Ecully, le 5 février 2020

P/Le directeur de l'E.C.L.
Le directeur des Etudes

Grégory VIAL